

THE STRUCTURE AND DYNAMIC
NATURE OF THE SOLAR
ATMOSPHERE

Michael Stewart Marsh

A THESIS SUBMITTED IN PARTIAL FULFILMENT
OF THE REQUIREMENTS FOR THE DEGREE OF
DOCTOR OF PHILOSOPHY

Centre for Astrophysics
Department of Physics, Astronomy and Mathematics
University of Central Lancashire

July 2005

Abstract

This thesis presents an examination of a range of dynamic phenomena present throughout the solar atmosphere, from the photosphere to the corona. Above the photosphere, where the plasma β is small, the emitting plasma structure and dynamics are tied intimately to the solar magnetic field.

Firstly, a wavelet analysis is applied to multi-temperature spectroscopic data observing network-internetwork regions across a coronal hole boundary region. The nature of quasi-periodic variability is investigated through the different temperature lines across the observed structures. Statistically significant periods are found within the range 100–900 seconds, along with short period wavepackets with periods 50–100 seconds. These oscillations are discussed in terms of possible wave mechanisms. An example of a time-dependent period is observed above the network region on the coronal hole boundary and possible theoretical origins are discussed.

Secondly, a detailed analysis is applied to an active region observed on the solar limb. A dynamic transition region loop, and closely associated ejection event are observed within the active region. These structures are characterised by their emission line profiles; the transition region loop is found to have a flow geometry of $-20 \rightarrow 40 \text{ km s}^{-1}$, and the ejection event is found to have a velocity gradient up to $-20 \rightarrow 50 \text{ km s}^{-1}$ across its width, suggesting a rotating transition region structure consistent with a macrospicule.

Thirdly, an upwardly propagating disturbance is observed along a coronal loop associated with a plage region with a velocity $50\text{--}195 \text{ km s}^{-1}$ perpendicular to the line of sight, and period of 5 minutes. A wavelet analysis reveals that the five minute period is present in co-spatial, co-temporal chromospheric and transition region observations. This is interpreted as the first

observation of a 5-min p-mode propagating through the chromosphere, transition region and into a coronal loop.

Fourthly, an observing campaign is designed and executed to probe the connectivity between the chromosphere, transition region and corona within active regions. Oscillations within the 3-min band are observed above the umbra of a sunspot active region. These oscillations show two closely separated frequencies of 6.1 & 7.1 mHz in the chromosphere, 5.9 & 7.3 mHz in the transition region and 5.9 & 7.3 mHz in the corona. These observations are interpreted as acoustic/maneto-acoustic wave modes propagating upwards through the chromosphere, transition region and into the corona. The frequencies are observed as oscillations in the chromosphere and transition region, and propagations in the emerging coronal loops, due to the combined effect of the temperature scale height in the different spectral lines and the diverging magnetic flux geometry above the sunspot. The energy flux of acoustic waves is estimated in the different temperature lines as $28.3 \text{ erg cm}^{-2} \text{ s}^{-1}$ in the chromosphere, $201.0 \text{ erg cm}^{-2} \text{ s}^{-1}$ in the transition region and $225.6 \text{ erg cm}^{-2} \text{ s}^{-1}$ in the corona.

Finally, future work is discussed in terms of progressing the work completed, and exploiting upcoming spaced based missions.

Contents

Abstract	2
Copyright	14
Acknowledgements	15
Publications	16
1 Introduction	18
1.1 The local star	19
1.2 The magnetic Sun	21
1.3 The photosphere	25
1.4 The chromosphere	27
1.5 The transition region	28
1.6 The corona	29
1.7 Magnetic heating mechanisms	31
1.7.1 Direct current dissipation	31
1.7.2 Wave mechanisms	31
1.8 Waves observed within the solar atmosphere	33
1.9 Optically thin emission	34
1.10 Thesis outline	35
2 Instrumentation	36
2.1 The Coronal Diagnostic Spectrometer (CDS)	36

2.2	CDS-The Normal Incidence Spectrometer (NIS)	38
2.2.1	Instrumental effects	38
2.3	CDS-The Grazing Incidence Spectrometer (GIS)	41
2.3.1	Instrumental effects	41
2.4	The Transition Region and Coronal Explorer (TRACE)	42
2.4.1	Instrumental effects	43
2.5	The Michelson Doppler Imager (MDI)	45
3	Signal Analysis	47
3.1	Fourier Analysis	47
3.2	Wavelet analysis	49
3.2.1	Significance levels	51
4	Periodicity Within a Coronal Hole Boundary Region	53
4.1	Introduction	53
4.2	Observations	55
4.3	GIS instrumental effects	56
4.4	GIS calibration	57
4.5	Time series analysis	57
4.5.1	Pixel summing method	57
4.5.2	Curve Fitting of Ne VII and Ca IX	59
4.6	Wavelet analysis	60
4.6.1	Evenly spaced time series	60
4.7	Results	61
4.7.1	Localised short periods	64
4.8	Time dependent periodicity	65
4.8.1	Error analysis	67
4.9	Discussion	68
5	Active Region Structure and Dynamics	73
5.1	Introduction	73

5.2	Observations	73
5.2.1	Data reduction	74
5.2.2	Observing program	77
5.3	Active Region Loop: Qualitative Structure	82
5.4	Active Region Loop: Geometry	85
5.5	Active Region Loop: Quantitative O V Structure	87
5.6	Active Region Ejection: Qualitative Structure	89
5.7	Active Region Ejection: Quantitative Length Structure	97
5.7.1	He I	98
5.7.2	O V	103
5.7.3	Active Region Ejection: Density Scale Heights	108
5.8	Active Region Ejection: Quantitative Width Structure	108
5.8.1	He I	109
5.8.2	O V	113
5.9	Summary and Discussion	114
5.9.1	Active region loop	114
5.9.2	Active region ejection	119
6	Propagating Loop Oscillations with CDS and TRACE	123
6.1	Introduction	123
6.2	Observations	124
6.3	Calibration of the data	125
6.4	Pointing discrepancy and correlation of the data	127
6.5	Data analysis	127
6.5.1	CDS data analysis	129
6.5.2	TRACE data analysis	129
6.5.3	Wavelet analysis	129
6.6	Results	131
6.7	Conclusions	135
6.7.1	Further progress	137

7	CDS Wide Slit & TRACE Active Region Dynamics	139
7.1	Introduction	139
7.2	CDS Studies	140
7.2.1	UCLAN_MV	140
7.2.2	LOOP2D.5	141
7.2.3	EJECT_V3	141
7.2.4	Active Regions with the CDS Wide Slit	142
7.3	CDS data reduction	142
7.3.1	UCLAN_MV	143
7.3.2	EJECT_V3	144
7.4	TRACE Sequences	146
7.4.1	TRACE data reduction	146
7.5	MDI Sequences	147
7.5.1	MDI data reduction	147
7.6	Spatial solar rotation correction	148
7.7	SOHO keyhole correction	150
7.8	Observational Outline – 13th March 2004	151
7.9	Data analysis techniques – 13th March 2004	156
7.9.1	CDS wide slit	156
7.9.2	Randomisation Significance Test	156
7.9.3	TRACE	157
7.10	Observational Results – 13th March 2004	158
7.10.1	CDS wide slit	158
7.10.2	TRACE	164
7.11	Acoustic wave energy flux	167
7.11.1	Plasma particle number density	169
7.11.2	Plasma mean particle mass	171
7.11.3	Acoustic wave flux in He I, O V and TRACE 171 Å	172
7.12	Summary and discussion	172

8	Conclusions and Further Work	179
8.1	Loop Variability Campaign	179
8.2	The Atmospheric Seismology Joint Observing Program	181
8.3	Future missions	184
A	Active Region Structure and Dynamics	186
A.1	Vector Path Extraction Method	186
A.2	Errors of fitted Gaussian parameters	188
A.3	Calculation of errors for fitted line intensity	188
A.4	Calculation of errors for measured Doppler velocity	188
A.5	Calculation of errors for average extracted profile	189
A.6	Figures	190
B	CDS Wide Slit & TRACE Active Region Dynamics	202
B.1	Loop Variability Campaign: Summary of observations	202
B.2	Figures	202
C	Contents of the CD-ROM	215
C.1	Active region structure and dynamics (Chapter 5)	215
C.2	CDS wide slit & TRACE active region dynamics (Chapter 7)	215
C.3	Html and pdf versions of the thesis	216

List of Tables

4.1	Analysed GIS lines	57
4.2	GIS Wavelet Results	62
4.2	Continued.	63
5.1	Ejection $\frac{1}{e}$ emission and density scale lengths in He I and O V for rasters 0–2 .	108
5.2	Summary of qualitative analysis results	119
5.3	Summary of quantitative analysis results	120
6.1	Summary of JOP 83 TRACE observations analysed for 7 th –9 th April.	125
6.2	Summary of JOP 83 CDS observations analysed for 7 th –9 th April.	126
7.1	Summary of loop variability campaign observations on 13th March 2004.	140
7.2	Summary of loop variability CDS rasters.	142
7.3	Estimated plasma particle densities at He I, O V and TRACE 171 Å temperatures	171
7.4	Estimated acoustic wave energy flux	172
B.1	Summary of loop variability campaign observations	203

List of Figures

1.1	The changing structure of the Sun with temperature	18
1.2	P-mode propagation and spherical harmonics	20
1.3	Rotation of the solar interior	20
1.4	Solar neutrino image	21
1.5	Magnetic flux emergence	22
1.6	The Sun-like star flux-flux relationship	24
1.7	The H & K magnetic cycles in sun-like stars	24
1.8	High resolution image of the photosphere	25
1.9	The H α chromosphere	27
1.10	The dynamic transition region	28
1.11	The corona	29
2.1	CDS optical layout	37
2.2	The TRACE telescope	42
2.3	The TRACE EUV response functions	44
3.1	Fourier power spectra of test time series	48
3.2	The Morlet wavelet	50
3.3	Wavelet power spectra of test time series	51
4.1	O V and Mg IX context images of GIS observations	54
4.2	GIS ghosting regions	56
4.3	GIS Ne VII 465 Å time series	58
4.4	Number of cycles observed (L/P) in the first network region N1	65

4.5	(L/P) in the internetwork region I. Period range 0–500 Sec.	66
4.6	(L/P) in the internetwork region I. Period range 500–1600 Sec.	67
4.7	(L/P) in the second network region N2.	68
4.8	Ne IV, Ne VII 465 and Ne VIII 780 Å time dependent periodicity	69
4.9	Ne VIII 770 Å, O VI and Fe XI time dependent periodicity	70
5.1	Off-limb background subtraction	74
5.2	Rest wavelength calculation methods for Doppler velocity maps	75
5.3	Time dependent spectral tilt in He I and O V	76
5.4	He I 584 Å context images	78
5.5	O V 629 Å context images	79
5.6	Fe XVI 360 Å context images	80
5.7	Active region loop He I and O V Doppler velocities and intensities	83
5.8	Schematic loop and plasma flow geometries	86
5.9	O V raster #0 loop profile	90
5.10	O V raster #1 loop profile	91
5.11	O V raster #2 loop profile	92
5.12	O V raster #3 loop profile	93
5.13	Active region ejection He I and O V Doppler velocities and intensities	95
5.14	Active region ejection Fe XVI intensity	96
5.15	He I raster 0 ejection profiles	100
5.16	He I raster 1 ejection profiles	101
5.17	He I raster 2 ejection profiles	102
5.18	O V raster 0 ejection profiles	105
5.19	O V raster 1 ejection profiles	106
5.20	O V raster 2 ejection profiles	107
5.21	He I raster 0 ejection width profiles	110
5.22	He I raster 1 ejection width profiles	111
5.23	He I raster 2 ejection width profiles	112
5.24	O V raster 0 ejection width profiles	115

5.25	O V raster 1 ejection width profiles	116
5.26	O V raster 2 ejection width profiles	117
6.1	7 th April NIS (He I, O V and Mg IX) and TRACE 171 Å context images	128
6.2	JOP 83 results	130
6.3	He I, O V, Mg IX and TRACE 171 Å coincident wavelet power spectra	134
6.4	He I, O V, Mg IX and TRACE 171 Å time series	135
7.1	CDS wide slit dispersion	143
7.2	EJECT_V3 line position trend and correction	144
7.3	MDI Doppler rotation and correction	148
7.4	TRACE data cube <i>x</i> and <i>y</i> offsets	149
7.5	SOHO keyholes	150
7.6	Mg VII/IX blend above sunspot umbra	152
7.7	AR 10570 observed with MDI, CDS and TRACE	153
7.8	EJECT_V3 observations of AR 10570	154
7.9	AR 10570 He I and O V intensity and 3-min power maps	158
7.10	He I & O V time series, relative amplitude and FFT	160
7.11	He I & O V time series correlation	162
7.12	Interpolated He I & O V time series correlation	164
7.13	AR 10570 TRACE running difference image	165
7.14	Co-temporal He I, O V and TRACE time series	166
7.15	Extrapolated magnetic field lines	175
7.16	Atmospheric layers above sunspot	175
7.17	MDI magnetic oscillations?	177
A.1	Vector path extraction	187
A.2	<i>y</i> axis average velocity/tilt	190
A.3	Mg IX 368 Å context images	191
A.4	Si X 347 347 Å context images	192
A.5	Si X 356 Å context images	193

A.6	He I 584 Å running difference images	194
A.7	O V 629 Å running difference images	195
A.8	Mg IX 368 Å running difference images	196
A.9	Fe XVI 360 Å running difference images	197
A.10	He I 584 Å Doppler velocity maps	198
A.11	O V 629 Å Doppler velocity maps	199
A.12	Mg IX 368 Å Doppler velocity maps	200
A.13	Fe XVI 360 Å Doppler velocity maps	201
B.1	EJECT_V3 s29640r00-03 spectral tilt	204
B.2	EJECT_V3 s29640r00-03 corrected spectral tilt	205
B.3	MDI WL and magnetogram of AR 10570	206
B.4	EJECT_V3 s29740r00-02 He I	207
B.5	EJECT_V3 s29740r00-02 O V	208
B.6	EJECT_V3 s29740r00-02 Mg VII/IX	209
B.7	UCLAN_MV s29739r00-04 Fourier power maps	210
B.8	UCLAN_MV s29739r00-04 He I FFTs	211
B.9	UCLAN_MV s29739r00-04 O V FFTs	212
B.10	TRACE running difference images	213
B.11	Wavelet power spectra	214

Copyright

Copyright in text of this thesis rests with the Author. Copies (by any process) either in full, or of extracts, may be made **only** in accordance with instructions given by the Author and lodged in the University of Central Lancashire library. Details may be obtained from the Librarian. This page must form part of any such copies made. Further copies (by any process) of copies made in accordance with such instructions may not be made without the permission (in writing) of the Author.

The ownership of any intellectual property rights which may be described in this thesis is vested in the Author, subject to any prior agreement to the contrary, and may not be made available for use by third parties without the written permission of the Author, which will prescribe the terms and conditions of any such agreement.

Further information on the conditions under which disclosures and exploitation may take place is available from the head of the Centre for Astrophysics.

Acknowledgements

First and foremost thanks to my Mum and Dad. Thanks for getting me to this point in the first place, and thanks for all the support while I have been here, from the major support, to the countless lifts from my dad, to my mum's attempts to feed me up on the too few occasions I managed to make it home.

Thanks to Robert for his enthusiastic supervision of the work, inspite of my sceptical nature, and for reading through all the various drafts of this thesis and other publications.

Thanks to PPARC for funding my PhD studentship. To Jack for his hospitality in D.C. on my visit to Goddard, for the entertaining ebriety in various parts of the world and the useful discussions that have greatly assisted this work. To ESA & NASA, the SOHO and TRACE teams at Goddard Space Flight Center for their assistance, and making my observing campaign possible, in particular to the CDS team for allowing the wide slit observations.

To all the people who have helped and entertained me away from work. My Family: Mum, Dad, Dave, Steve, Chris, Karen, Louis and Olivia. Team Marsh: Me, Ste, Matt, Dan, Shaun, Baz, Pete...the list goes on. To all the friends I have met along the way, and all my different house mates. My current housemates and friends, that I haven't seen nearly enough; Lorraine for the 'heated discussions', looking after us and forbidding me from buying a playstation; Kelly for the brain food and Nathan for the surprise when we cross paths. My roomies Nicola, Anne-Marie and Suzanne for entertaining me at four in the morning. To all the good times, from the Union to 254a and their many connections! Doug, Dan, Matty Jones, Luppy, T Bear, Gaz, Jenny, Panos, Peris, Helen, Eldon St, ...too many to mention! + My CFA & crossword buddies. If I forgot you, sorry, but after writing this I can barely remember my own name, however the fact that you are reading this means you are one of my true friends.

Publications

Refereed Publications

Marsh, M.S., Walsh, R.W., 2005, 'The Propagation of Sunspot Waves Through the Chromosphere, Transition Region and Corona Along the Umbral Magnetic Field', *in preparation*.

Marsh, M.S., Walsh, R.W., De Moortel, I., Ireland, J., 2003, 'Joint Observations of Propagating Oscillations with SOHO/CDS and TRACE', *A&A*, 404, L37.

Marsh, M.S., Walsh, R.W., Bromage, B.J.I., 2002, 'A Wavelet Analysis of Quasi-Periodic Variability Across a Solar Coronal Hole Region', *A&A*, 393, 649.

Non-Refereed Publications

Marsh, M.S., Walsh, R.W., 2004, 'Joint CDS and TRACE Observations of Active Region Dynamics', *ESA SP-575*, 108.

Marsh, M.S., Walsh, R.W., De Moortel, I., Ireland, J., 2004, 'Longitudinal Oscillations in Coronal Loops: Joint Observations with SOHO/CDS and TRACE', *ESA SP-547*, 519.

Marsh, M.S., Walsh, R.W., Bromage, B.J.I., 2002, 'Observations of Time Dependent Periodicity Within the Coronal Hole Boundary', *ESA SP-505*, 497.

Marsh, M.S., Walsh, R.W., Bromage, B.J.I., 2002, 'A Wavelet Analysis of Quasi-Periodic Variability Within the Solar Corona', *ESA SP-508*, 319.

“Dang it, Jim, I’m an astronomer, not a doctor! I mean I am a doctor, but I’m not that kind of doctor! I have a doctorate, it’s not the same thing! You can’t help people with a doctorate! You just sit there and you’re useless!”

Disney’s Treasure Planet

Chapter 1

Introduction

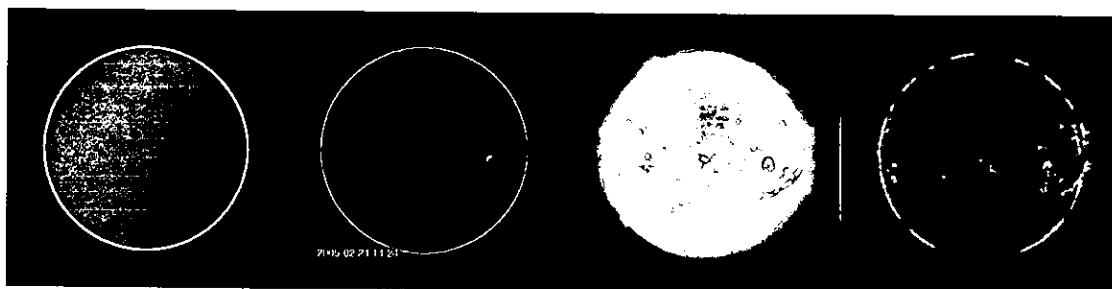


Figure 1.1: The changing structure of the Sun with temperature on the 24th February 2005; from left to right MDI white light continuum $T \sim 5780$ K, MDI photospheric magnetogram formed from the Ni I 6768 Å line, EIT He II 304 Å $T \sim 60,000$ K and EIT Fe IX 171 Å $T \sim 1,000,000$ K. The white light continuum images the photosphere, and indicates the inner regions of the sun that may be approximated by hydrodynamic equilibrium. The magnetogram shows the distribution of magnetic flux during this period of low solar activity. The He II and Fe IX images show the complex structures visible at chromospheric and coronal temperatures due to the magnetic field. Plasma within prominences and spicules emit at chromospheric temperatures, at the solar limb, across a range of altitudes, co-spatial with coronal emission.

This thesis details an observational analysis of the structure and dynamics of the directly observable regions of the solar atmosphere. Specifically the photosphere, chromosphere, transition region and corona. It has become the convention to consider these regions as an indication of altitude within the solar atmosphere. However, this is a hydrostatic over-simplification arising from theoretical attempts to model the physical properties of the atmosphere (such as density and temperature). In general, the density decreases with altitude whilst, paradoxically,

the temperature increases. However, the introduction of magnetic flux into the solar atmosphere generates a plethora of dynamic structures and phenomena that are not understood. This magnetic atmosphere can contain plasma across a large range of temperatures, densities and altitudes (Fig. 1.1). The terms delineating the different regions of the atmosphere should, therefore, be considered as an indication of the temperature of emitting plasma, rather than a definite altitude.

1.1 The local star

The Sun is a spectral class G2V star. Stellar observations of other solar mass stars allow the Sun, at a single point in time, to be interpreted in the context of its whole evolution. The Sun's close proximity allows detailed research into its physical structure and properties such as mass, radius, density, temperature, pressure, opacity, etc. This has allowed the development of precise models of the solar atmosphere, and provides a unique test of fundamental atomic and nuclear physics.

The Sun has a mass of 1.989×10^{30} kg, radius of 6.960×10^8 m, mean bolometric luminosity of 3.844×10^{26} W m² and age of 4.57×10^9 years. Current estimates using the standard solar model give a predicted core temperature of 15.7×10^6 K (in agreement with observed neutrino fluxes to within 2%), density of 1.52×10^5 kg m⁻³ and pressure of 2.37×10^{16} Pa.

Although only the outer regions of the solar atmosphere are directly observable, significant insight into the structure and dynamics of the solar interior has been attained using empirical techniques. The development of helioseismology, and observations of the solar neutrino flux have allowed the refinement of the standard model of the solar atmosphere to a high degree of precision. Helioseismology (see recent review by Christensen-Dalsgaard 2002) utilises observations of solar p-mode frequencies (Fig. 1.2) to constrain the values of density, ratio of specific heats γ and sound speed within the interior. Observed splitting of the p-mode frequencies have allowed the internal rotation rate of the Sun to be inferred as a function of depth, and solar latitude (Fig. 1.3). The convection zone is then observed to extend to a depth of $0.7 R_{\odot}$. This boundary between the radiative and convection zones is termed the tachocline, and is thought to be the region where the solar magnetic field is generated due to the shear effect of

CHAPTER 1. INTRODUCTION

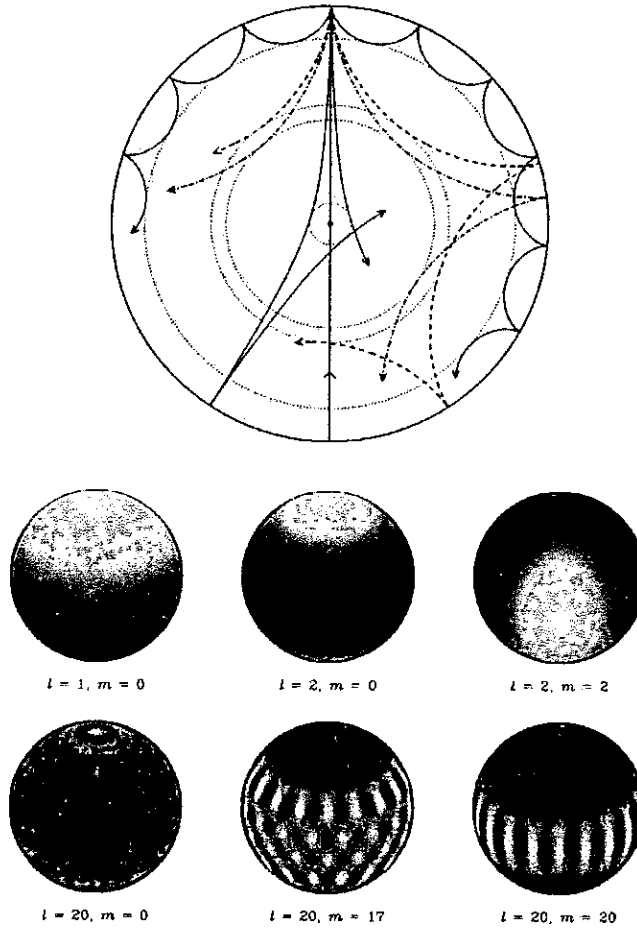


Figure 1.2: *Upper*: P-mode propagation within the solar interior. Each mode is refracted by the increase in sound speed with depth. The modes are reflected at the photospheric surface due to the sharp decrease in density. *Lower*: Examples of the spherical harmonics produced by the p-mode oscillations for varying degree l and order m (from Christensen-Dalsgaard 2002).

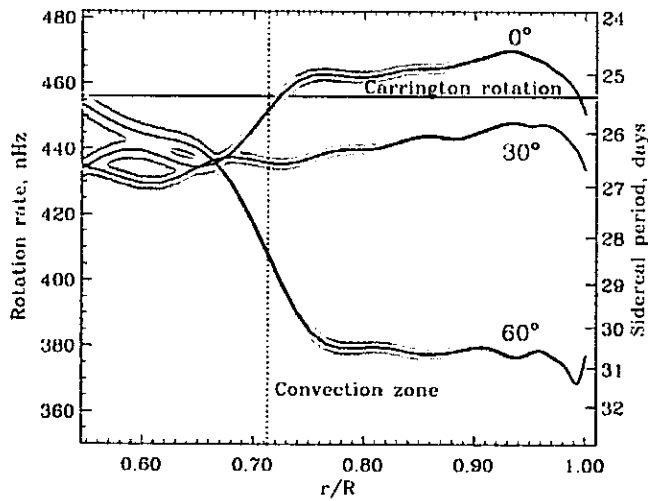


Figure 1.3: Rotation rate with solar radius inferred from splitting of the p-mode frequencies, the dotted line indicates the depth of the convection zone (from Kosovichev et al. 1997).

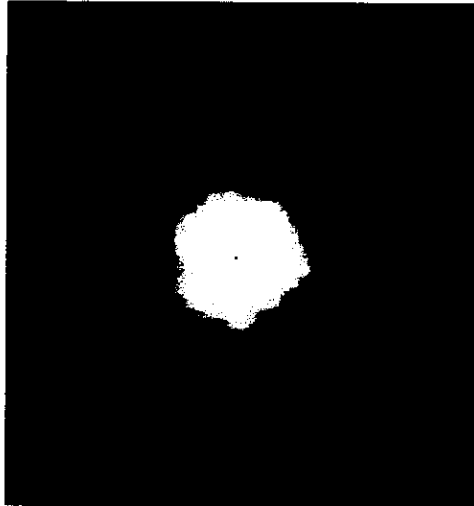


Figure 1.4: This $90^\circ \times 90^\circ$ image shows a 500-day exposure of data from the Super-Kamiokande detector. The image shows a highly scattered image of the detected neutrinos produced in the solar core. The dark spot in the centre of the image indicates the angular size of the solar disk.

the non-uniform rotation.

The frequencies of the observed p-modes have been determined to a precision on the order of 0.1–0.01%. Such precise observations have allowed the refinement of the solar model to include the effect of changes in the equation of state, opacity, abundances and gravitational stratification of heavier elements such as Helium. This high degree of precision suggests that, considering the core temperature, the paucity of observed neutrino flux probably requires a modification to the electro-weak theory rather than the solar model. These observations imply a non-zero neutrino mass, and oscillation between the neutrino flavours (Ahmad et al. 2002). Figure 1.4 shows a $90^\circ \times 90^\circ$ field of view image from the Super-Kamiokande neutrino detector, integrated over 500 days. In effect, this is a highly scattered neutrino image of the solar core.

1.2 The magnetic Sun

The magnetic field of the Sun is believed to be generated by a self excited magneto-hydrodynamic dynamo (Priest 1982). The rotation of the highly conducting plasma induces a poloidal magnetic field within the solar interior. The shear produced by the differential rotation, that appears

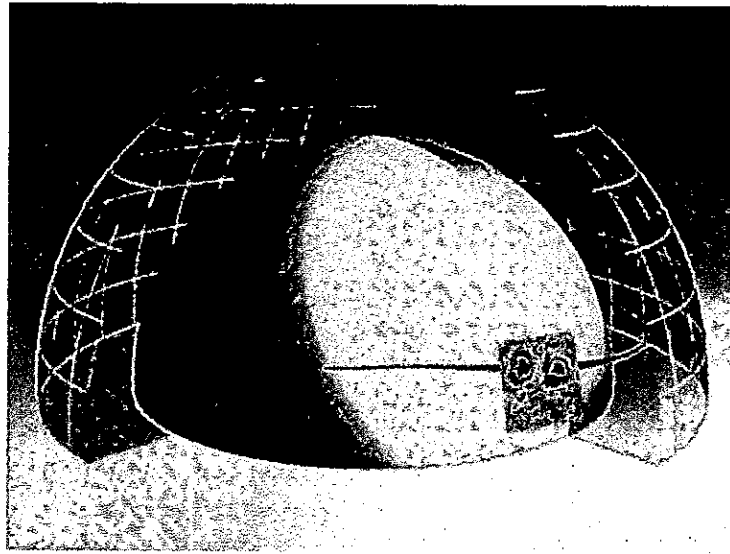


Figure 1.5: Schematic diagram representing the convection of a magnetic flux tube from the tachocline region, and emergence in a bipolar sunspot region within the photosphere. The gridded hemisphere represents the photosphere, and the inner hemisphere represents the base of the convection zone (from Caligari et al. 1995).

to begin in the tachocline region, gradually transforms the field from a poloidal to a toroidal geometry. If the field strength within a magnetic flux tube reaches a critical value (~ 10 T, Caligari et al. 1995); the flux tube becomes unstable to convection, and the magnetic buoyancy effect forces the field through the convection zone to the solar surface. The combination of the solar dynamo, differential rotation and convection above the tachocline give rise to the solar magnetic cycle. The most prominent is the ~ 11 year Schwabe cycle, apparent in the modulation of photospheric magnetic flux, e.g. sunspot numbers. Strong flux tubes that are convected to the solar surface emerge as active regions such as sunspots and plage (Fig 1.5). The magnetic nature of sunspots was reported by Hale (1908) from observations of their Zeeman effect. The spots tend to follow observed trends indicative of the solar dynamo properties. Over the course of the Schwabe cycle sunspots appear around $\pm 35^\circ$ latitude, and progressively emerge at lower latitudes towards the equator at solar maximum. Sunspots generally consist of bipolar pairs with leading and trailing components of opposite polarity. The leading component tends to be closer to the solar equator, and the polarities of the components are opposite in the Northern and Southern hemispheres. These polarities are reversed after solar minimum, and thus a cycle of ~ 22 years is required for the polarity of the bipoles in each hemisphere to return to the same

CHAPTER 1. INTRODUCTION

configuration. This 22 year Hale cycle represents a complete cycle of the solar magnetic field. In addition to the Schwabe and Hale cycles, solar activity is modulated by longer cycles such as the 80–90 year Gleissberg cycle. Indirect observations of solar activity, using cosmogenic radionuclides, suggest additional longer period cycles exist which may significantly affect solar activity (Beer 2000).

Observations of cool, Sun-like, stars reveal a relationship between the surface magnetic activity, and emission indices of the outer atmosphere. It is found that the radiative flux density of different temperature regions in the outer atmosphere of F–M type stars are related by power laws (Fig 1.6). Solar observations show that the emission flux from various chromospheric, UV and X-ray lines are related to the magnetic flux. Observations of the emission indices in Sun-like stars can then be related to their magnetic flux. Observations of magnetic cycles in Sun-like stars were carried out by Wilson (1978) using the chromospheric Ca II H and K lines. It is found that many Sun-like stars exhibit magnetic cycles similar to the Sun, and some show Maunder minimum type periods of low activity (Fig 1.7). Observations of these stars allow the solar cycle to be placed in the context of the activity cycle of other Sun-like stars.

CHAPTER 1. INTRODUCTION

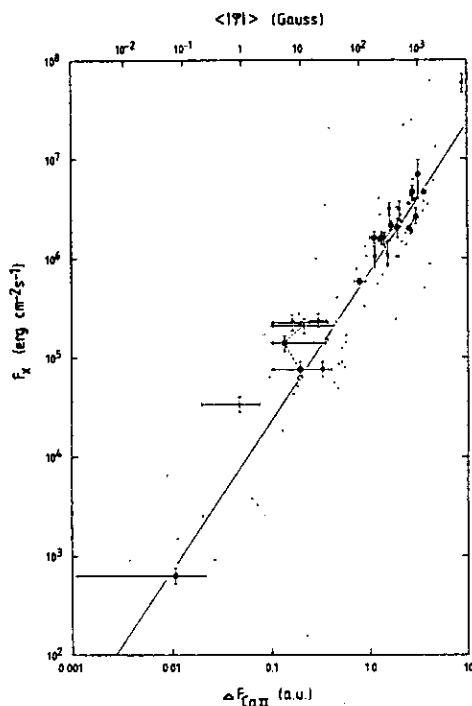


Figure 1.6: The chromospheric Ca II H & K flux in Sun-like stars is related to the soft X-ray flux by a power law index of 1.5. The upper scale indicates the relationship between the H & K flux and the magnetic flux (from Schrijver et al. 1992).

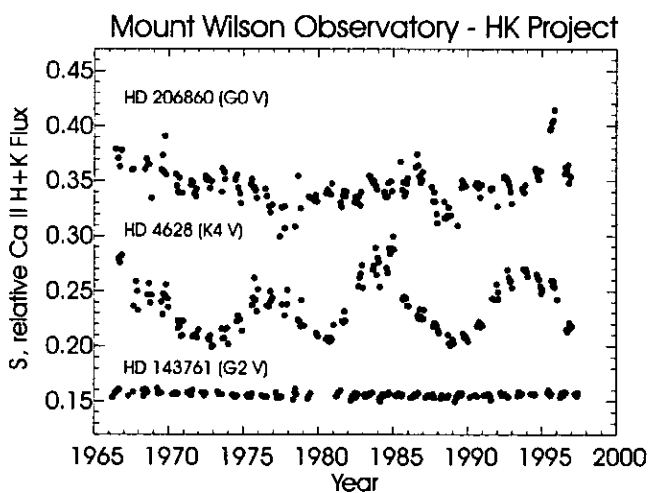


Figure 1.7: The observed Ca II H and K flux in Sun-like stars relates to the stellar magnetic flux. The upper star shows a typical young solar-like star with a largely irregular cycle. The two lower typical stars of similar age to the Sun show a magnetic cycle or constant activity (from Baliunas et al. 1998).

1.3 The photosphere

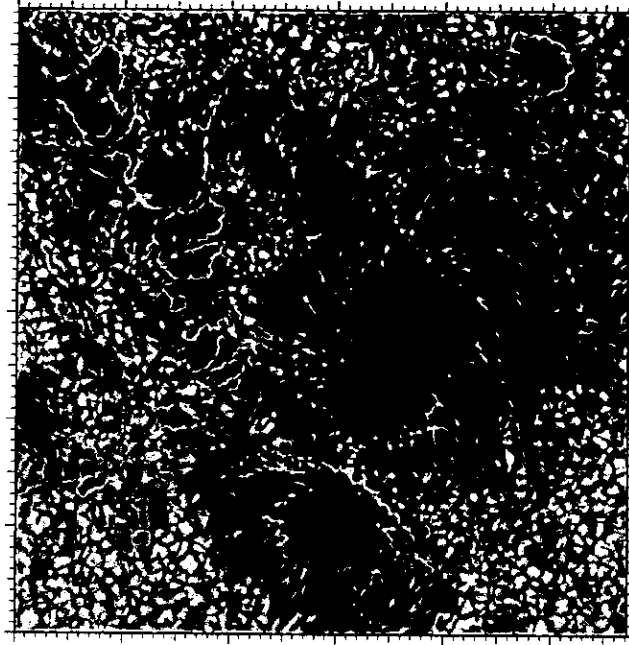


Figure 1.8: High resolution (~ 100 km) image of the photosphere obtained with the Swedish 1-meter Solar Telescope on La Palma, tick scale represents 1000 km. Image courtesy of the Royal Swedish Academy of Sciences.

The solar photosphere is the surface from which most energy is emitted from the Sun. Since optical depth is dependent upon wavelength, different wavelengths define different photospheric depths. The visible photosphere is commonly defined as the surface, at the top of the convection zone, where the optical depth at 500 nm $\tau_{500} = \frac{2}{3}$. The high temperature within the convection zone results in partial ionisation of the plasma. The increased opacity induces a large temperature gradient making the plasma convectively unstable. The resulting convection pattern carries energy to the surface, and is visible in the photosphere, on the smallest scales, as granular convection cells (Fig 1.8). The granules have a size of the order 100 km and evolve on time-scales on the order of 10 minutes (Spruit et al. 1990). Observations of the horizontal velocity flow of granules reveal convection patterns on larger scales. Mesogranulation (Muller et al. 1992) is observed as a cellular horizontal flow pattern with a size on the order of 5000 km, and a lifetime of a few hours. Supergranulation (DeRosa & Toomre 2004) represents the horizontal flow pattern of convection observed on the largest scales. Supergranules are visible in

CHAPTER 1. INTRODUCTION

Dopplergrams with a typical size of 20,000 km, and are visible on timescales on the order of a day. The rise of a large scale convective plume causes a diverging horizontal flow pattern, in the photosphere, from the centre of the supergranule to its boundary. This transports magnetic flux tubes into the cellular network pattern of the supergranule boundaries. Heating associated with this concentration of magnetic flux is visible as emission in chromospheric lines, thus outlining the chromospheric network.

Apart from convection, the other principle source of structure in the photosphere is the magnetic flux. Magnetic flux tubes are arranged in observed structures such as filigree, faculae and sunspots on larger scales. Filigree (Dunn & Zirker 1973) are observed as bright points at visible wavelengths within the dark inter-granular lanes, particularly in the wings of $H\alpha$ and Fraunhofer G band filtergrams. The filigree appear as circular or elongated bright points with a size <200 km, and a lifetime of around 10 minutes. It appears that the granulation concentrates the magnetic flux into small flux tubes with a field strength around 1500 G. The concentration of flux results in a reduction of plasma density within the flux tube causing the increased emission of the bright points. Faculae are observed as regions of increased emission in the visible and chromospheric emission lines (Chapman 1994). The faculae regions are composed of ~ 1500 G flux tubes that show increased emission contrast towards the limb. This is thought to be the effect of observing an increased depth into the photosphere, resulting from evacuation of plasma due to the magnetic field, and increased heating in the upper photosphere. Sunspots (Thomas & Weiss 1992) are the manifestation of magnetic flux tubes emerging from the photosphere on the largest scale. Sunspots appear as, cool, dark regions of emission relative to the surrounding photosphere (Fig. 1.8). Typical sunspots are approximately circular in shape, with approximate radii R of 10,000–15,000 km. The reduced temperature and emission is primarily due to the suppression of convection by the strong magnetic field below the spot. The central umbra of the spot, consisting of nearly vertical magnetic field of 2000–3500 G, has a radius of $0.4R$, a temperature 2000–4000 K below the average photosphere and $\sim 25\%$ of the radiative flux. The umbra is surrounded by the penumbra with $\sim 75\%$ of the emission rate of the photosphere, and typical field strengths of 700–1000 G. The penumbra consists of bright and dark magnetic flux tubes significantly inclined to the vertical, with a complicated

comb-like structure. The flux becomes increasingly inclined with radius; the bright filaments have an inclination of $\sim 70^\circ$ at the umbral boundary, and the dark filaments are inclined by a further $\sim 30^\circ$, approaching horizontal at the penumbral boundary.

1.4 The chromosphere

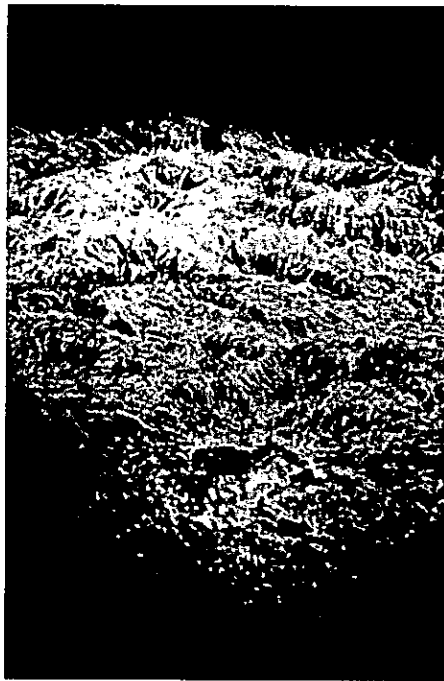


Figure 1.9: $H\alpha$ image of the chromosphere: on-disk spicules can be seen in absorption outlining the supergranulation magnetic network. Image courtesy of the National Solar Observatory.

The solar chromosphere (Bray & Loughhead 1974) is the region of the atmosphere, above the photosphere, that becomes visible during total eclipses of the Sun, and is observed to possess an inhomogeneous structure. Above the photosphere the atmospheric density becomes sharply stratified, and the magnetic field becomes the most significant source of structure. At the limb plasma at chromospheric temperatures can be seen to rise to altitudes normally associated with coronal emission. In general, chromospheric spectral lines are observed as absorption lines on disk, and emission lines off the limb. The chromospheric network is outlined by the increased emission in chromospheric lines, due to the concentration of magnetic flux at the supergranular boundaries. The magnetic field structures the atmosphere into a number

of filamentary features such as spicules (Suematsu 1998) and prominences (Tandberg-Hanssen 1995). The background, or basal, chromospheric emission produced in the internetwork regions of solar/stellar atmospheres is thought to be due to the dissipation of acoustic shock waves (Carlsson & Stein 1997; Buchholz et al. 1998). These shocks are visible in chromospheric lines as bright ‘grains’ in the internetwork regions. As described previously, there is an additional excess chromospheric emission connected to the concentration of magnetic flux. This flux emerges in the magnetic network, and active regions. It is not yet clear if this emission is due to the dissipation of wave mechanisms or electric currents.

1.5 The transition region

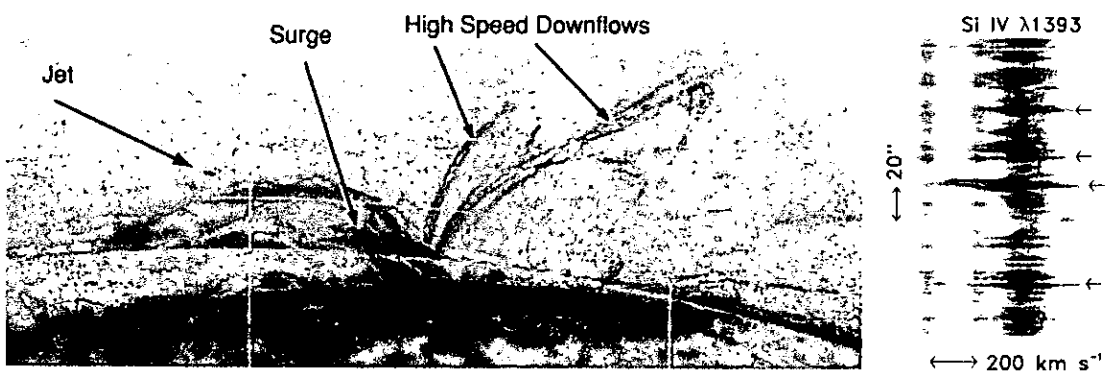


Figure 1.10: Left: HRTS image of the dynamic structures observed in the C IV transition region line. Right: HRTS Si V spectrum indicating large Doppler shifts due to explosive events.

The transition region is characterised by plasma at a temperature around 10^5 K, and so forms the interface between the chromosphere and the corona. As in the chromosphere, the structure in the transition region is also dominated by the magnetic field. Plasma is confined to motions parallel to the magnetic field direction, and observations in transition region lines show that plasma emitting at this temperature is highly dynamic. This is observed in a number of phenomena such as high speed plasma flows (Brekke 1999), macrospicules (Pike & Harrison 1997), jets (Innes et al. 1997), blinkers (Bewsher et al. 2003), explosive events (Dere et al. 1989a), etc. Figure 1.10 shows some of the dynamic phenomena and large Doppler shifts observed in the transition region with the High Resolution Telescope and Spectrograph (HRTS) instrument.

1.6 The corona



Figure 1.11: Composite image of the inner ‘on-disk’ corona viewed in the EUV with EIT 284 Å, and the outer corona viewed at visible wavelengths with the LASCO C2 coronagraph. Images courtesy of SOHO/EIT and SOHO/LASCO.

The corona is defined by the high temperature plasma in the outer regions of the Sun’s atmosphere (for a recent review see Aschwanden 2004). The plasma within the corona has a temperature ranging from $\sim 1 \times 10^6$ K up to $\sim 50 \times 10^6$ K in flaring regions. In the corona, the plasma β has dropped to such a level that the plasma is effectively totally dominated by the magnetic field. It is constrained to motion parallel to the magnetic field, and the coronal emission outlines the large scale magnetic structure. Figure 1.11 shows a composite EIT Fe XV, and LASCO C2 image. The EIT image shows the enhanced emission on-disk associated with the closed field of active regions. The lack of emission within the open field coronal hole regions is also visible. The LASCO image shows the outer regions of the corona structured into streamers, and a CME eruption is visible towards the bottom left of the image.

The magnetic field induces coronal emission which is dynamic over a range of time scales from years down to the limiting cadence of current observations. The radiative flux from

CHAPTER 1. INTRODUCTION

plasma emitting at coronal temperatures varies by 1–2 orders of magnitude over the Schwabe cycle; observations of flares, coronal mass ejections (CME's) and wave processes show that the corona is dynamic over time-scales of seconds. A number of complex magnetic structures are observed from emission at coronal temperatures. Coronal bright points are connected to small magnetic bipoles, and appear randomly distributed over the solar surface (Golub et al. 1974). The magnetic field emerging from active regions is observed as emission along magnetic loops at coronal temperatures (see Bray et al. 1991). The loops cover a large range of lengths from $\sim 10^4$ – 10^5 km, and temperatures from <1 MK up to ~ 10 MK, appearing as emission in the EUV and X-rays. They may be loosely categorised as cool, with a temperature <1 MK, and hot with plasma >1 MK. Generally, cooler loops are found to be highly dynamic on short time-scales, possessing high velocity flows, particularly at cooler transition region and chromospheric temperatures. The hotter loops tend to be more stable, and may be visible for many days.

At the extreme end of the spectrum are flare loops. These are impulsively heated to very high temperatures during the flare, and more energetic events produce an arcade of post-flare loops. Often associated to energetic flares are coronal mass ejections (CMEs, see Low 2001). CMEs consist of large (10^{12} Kg) impulsive ejections of plasma at coronal temperatures into the heliosphere (see Fig. 1.11).

The primary source of solar mass loss is the solar wind consisting of a continuous outflow of plasma along the open magnetic field; the precise acceleration mechanism of the solar wind is still not understood. The slow solar wind has a velocity of ~ 400 km s^{-1} emanating from coronal streamer structures, visible in Fig 1.11. The fast solar wind has a velocity of ~ 750 km s^{-1} , and originates in coronal hole regions (see Cranmer 2002). Coronal holes are characterised by predominantly unipolar regions of open magnetic flux with low plasma density. During solar minimum coronal holes are confined above the polar regions with opposing polarity; as activity increases during the Schwabe cycle, the location of coronal holes extends down to equatorial latitudes. During solar minimum the polarity of the polar holes reverses, and so the original polarity is returned over the course of the Hale cycle. Coronal holes are observed to possess near rigid rotation requiring a continuous magnetic reconnection process at

the coronal hole boundary, due to the photospheric differential rotation.

1.7 Magnetic heating mechanisms

The mechanism by which energy is transported and dissipated to heat solar/stellar coronae is an important and unresolved problem in modern astrophysics. It is not understood why, as we move outward through the solar atmosphere above the photosphere, we observe an increase in the plasma temperature. However, it is clear that “coronal heating” is related to the magnetic field. Narain & Ulmschneider (1996) give a comprehensive review of solar/stellar chromospheric and coronal heating mechanisms. Walsh & Ireland (2003) review the theoretical coronal heating mechanisms, and overview recent observations. The possible coronal heating mechanisms may be classified into slow DC mechanisms and fast AC mechanisms by the time-scale over which the magnetic field is driven. The DC mechanisms operate by dissipation of electric currents, and the AC mechanisms by dissipation of Magneto-Hydrodynamic (MHD) waves.

1.7.1 Direct current dissipation

The photospheric plasma has a large β and magnetic Reynolds number, and the magnetic field is largely driven by random photospheric motions, due to granulation. The continuous random motion of the footpoints leads to braiding of the magnetic flux. This generates electric currents on small length scales allowing magnetic reconnection to release the magnetic energy of the flux into kinetic energy of the plasma (see Priest & Forbes 2000). This mechanism is not considered further in this thesis.

1.7.2 Wave mechanisms

The dissipation of wave modes is an important mechanism that must contribute to coronal heating to some degree. Thus, observational quantification of wave mechanisms is necessary to determine the heating mechanisms present, and to establish their significance in the heating and structure of the outer solar atmosphere. For a review of MHD waves within the corona see Roberts (2000). The sound speed within an ideal gas with equilibrium pressure P_0 , plasma

CHAPTER 1. INTRODUCTION

density ρ_o and ratio of specific heats γ is given by

$$c_s = \left(\frac{\gamma P_o}{\rho_o} \right)^{\frac{1}{2}}.$$

The propagation speed of a perturbation along a line of magnetic flux of equilibrium field strength B_o and magnetic permeability of the medium μ , is given by the Alfvén speed

$$\nu_A = \left(\frac{B_o^2}{\mu \rho_o} \right)^{\frac{1}{2}}.$$

The MHD wave equations give three solutions for slow magneto-acoustic, fast magneto-acoustic and Alfvén waves. Alfvén waves arise from the magnetic tension force along the magnetic field, and propagate along the field at the Alfvén speed. Alfvén waves are non-compressional, producing an oscillation in emission line Doppler velocity, without causing a radiative flux oscillation. Magneto-acoustic waves are compressive modes, and so may be observed as oscillations in the radiative flux and Doppler velocity of emission lines. The solutions for the slow mode show that magnetic flux tubes act as natural wave-guides, and are guided within 26.5° of the magnetic flux vector. The slow mode speed is given by

$$\frac{1}{c_{slow}^2} = \frac{1}{c_s^2} + \frac{1}{\nu_A^2},$$

and is always below the sound and Alfvén speeds. The propagation of the fast mode wave is largely isotropic, and thus can propagate across the magnetic flux. The fast mode speed is given by

$$c_{fast}^2 = c_s^2 + \nu_A^2,$$

thus always propagates at super-sonic/Alfvénic speeds.

The magneto-acoustic waves may be considered in the case of a magnetic flux tube geometry. These waves are described by Bessel functions, where the mode number n describes the geometry of the tube oscillation. In the case where $n = 0$, the tube cross-sections has a symmetric oscillation about its axis, termed the sausage mode. $n = 1$, termed the kink mode, corresponds to a lateral displacement of the tube cross-section. Modes with $n > 2$ are termed

fluting modes, consisting of distortions of the tube cross-sections about its axis.

The dissipation of MHD wave modes may provide an important contribution to heating of coronal plasmas. These waves may be damped by theoretical mechanisms such as phase mixing and resonant absorption (see Aschwanden 2004).

1.8 Waves observed within the solar atmosphere

The observations of oscillations in the corona have largely been interpreted as magnetoacoustic, Alfvén, or kink mode oscillations. Aschwanden et al. (1999) report the first observation of kink mode oscillations in a coronal loop, and more recently, Nakariakov & Ofman (2001) develop a method of determining the magnetic field strength in coronal loops by using the kink mode period and loop length. Deforest & Gurman (1998) report on the observation of compressive wave trains in polar plumes; it is suggested that these may be caused by the presence of magneto-acoustic waves. Recent results on observations that are interpreted as slow magneto-acoustic modes are described by Ireland et al. (1999), De Moortel et al. (2000), Banerjee et al. (2001b), Hansteen et al. (2000), O'Shea et al. (2001), Robbrecht et al. (2001). Wang et al. (2003) report the observation of standing slow magneto-acoustic waves in hot, post flare, coronal loops. Williams et al. (2002) observe the propagation of a fast magneto-acoustic wave within a coronal loop using ground based high cadence observations of a solar eclipse. Many of these recent studies use wavelet analysis allowing the time dependence of the periods present to be studied.

Beckers & Tallant (1969) observe intensity and velocity oscillations with an approximate 3-min period visible in the Calcium H and K lines above sunspot umbrae. Gurman et al. (1982) observe 3-min intensity and velocity oscillations above sunspots in the C IV Ultraviolet line with the Ultraviolet Spectrometer and Polarimeter (UVSP) on the Solar Maximum Mission (SMM). More recently the 3-min oscillations above sunspots have been observed with the Solar and Heliospheric Observatory (SOHO). 3-min intensity oscillations are present in chromospheric, and transition region lines associated with sunspot plumes above sunspot regions observed with the Coronal Diagnostic Spectrometer (CDS) (Fludra 2001). The amplitude of the oscillations is found to reach a peak in the transition region lines. Brynildsen et al. (2002)

CHAPTER 1. INTRODUCTION

confirm this result with observations using CDS. They also find oscillations at the footpoints of Transition Region and Coronal Explorer (TRACE) coronal loops. O’Shea et al. (2002) suggest that time delays between the oscillations in different lines are due to upwardly propagating slow magneto-acoustic waves. Brynildsen et al. (2003) interpret observations of oscillations in the wings of transition region lines as upwardly propagating acoustic waves.

Intensity disturbances propagating along active region loops are observed by Berghmans & Clette (1999) in Extreme ultraviolet Imaging Telescope (EIT, Delaboudiniere et al. 1995) 195 Å data. Nightingale et al. (1999) observe equivalent disturbances using TRACE. Similar propagations are observed in TRACE 171 Å and quantified by De Moortel et al. (2002c,a). They observe propagating oscillations in the footpoints of large diffuse coronal active region loops. These oscillations are interpreted as slow magneto-acoustic waves with propagation speeds in the range 70–235 km s⁻¹ with periods of 282 ± 93 s and short damping lengths (8.9 ± 4.4 Mm). De Moortel et al. (2002b) suggest a relation between 3 minute oscillations found in TRACE coronal loops situated above sunspot regions and 5 minute oscillations found in “non-sunspot” loops.

1.9 Optically thin emission

The intensity of an optically thin spectral line is given by

$$(\lambda_{ij}) = \int_h Ab(X)C(N_e, T, \lambda_{ij})N_e N_H dh$$

(λ_{ij}) = the intensity of a spectral line of wavelength λ formed from transition $i \rightarrow j$.

$Ab(X)$ = abundance of the observed element relative to Hydrogen.

$C(N_e, T, \lambda_{ij})$ = the contribution function contains all the atomic physics parameters.

$N_e, N_H dh$ are the number densities of electrons and hydrogen and dh is along the line of sight.

This model of emission from coronal lines makes three main assumptions that the plasma is in a steady state, the ionization processes can be separated from the level balance processes

CHAPTER 1. INTRODUCTION

within an ion and the lines are optically thin. This equation can be rewritten as

$$I(\lambda_{ij}) = Ab(X) \int_h C(N_e, T, \lambda_{ij}) DEM(T) dT \quad [\text{erg cm}^{-2} \text{s}^{-1} \text{sr}^{-1}],$$

where the Differential Emission Measure (DEM) gives the amount of plasma emitting along the line of sight in the temperature interval $T + dT$

$$DEM = N_e N_H \frac{dh}{dT} \quad [\text{cm}^{-5} \text{K}^{-1}].$$

1.10 Thesis outline

This thesis presents an analysis of dynamic structures observed within the solar atmosphere using spaced based spectroscopic and imaging instrumentation. The response of the atmosphere to these magnetically dominated structures is investigated at photospheric, chromospheric, transition region and coronal temperatures.

This work makes use of observations that include the He I 584Å line, formed at upper chromospheric/lower transition region temperatures. Hereafter this line is referred to as a chromospheric line, following the convention used by the majority of research which utilises SOHO data.

An introduction to the instrumentation used is given in Chapter 2. Chapter 3 introduces the signal analysis methods used extensively throughout this thesis. In Chapter 4 the time dependent nature of periodicity within a coronal hole boundary region is analysed. Chapter 5 analyses the structure and dynamics of the emission line parameters within an active region, observed at the solar limb. Chapter 6 investigates the chromospheric and transition region signatures of longitudinal waves observed within a TRACE coronal loop associated with a plage region. Chapter 7 advances this research, extending the observations to longitudinal waves within TRACE sunspot loops using new spectroscopic imaging observations at chromospheric and transition region temperatures. Chapter 8 concludes with plans for future extensions to this research, using the knowledge obtained from this thesis work and the potential of upcoming space based missions.

Chapter 2

Instrumentation

The analysis within this thesis makes use of data from the CDS-NIS, CDS-GIS and MDI instruments on-board the SOHO satellite (Domingo et al. 1995), and the TRACE satellite (Handy et al. 1999). The CDS-NIS and CDS-GIS instruments are the normal incidence and grazing incidence spectrometers comprising CDS, producing EUV spectroscopic data across a wide range of temperatures from the chromosphere, transition region and corona. The MDI instrument produces white light intensitygrams, Dopplergrams and magnetograms. The TRACE satellite is primarily an EUV/UV imaging telescope, and produces high resolution images from chromospheric to coronal temperatures.

2.1 The Coronal Diagnostic Spectrometer (CDS)

The Coronal Diagnostic Spectrometer (CDS) is one of the twelve instruments carried by the Solar and Heliospheric Observatory (SOHO) satellite. SOHO was launched in 1995 and is located in a 6 month orbit around the L1 Lagrange point. The CDS instrument was designed to investigate the outer solar atmosphere by observing EUV spectral emission lines in the wavelength range 150–800 Å (see Harrison et al. 1995). CDS consists of a normal incidence spectrometer (NIS), and due to the decreased reflectivity at shorter EUV wavelengths, a grazing incidence spectrometer (GIS). The spectroscopic data allow the measurement of line intensity, Doppler velocity, non-thermal broadening, combined with abundance, density and temperature diagnostics across a wide range of temperatures.

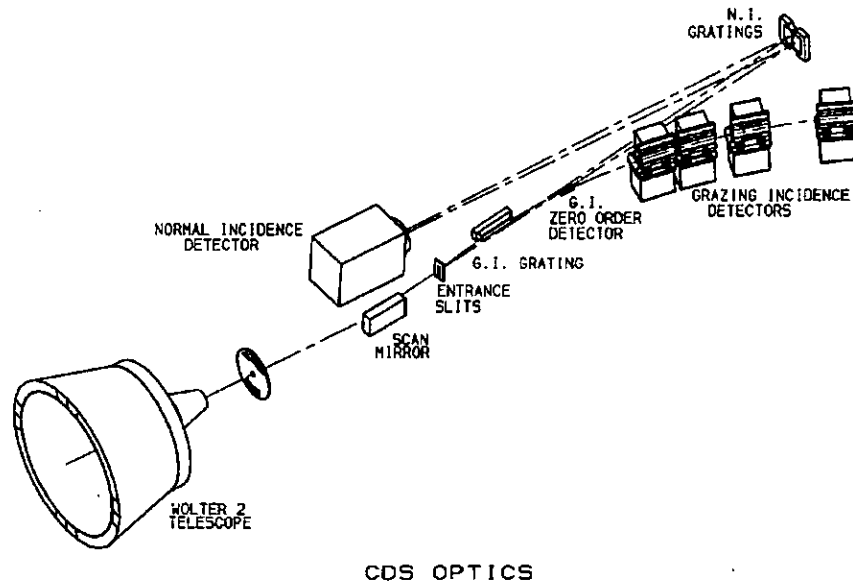


Figure 2.1: CDS optical layout, SOHO/CDS.

The CDS package consists of a grazing incidence Wolter-Schwartzchild type 2 telescope design (Fig. 2.1). The optical path of the telescope first consists of grazing incidence reflections off its paraboloid, then hyperboloid surfaces. Two apertures then select separate optical paths for the NIS and GIS. A grazing incidence scan mirror allows the image to be scanned in the East-West direction, over the entrance slits, allowing the formation of rastered images. There are a total of six entrance slits available, with three designed for the NIS and GIS respectively. After passing through the entrance slits, the optical path then passes to the normal incidence or grazing incidence reflection gratings of the NIS and GIS respectively, dependent upon which instrument is in operation.

NIS data is used extensively throughout this thesis; the following section details the NIS instrument. The GIS instrument is briefly described in Sect 2.3. A recent report on the present status of the CDS calibration is given by Lang et al. (2002).

2.2 CDS-The Normal Incidence Spectrometer (NIS)

The three entrance slits designed for use with the NIS have dimensions of $2'' \times 240''$, $4'' \times 240''$ and $90'' \times 240''$. The NIS consists of two normal incidence toroidal gratings which disperse astigmatic images of the selected entrance slit onto a two dimensional detector. The gratings disperse two different wavelength ranges between $310 \text{ \AA} - 380 \text{ \AA}$, and $520 \text{ \AA} - 630 \text{ \AA}$. The orientation of the two gratings are offset slightly from each other, so as to disperse the two wavelength ranges vertically adjacent on the same detector. The two wavelength bands are designated NIS1 and NIS2.

The NIS detector system, the Viewfinder Detector Subsystem (VDS), consists of three main components. The incident radiation is converted to electrons, via the photoelectric effect, and intensified using a microchannel-plate (MCP). The electrons are converted to visible light by a phosphor coated fibre-optic output, then focused by a lens onto the CCD detector. The CCD is an array of 1024×1024 , $21 \mu\text{m}$, square pixels. The CCD is arranged to use 1024 spectral pixels and 512 spatial pixels, for each NIS1 and NIS2 wavelength band.

The dominant noise within the VDS is a combination of Poisson distributed noise, due to the photon counting statistics, and the photon shot noise of the MCP (Thompson 2000). The photon shot noise is due to variability in the amplification across the MCP, termed the pulse height distribution (PHD), which is strongly dependent on the voltage across the MCP. It is assumed that the noise due to the PHD is comparable to the photon counting noise, so the combined noise $\sigma = \sqrt{2N}$. At low intensities the readout noise may become a significant factor. The total noise is then given by $\sigma = \sqrt{|2N| + R^2n}$, where N is the total number of counts, R is the readout noise per pixel and n is the number of pixels summed over. A conservative approach may use $R=1$ (see Thompson 2000).

2.2.1 Instrumental effects

A detailed description of the CDS calibration can be found in Lang et al. (2002), and references within.

CHAPTER 2. INSTRUMENTATION

Broadened line profiles

In 1998 SOHO lost attitude control, and CDS was recovered four months later. During this time CDS was exposed to high temperatures well above its normal operating range. After the recovery, it was found that the spectral line profiles were broadened. The NIS1 lines are worst affected with additional wings on either side of the line profiles. The NIS2 lines are affected to a lesser extent, and have wings predominantly in the red side of the lines. A detailed description of the broadened line profiles is given in Thompson (1999).

Spectral rotation and tilt effects

The spectral rotation effect is caused by a misalignment between the grating and detector. The dispersion direction is then not parallel to the CCD rows. Thus, in uncorrected data the rows of pixels do not correspond to constant solar y coordinates. The spectral tilt effect is caused by a misalignment of the grating and the slit. The spectral lines are then not perpendicular to the dispersion direction. The rotation and tilt effects are corrected by the CDS routine NIS_ROTATE in the *SolarSoft* software tree.

Scan mirror affect on dispersion

Movement of the scan mirror to build up rasters in the East-West direction produces a non-linear change in the position of the lines on the detector. Corrections for this effect are applied by NIS_ROTATE.

NIS1/NIS2 alignment

Due to variations introduced by the pointing of CDS, a slight spatial offset is observed between observations using NIS1 and NIS2. Corrections are applied by NIS_ROTATE using the /ALIGN keyword.

MCP burn-in

A detailed description of the MCP burn-in is given in Thompson (1998) and Lang et al. (2002). The MCP becomes less sensitive with exposure to radiation. Since the positions of the spectral

CHAPTER 2. INSTRUMENTATION

lines on the MCP are fixed, the detector has a loss of responsivity at these positions. This effect is termed burn-in, and is proportional to the intensity of the lines. The majority of observations use the narrow 2'' or 4'' slits. The burn-in of the narrow slits are corrected by using uniform intensity observations with the wide (90'' \times 240'') slit. To do this a number of wide slit exposures of the quiet sun are averaged together to smooth out the spatial structure. The average intensity along the slit direction is then used to fit the burn-in profiles of the narrow slits which can then be corrected. Along with the narrow slit burn-in, there is an additional contribution due to exposure of the wide slit on the MCP. The wide slit burn-in is also corrected for exposure to quiet sun, and related to the increase in He I intensity for active regions. However, in active regions some higher temperature lines have a significant increase in intensity compared to He I. Thus, observations of intense active regions with the wide slit will produce an extra uncalibrated burn-in in the region of these lines. For this reason, observations of active regions with the CDS wide slit are not normally permitted. The burn-in corrections are applied by the routine VDS_CALIB.

Detector saturation

The full well capacity of the CCD is $\sim 150,000 e^-$. However, the saturation level of the data is limited by the Analogue-to-Digital Converter (ADC) used to encode the data. NIS uses a 12-bit ADC; thus, the maximum level of ADC counts is limited to 4096. The conversion factor to photon-events is determined by the voltage across the MCP (see Harrison et al. 1995).

Cosmic rays

A discussion of cosmic ray removal is given in Thompson et al. (1998). CDS cosmic ray removal in this thesis is implemented using the routine CDS_NEW_SPIKE.

NIS bias

To prevent negative values being passed to the ADC a bias level is added to the data which must be subtracted during calibration, this is performed by the VDS_DEBIAS routine.

Flatfield

Pixel to pixel sensitivity variations are corrected using the routine VDS_CALIB by dividing by a flatfield array Thompson (1994).

NIS1 low level fixed pattern effect

NIS1 has a low level fixed pattern effect due to the readout electronics. In the dispersion direction every fourth pixel has a very slight reduction in intensity. Corrections for this effect are applied by the routine VDS_CALIB.

2.3 CDS-The Grazing Incidence Spectrometer (GIS)

The three entrance slits designed for use with the GIS have dimensions of $2'' \times 2''$, $4'' \times 4''$ and $8'' \times 50''$. The GIS uses a spherical, grazing incidence, reflection grating to produce stigmatic 1-D spectroscopic data. The GIS uses four flat detectors located at a tangent to the grating Rowland circle, covering wavelength ranges of 151–221 Å, 256–338 Å, 393–493 Å and 656–785 Å.

The GIS detectors are identical and use a MCP to act as a photomultiplier, and a Spiral Anode (SPAN) detector. The spectral dispersion position is determined from an look-up table loaded onboard the instrument. A detailed description of the GIS instrumentation is given in Harrison et al. (1995).

2.3.1 Instrumental effects

GIS suffers from a number of instrumental effects which are summarised below. Detailed descriptions of the GIS instrument, calibration and analysis are given by Bentley (1999) and Breeveld (2000b,a).

Ghosting

The analogue electronics of the GIS detectors are affected by electronic noise. This results in an uncertainty in the position of an event on the detector within “ghosting” regions on the

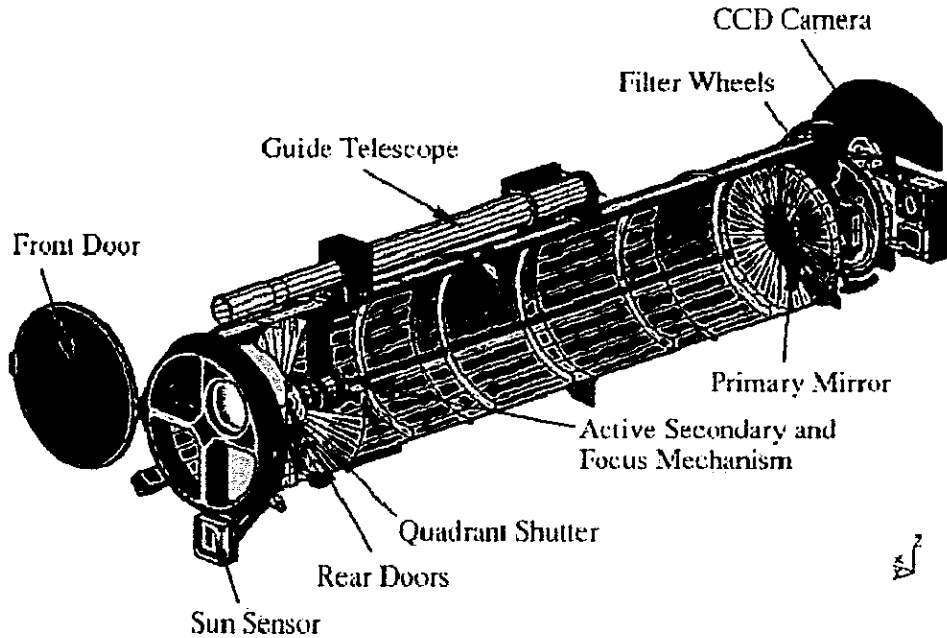


Figure 2.2: The TRACE telescope, Handy et al. (1999)

detector. This means, within ghosting regions, counts can be redistributed to other ghosting regions within the spectrum. These regions can be determined and excluded from analysis, or corrections can be attempted. Current observations can be designed to avoid ghosting regions in particular parts of the spectrum, by setting an appropriate look-up table.

Fixed patterning

Due to an inadequate resolution in the calculated look-up table, at certain spectral pixel locations, photon-events may be incorrectly attributed to adjacent pixels positions. The total number of photon-events is conserved, and the effect may be reduced by smoothing the spectra.

2.4 The Transition Region and Coronal Explorer (TRACE)

The Transition Region and Coronal Explorer (TRACE Handy et al. 1999) is a single instrument, imaging satellite, with a number of EUV, UV and visible bandpasses covering photospheric to coronal temperature regions. TRACE was launched in 1998, and is located in a

CHAPTER 2. INSTRUMENTATION

sun synchronous polar orbit. TRACE was designed to investigate the dynamic nature of the solar atmosphere using high resolution ($\sim 1''$) imaging in three EUV bandpasses (171, 195 and 284 Å), four UV bandpasses (1216, 1550, 1600 and 1700 Å) and a white light (WL) channel. An overview of the first TRACE observations is given by Schrijver et al. (1999).

The TRACE instrument uses a Cassegrain telescope design (Fig. 2.2). The optical path of the telescope is separated into quadrants using a combination of filters and multilayer coatings, on matching quadrants of the primary and secondary mirrors, to select the different bandpasses. To cut-out visible light, at the aperture of the telescope in the UV quadrant a broadband UV filter is used, and in the three EUV quadrants thin-film Aluminium filters are used. A quadrant shutter is employed to select the optical path to the mirror quadrants. The shutter wheel has two openings: a narrow opening is used for short exposures (< 20 ms) by making multiple passes across the CCD; a wide opening is used for longer exposures by illuminating the whole CCD at once. The primary and secondary mirror quadrants have matched coatings for the different bandpasses. Three of the quadrants are coated for the EUV bands, and one is coated for the UV band. Behind the primary mirror, and in front of the CCD, are two filter wheels. The two filter wheels are each divided into four quadrants, and different combinations of filters are used to select the different bandpasses. In each filter wheel, one quadrant uses a thin-film Al filter for the EUV bands, one quadrant is open, and two quadrants are used for different UV filters. Different combinations of the UV filters are used to select each UV bandpass; one of the UV filters is used for the WL channel. The CCD is a 1024×1024 array with a fluorescent lumogen coating used to convert the UV/EUV photons to visible wavelengths detected by the CCD.

The EUV response functions are shown in Fig. 2.3. The 171 Å channel is centered around 173 Å, but labeled 171 to be consistent with the EIT channels.

2.4.1 Instrumental effects

TRACE data is subject to the following instrumental effects, described in further detail by Handy et al. (1999) and with reference to the TRACE Analysis Guide.

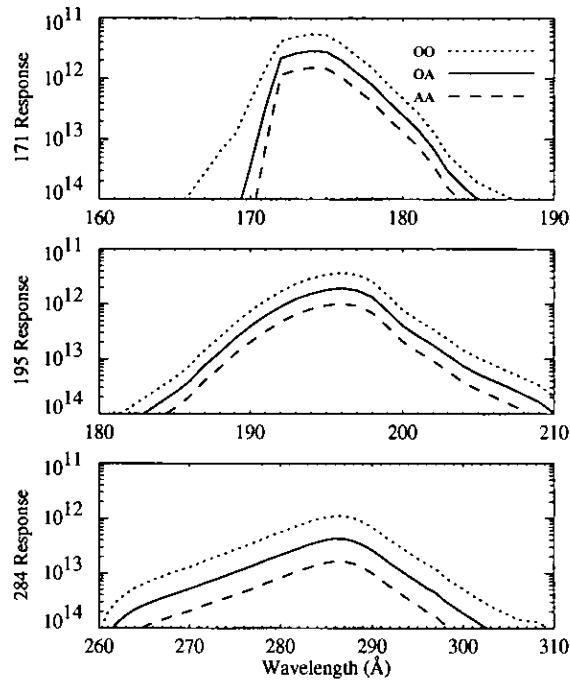


Figure 2.3: The TRACE EUV response functions, Handy et al. (1999). OO indicates both filter wheels in the focal plane using open quadrants, OA indicates one of the focal plane filter wheel quadrants is open and the other is using an Al filter, and AA indicates both filter wheels are using Al filter quadrants.

TRACE pointing

The pointings recorded within the TRACE data structures are given with reference to the pointing of the WL channel. Due to variations in the best focus position of the secondary mirror, the actual pointings of the different wavelength channels are offset from the WL pointings. The offsets for each day are measured and are available within the *SolarSoft* database. The offsets are different within the different channels, and are on the order of a few arcsec; e.g. the TRACE 171 Å data presented in Chapter 7 are offset 2.1" W and 4.35" S of the WL pointing coordinates. These pointing corrections are applied using the `/wave2point` keyword with the `trace_prep` routine.

The TRACE pointing is also affected by an orbital variation, related to the spacecraft temperature. It is thought to be caused by a flexing between the guide telescope and the main telescope, and is on the order of 1". Changing of the quadrant shutter and filter wheels are also thought to cause a further variation on the order of 0.1".

Image compression

The TRACE image data is compressed with a 12-bit JPEG algorithm using 8×8 pixel blocks. Artifacts of the compression may be visible within the data, particularly if the data is badly affected by cosmic rays.

Cosmic rays

Since TRACE has a polar orbit, when it is within high latitude regions, or within the South Atlantic Anomaly, it is affected by an increased number of charged particle hits on the CCD. These appear as spikes, or streaks within the data, and are removed using the `/unspike` and `/destreak` keywords of the `trace_prep` routine.

Readout noise

The CCD suffers from low level electronic readout noise, manifested as a “herring bone” pattern within the data. The mesh of the entrance filters also causes a low level diffraction pattern, particularly visible in intensely flaring regions. The pattern artifacts are removed using Fourier methods and are applied using the `/deripple` keyword with `trace_prep`.

2.5 The Michelson Doppler Imager (MDI)

The Michelson Doppler Imager (MDI, Scherrer et al. 1995), one of the instruments on the SOHO satellite, is designed to study photospheric oscillations and helioseismology. MDI produces images of intensity, Doppler velocity, and longitudinal magnetic field. The MDI instrument consists of a refracting telescope, a series of filters and two tunable Michelson interferometers to observe the Ni I 6768\AA absorption line. The interferometers produce a 94 m\AA bandpass that can be scanned across the Ni line. Intensitygrams at five different positions across the line are used to derive the MDI observations of continuum intensity, Doppler velocity and magnetic field strength. The Doppler velocity is calculated using the ratio of the differences between different intensitygrams. The longitudinal magnetic field strength is calculated by measuring the Doppler shifts in left and right circularly polarised light. MDI produces data in two different

CHAPTER 2. INSTRUMENTATION

observing modes: The full disk mode has a resolution of $4''$, and the high resolution mode has a $11' \times 11'$ field of view centred $160''$ North of the solar equator with $1.25''$ resolution. There are four main observing programs performed by MDI to investigate the structure and dynamics of the p-mode oscillations. These observing programs define the observed data products and full disk/high resolution modes used, depending upon the available telemetry. MDI data is calibrated by the MDI investigation team, and is made available calibrated to physical units.

Chapter 3

Signal Analysis

3.1 Fourier Analysis

The Fourier transform is used mathematically to transform a function from one domain into its transform domain. In the physical sense, it is used to transform a signal between the time and frequency domains. The discrete Fourier transform is defined as

$$f(\nu) = \frac{1}{N} \sum_{t=0}^{N-1} f(t) e^{-\frac{i2\pi\nu t}{N}} \quad (3.1)$$

and the inverse transform is defined as

$$f(t) = \frac{1}{N} \sum_{\nu=0}^{N-1} f(\nu) e^{\frac{i2\pi\nu t}{N}} \quad (3.2)$$

where $f(t)$ is a finite data series, and $t = 0, 1, 2, \dots, N-1$. The Fourier transform can be used to determine the characteristic sinusoidal frequencies necessary to reconstruct a given time series.

Figure 3.1 shows the Fourier transforms for the following sinusoidal functions.

- a) $\sin\left(\frac{2\pi}{10}t\right) + 1$ $0 < t < 100$ $\sin\left(\frac{2\pi}{30}t\right)$ $100 < t < 200$
- b) $\sin\left(\frac{2\pi}{10}t\right) + \sin\left(\frac{2\pi}{30}t\right) + 1$ $0 < t < 200$
- c) $\sin\left(\frac{2\pi}{30}t\right) e^{-\frac{t}{100}} + 15$ $0 < t < 200$
- d) $\sin\left(\frac{2\pi}{10-\frac{t-70}{20}}t\right) e^{-\frac{t}{100}} + 15$ $70 < t < 130$

Time series a) consists of a sine function with a period of 10 s for the first 100 seconds,

CHAPTER 3. SIGNAL ANALYSIS

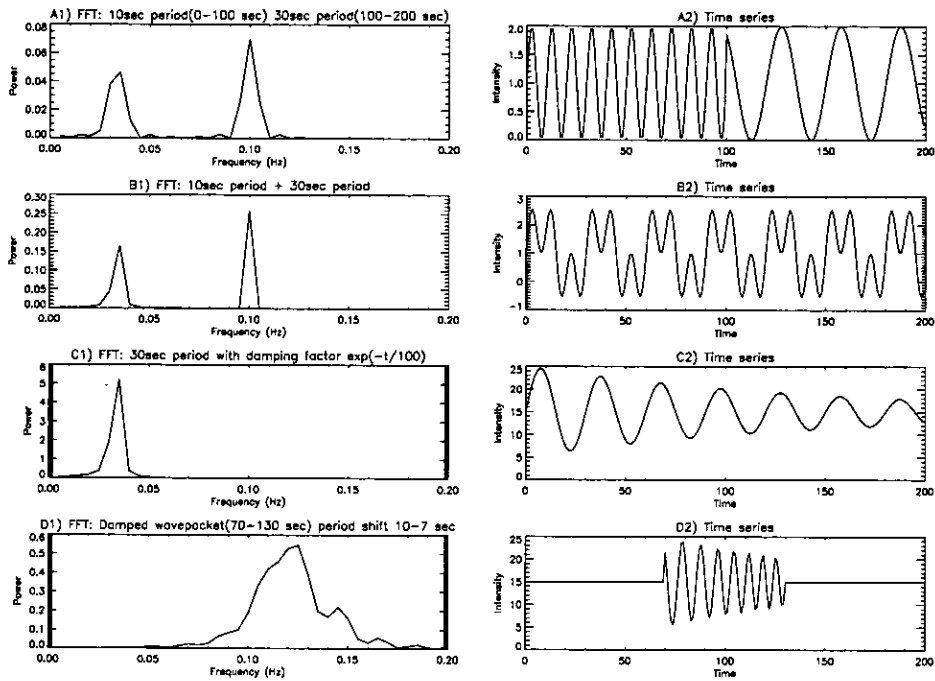


Figure 3.1: FFT power of sinusoidal time series. Time series **a**) 10 s period (0–100 s), 30 s period (100–200 s). **b**) 10 s + 30 s period. **c**) Exponentially damped 30 s period. **d**) Isolated wave packet (70–130 s) with a period shift from 10–7 s, and exponential damping.

and a sine function with a period of 30 s for the last 100 seconds. Time series **b**) consists of the superposition of two sine functions of period 10 and 30 seconds. Time series **c**) is a 30 s period sine wave damped by an exponential decay function. Time series **d**) is an exponentially damped, isolated wave packet between 70–130 s, with a shift in period from 10–7 s.

Considering Fig. 3.1, the Fourier transform reveals the frequencies present within the time series. However, the Fourier transform does not give an indication of how the properties of the oscillation change with time, such as the amplitude, or the time localisation/dependence of the frequencies. The FFT of time series **a**) & **b**) are almost identical, although the time series are very different. The FFT of time series **c**) does not give an indication of the dampening of the oscillation amplitude. Although the distribution of power is broadened in the FFT of time series **d**), the exact nature of the time series cannot be determined from the Fourier transform alone.

3.2 Wavelet analysis

Unlike the Fourier transform, which returns the frequency information of the time series as a whole, the wavelet transform returns wavelet scale information as a function of time. The wavelet scale is proportional to the Fourier period, and can be converted using a correction factor dependent upon the wavelet function used. Wavelet analysis allows the investigation of the time dependence of periodicity within the data. This makes the technique useful for investigating periods that are localised in time, or have a time variable period.

A detailed description of the wavelet transform and wavelet analysis is given in Farge (1992) and Torrence & Compo (1998); a summary of the method is presented here. Assuming a time series x_n of N observations and constant sample spacing δt , the continuous wavelet transform is defined as the convolution of x_n with a scaled and translated wavelet (or mother) function $\psi(\eta)$, where η is a non dimensional time parameter. Acceptable wavelet functions are localised in time and frequency space with zero mean. Thus ψ is assumed to be normalised, i.e. $\int_{-\infty}^{+\infty} \psi\psi^* d\eta = 1$. The Morlet wavelet is used as the wavelet function for the analysis applied in this thesis. The Morlet wavelet consists of a plane wave modulated by a Gaussian, and is applied as it represents the oscillatory nature of periodicity that we may expect in the solar atmosphere. Figure 3.2 shows the real and complex components of the Morlet wavelet.

The Morlet wavelet is defined as

$$\psi(\eta) = \pi^{-1/4} \exp(i6\eta) \exp\left(-\frac{\eta^2}{2}\right). \quad (3.3)$$

The continuous wavelet transform is defined as

$$W_n(s) = \sum_{n'=0}^{N-1} x_{n'} \sqrt{\frac{\delta t}{s}} \psi^* \left[\frac{(n' - n)\delta t}{s} \right], \quad (3.4)$$

where $\eta = (n' - n)\delta t/s$, s is the wavelet scale, ψ^* indicates the complex conjugate and n allows the wavelet function to be translated in time. Varying the wavelet scale s and translating along the time index n allows a two-dimensional power spectrum to be formed. This describes how the periods present vary with scale, and as a function of time. The wavelet power spectrum is then defined as $|W_n(s)|^2$

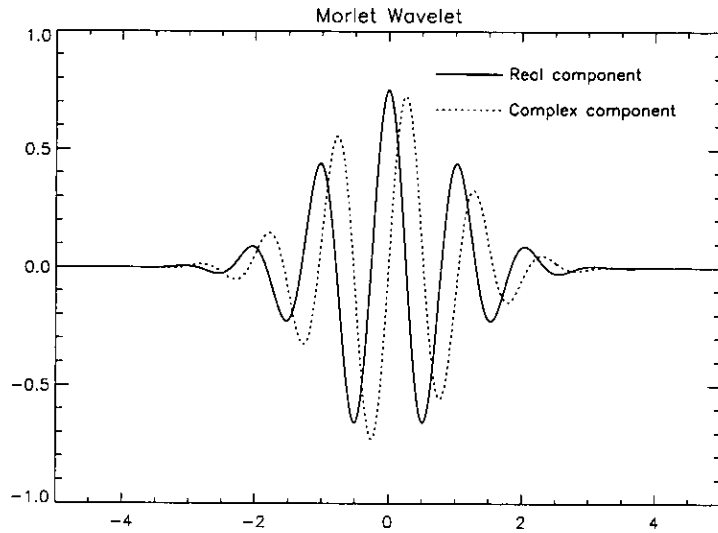


Figure 3.2: The real and complex components of the Morlet wavelet.

The time series and wavelet function are finite. This means that the wavelet transform suffers from edge effects at the ends of the time series by an amount proportional to the wavelet scale. A cone of influence (COI) indicates where these edge effects become significant; this is defined by the region in which the wavelet power drops by a factor of e^{-2} . Areas of the wavelet power spectrum outside the region bounded by the cone of influence and the time axis suffer from these edge effects, and should not be included in any analysis.

Figure 3.3 shows the corresponding wavelet power spectra of the time series used to form the Fourier transforms in Fig. 3.1. Time is represented along the abscissa; wavelet scale is represented by the ordinate, and the axis has been corrected to the equivalent Fourier period and is plotted on a logarithmic scale. The bell shaped curve indicates the cone of influence, and only the region bounded by the COI and the abscissa is considered free from edge effects. Wavelet power is indicated by grey scale shades, with darker shades representing greater power. Significant power is enclosed by 99% confidence contours, described in more detail in the next section.

Comparing Figs. 3.3 and 3.1, it is clear that the wavelet power spectra contain much more information than the Fourier power spectra. The wavelet power spectrum for time series a) reveals that the 10 and 30 s period are present within different halves of the time series, compared

CHAPTER 3. SIGNAL ANALYSIS

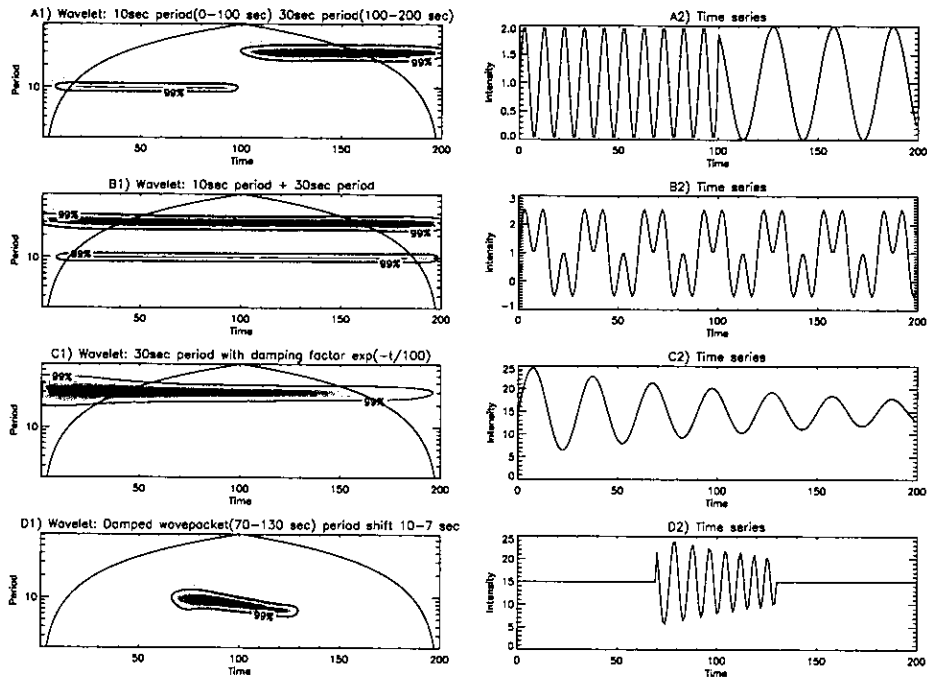


Figure 3.3: Corresponding wavelet power spectra for the time series in Fig. 3.1. **a)** 10 s period (0–100 s), 30 s period (100–200 s). **b)** 10 s + 30 s period. **c)** Exponentially damped 30 s period. **d)** Isolated wave packet (70–130 s) with a period shift from 10–7 s, and exponential damping. The curved line in the wavelet power spectrum indicates the cone of influence.

to the power spectrum for time series b) which shows that the periods are present throughout the time series. The power spectrum for time series c) shows a reduction in the power of the 30 s period over time, indicating that the oscillation is damped. The power spectrum for time series d) reveals that the oscillation is an isolated wave packet, the change in period and damping of the oscillation can also be observed from the wavelet power spectrum.

3.2.1 Significance levels

To place a confidence or significance level on any periods present in the wavelet power spectrum, a background noise spectrum must be assumed. Any power present in the analysis is calculated by comparing the data power spectrum to the background noise spectrum. Contours of significance are formed, inside which the wavelet power is considered significant within a given confidence level. Poisson distributed noise is assumed, from the photon counting statistics. The variance of the Poisson distribution is equal to the distribution mean, and $\sigma^2 = \text{Variance}$.

CHAPTER 3. SIGNAL ANALYSIS

Then assuming a stationary time series x_i of N observations, the Poisson noise is given by $\sigma_p^2 = \bar{x}$, where $\bar{x} = \frac{1}{N} \sum_{i=0}^{N-1} x_i$.

Following the method of De Moortel (2000) and Torrence & Compo (1998), the distribution of local wavelet power is

$$\frac{|W_n(s)|^2}{\sigma_p^2} \rightarrow \frac{1}{2}\chi_2^2$$

where “ \rightarrow ” indicates “is distributed as”, and χ_2^2 is the χ^2 distribution with two degrees of freedom. The probability that the power level due to noise P_σ is greater than the power level at a given detection level P_{det} is

$$Prob(P_\sigma > P_{det}) = Q(P_{det}|2)$$

where Q is the integral probability of the χ^2 distribution. $(1 - p)$ is defined as probability that the local wavelet power is greater than the detection level, and is not due to noise.

$$\Rightarrow p = Q(P_{det}|2); \quad \text{or} \quad P_{det} = 2 \ln \frac{1}{p}.$$

For the analysis in this thesis a significance level of 99.0% is used, or $p = 0.01$, implying that there is a 1.0% probability that any significant power is caused by chance, occurring when

$$\frac{|W_n(s)|^2}{\sigma_p^2} > \ln \frac{1}{p}.$$

Chapter 4

Observed Periodicity Within a Network/Internetwork and Coronal Hole Boundary region

4.1 Introduction

In the following, high time resolution (≈ 13 sec cadence) CDS/GIS time series data are analysed for evidence of quasi-periodic variability in the solar corona. The observations are obtained from a GIS study of a network/internetwork area located near a coronal hole boundary region taken in October 1997. A wavelet analysis is applied to EUV emission lines covering a temperature range of $\log T_e = 5.3\text{--}6.1$ K (Table 4.1). Statistically significant periods are found within the range 100–900 seconds and 1500 seconds with observations of short wavepackets with periods of the order 50–100 seconds with durations of 2–5 cycles. Observations of a decay in the driving period over time are also described. Note that this work has been published in Marsh et al. (2002).

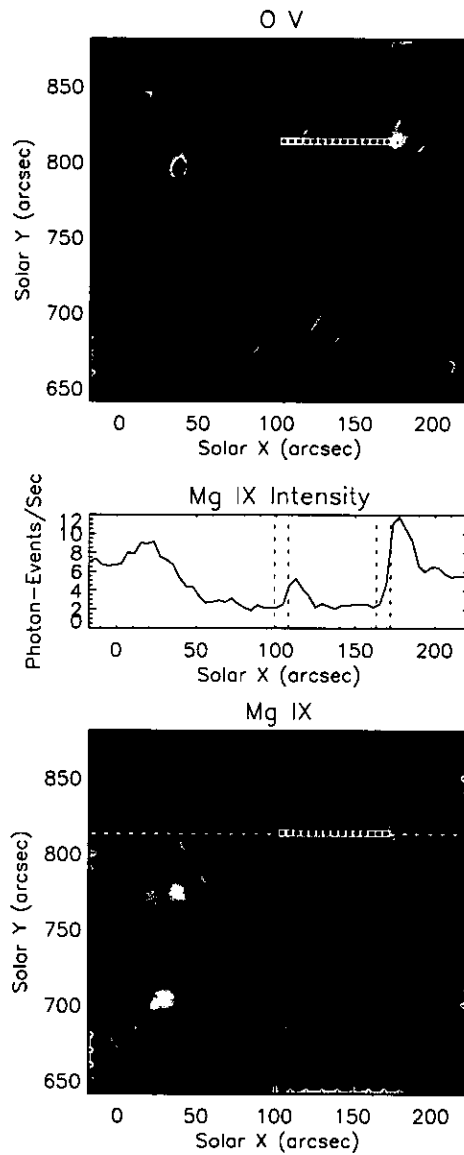


Figure 4.1: Positions of the GIS observations overlying O V 629 Å and Mg IX 368 Å NIS context images. The observing sequence runs from right to left. The O V image reveals the chromospheric network pattern as high intensity regions. The GIS observations begin and end in the network, with most of the sequence passing over the internetwork regions. The Mg IX image displays the location of the coronal hole. The GIS observations begin at the hole boundary and end within the centre of the hole. The middle plot shows Mg IX intensity along dotted line in the Mg IX context image. The vertical dotted lines mark the location of the first and last two GIS observing positions which lie over the two network regions. The hole boundary appears at around 40'' and 170'' with the lower intensity coronal hole region in between.

4.2 Observations

The observations analysed in this chapter were obtained from a CDS-GIS study performed on 15th October 1997 at 21:21 UT. This study contained fifteen positions of the GIS slit, beginning at a coronal hole boundary and crossing into the coronal hole in the West-East direction. At each position 100 exposures of 5 seconds duration were taken resulting in a cadence of approximately 6 seconds after taking into account instrumental overheads. The study uses the $4'' \times 4''$ slit, stepping in the West-East direction by 4 arcsec increments for each successive position. It should be noted that the GIS grating is astigmatic i.e. images are not resolved spatially. Therefore the GIS spectra are one-dimensional.

Figure 4.1 shows NIS images in the O V 629.7 Å line (peak emission at a temperature of $\log T_e=5.4$ K) and the Mg IX 368 Å line (peak emission at $\log T_e=6.0$ K) showing the chromospheric network pattern and the coronal hole region respectively. Plotted over the images are the 15 positions of the $4'' \times 4''$ GIS slit with each box representing the slit boundary. The NIS observations preceded the GIS observations by ≈ 40 minutes. This has been taken into account with respect to solar rotation when plotting the slit positions. The O V image shows the positions of the observations relative to the bright and dark emission corresponding to the network and internetwork regions respectively. The Mg IX image shows the positions of the observations relative to the coronal hole region. The middle plot in Fig. 4.1 shows the Mg IX intensity across the dotted line in the Mg IX context image. This displays the lower intensity region of the coronal hole, and the brighter quiet sun regions. The position of the coronal hole boundary region can be estimated from the extent of the intensity transition between the coronal hole and quiet sun regions. The vertical dotted lines in this plot show the location of the first and last two positions of the GIS observations. These are located over the bright network regions, with the first two also positioned over the coronal hole boundary region. The slight misalignment between these positions and the network regions can be accounted for by the CDS pointing error ($\approx 5''$), and the time delay between the NIS and GIS observations.

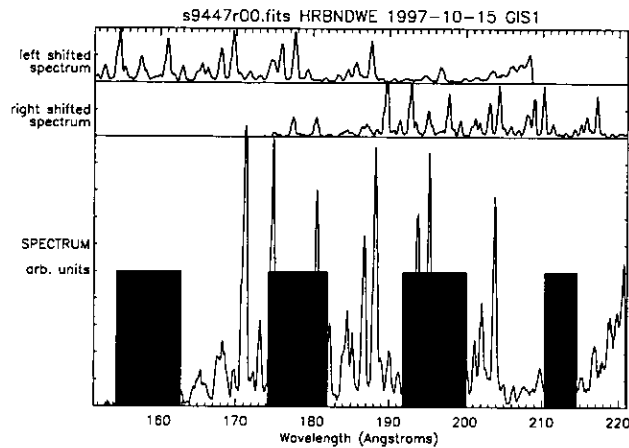


Figure 4.2: Single detector spectrum with bars indicating the ghosting regions

4.3 GIS instrumental effects

GIS suffers from a number of instrumental effects which are described in more detail in the CDS software notes 54, 55, and 56 (Bentley 1999; Breeveld 2000b,a). “Ghosting” is one of the instrumental effects that occurs because the analogue electronics in the GIS detectors are affected by electronic noise. This results in an uncertainty in the position of an event on the detector. Consequently, counts occurring at one position on the detector can be wrongly recorded as occurring in a different part of the spectrum. However, the regions of the spectrum that are affected (ghosting regions) can be calculated. Standard CDS software procedures are available to display the ghosting regions (Fig. 4.2), and if possible “shift” the ghosted counts back to their correct position (see CDS software notes 54–56). For this analysis it was decided to avoid spectral lines located in ghosting regions completely, thus eliminating any effect of ghosting, or its correction, on the intensity of the lines. However, this restricts the number of lines available for analysis; the lines analysed should also be isolated, unblended and have maximum signal to noise. Considering these criteria, the lines were identified and selected with reference to Del Zanna (1999). The lines selected for analysis are listed in Table 4.1.

Another instrumental effect, namely “Fixed Patterning” is due to inadequate resolution in the calculation of the position of a photon-event on the detector. This means that adjacent pixels can share varying amounts of counts i.e. some pixels can show enhanced counts while others show a reduced number of counts. Fixed patterning can be reduced by smoothing the

Table 4.1: Spectral lines analysed with emitting ion, emitted wavelength, and log of peak emission temperature.

Ion	Wavelength Å	Log T_e
Ne IV	469.9	5.31
Ne VII	465.2	5.88
Ne VIII	780.3	5.95
Ne VIII	770.4	5.96
O VI	173.0	5.97
Fe IX	171.1	6.00
Fe XI	180.4	6.05
Fe XIII	203.8	6.07

spectral data.

The original data were taken at a cadence of ≈ 6 seconds. However the data were summed over two exposures to increase the signal to noise ratio giving a cadence of ≈ 13 seconds.

4.4 GIS calibration

Data is normally calibrated using the standard CDS software routine GIS_CALIB. This applies corrections for the various dead times and non-linearities across the GIS detector. The current observations are of a low intensity quiet-sun/coronal hole region; thus dead time corrections should have little effect. Also the analysis is concerned with variations in intensity so the absolute intensity need not be calculated. Since small variations in intensity are being investigated and the calibration applies unnecessary modifications to the data (which may introduce errors affecting the detected periodicities) no intensity calibration is applied in this analysis. Any cosmic ray strikes in the data will be visible in the time series formed as a saturation in intensity. Pre-launch wavelength calibrations are applied automatically when the data is read.

4.5 Time series analysis

4.5.1 Pixel summing method

The time series in this study were formed using the simple method of summing the number of counts across the spectral pixels covered by each line. The exposures from the first position in the study showed no significant Doppler motion of the lines. It is also found that the wavelet

CHAPTER 4. PERIODICITY WITHIN A CORONAL HOLE BOUNDARY REGION

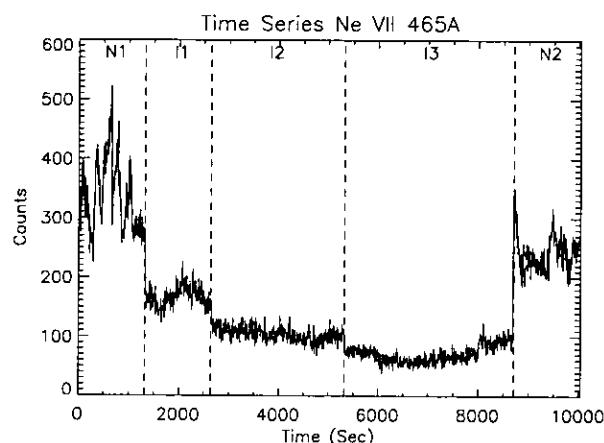


Figure 4.3: Ne VII 465 Å time series for whole study. The dotted lines indicate where the time series is broken down into blocks with two network (N1,N2) and three internetwork (I1,I2,I3) regions. Note that progression in time corresponds to slit movement from West to East across the sun. Each of the 15 slit positions is observed for approximately 660 sec.

analysis is quite insensitive to summing across different pixel ranges close to the line. The time series were formed by summing across each emission line with a pixel range that encompasses the entire line to allow for any slight Doppler variation that might be present. A method of determining the lines intensity by curve-fitting was not applied as the data would have to be smoothed to reduce the fixed patterning. This would also smooth more noise into the lines estimated intensity. The process itself would also introduce fitting errors and would also be increasingly unreliable for low intensity lines. The simplest and most accurate method of determining the lines total intensity appears to be one of summing the counts across a pixel range, on condition that the line does not show significant Doppler motion. The background level is ≈ 0.1 photon-events/pixel/sec with slight variation across the different detectors. In this analysis the background is assumed to be negligible relative to the intensity of the lines and is assumed to be zero.

Figure 4.1 indicates that the observing sequence begins in a bright network region, passes through an internetwork region and ends in a less intense network region. The first slit position is located at the western boundary of a coronal hole with the rest of the positions located within the hole itself. These changes in structure imply that a concatenated time series formed from the whole study would show variations in intensity representing different structures over which

CHAPTER 4. PERIODICITY WITHIN A CORONAL HOLE BOUNDARY REGION

the slit is positioned. Fig. 4.3 shows the concatenated time series for the whole study in the Ne VII 465 Å line. Clearly visible are the bright network regions at the beginning and end of the time series, along with the low intensity internetwork region in between.

As described in Chapter 3 the wavelet analysis is performed assuming Poisson distributed noise. To make this assumption the time series must be considered as stationary i.e. the time series must have a constant mean and variation. From Fig. 4.3 clearly this is not the case for the entire time series. To perform the analysis the time series must be broken down into blocks that show similar structure. It is then assumed that these time series blocks are stationary. Considering Fig. 4.3 it can be seen that the network regions at the beginning and end of the time series can be split into two separate time series without discontinuities. The internetwork region can also be split into three separate continuous time series with each analysed separately. As each spectral line has a different emission temperature, the time series for each line is broken down into different size blocks representing changing emission structure with temperature. Also note that the maximum measurable period is limited by the length of the time series being analysed.

4.5.2 Curve Fitting of Ne VII and Ca IX

The Ne VII 465.2 Å line is situated close to the Ca IX 466.2 Å line. Although neither of the lines appear to show any significant Doppler motion, a curve fitting method was applied to the data to determine the intensity of the Ne VII line. This was applied using the standard CDS software procedure CFIT_BLOCK. Multiple Gaussians can be fitted to the data allowing the intensity of the Ne VII line to be isolated from any effect the Ca IX line may have. A 10pt smooth was first applied to the data to reduce the fixed patterning; this was to reduce any fitting errors produced by the automated routine that CFIT_BLOCK employs. The time series obtained by this Gaussian fitting method and its associated wavelet power spectrum were compared to those produced by the simple summing method, and found to be almost identical.

As mentioned previously, before Gaussian fitting is applied to GIS data it must first be smoothed to reduce the fixed patterning. This allows the possibility that some of the counts from Ca IX may be smoothed into the Ne VII line and vice versa. To eliminate this effect as a

possibility, another test was performed on extracting the time series. This method used the fact that under a 10pt smooth any counts merged into the Ne VII line will cause an asymmetry in the right hand side of the Ne VII profile. To determine the intensity of the Ne VII line, the centre of the line is found by the fact that points either side of it should show the minimum amount of asymmetry. The counts in the left hand side of the line can then be determined and doubled to reproduce the total counts within the line. Again, the time series and wavelet power spectrum were almost identical to those produced by the simple summing method, giving agreement within the level of noise.

This demonstrates that the Ca IX line has a negligible blending effect on the Ne VII line in these data, and that the simple summing method is an acceptable method of extracting the time series.

4.6 Wavelet analysis

Unlike the Fourier transform, which returns frequency information on the time series as a whole, the wavelet transform returns wavelet scale information as a function of time (see Chapter 3). Wavelet scale is proportional to the Fourier period and is easily calculated. Consequently, wavelet analysis allows the investigation of the time dependence of periods within the data. This makes the technique useful for investigating periods that are localised in time.

4.6.1 Evenly spaced time series

Wavelet analysis requires evenly sampled data. Although the exposure time for this study is 5 seconds, after instrument overheads are taken into account this is increased. Examination of the studies timing data shows that the average exposure spacing is 6.6 sec with a standard deviation of 0.23 sec. This leads to a 3% fractional error in the cadence of the study and any significant periods detected. Any irregular spacing in time between slit positions is linearly interpolated by rounding down to an integer spacing of this mean cadence. Typically, adjacent slit positions are interpolated using 1 or 2 data points. Any localised periods occurring at a boundary between positions are indicated in the results to be aware of any effect which non-integer spacing may cause.

4.7 Results

Table 4.2 lists the results from the wavelet analysis which were read directly from the wavelet power spectra. Listed in the table are the occurrence times from the beginning of the study and the value of any periods present in the data. The stated values indicate the period and time of maximum wavelet power (Max). Wavelet analysis does not return an exact value of period or time; instead contours of significance are formed around any power lying within a given significance level as shown in Figs 4.8 & 4.9. The ranges given in the table indicate the extent of these significance levels along the period and time axes. In cases where the contour levels for a particular period fall outside the COI, then the ranges limited by the COI are given and indicated by (c). The periods present in the spectra were divided into two classes: bands (b) and localised (o) bursts. These are either bands of power that extend across the COI, or localised bursts of power that persist for only a few cycles. In the cases where no (Max) is given only the lower values of the period range can be valid given that the time range within the COI must be long enough to allow one complete cycle. Results marked with a † occur at points in the time series where the interval between positions has been interpolated. The physical region in the study where the period is observed is also listed. Positions 00–01 cover the first network region (N1), positions 13–14 are located over the second network region (N2) and positions 02–12 overlie the internetwork region.

The temporal information that wavelet analysis returns allows other properties of the detected periods to be determined. The number of cycles of a given period can be obtained from the wavelet power spectra. Here the given period is that having maximum wavelet power within the contour level, and the extent of the period in time is given by the range in time of the contour level, e.g. a period of 200 sec persisting for 800 sec has 4 detected cycles. Figs. 4.4–4.7 show the number of cycles observed for each detected burst of periodicity in the first network region (Fig. 4.4), internetwork region (with same period range as network regions Fig. 4.5), internetwork region with longer period range (Fig. 4.6) and second network region (Fig. 4.7). It should be noted that the number of cycles in the longer periods may be limited by the COI depending on the length of the time series, particularly in the network regions. With this in mind, to produce a stationary signal the time series for Fe XI had to be formed from single

CHAPTER 4. PERIODICITY WITHIN A CORONAL HOLE BOUNDARY REGION

Table 4.2: Wavelet results for each spectral line including period and time of occurrence from the beginning of the study. Ranges indicate limits of contours formed by the 99% confidence level. Values limited by COI are indicated by (c). (Max) indicates period and time values of maximum wavelet power. Periods are classed as either bands (b) or localised bursts (o). † indicates periods that occur on a boundary between slit positions in the time series. The physical location in which the period occurs is listed as either the first/second network region (N1/N2) or the internetwork region (I). Periods and times are given in sec.

Ion Wavelength Å	Period Range (Max)	Time Range (Max)	Class	Location
Ne IV 469	48–99 (77)	266–632 (451)	o	N1
—	94–117 (105)	988–1174 (1091)	o	N1
—	96–233 (155)	540–898 (703)	b	N1
—	180–342 (227)	314–928 (317)	b	N1
—	171–225 (194)	4038–4365 (4187)	o	I
—	281–1445c (760)	2370c–4276c (3233)	b	I
—	54–64 (59)	5930–6004 (5967)	o	I
—	50–66 (58)	8490–8596c (8558)	o	I
—	66–93 (79)	8185–8477 (8328)	o	I
—	753–1081 (914)	6377c–7626c	b	I
—	76–113 (93)	9324–9472 (9389)	o †	N2
—	113–142 (130)	9545–9856c (9828)	b	N2
—	203–262 (236)	8988c–9424	b	N2
—	336–482c	9177c–9552c	b	N2
Ne VII 465	40–90 (66)	576–749 (656)	o †	N1
—	101–169 (139)	219–881 (685)	o	N1
—	184–273 (219)	283c–1032 (390)	b	N1
—	243–367 (311)	1671c–2265c (1793)	b	I
—	96–129 (111)	4602–4746 (4667)	o †	I
—	435–551 (489)	3874–4726c (4345)	b	I
—	40–106 (84)	7993–8148 (8067)	o †	I
—	148–687	7440–8341c (8018)	o	I
—	356–529 (443)	5849c–6433 (6079)	o	I
—	39–84 (59)	8825–8973 (8899)	o	N2
—	85–143 (135)	9496–9832 (9794)	b	N2
—	178–274 (222)	9002–9715 (9491)	b	N2
Ne VIII 780	42–58 (50)	302–424 (358)	o	N1
—	116–138 (126)	324–800 (517)	b	N1
—	180–255 (198)	398–1036 (734)	b	N1
—	44–73 (56)	2174–2304 (2230)	o	I
—	101–156 (126)	2860–3128 (2983)	o	I
—	405–671 (547)	4102–5535 (4920)	o	I
—	1458–1894	4707c–6577c (5804)	b	I
—	39–57 (48)	9000–9103 (9057)	o	N2
—	61–85 (72)	9599–9910c(9690)	o	N2

CHAPTER 4. PERIODICITY WITHIN A CORONAL HOLE BOUNDARY REGION

Table 4.2: Continued.

Ion Wavelength Å	Period Range (Max)	Time Range (Max)	Class	Location
Ne VIII 770	85-291 (201)	285c-1095c (754)	b	N1
—	83-138 (100)	1852-2091 (1962)	o †	I
—	40-55 (47)	2770-2938 (2837)	o	I
—	56-69 (61)	3890-4035 (3968)	o	I
—	59-85 (72)	8066-8267 (8166)	o	I
—	294-364 (324)	3386-4203 (3789)	o	I
—	159-290 (236)	9256-9705c (9461)	o	N2
—	313-482c	9126c-9537c (9254)	b	N2
O VI 173	36-50 (42)	966-1042 (1000)	o	N1
—	831-165 (107)	519-827 (627)	o †	N1
—	155-470c (234)	224-871 (366)	b	N1
—	125-162 (140)	1945-2288 (2094)	o	I
—	187-283 (235)	1670-2176 (1923)	o	I
—	97-134 (118)	8123-8446 (8303)	o	I
—	173-228 (203)	5781-6122 (5930)	o	I
—	466-969 (626)	6445c-8018c (7570)	b	I
—	193-277 (229)	9010c-9742c (9412)	b	N2
Fe IX 171	185-306 (245)	270c-893 (353)	b	N1
—	209-247 (228)	4673-4998 (4830)	o	I
—	314-542 (409)	3184c-3912 (3520)	o	I
—	116-482c (212)	9103c-9577c (9367,9394)	b †	N2
Fe XI 180	79-104 (90)	6030-6155 (6092)	o	I
—	99-116 (107)	5420-5582 (5507)	o	I
—	146-215 (178)	2929-3465 (3153)	o	I
—	1288-1651 (1525)	3950c-6864c (5370)	b	I
Fe XIII 203	75-112 (92)	114c-297 (194)	o	N1
—	205-239 (222)	3346-3935 (3620)	o	I
—	60-155 (123)	9135-9619 (9380)	o †	I
—	104c-128 (117)	8840c-9007 (8864)	o	N2
—	228-482c	9103c-9705c (9382)	b	N2

positions in the network regions with periods above ≈ 170 seconds falling outside the COI. The network regions showed no distinct periods in this line.

The first and brightest network region shows a range of approximately 1.5–5 cycles, with three short periods having around two cycles and a 77 second period in Ne IV with ≈ 4.75 cycles; the longer periods tend to cover a range of cycles. Note that hereafter the term short periods will be used to describe these periods < 100 sec.

The internetwork region has between 1.25–4 cycles within the range of detected periods. There are ten short periods present covering a range of cycles from 1.2–3.7. Figure 4.5 shows that the majority of the periods are found below 500 seconds, compared to Fig 4.6. One possibility is that the periods are limited by the COI; however, due to the greater length of the time series in the internetwork region periods up to ≈ 1000 seconds will be unaffected by the COI.

The second network region shows a range of 1.5–4.25 cycles. Three short periods are present with 1.5–2.5 cycles with a 72 second period in Ne VIII having 4.25 cycles. The longer periods tend to lie in the range of 1.5–3.2 cycles. There are a smaller number of distinct periods present in the second network region (Fig 4.7), appearing to have less cycles than those in the first network region.

Considering Fig. 4.5 it appears that there are more short periods present in the internetwork region than the network regions. However, the first and second network regions cover the first two and last two positions respectively (≈ 1300 sec), where as the internetwork region covers eleven positions in between (≈ 7300 sec). Thus considering the length of observing time it is possible that the network regions have a greater density of short periods per unit time. It is also possible that some of the short periods fall below the 99% confidence level in the internetwork, due to the lower intensity level giving a reduced signal to noise ratio.

4.7.1 Localised short periods

The results presented in this chapter show a number of short periods < 100 seconds across the whole temperature range $\log T_e = 5.3$ –6.1 K. The shortest period presented here from Table 4.2 is 42 sec. At a cadence of ≈ 13 sec this would give three data points for one cycle. Here it is assumed that, for the Morlet wavelet which essentially is a plane wave, at least five data points

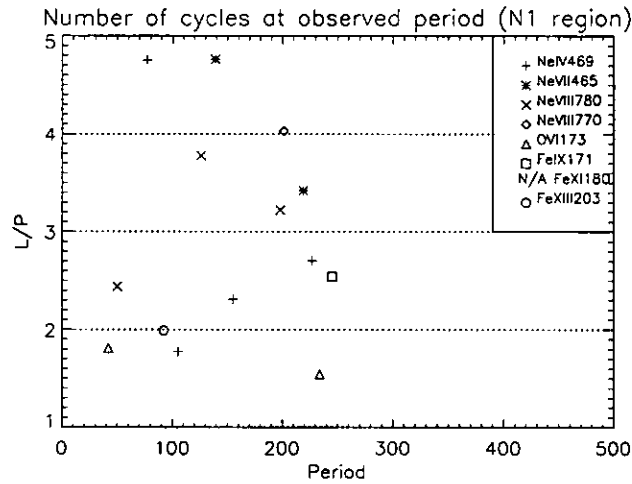


Figure 4.4: Number of cycles observed (L/P) for each period in the first network region N1. L is the extent of the period in time, P is the period.

are necessary to define an oscillation. The analysis was repeated again with a cadence of ≈ 6 sec to verify that the short periods are real; the 42 sec period then has six data points. All the short periods were still present except for the 59 sec period found in Ne IV. This may be present in the ≈ 13 sec analysis due to the increased signal to noise.

4.8 Time dependent periodicity

As mentioned previously wavelet analysis returns frequency information as a function of time. Compared to Fourier methods this gives the advantage that any change in the periods present can be determined. The wavelet analysis shows a period of ≈ 220 sec present in the first network region in all but the Fe XI and Fe XIII lines. This period may not be present in these lines in the first network region, since two separate time series were formed to produce stationary time series. Considering the length of these two time series, the maximum measurable period would be limited to ≈ 170 sec by the COI.

This period appears in the wavelet power spectra as a band of power that stretches across the COI; the band of power also shows a decrease in period with time. Figures 4.8 & 4.9 show for each line: the time series (note the different scales on the y-axis), wavelet power spectrum with the position of the maximum in the band of power and the change in period of

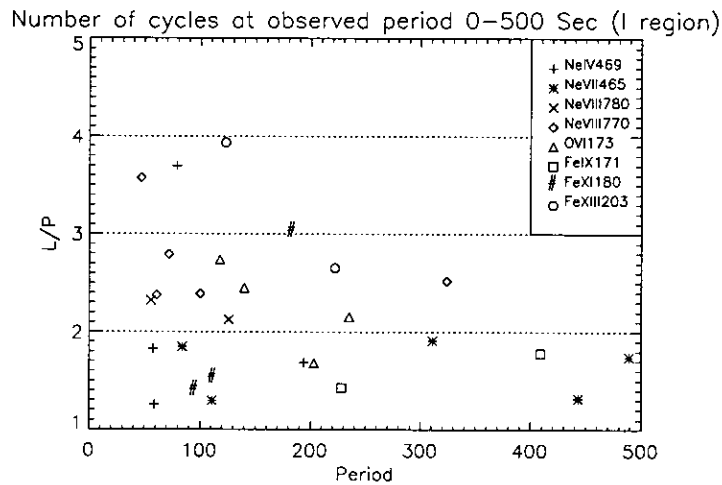


Figure 4.5: (L/P) in the internetwork region I. Period range 0–500 Sec.

maximum wavelet power with time. Considering Figs. 4.8 & 4.9, the band of power displays a decay in period by 10–20% in all the lines but one. The exception is O VI which shows a different form than the other lines. O VI has the lowest signal to noise ratio of all the lines in the study. However, it is possible the difference may be caused by a real structure emitting at this temperature.

Considering the other lines, it appears that the contours of significance represent the same underlying structure in the wavelet power. As explained in Chapter 3 the contours of significance enclose areas having greater wavelet power than expected for Poisson distributed noise. Thus, the signal to noise ratio will affect the boundary of the contour levels. The Ne VII line has the largest signal to noise ratio of the analysed lines. Examining the wavelet power spectrum for Ne VII in Fig. 4.8 we see the band of power with the marked maximum, and power in a “U” shape below. At the time around 500 sec, and at a period of approximately 170 sec a small area that drops below the significance level is observed. The wavelet power spectra for the other lines around this band show a very similar structure. It appears that the underlying wavelet power in this region of the spectrum is almost the same for all the lines, but that the contours of significance enclose this power to a varying extent. Figs. 4.8 & 4.9 show that the period causing this band of power is present in these lines at the same point in time and also in location.

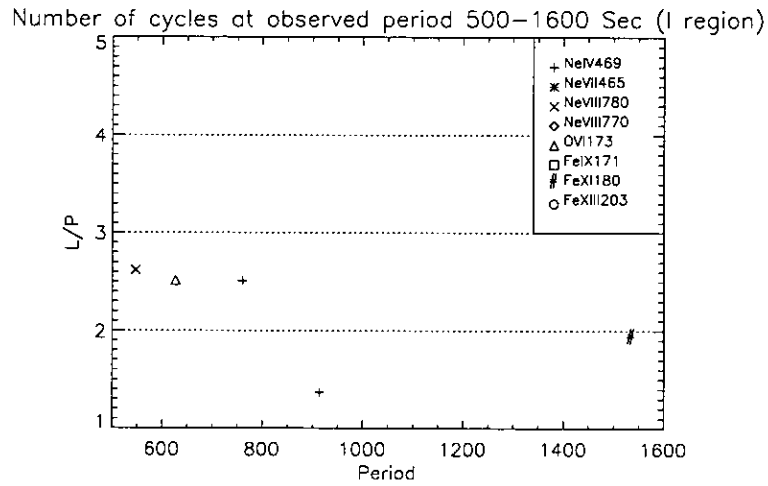


Figure 4.6: (L/P) in the internetwork region I. Period range 500–1600 Sec.

4.8.1 Error analysis

Figures 4.8 & 4.9 show the change of maximum wavelet power with time and the associated error bars. To determine this error it was necessary to measure the error in the ability of the wavelet analysis to determine the correct position of maximum wavelet power. To do this sinusoidal time series were formed to represent the time-dependent ≈ 220 sec band of power for each line. These time series were given a mean equal to the time series mean for each spectral line. The amplitude of the sine wave was then assigned a value to give a variation equal to that of the original data.

Poisson distributed noise was then added to these time series, the wavelet power spectra formed and the position of maximum wavelet power measured. This process was iterated 1000 times to determine the maximum and minimum limits of the position of maximum wavelet power. The location of maximum wavelet power will be affected by the addition of Poisson noise; the limits then give an estimate of the error in the wavelet analysis method, assuming Poisson noise. These limits are then given as the errors on maximum wavelet power for each line, shown in the plots on the right hand side of Figs. 4.8 & 4.9.

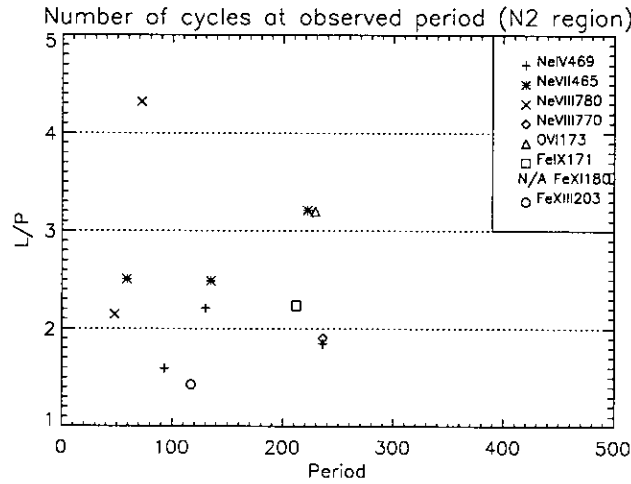


Figure 4.7: (L/P) in the second network region N2.

4.9 Discussion

A wavelet analysis method is employed to investigate oscillations within transition region/coronal spectral lines. The temporal information returned by wavelet analysis allows a deeper investigation of the periodicities present when compared to Fourier methods. The two-dimensional power spectra allows the investigation of oscillations localised in time, and the time dependence of any periodicity to be measured. Previous work on waves in coronal hole regions (see Deforest & Gurman 1998; Banerjee et al. 2001a, and references within) concentrates on the observation of polar plumes and report waves with periods of the order of 10–70 minutes. Original results are also presented of the observation of short wave packets and of a change in driving period with time.

McAteer et al. (2004) apply an automated wavelet analysis technique to TRACE UV observations of oscillations in the chromospheric network and internetwork regions. They observe a range of oscillation periods and lifetimes. The most frequent oscillation periods of 283 s and 252 s are observed in the network and internetwork respectively, with lifetimes of 2–3 cycles. A tendency of the oscillations to recur at the same location is observed.

Several authors report on the observation of short periods <100 seconds. Using CDS-NIS (Normal Incidence Spectrometer) active region data Ireland et al. (1999) find short periods of the order 60–70 seconds that persist for 2–6 oscillations in Fe XVI 360 Å ($\log T_e = 6.4$ K)

CHAPTER 4. PERIODICITY WITHIN A CORONAL HOLE BOUNDARY REGION

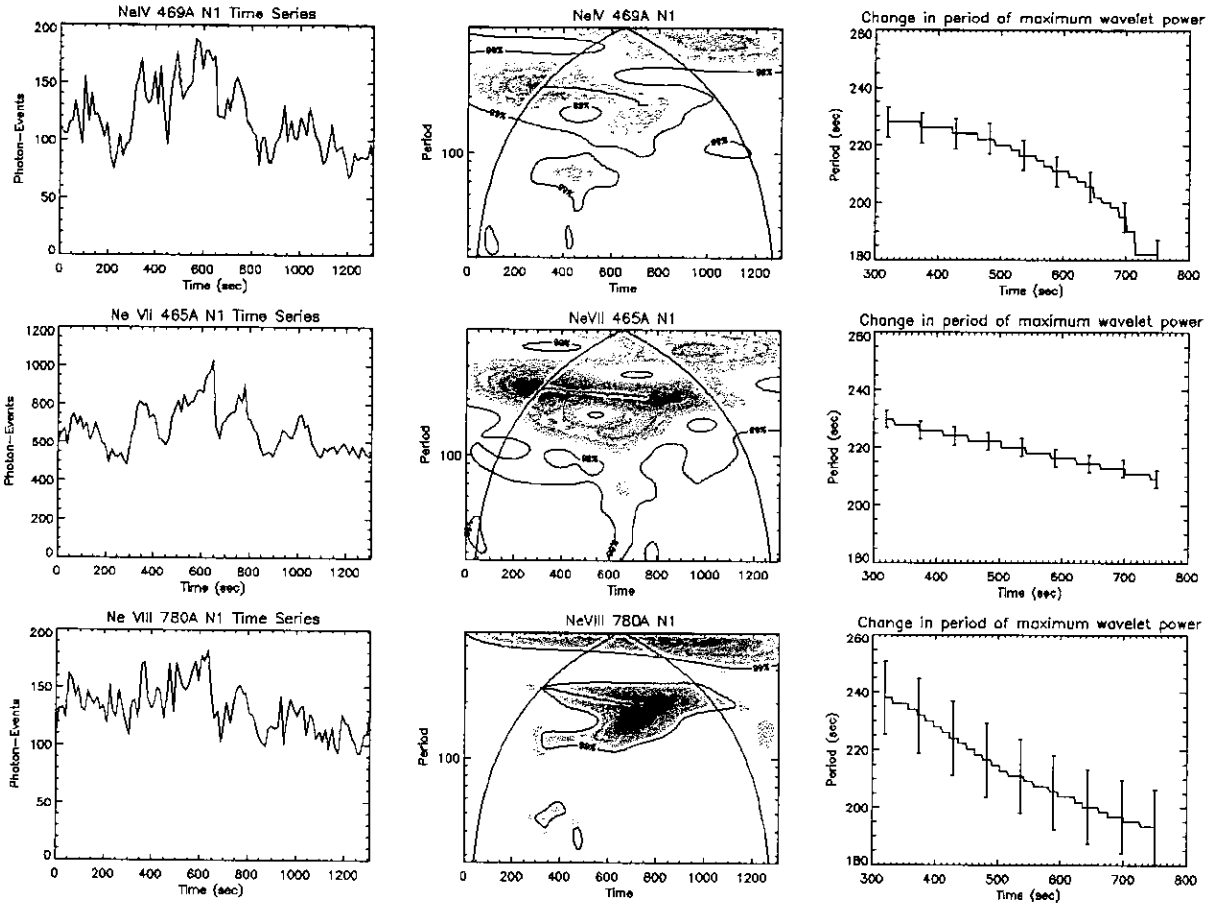


Figure 4.8: Characteristics of significant power (N1 region) in Ne IV 469 Å, Ne VII 465 Å, and Ne VIII 780 Å: Time series, wavelet power spectrum and period-time variation of maximum wavelet power.

coronal line intensity time series, with no significant short periods in Mg IX 368 Å ($\log T_e = 6.0$ K) or O V 629 Å ($\log T_e = 5.3$ K). O’Shea et al. (2001) also present results of active region observation using NIS data in the same lines. They find short periods > 50 seconds in velocity time series formed from Mg IX 368 Å and O V 629 Å with no short periods in Fe XVI 335 Å. In the intensity time series they find periods > 50 seconds in Mg IX and Fe XVI.

Hansteen et al. (2000) perform intensity and velocity time series analysis using SUMER (Solar Ultra-Violet Measurements of Emitted Radiation) observations of a quiet sun network/internetwork region using Ca II 1334 Å, C III 977 Å, and O VI 1032 Å upper chromosphere and transition region lines. Periods between 60–100 seconds are found in the intensity signal over a network position; 100 second periods in intensity are also found in the internetwork region with periods

CHAPTER 4. PERIODICITY WITHIN A CORONAL HOLE BOUNDARY REGION

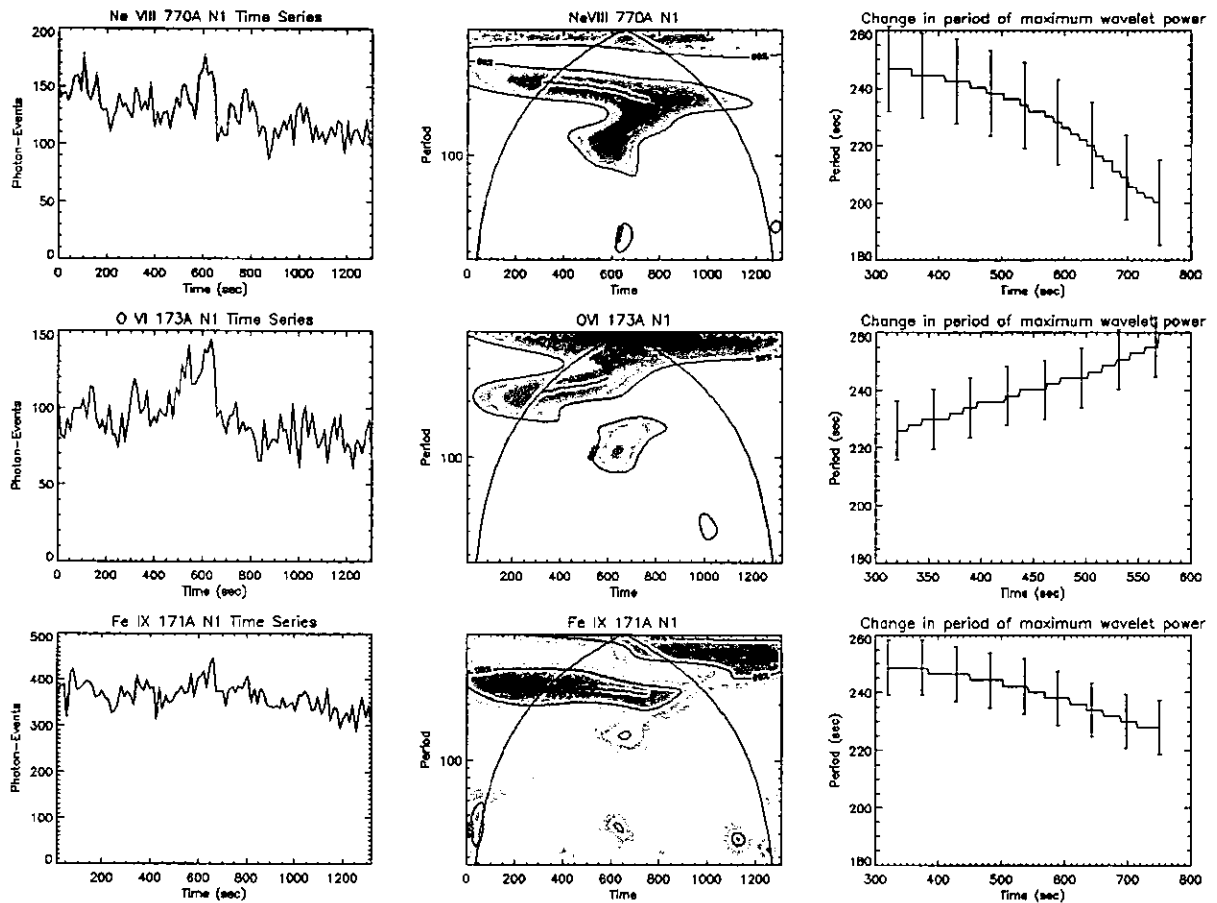


Figure 4.9: Characteristics of significant power (N1 region) in Ne VIII 770 Å, O VI 173 Å, and Fe XI 171 Å: Time series, wavelet power spectrum and period-time variation of maximum wavelet power.

around 60 seconds in the velocity signal. They find that short periods are more predominant in C III and suggest that there is even greater power at short periods in O VI but the observations are restricted by a high noise level. McKenzie & Mullan (1997) use Yohkoh X-ray light curves obtained from a number of coronal loops and find periods in the range 10–62 seconds. Koutchmy et al. (1983); Rušin & Minarovjech (1991); Cowsik et al. (1999); Singh et al. (1997) all use off-limb observations of the corona either in the red/green coronal lines or optical continuum and find periods in the range 5-90 seconds.

In the previous work listed above short periods are found predominantly in the high temperature coronal lines with the exception of Hansteen et al. (2000) who state that they find power below 100 seconds in the upper chromospheric C II 1334 Å line. It is significant that

CHAPTER 4. PERIODICITY WITHIN A CORONAL HOLE BOUNDARY REGION

this current analysis finds short periods in intensity present in lines across the temperature range $\log T_e=5.3-6.1$ K. We find short periods that are not confined to coronal temperatures but are also found in the transition region. These short periods are found in both the network and internetwork regions. Considering the length of observing time the short periods appear to show a greater density in time within the network regions. This could be due to the changing magnetic structure and decreased flux density in the internetwork compared to the network. Another possibility is that fewer periods are detected due to the lower intensity, and therefore lower signal to noise ratio in the internetwork.

A period of ≈ 220 sec is observed in all but the two highest temperature lines over a network region on a coronal hole boundary. This was the only very clear example of a co-temporal oscillation present within different lines. O'Shea et al. (2001) state that they find one of the primary periods present in Mg IX and Fe XVI at a frequency of 4.5 mHz (≈ 220 sec) in observations of active region oscillations. Hansteen et al. (2000) also find this period in observations of quiet sun regions. The magnitude of this period shows a decay with time of 10–20% throughout the lines. Since the GIS grating is astigmatic and observes one area “on disc” information about the periodicities as a function of height cannot be derived. It is also difficult to simply use the ion emission temperature to derive height through the transition region and corona. However, it can be stated that this band of power experiences a decay in the value of its period and the decay of this period is present in a number of lines emitting at temperatures in the range $\log T_e=5.3-6.1$ K at the same point in time and at the same location. This suggests that the driver experiences a decay in its period or there is some change in the physical conditions resulting in the observed time dependence. The periods presented here are consistent with previous work in that they could be interpreted as slow mode magneto-acoustic waves or possibly fast mode in the case of the short periods. Considering the time series in Figs. 4.8 & 4.9, no significant change of phase is visible in the ≈ 220 sec period between the different lines. Also, because this band of power is limited by the COI, no information on any lag in the start time between different lines can be observed.

Another possible cause of this time dependence is the motion of the slit across an inhomogeneous magnetic structure. This implies different locations across the structure would contain

CHAPTER 4. PERIODICITY WITHIN A CORONAL HOLE BOUNDARY REGION

waves of slightly different period; this may be a possible signature of phase mixing. However, this possibility is perhaps less likely considering the smooth decay in period, and the fact the data is concatenated from two different positions of the slit to produce the time series for the first network region.

Solar rotation can be excluded as a cause of this period, as periods on the order of an hour would be expected due to material passing under the slit. It is interesting to note that examples of a ≈ 220 sec period can be found in the second network region although these examples are less consistent and extensive in time. It is possible that this may be caused by the lower intensity of the second network region which is located within the coronal hole. Alternatively the observation of this period and its decay in the first network region could be connected to its location on a coronal hole boundary, or the higher intensity could possibly indicate some underlying activity.

This work is limited by the resolution of current instruments. For the analysis of short periods the most critical factor is obtaining as high a cadence as possible whilst maximising signal to noise. A higher cadence would increase the data point resolution of the short periods reducing the minimum detectable period, and high signal to noise would increase the confidence level available. In this particular work a longer observing time over the network regions would have been useful in observing the time dependent period.

Chapter 5

Active Region Structure and Dynamics

5.1 Introduction

This chapter undertakes an analysis of the structure and dynamics of an active region using CDS-NIS spectroscopic data. The region is analysed in terms of its emission, Doppler velocity and line width structure. The observations contain two particularly interesting structures, an apparently twisted transition region loop, and a related ejection structure. These two structures are investigated in detail in terms of the spatial distribution of the emission line profile parameters.

5.2 Observations

The observations consist of rastered spectroscopic CDS-NIS data taken as part of the long term CME Onset Study program. This study is used typically to observe the solar limb in a number of lines to obtain observations of possible coronal mass ejection onsets. These present observations target the Western solar limb on the 8th February 1997. The data observes an active region and its associated dynamic structures, and consists of $240'' \times 240''$ rastered images in the following lines: He I 584 Å, O V 629 Å, Mg IX 368 Å, Fe XVI 360 Å, Si X 347 Å and Si X 356 Å.

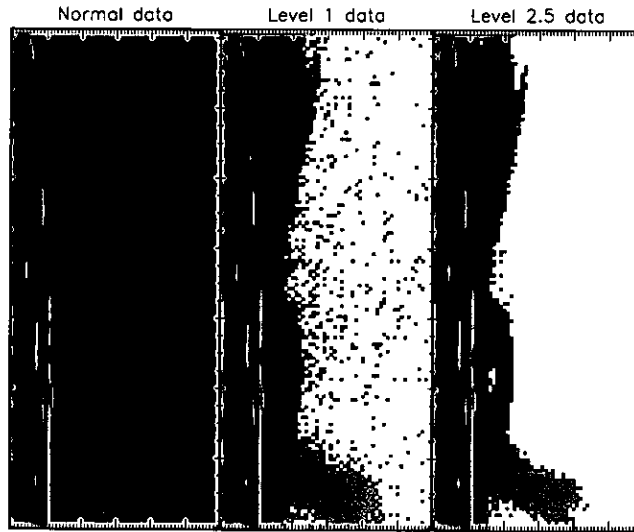


Figure 5.1: O V off-limb background noise removed using different low intensity thresholds estimated from the approximate line centre position. Running left to right (darker shades indicate greater intensity): Original calibrated data, < 1 photon-event pixels removed, < 2.5 photon-event pixels removed. The 2.5 photon-event level removes the background noise and retains the off-limb loop emission.

5.2.1 Data reduction

The data analysed here observes the solar limb; the off-limb regions record very low emission in the cooler lines, in addition to detector noise. This off-limb background noise should be removed, or marked as missing before the data are fitted. This is done by applying a binary mask method to the data. The mask is defined by setting a low intensity threshold level. The intensity of each spatial pixel is estimated using the intensity of spectral pixel #8 in each spectral window; this approximately corresponds to the central line position. Pixels with values lower than the threshold level are flagged as missing. A number of threshold levels are tested and a final value of 2.5 photon-events is chosen to remove the off-limb background noise, whilst retaining the off-limb emission structure (Fig. 5.1).

The spectral line profiles within the data are fitted with Gaussian functions using the CDS Component Fitting System (CFIT) (see Haugan 1997). The fitted line profiles allow the total line intensity, line position, and line width to be measured. The spectral line position is used to calculate the plasma Doppler velocity. However, an accurate absolute wavelength calibration is not available for CDS. The official CDS wavelength calibration and the theoretical line position

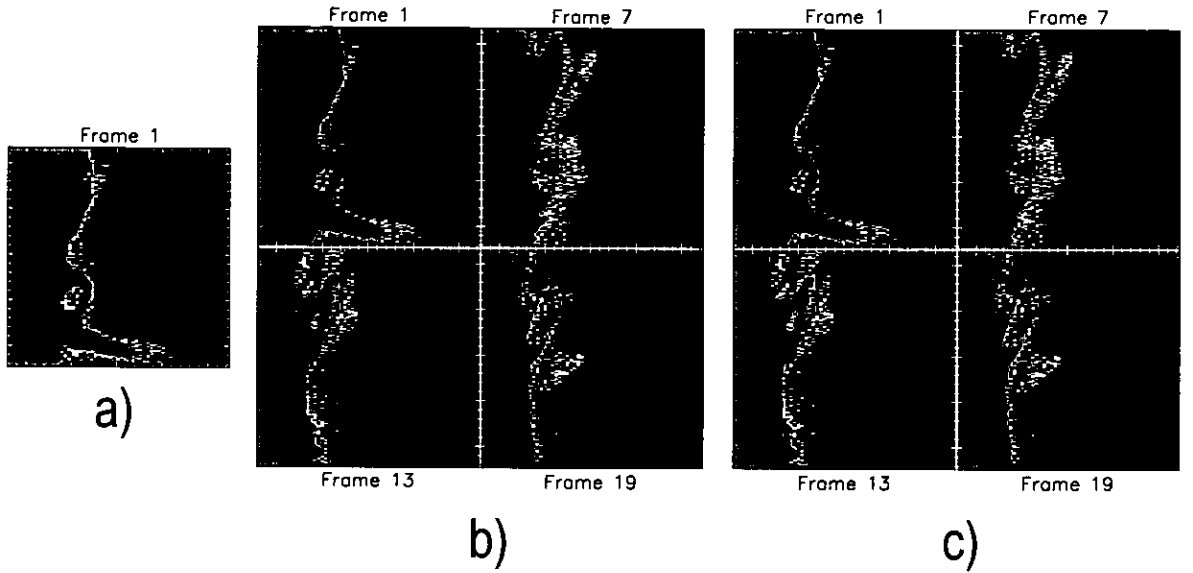


Figure 5.2: O V Doppler maps calculated using different methods to calculate the rest wavelength. **a)** Doppler velocity map calculated using wavelength given in fits file header as rest wavelength. **b)** Constant rest wavelength calculated using the average line position over the first column of pixels from the first raster of the study. **c)** Running rest wavelength calculated for each frame. Calculated using the average line position over the first five columns in each frame.

are insufficient to calculate an absolute velocity. Figure 5.2a shows an example of an O V Doppler map calculated using the rest wavelength given in the fits file data header. This value of the rest wavelength, and the standard wavelength calibration results in a red-shift of all emission. The standard wavelength calibration is not an accurate reflection of the spectral dispersion position. The relative Doppler velocity can be calculated using the line positions relative to a mean line position within the raster, used as an estimate of the rest wavelength. A number of different methods of calculating the average line position on-disk are tested. If the line position on-disk is averaged over a large enough region, the small scale velocity structure will average out to give an estimate of the line rest wavelength. Figure 5.2b shows the O V Doppler maps calculated using the line position averaged over the first column of pixels from the first raster in the study. Using this constant line position, the Doppler map for the first frame (raster) shows a reasonable velocity structure that may be expected for this region. However, if we compare the frames throughout the study, a progressively increasing blue shift is observed within each raster. This is clear to see in the on-disk region within each frame in Fig. 5.2b.

CHAPTER 5. ACTIVE REGION STRUCTURE AND DYNAMICS

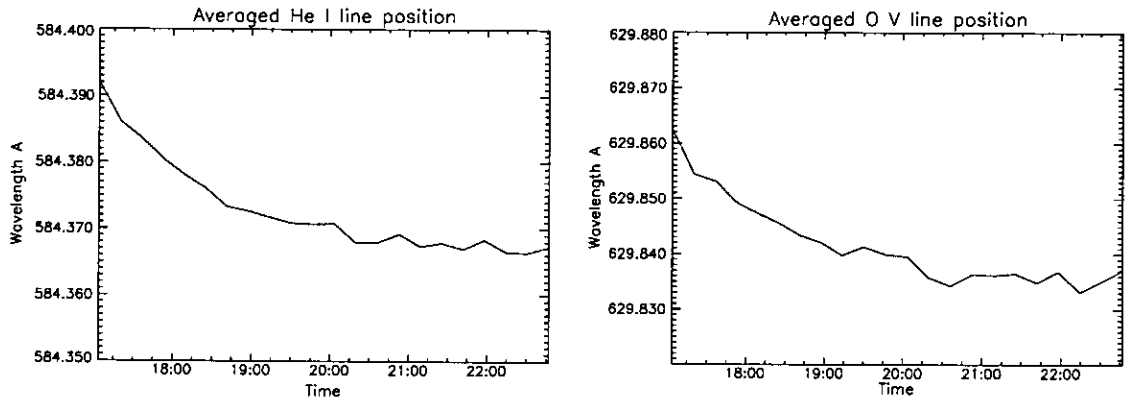


Figure 5.3: Calculated rest wavelength of He I and O V for each frame over time. The average line position calculated from the first five pixel columns shows the time dependent trend due to the non-constant spectral tilt effect.

This suggests that the dispersion position on the detector becomes progressively more blue shifted with time. The CDS calibration routine `NIS_ROTATE` corrects for the instrumental spectral rotation and tilt effects. The standard correction uses a constant correction factor for the tilt effect. However, it is found that the spectral tilt can be time dependent and is affected by temperature, pointing and mirror position (Bewsher 2002). Since the average line position is not constant in time, the average line position on-disk is calculated for each frame. Figure 5.2c shows the O V Doppler maps calculated using the mean line position over the first five pixel columns, in each respective frame, as the rest wavelength. In each frame, the average taken over the first column of pixels shows similar results to the average taken over the first five columns. The analysis of this chapter uses the latter method; averaging over a larger area reduces the effect of any large-scale velocity structure on the average line position. The time dependent tilt effect is corrected in each frame, and the granulation velocity structure is visible on-disk in Fig. 5.2c. Figure 5.3 shows the value of the calculated rest wavelength for He I and O V in each frame over time. This represents the time variability of the spectral tilt effect. The tilt shows a negative exponential type trend in both He I and O V. The progressive blue shift is visible in the on-disk region in the Doppler maps of Fig. 5.2b. Bewsher (2002) finds this tilt variation in observations of active regions, whilst the observed effect is much less significant in quiet sun regions. The data analysed doesn't show any significant spectral tilt, in the y direction, along the length of the slit as shown in Fig. A.2 in Appendix A.

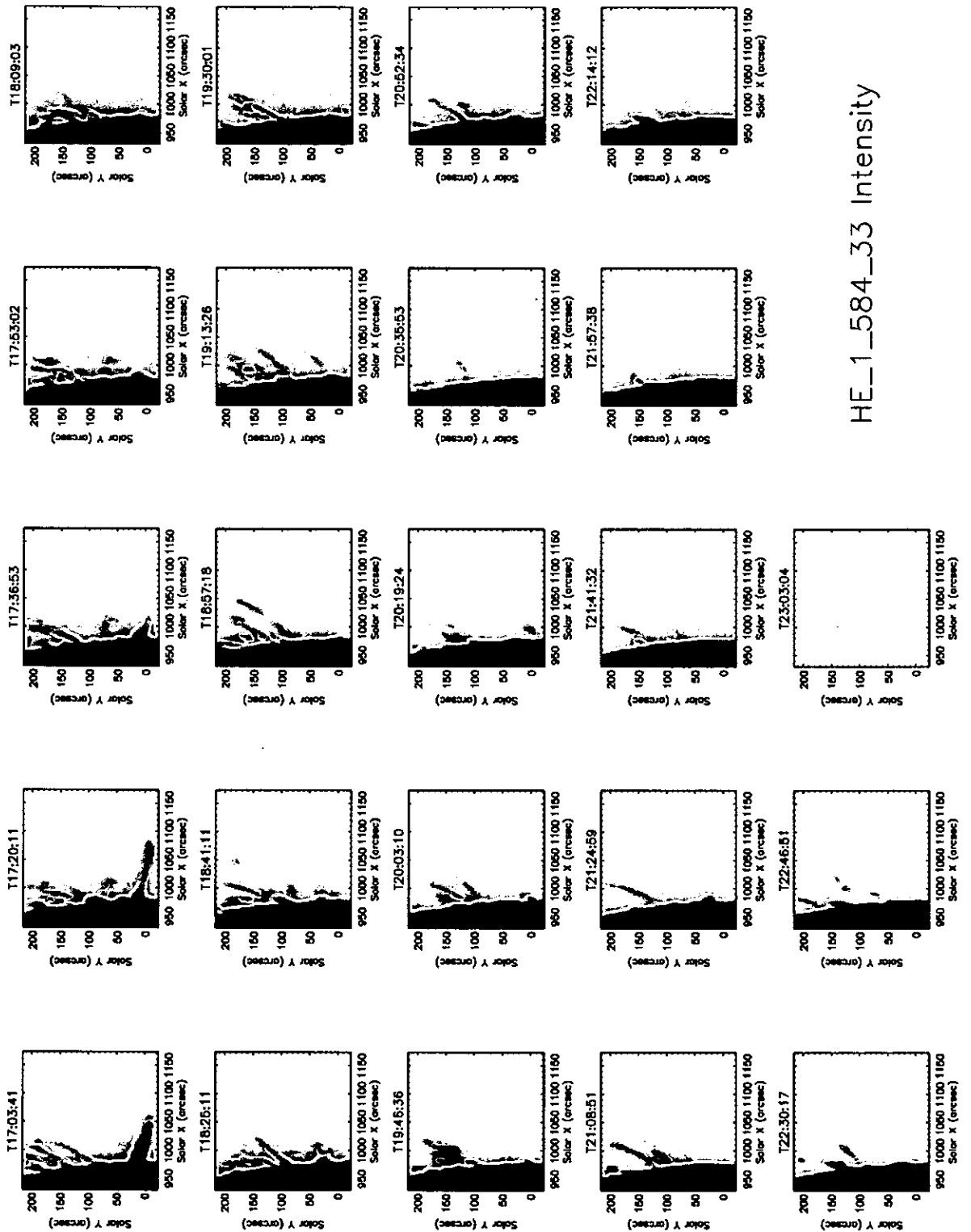
5.2.2 Observing program

The observations are pointed just off the western limb of the sun at solar coordinates [1049, 97], from 17:03–23:14 on the 8th February 1997. NOAA active region AR 8015 is centred within the field of view, located at the very edge of the Western limb. The data consists of 23 EJECT_V3 v18 rasters with constant pointing. The raster uses 60 positions of the $4'' \times 240''$ slit to form $240'' \times 240''$ rastered images with a pixel size of $4.06'' \times 1.68''$. The raster includes windowed detector data in the following lines: He I 584 Å, O V 629 Å, Mg IX 368 Å, Fe XVI 360 Å, Si X 347 Å and Si X 356 Å, with peak formation temperatures of Log T=4.4, Log T=5.4, Log T=6.0, Log T=6.19, Log T=6.06 and Log T=6.06 respectively. Each slit position has an exposure of 10 s giving a total raster duration of ~ 16 minutes. The first four lines cover temperatures from the chromosphere to the corona; the Si lines can be used as a coronal electron density diagnostic, using a line ratio method. The data can be used to produce a “movie” of the active region evolution across the large temperature range of the lines. The CD-ROM contains movies of intensity, running intensity difference and Doppler velocity, for all the lines. They show the dynamic nature of the region, particularly in the cooler He I and O V lines. The movies can be viewed from the Chapter 5 menu on the CD-ROM.

Figures 5.4–5.6 show context images for all raster frames in He I, O V and Fe XVI. Figures A.3–A.13 in Appendix A show the context images for Mg IX and the Si X lines, the running difference image sequences for He I, O V, Mg IX and Fe XVI, and the Doppler velocity sequences for He I, O V, Mg IX and Fe XVI. The running difference sequences for the Si X lines are not included since their low signal to noise level results in a difficulty in resolving any significant structure. The coronal lines Mg IX, Fe XVI, and Si X have relatively low intensities and only show significant emission structures above the solar limb. This makes it difficult to fit the position of the line profiles accurately. The assumption that averaging the fitted line positions gives a good estimate of the line rest wavelength is less valid in the corona, since the corona is composed of large scale loop structures.

The same method is used to calculate the rest wavelength for all of the lines. This method does not result in a reliable value for the coronal lines, as can be seen in the Doppler maps for Mg IX and Fe XVI. Thus, the absolute velocities have little significance in these lines; however,

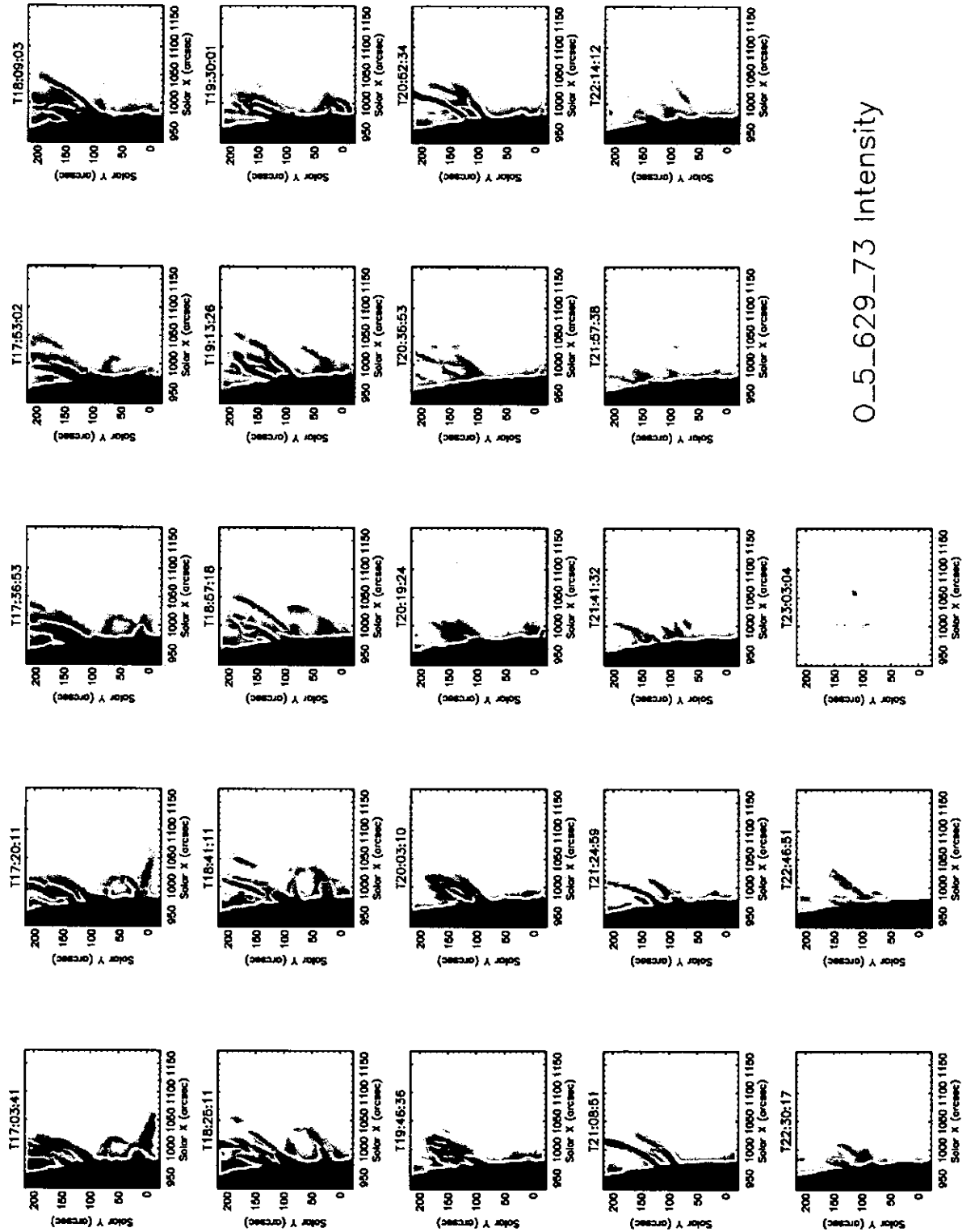
CHAPTER 5. ACTIVE REGION STRUCTURE AND DYNAMICS



HE_1_584_33 Intensity

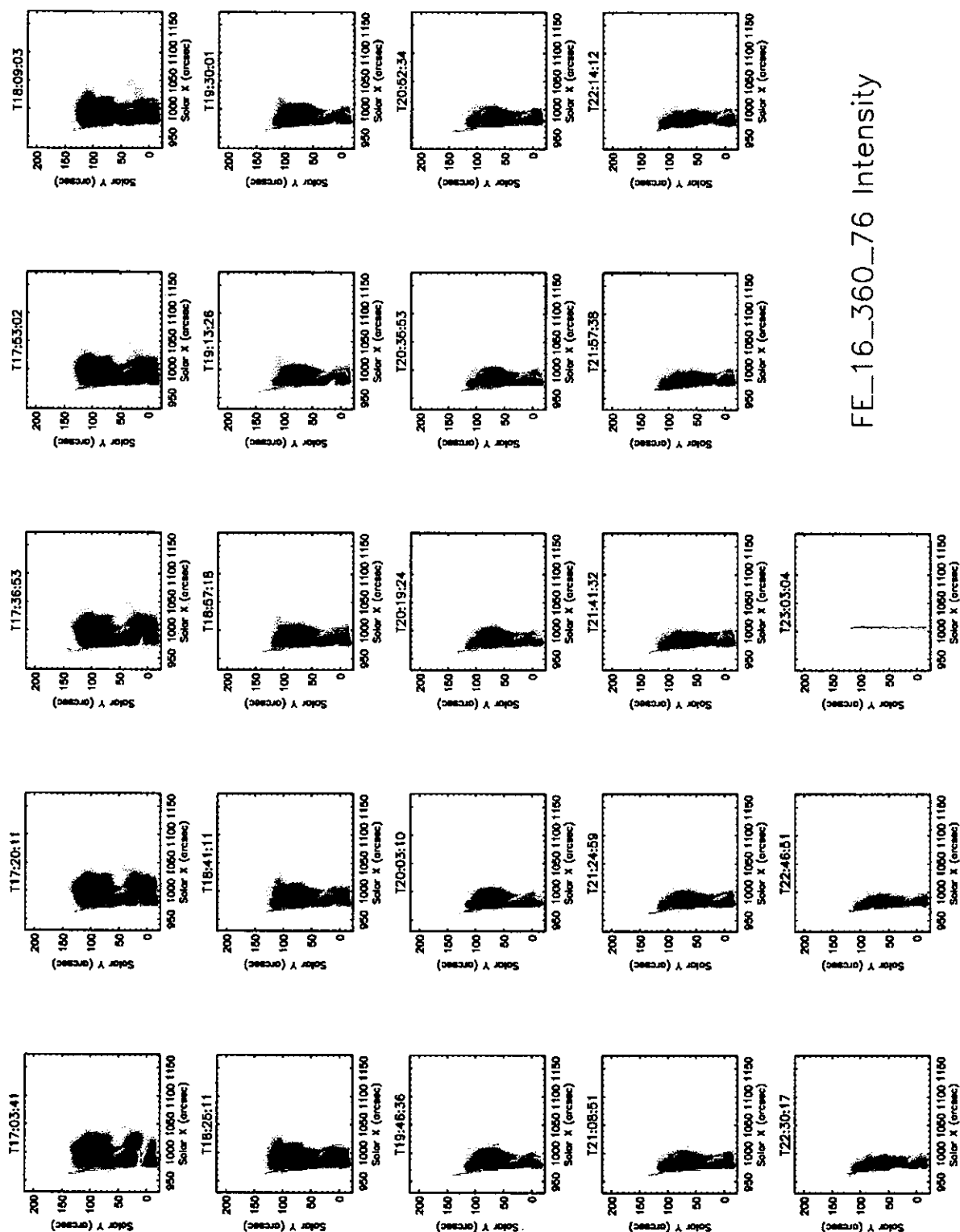
Figure 5.4: He I 584 Å negative context images for all rasters.

CHAPTER 5. ACTIVE REGION STRUCTURE AND DYNAMICS



0_5_629_73 Intensity

Figure 5.5: O V 629 Å negative context images for all rasters.



FE_16_360_76 Intensity

Figure 5.6: Fe XVI 360 Å negative context images for all rasters.

CHAPTER 5. ACTIVE REGION STRUCTURE AND DYNAMICS

information can be gained regarding the relative velocities.

Considering Figures 5.4–5.6, a number of dynamic emission structures are visible in He I (Fig. 5.4). There are a number of apparent flows, and time variable emission along loop structures throughout the observations. An ejection of plasma (possibly a macrospicule) is visible from the beginning of the observations. Rasters 1–3 show a small loop just North of the ejection. The southern leg of the loop appears to share the same footpoint region as the ejection, along the line of sight of the observations. North of $100''$ in solar y , there appears to be highly dynamic emission from loop structures, that extend Northward out of the field of view of the observations, visible in intensity and running difference images. There appears to be high velocity flows along these loops that evolve on time scales shorter than the ~ 16 minute cadence of the observations. It should be noted that these data are rastered observations that are formed over a relatively long time compared to the observed variability. Also CDS rasters in the West–East direction, and so points along the solar x direction are not observed at exactly the same time.

In O V (Fig. 5.5) the emitting structures appear to be even more dynamic. Similar flow and time variable loop structures are observed, but have a more complex structure than in He I. The plasma ejection is again visible in rasters 0–2 at the same location as in He I. The small loop just North of the ejection also shows emission in O V. Unlike He I, the loop is visible from the beginning of the observations in raster 0, and is clearly observed up to raster 3. The loop emission suggests a knotted, or twisted nature. The O V Doppler maps show a complex velocity structure along the loop, indicating plasma flow. A detailed analysis is required to determine the nature of the loop structure. As in He I, above $100''$ in solar y , there are a number of loop structures that show highly dynamic variability, or high velocity flows that are difficult to resolve with the observation cadence.

In Fe XVI (Fig. 5.6) there appears a diffuse background emission from the high temperature coronal loops. It is difficult to relate the structures observed in He I and O V to the coronal emission structure. The emission from Fe XVI is much less dynamic, and shows a general reduction in emission over the course of the study. This may be expected to be caused by solar rotation, rather than mass loss, as the sun rotates $\approx 3.5^\circ$ over the ~ 6 hr duration of the

observations. The plasma ejection is visible in Fe XVI as absorption in rasters 0–2. The ejection is also visible as much weaker absorption in Mg IX, and the Si lines.

Clearly the structure and dynamics of the active region show large differences across the different temperature lines. Of particular interest are the apparent twisted loop structure, and the plasma ejection. The literature describes many types of ejection events such as jets, surges, spicules and macrospicules. However, there is no clear distinction of what defines each phenomenon. Detailed analysis of these kind of structures is necessary to characterise their physical parameters which can then be used to define these features, rather than their physical appearance. This chapter concentrates on the analysis of the loop and ejection structures.

5.3 Active Region Loop: Qualitative Structure

Figure 5.7 shows the Dopplermaps and intensities of the active region loop, in He I (left) and O V (right). The intensity contours are overplotted in each corresponding Dopplergram. The data have been rotated 90° to align the solar Western limb with the x axis. Solar- x and solar- y then run along the y and x axes respectively. Considering He I, in rasters 1–2, “blobs” appear to be ejected upward along the Northern leg of the loop, and fall back down toward the solar limb in raster 3. This motion is apparent in the He I running difference images in Appendix A Fig. A.6. The instantaneous velocity of the plasma “blobs” is estimated from their motion between consecutive rasters. These estimated velocity vectors are estimated from the motion between frame i and $i + 1$, and are indicated on frame i in the intensity plots of Fig. 5.7. Assuming that the changing emission structure in rasters 1–3 is due to motion of the same plasma, from raster 1–2, the plasma blob has an instantaneous velocity of 5.6 km s^{-1} upwards along the loop leg outlined by the He I emission. From rasters 2–3 the plasma has an instantaneous velocity of 4.3 km s^{-1} down the loop leg. The He I line position is not fitted well in this region, due to the low intensity of the plasma emission. Therefore, the Dopplergrams do not give a good indication of the line of sight velocity of the plasma blobs in He I.

The righthand plots in Fig. 5.7 show the O V Dopplermaps and intensities of the active region loop. The Southern leg of the loop appears to share the same footpoint as the ejection, along the line of sight. There is an apparent increase in emission at this footpoint. This is

CHAPTER 5. ACTIVE REGION STRUCTURE AND DYNAMICS

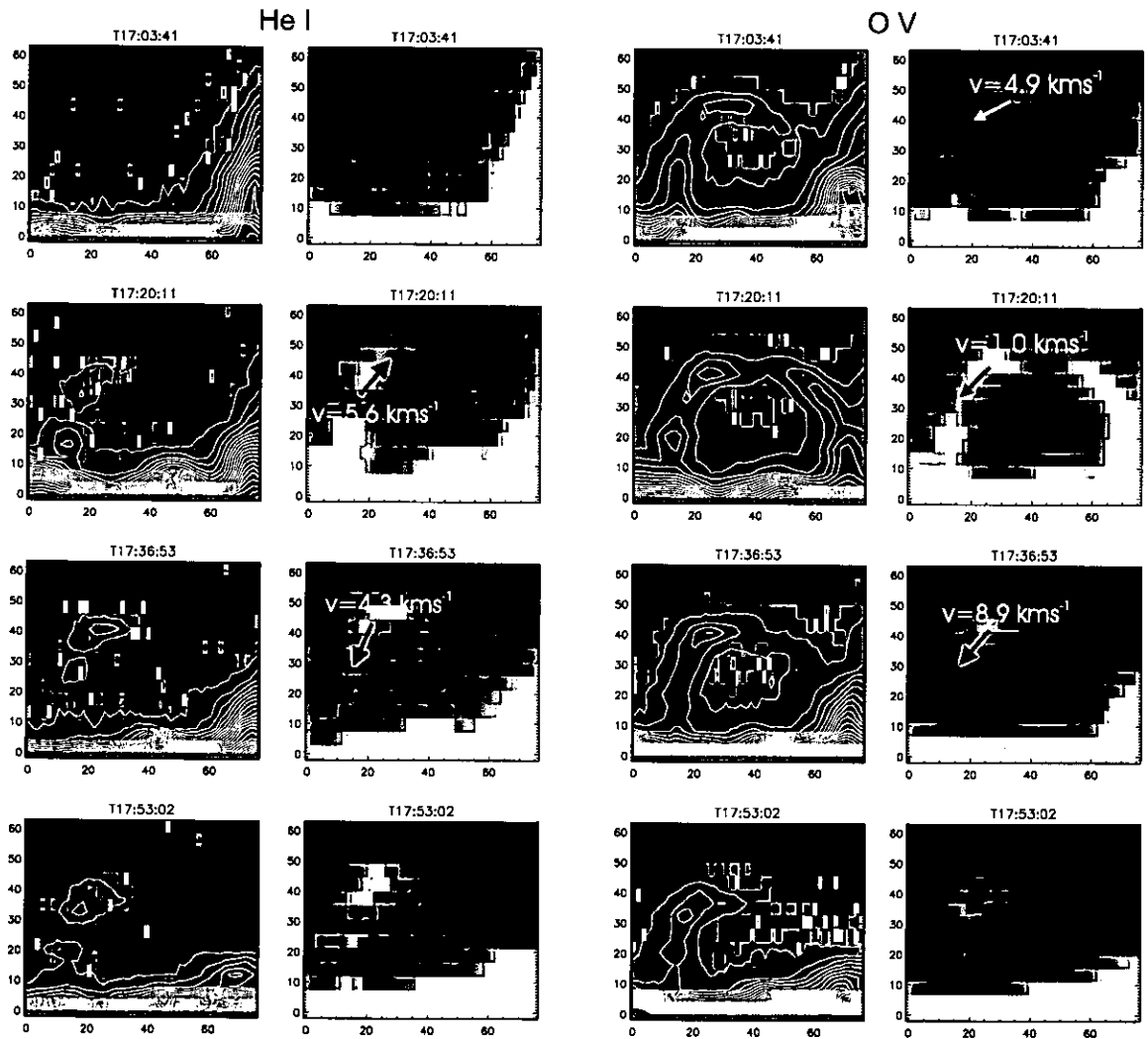


Figure 5.7: Dopplermaps and intensities of the active region loop in rasters 0–3 (top to bottom) for He I and O V. Intensity contours are overlotted on each Dopplermap. The instantaneous velocity vectors of intensity structures are estimated by motion between consecutive rasters, and overlotted on the intensity plots. Solar North/West are to the left/top respectively.

CHAPTER 5. ACTIVE REGION STRUCTURE AND DYNAMICS

likely to be due in part to the increased column depth along the line of sight through the two optically thin emission structures, rather than an increase in density. In raster 0, the Northern leg of the loop has more intense emission up to the loop apex, where the emission fades along the Southern leg. In raster 1, the loop emission suggests a knotted, or twisted structure along its length. The Northern leg has two “knot” structures; the loop then appears to fade at the apex and become more intense again in the Southern leg. This gives the impression of a twist in the emission structure, or magnetic field, along the loop. The two knot structures appear at similar locations as the emission “blobs” in He I. The apparent twisted structure in the loop could be due to three possibilities. A twisted magnetic field would cause an increase in the column depth through the loop emission at the location of the twist, resulting in increased intensity due to line of sight effects. The structure could be caused by a density effect, due to non-uniform ejection of plasma into the loop. Another possibility is that the knots are due to a temperature effect. The loop could have a uniform density, but at the location of the knots the plasma temperature is close to the peak of the contribution function of the line. It is difficult to see a velocity pattern related to the intensity structure to indicate a geometrical twist along the loop. It is most likely that the emission structure along the loop is due to a combination of a density effect, and the formation temperature of the two lines.

Assuming that the changing emission structure in each raster is due to motion of the same plasma structures, an intensity enhancement can be identified which appears to travel down the Northern (left) loop leg in rasters 0–3. From rasters 0–1, the enhancement has an estimated instantaneous velocity of 4.9 km s^{-1} downwards along the loop leg. From rasters 1–2 the enhancement shows much less movement, and has an instantaneous velocity of 1 km s^{-1} . Rasters 2–3 suggest an increased velocity of 8.9 km s^{-1} down the loop leg. The O V Doppler map for raster 0 shows a blue shift along the Northern (left) leg of the loop, and a red shift along the Southern (right) loop leg. Raster 1 shows a complex mixed velocity structure along the loop. Raster 2 shows a clear separation of blue/red shift in the Northern/Southern legs of the loop. Raster 3 shows a complex mix of velocities, as in raster 1, but with significant emission in the Northern leg only.

5.4 Active Region Loop: Geometry

He I shows an ejection of plasma upwards along the Northern loop leg, whilst, at the same time O V shows a downflow of plasma. It appears that at certain times there could be oppositely directed flows along the loop in the two different temperatures. At the time when He I suggests an oppositely directed flow (rasters 1–2), O V shows a complex, mixed, Doppler flow pattern along the loop. Could this disturbance to the O V flow be caused by the ejection of oppositely directed, cooler, plasma?

The O V Doppler flow pattern in rasters 0 and 2 can be produced by a number of different combinations of the plasma flow direction and loop geometry. The schematic diagrams in Fig. 5.8 show four combinations of loop and plasma flow geometries that may produce the observed velocities, assuming that the loop emerges radially from the solar surface, or the plane of the loop is normal to the surface. Figure 5.8a demonstrates that a syphon type flow, with the loop located on the near side of the solar limb, requires a North→South flow direction to produce the observed velocity pattern. Figure 5.8b shows that if the loop emerges radially on the far side of the solar limb then a South→North syphon flow is required. Figure 5.8c shows that plasma upflow along the loop legs can produce the observed Doppler pattern if the Southern leg is in the foreground compared to the Northern leg. Figure 5.8d shows that draining of plasma down the loop legs produces the same results if the Northern loop leg is in the foreground compared to the Southern leg.

The O V intensities appear to show a flow from the Southern leg to the Northern leg which is supported by the O V Doppler maps. The clear blue shift in the Northern leg in rasters 0 and 2 appears to be due to the strong downflow of plasma visible in O V intensity. This indication of the plasma flow direction can be used to imply the geometry of the loop. The downflow in the Northern leg, observed in O V intensity, discounts the geometries shown in Fig 5.8 (a & c). The combination of the O V Doppler velocities and intensity maps implies geometries of either: a far side loop, or more generally a loop which has a plane inclined away from the observer, with a South→North directed syphon flow; or, a near side loop draining plasma from each leg with the Northern leg in the foreground. It is not possible to distinguish between the two geometries conclusively, even though the energetics are very different between the two

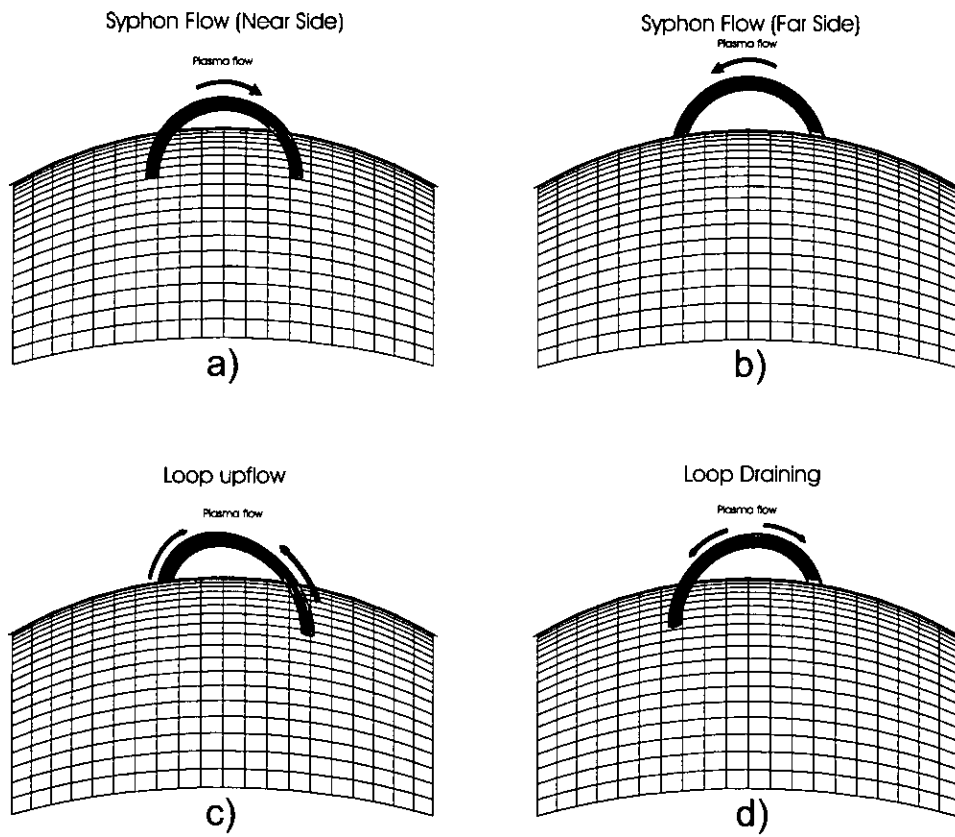


Figure 5.8: Schematic diagrams indicate the possible geometries of the loop and plasma flow to produce the observed O V Doppler pattern in Fig. 5.7. **a)** Near side North→South syphon flow. **b)** Far side South→North syphon flow. **c)** Upflow along the loop legs with the Southern leg in the foreground. **d)** Plasma draining along the loop legs with the Northern leg in the foreground.

flow processes. An indication may come from the fact that the Southern leg of the loop appears to share the same footpoint, along the line of sight, as the plasma ejection. The ejection is clearly a highly energetic process. If the loop and the ejection do share the same footpoint region then we may expect energy to be introduced into the Southern footpoint of the loop. An asymmetric heating of the loop footpoints in this way will produce a South→North directed syphon flow.

5.5 Active Region Loop: Quantitative O V Structure

In order to understand the structure and dynamics of active region loops, the physical parameters of the loop need to be measured. The theoretical models of loop formation, structure, heating, etc, can then be tested against the observations. To examine the intensity, velocity and line width structure of the loop in more detail, these parameters are measured as a function of distance along the loop axis. A vector path extraction method is used to extract the data along any path, as described in Appendix A.1. A path is defined along the loop, from the Northern to the Southern footpoint, for each raster. Once the data has been extracted, the data is in the form of a 2-D array of cross sections extracted along the length of the path. The extracted data strips have a y dimension equal to the length of the cross sections ($\sim 10''$), and an x dimension equal to the length of the defined path. Figures 5.9–5.12 show the extracted loop intensity, Doppler velocity, and line width profiles for rasters 0–3. The righthand plots show the location of the extracted loop path in the context of the intensity, velocity and line width structure; the white points indicate the cross sections that define the path. The lefthand plots show the data extracted along the loop, and the average profile as a function of length along the loop in intensity, velocity and line width.

Figure 5.9 shows the profiles of the extracted path along the O V loop for raster 0. Considering the strip of extracted intensity cross sections; the left hand edge represents the Northern footpoint of the loop, the central region is the apex, and the righthand edge represents the Southern footpoint. The average intensity profile shows that the emission in the Northern leg of the loop is constant $\sim 15''$ above the intensity decay of the O V limb. As $I \propto n_e^2$, if all other variables are constant, this implies a constant mean density of the Northern footpoint

CHAPTER 5. ACTIVE REGION STRUCTURE AND DYNAMICS

emission. Moving along the length of the loop, the emission decreases before a slight increase to constant emission over $\sim 10''$ at the apex of the loop. In the Southern leg of the loop the intensity decreases to low level emission before increasing again at the O V limb of the Southern footpoint. In Doppler velocity, the Northern leg of the loop shows a clear blue-shift with a mean velocity of $\sim -20 \text{ km s}^{-1}$ over the first $\sim 30''$. Moving along the loop, the velocity becomes less blue-shifted tending towards zero at the apex of the loop. This may suggest that the footpoints of the loop have an approximate North-South alignment, and that the plane of the loop is inclined towards the line of sight. The velocity in the Southern leg of the loop becomes red-shifted, reaching a peak of $\sim 30 \text{ km s}^{-1}$, and falls to zero at the Southern footpoint. Within the errors, the loop shows a general velocity gradient along its length demonstrating a flow of plasma along the loop. The observations from section 5.4 suggest that the Northern leg of the loop has a downflow of plasma, and that the loop appears to have a North-South alignment, also suggested by zero velocity at the loop apex. The combination of these factors suggest that the most likely geometry is that of a radial loop located on the far side of the solar limb, or more generally that the plane of the loop is inclined away from the line of sight and supports a syphon-like plasma flow. Within the errors, it is not possible to observe any significant trends of the line width along the loop.

Figure 5.10 shows the profiles of the extracted path along the O V loop for raster 1. The strip of extracted intensity cross sections shows a more structured emission along the loop than raster 0. The left hand side, or Northern leg of the extracted loop cross sections shows two intensity enhancements. The two enhancements of emission occur at $13''$ and $45''$ along the loop path. The "blobs" have an estimated $\approx 67\%$ enhancement of mean emission above the seemingly uniform background in which they are embedded. There is no obvious pattern within the velocity along the loop to indicate that the increase in emission is due to a twist in the loop. Again, assuming that the increase in emission is entirely due to an increase in density, the increase in intensity corresponds to a density enhancement of $\approx 29\%$ in the mean density of the plasma, within these regions of the loop. At the apex of the loop the mean emission is reduced, but this then increases to a level of constant emission/density across $\approx 20''$ within the Southern leg of the loop, finally before increasing again due the combined emission of the

loop and ejection at the Southern loop footpoint. The velocity of the loop shows a blue shifted region within the Northern leg. This mean blue shift of $\approx -17 \text{ km s}^{-1}$ occurs in the fainter emission region that extends beyond the outer edge of the defined loop path. Within the errors, there is no significant trend in the velocity along the rest of the loop. There is also no significant structure, or trend, within the mean line width profile along the loop.

Figure 5.11 shows the profiles of the extracted path along the O V loop for raster 2. The strip of extracted cross sections, and profile of mean intensity show relatively uniform emission within the Northern loop leg, increasing slightly before the apex. The Southern leg of the loop has a low emission level, down to the O V limb. The Doppler velocity along the loop shows a distinct separation of blue/red shift in the Northern/Southern loop legs respectively. The Northern leg has a minimum mean velocity of $\approx -26 \text{ km s}^{-1}$ at its base, and increases towards zero at the loop apex. The mean velocity becomes red-shifted from the apex into the low intensity emission within the Southern leg of the loop. The Southern leg has a maximum mean velocity of $\approx 40 \text{ km s}^{-1}$ located $80''$ along the loop path. As in raster 0, this velocity trend along the loop suggests a syphon-like plasma flow geometry with the plane of the loop inclined away from the line of sight. It is not possible to derive any conclusions about structure within the mean line width profile, considering the magnitude of the errors, particularly within the low intensity Southern loop leg.

Figure 5.12 shows the profiles of the extracted path along the O V loop for raster 3. The strip of extracted cross sections, and profile of mean intensity show relatively low emission with two small increases in emission within the Northern loop leg, above the O V limb. At the loop apex and upper region of the Southern leg the emission is zero, implying an absence of plasma. The base of the Southern leg has a low level of emission before rising again at the O V limb. The velocity and line width data do not show any significant structure within the observed emission.

5.6 Active Region Ejection: Qualitative Structure

Figure 5.13 shows the Doppler velocities and intensities of the active region plasma ejection in rasters 0–3 for He I and O V. The intensity contours of the ejection are overplotted in each

CHAPTER 5. ACTIVE REGION STRUCTURE AND DYNAMICS

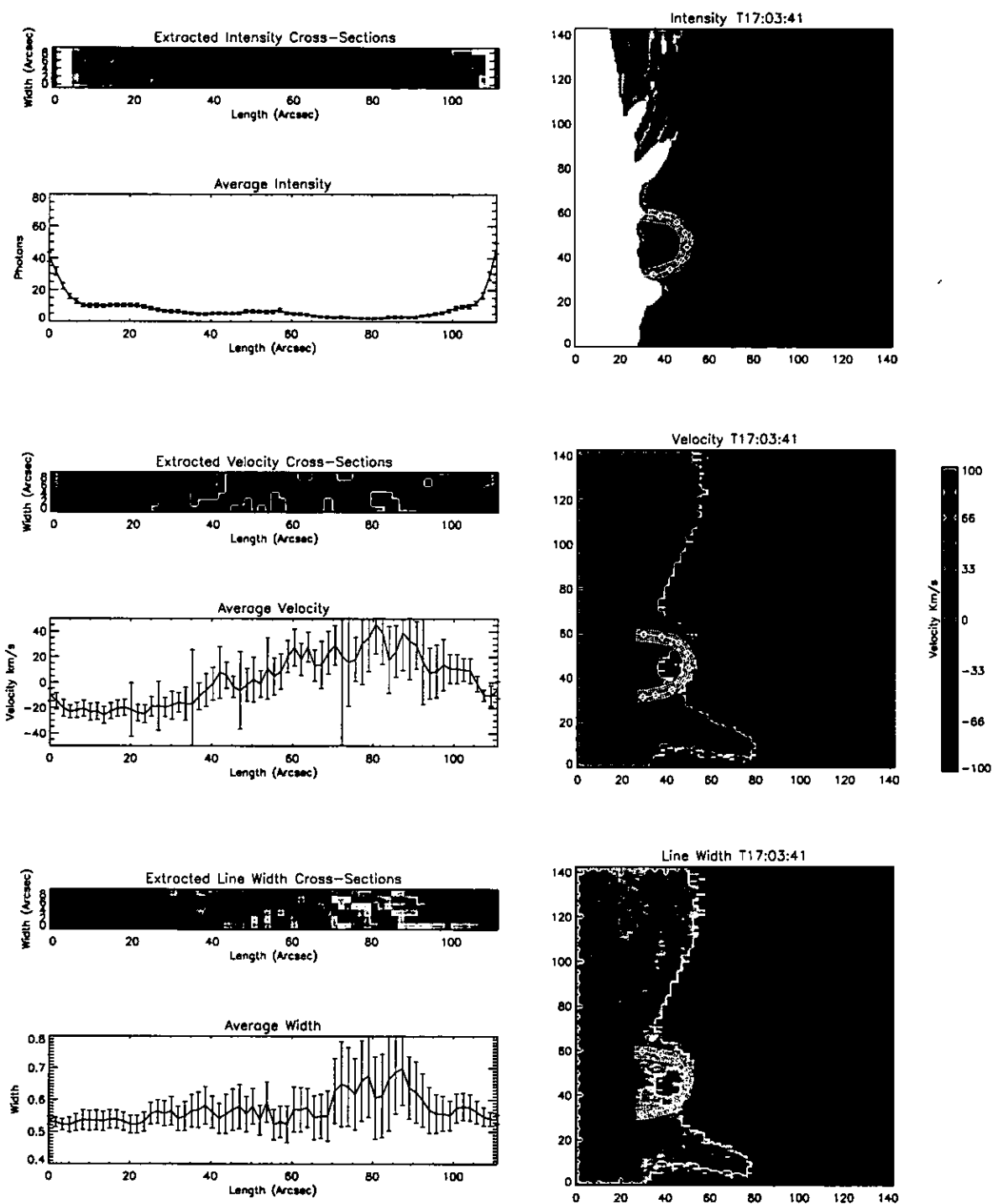


Figure 5.9: O V raster #0 line parameters along the loop. Top: Context image of extracted path in O V intensity, extracted 2-D intensity structure along the length of the loop, average (mean) intensity profile as a function of length along the loop. Middle: Context image of extracted path in O V Doppler velocity, extracted 2-D velocity structure along the length of the loop, average velocity profile as a function of length along the loop. Bottom: Context image of extracted path in O V line width, extracted 2-D line width structure along the length of the loop, average line width profile as a function of length along the loop.

CHAPTER 5. ACTIVE REGION STRUCTURE AND DYNAMICS

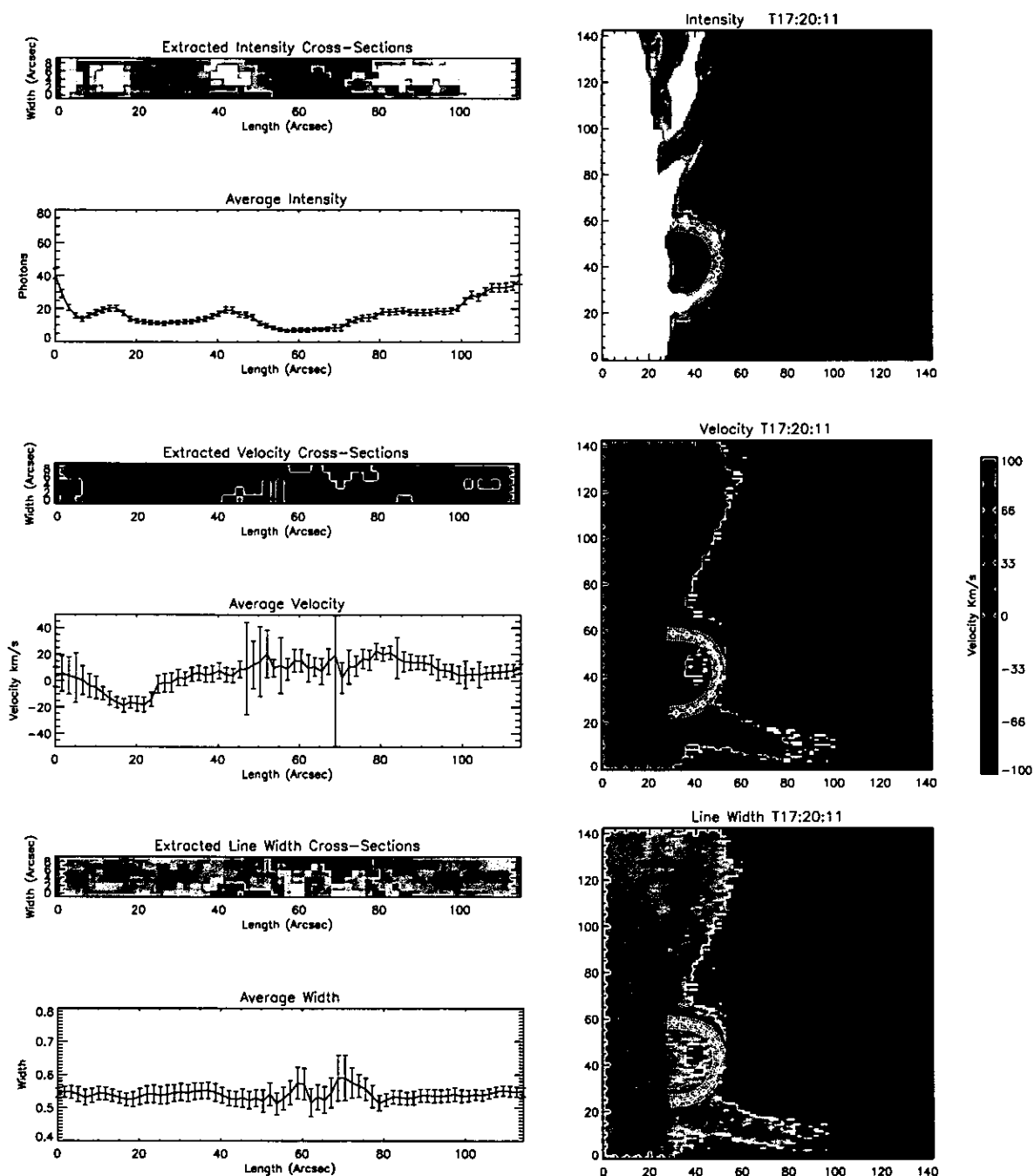


Figure 5.10: O V raster #1 line parameters along the loop. Top: Context image of extracted path in O V intensity, extracted 2-D intensity structure along the length of the loop, average (mean) intensity profile as a function of length along the loop. Middle: Context image of extracted path in O V Doppler velocity, extracted 2-D velocity structure along the length of the loop, average velocity profile as a function of length along the loop. Bottom: Context image of extracted path in O V line width, extracted 2-D line width structure along the length of the loop, average line width profile as a function of length along the loop.

CHAPTER 5. ACTIVE REGION STRUCTURE AND DYNAMICS

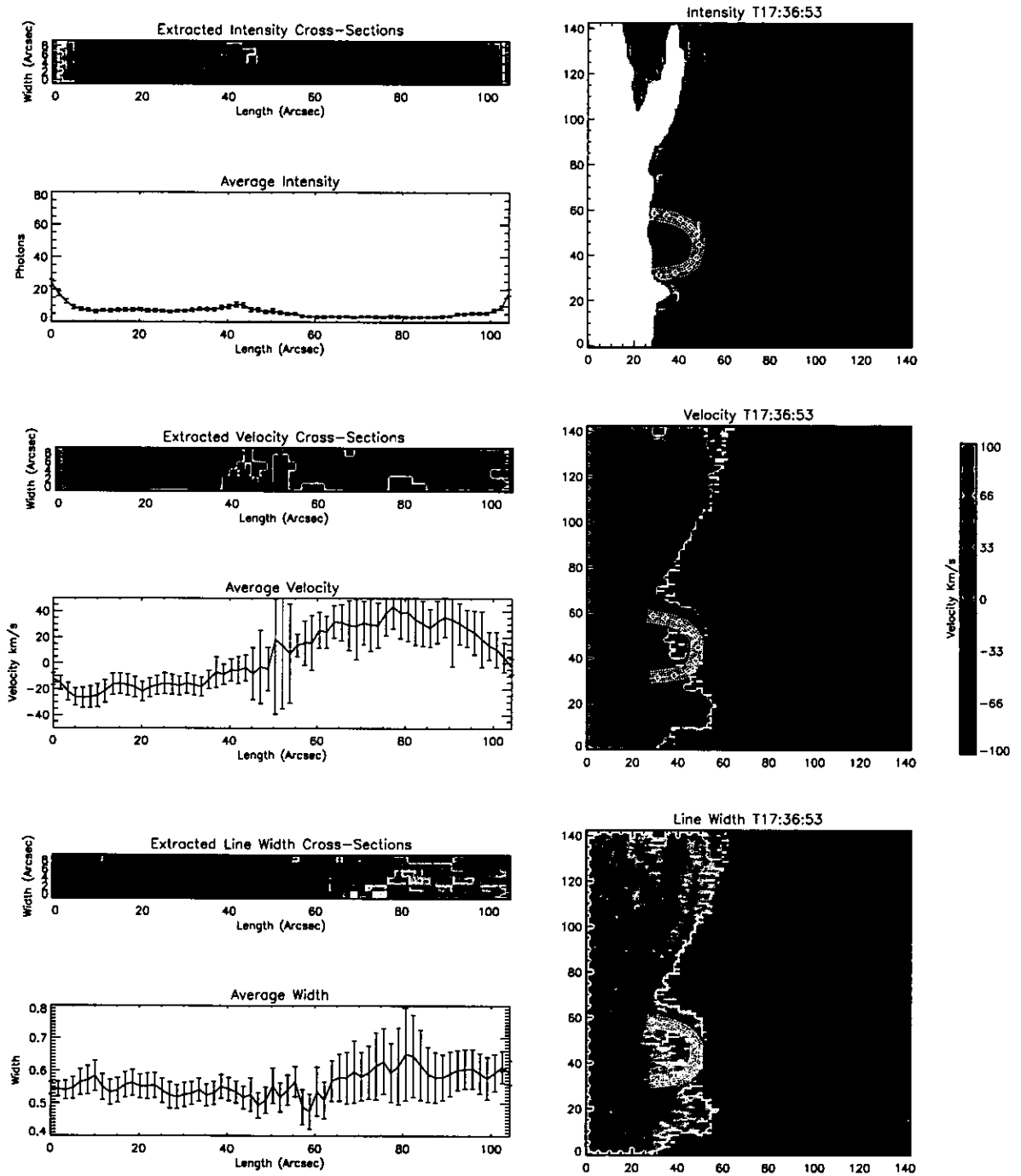


Figure 5.11: O V raster #2 line parameters along the loop. Top: Context image of extracted path in O V intensity, extracted 2-D intensity structure along the length of the loop, average (mean) intensity profile as a function of length along the loop. Middle: Context image of extracted path in O V Doppler velocity, extracted 2-D velocity structure along the length of the loop, average velocity profile as a function of length along the loop. Bottom: Context image of extracted path in O V line width, extracted 2-D line width structure along the length of the loop, average line width profile as a function of length along the loop.

CHAPTER 5. ACTIVE REGION STRUCTURE AND DYNAMICS

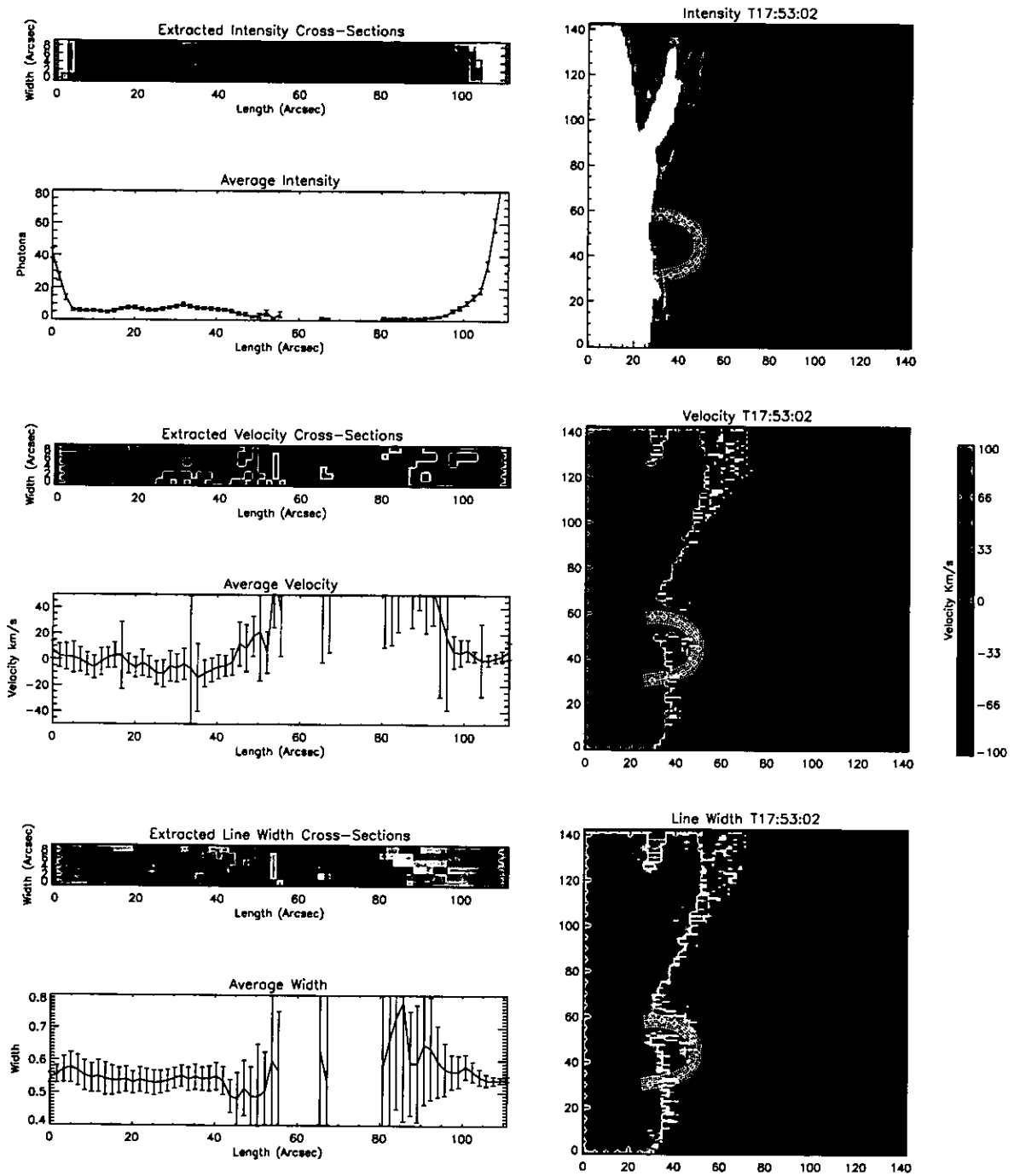


Figure 5.12: O V raster #3 line parameters along the loop. Top: Context image of extracted path in O V intensity, extracted 2-D intensity structure along the length of the loop, average (mean) intensity profile as a function of length along the loop. Middle: Context image of extracted path in O V Doppler velocity, extracted 2-D velocity structure along the length of the loop, average velocity profile as a function of length along the loop. Bottom: Context image of extracted path in O V line width, extracted 2-D line width structure along the length of the loop, average line width profile as a function of length along the loop.

CHAPTER 5. ACTIVE REGION STRUCTURE AND DYNAMICS

corresponding Dopplergram. Solar- x and solar- y are aligned with the x and y axes respectively. The ejection is located $\approx 25''$ North on the West solar limb with a non-radial ejection angle of $\approx 103^\circ$, clockwise from solar North. The instantaneous, perpendicular, velocity of the ejection is estimated from the motion between consecutive rasters. The estimated velocity is indicated on the intensity plots. Considering He I, in raster 0 the ejection appears as a broad, relatively intense column of emission. An estimation of the width of the ejection is made halfway along the length of the intensity contour, with the length estimated by the extension of the contour above the apparent limb. In raster 0, the ejection has an estimated width and length of $\sim 30''$ and $\sim 75''$ respectively. From rasters 0-1 the ejection has an instantaneous velocity of 16 km s^{-1} outward from the solar limb. In raster 1, the ejection appears to become more extended, narrow and diffuse; there appears to be a central core of brighter emission surrounded by a sheath of more diffuse emission. The estimated width and length are $\sim 15''$ and $\sim 100''$ respectively. From rasters 1-2 the ejection has an instantaneous velocity of 46 km s^{-1} downward towards the solar limb. The ejection seems to have decayed in raster 2, and appears as wider ($\sim 20''$) emission extending $\sim 30''$ above the limb, giving the impression that plasma is falling back towards the limb. From rasters 2-3 the ejection has a downwards instantaneous velocity of 19 km s^{-1} . The Doppler velocity maps suggest a velocity gradient across the width of the ejection. Particularly in raster 2, the Northern edge appears blue shifted and the Southern edge appears more red-shifted; this suggests that the ejection may possess a bulk rotation.

The lower plots in Fig. 5.13 show the O V Dopplermaps and intensities of the ejection. In raster 0 the ejection appears more diffuse compared to the emission in He I. The ejection has an estimated width of $\sim 25''$, and length of $\sim 80''$ respectively. From rasters 0-1 the ejection has an instantaneous velocity of 20 km s^{-1} away from the solar limb. As in He I, the ejection becomes more narrow and extended in raster 1, with an estimated width and length of $\sim 20''$ and $\sim 110''$ respectively. This gives a more impulsive appearance with a more diffuse structure than He I. The ejection has an instantaneous velocity of 46 km s^{-1} between rasters 1-2 downwards towards the limb. In raster 2, as in He I, the ejection appears to have decayed and extends just above the limb with an estimated width and length of $\sim 25''$ and $\sim 50''$ respectively, suggesting the plasma may be falling back towards the limb. The instantaneous velocity between rasters

CHAPTER 5. ACTIVE REGION STRUCTURE AND DYNAMICS

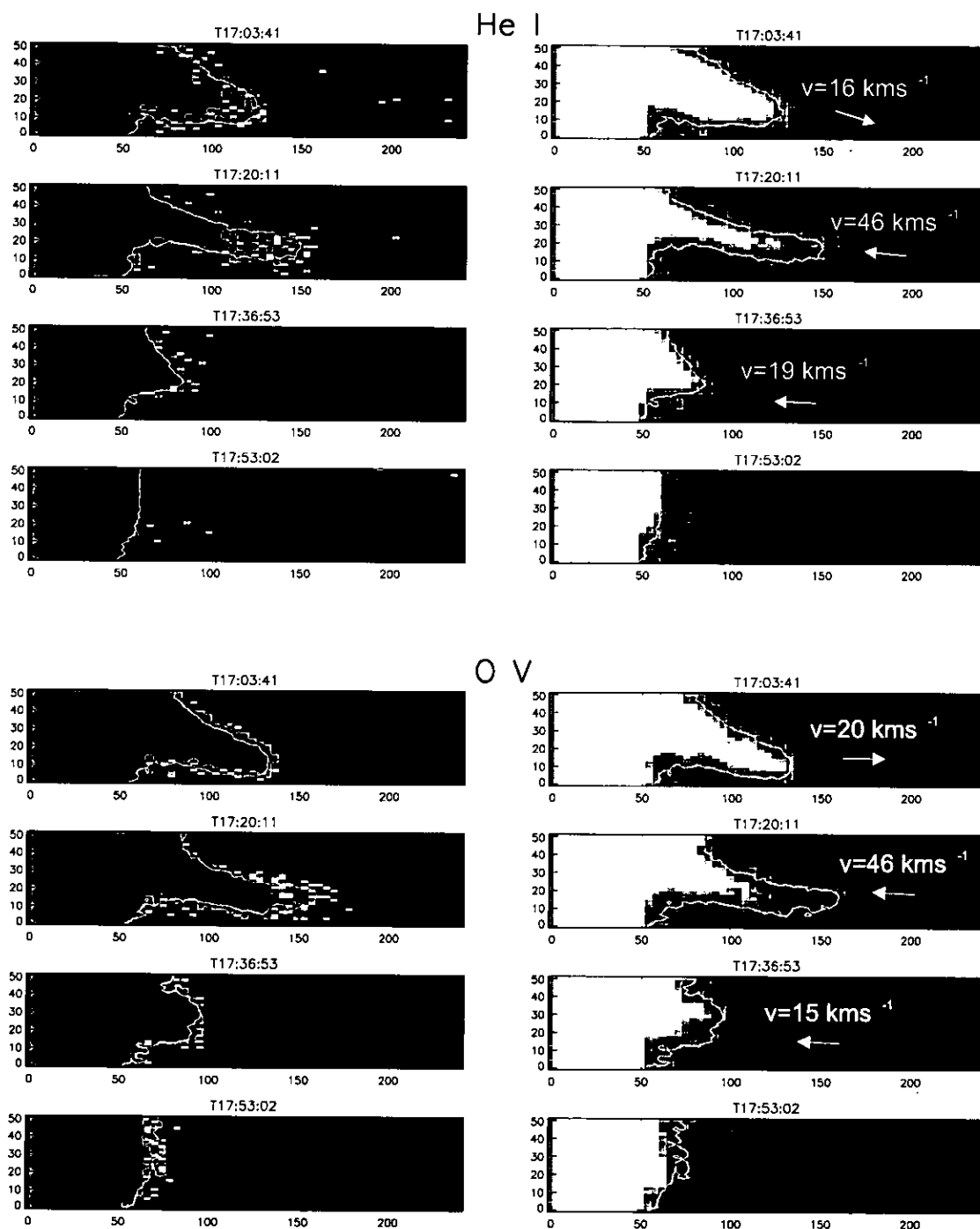


Figure 5.13: Dopplermaps (left) and intensities (right) of the active region ejection in rasters 0-3 (top to bottom) for He I and O V. Intensity contours are overlotted on each Dopplermap. The instantaneous velocity vectors of the intensity contours are estimated by their motion between rasters, and overlotted on the intensity plots.

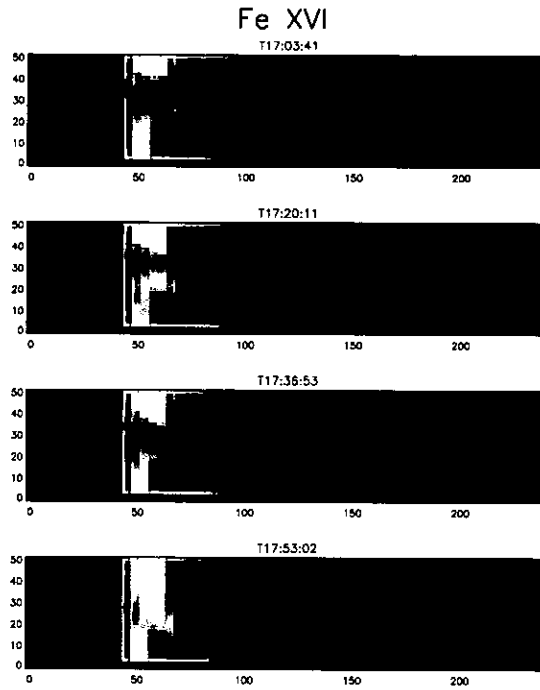


Figure 5.14: Fe XVI intensity for rasters 0–3 at the location of the active region ejection, observed as emission in He I and O V. In Fe XVI the ejection is clearly visible as a channel of absorption in rasters 0–2.

2–3 is 15 km s^{-1} downwards towards the limb. The Doppler maps for raster 1 and 2 show a velocity gradient across the width of the ejection. A velocity gradient such as this suggests a rotation of the ejection about its axis. Particularly in raster 1, the Northern edge of the ejection is blue shifted, and the Southern edge appears red-shifted. This suggests that the ejection is rotating in a similar manner to the “solar tornadoes” described by Pike & Mason (1998).

Figure 5.6 and Figures A.3–A.5 in Appendix A show that the ejection is observed as absorption in the coronal Fe XVI, Mg IX and Si X lines. The absorption suggests that the ejection is composed of cool plasma, optically thick to coronal emission, with a maximum temperature $< \text{Log } T=6.0$, and a minimum temperature $> \text{Log } T=4.4$. The absorption in the coronal lines also suggests that the ejection is located in the foreground compared to the coronal emission which originates from high temperature active region loops that have rotated well beyond the limb. Figure 5.14 shows the ejection region observed in Fe XVI which shows the largest contrast between the absorption and the surrounding emission. In raster 0, the absorption of the ejection appears much narrower ($\sim 10''$), than the He I or O V emission, and extends down to

the Fe XVI limb which appears $\sim 10''$ below the He I and O V limb. In raster 1, the absorption of the ejection is still visible, but has much less contrast with the background emission (Mg IX and Si X display a similar behaviour). This could be caused by an increase in coronal emission along the line of sight. However, the general region doesn't appear to show an increase in emission. Comparing with the He I and O V emission there is no evidence to suggest a sudden increase in density, abundance of coronal ions, or geometry (column depth) to produce the increased emission. Another possibility is that the ejection itself shows an increase in emission at coronal temperatures. An increase in the peak temperature of the ejection plasma will produce an increased emission in the coronal lines. This also occurs during, what appears to be, a more impulsive phase of the ejection in He I and O V. Once again, in raster 2 the ejection absorption becomes more clearly defined with increased contrast relative to the surrounding emission, although less so than in raster 0. This increased absorption may be explained by a reduction in the peak temperature of the ejection plasma, representing a cooling phase of the ejection plasma.

5.7 Active Region Ejection: Quantitative Length Structure

As mentioned previously the literature describes a number of plasma ejection structures such as spicules, macro-spicules, jets, surges, etc. The physical properties must be measured to determine the connection between them, and the physical mechanisms which cause these structures. A vector path extraction method is used as in section 5.5. Appendix A.1 describes the vector extractions method. A single vector is defined from solar East-West along the axis of the ejection to extract the data in a coordinate system parallel to the ejection axis. Once the data has been extracted, the data is in the form of a 2-D array of cross sections extracted along the length of the ejection. The extracted data strips have a y dimension equal to the length of the cross sections ($\sim 27''$), and an x dimension equal to the length of the path ($\sim 88''$). Figures 5.15–5.20 show the extracted ejection intensity (top), Doppler velocity (middle), and line width (bottom) profiles for rasters 0–2 in He I and O V. The righthand plots show the location of the extracted ejection path in context of the intensity, velocity and line width structure. The white points indicate the cross sections along the defined path. The lefthand plots show the extracted 2-D

data along the ejection, and the mean profile as a function of length for intensity, velocity and line width. The mean intensity profile of the ejection as a function of length is fitted, using a least squares fitting technique, with an exponential function of the form

$$y = \alpha e^{(\beta x)} + \gamma$$

where y is the mean intensity in photon-events, and x is the distance along the ejection in arcseconds. The fitted values of α , β , γ and their 1σ errors are indicated on the mean intensity profile plots.

5.7.1 He I

Figure 5.15 shows the extracted He I ejection data for raster 0. Considering the strip of extracted intensity cross sections, the left hand edge represents the base of the ejection structure, while moving progressively right along the data displays each cross section of the ejection, perpendicular to the axis. The mean intensity profile shows an almost linear decay in intensity along the length of the ejection. The exponential function fitted to the data has a small exponential decay index of -0.0114 ± 0.0014 . Assuming that the ejection has constant temperature, abundance and column depth profiles along its length then the decay in intensity is likely to be due to a decay in density. This suggests a linear decrease in density with length along the ejection. The strip of extracted velocity cross sections suggests that the Northern edge of the ejection may be more blue-shifted than the Southern edge. The Southern edge of the ejection around $20''$ along the ejection shows a significant red-shift compared to the general velocity structure. The mean velocity profile along the ejection does not show any significant structure or trends within the errors. In contrast, the mean line width profile may suggest a reduction in the mean line width towards the end of the ejection. However, the sudden reduction around $40''$ is due to badly fitted pixels.

Figure 5.16 shows the extracted He I ejection data for raster 1. The strip of extracted intensity cross sections shows that the ejection has a more narrow, extended and diffuse emission. The mean intensity profile along the length of the ejection shows an exponential decay. The data is fitted well with an exponential function with a much larger decay index than in raster 0 of

CHAPTER 5. ACTIVE REGION STRUCTURE AND DYNAMICS

-0.1187 ± 0.0060 . Within the errors, the data is fitted very closely by the exponential function up to $\sim 40''$ along the ejection. Between 40–60 arcsec, the ejection shows a slight enhancement of mean intensity above the exponential profile. The increase of the two points located around $68''$ is due to the badly fitted pixels indicated in white on the plot of extracted cross sections. The analysis suggests an exponential decay in density with length along the ejection. The strip of extracted velocity cross sections shows that the Northern edge of the ejection is blue shifted, and the Southern edge is generally more red-shifted. This velocity gradient along the width of the ejection implies a rotation of the ejection structure. No significant information can be derived from the mean velocity profile, due to the large errors. The mean line width profile shows a slight increase over the first $25''$ then undergoes a general decrease along the length of the ejection. This suggests a possible decrease in the non-thermal broadening of the line width.

Figure 5.17 shows the extracted He I ejection data for raster 2. The strip of extracted intensity cross sections shows that the ejection emission extends over a much shorter length. The mean intensity profile shows a close fit to an exponential decay function within the errors. The fitted function has a decay index of -0.0703 ± 0.0032 . The intensity has a smaller decay rate as a function of length than raster 1, but still much larger than raster 0. This implies that the ejection has a smaller density decay rate as a function of length than raster 1, but larger than raster 0. The strip of extracted velocity cross sections indicates that the Northern edge of the ejection is blue-shifted, and the Southern edge is red-shifted. This velocity gradient, again, suggests a rotation of the ejection plasma. The errors in the mean velocity profile do not allow any significant information to be obtained on the structure, or trend as a function of length. The large red-shift around $35''$ is caused by the badly fitted pixel indicated in red on the plot of extracted velocity cross sections. This pixel also causes the sharp reduction in line width in the mean line width profile. Thus, no significant structure, or trends can be identified easily within the mean line width profile.

CHAPTER 5. ACTIVE REGION STRUCTURE AND DYNAMICS

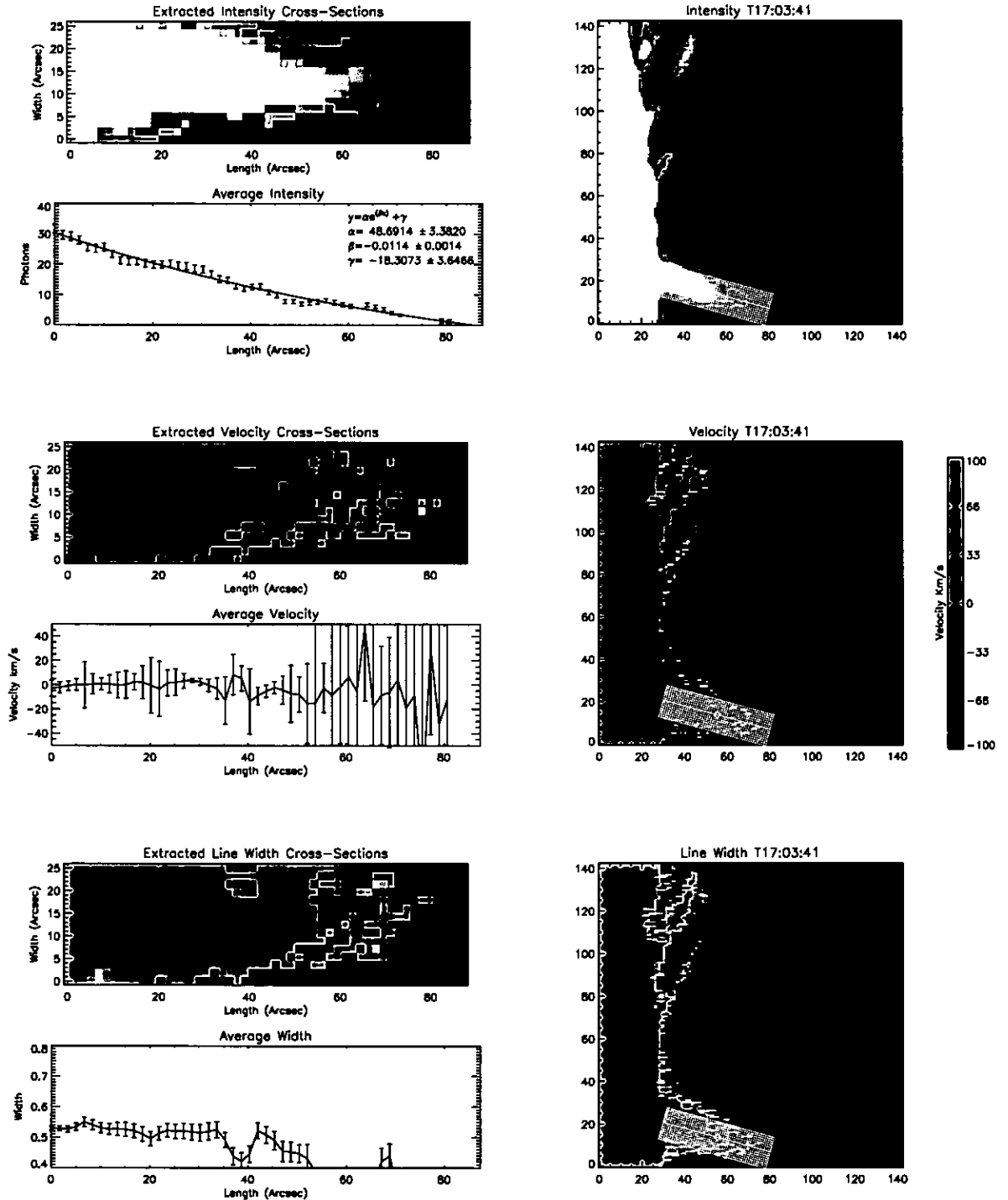


Figure 5.15: He I raster 0 line parameters along the ejection. Top: Context image of the extracted path in He I intensity, extracted 2-D intensity structure along the length of the ejection, average (mean) intensity profile as a function of length along the ejection. Middle: Context image of the extracted path in He I Doppler velocity, extracted 2-D velocity structure along the length of the ejection, average velocity profile as a function of length along the ejection. Bottom: Context image of the extracted path in He I line width, extracted 2-D line width structure along the length of the ejection, average line width profile as a function of length along the ejection.

CHAPTER 5. ACTIVE REGION STRUCTURE AND DYNAMICS

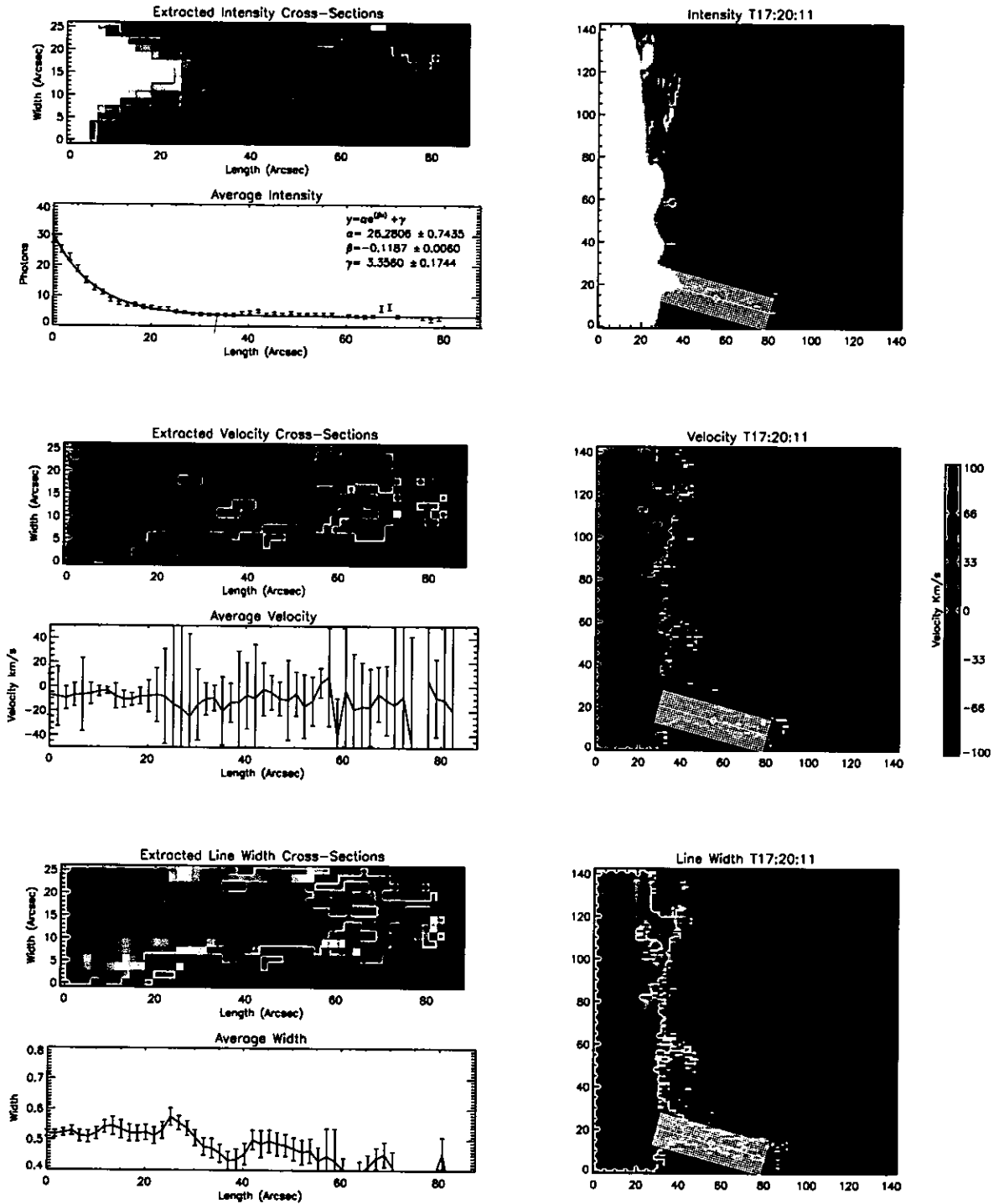


Figure 5.16: He I raster 1 line parameters along the ejection. Top: Context image of the extracted path in He I intensity, extracted 2-D intensity structure along the length of the ejection, average (mean) intensity profile as a function of length along the ejection. Middle: Context image of the extracted path in He I Doppler velocity, extracted 2-D velocity structure along the length of the ejection, average velocity profile as a function of length along the ejection. Bottom: Context image of the extracted path in He I line width, extracted 2-D line width structure along the length of the ejection, average line width profile as a function of length along the ejection.

CHAPTER 5. ACTIVE REGION STRUCTURE AND DYNAMICS

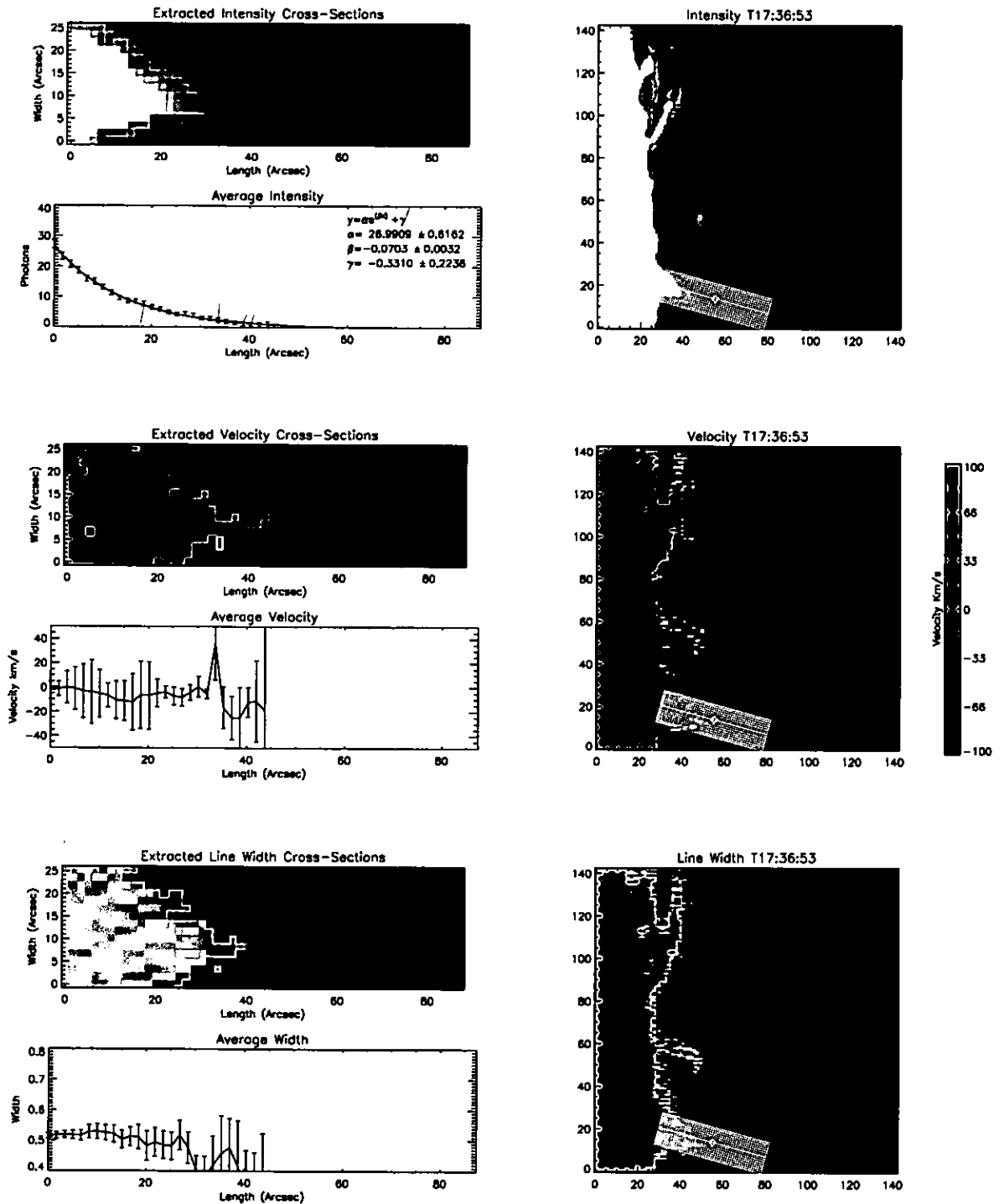


Figure 5.17: He I raster 2 line parameters along the ejection. Top: Context image of the extracted path in He I intensity, extracted 2-D intensity structure along the length of the ejection, average (mean) intensity profile as a function of length along the ejection. Middle: Context image of the extracted path in He I Doppler velocity, extracted 2-D velocity structure along the length of the ejection, average velocity profile as a function of length along the ejection. Bottom: Context image of the extracted path in He I line width, extracted 2-D line width structure along the length of the ejection, average line width profile as a function of length along the ejection.

5.7.2 O V

Figure 5.18 shows the extracted O V ejection data for raster 0. The strip of extracted intensity cross sections shows a different emission structure than in He I. The emission is asymmetric along the first half of the ejection's length. The Northern side shows increased emission relative to the Southern side. There also appears to be another increase in emission further along the length of the ejection around $55''$. The mean intensity profile shows an exponential decay along the ejection. The mean intensity is fitted with an exponential function with a decay index of -0.1152 ± 0.0033 . Within the errors, initially the mean profile corresponds well to the exponential function. Between 10–20 arcsec the mean intensity is decreased relative to the exponential decay. The mean intensity shows an enhancement above the fitted exponential decay function between 40–60 arcsec before reducing again at the end of the ejection. These variations in intensity suggest corresponding variations in density, assuming all other variables affecting emission remain constant. The strip of extracted velocity cross sections shows a mixed velocity distribution along the ejection, with predominantly red-shifted plasma. The mean velocity profile does not show any significant trend within the errors, but shows a general red-shift of $\sim 10 \text{ km s}^{-1}$. The mean line width profile shows variations along the ejection, but no significant variations can be observed considering the errors.

Figure 5.19 shows the extracted O V ejection data for raster 1. The strip of extracted intensity cross sections shows a more uniform emission across the width of the ejection. The mean intensity profile of the ejection is closely fitted by the exponential function with a decay index of -0.0678 ± 0.0029 . The close fit suggests a smoother distribution of emission along the ejection, with a possible uniform exponential decay in density. The strip of extracted velocity cross sections shows a clear dichotomy of the velocity structure within the ejection. There are separate regions that show a strong red/blue-shift; these regions do not have a simple N–S distribution indicative of a symmetric, rigidly rotating, column of plasma. The red-shifted plasma is generally located towards the base of the ejection, and along the Southern edge. The blue-shifted plasma is generally located towards the upper part of the ejection, and along the Northern edge.

It should be expected that the ejection does not show a symmetric velocity gradient across

CHAPTER 5. ACTIVE REGION STRUCTURE AND DYNAMICS

its width. It is observed over rasters 0–2 that the plasma has a velocity component perpendicular to the line of sight. The ejection also appears to have rotational velocity. Thus, we would expect the locus of a particular plasma element to have a helical geometry. The velocity gradient across the width of the ejection is then dependent on the pitch angle of the helix, and the angle of the ejection axis relative to the line of sight. For example, we could speculate the velocity pattern could be produced if the ejection axis is slightly inclined away from the line of sight, and the ejection plasma has a rotation angle of $-\pi$ (anti-clockwise, if viewed from above the ejection axis) between ~ 20 – 60 arcsec along the length of the ejection. The mean velocity profile shows that red-shifted plasma dominates at the base of the ejection, with a mean velocity of $\sim 25 \text{ km s}^{-1}$. The mean velocity reduces to zero approximately halfway along the ejection. The upper part of the ejection has an approximately constant $\sim -10 \text{ km s}^{-1}$ blue-shift. The line width does not show any significant structure spatially, or in the mean width profile along the ejection.

Figure 5.20 shows the extracted O V ejection data for raster 2. The strip of extracted intensity cross sections shows that the ejection has a much shorter length. Again, the mean emission along the ejection can be approximated by an exponential decay function. The fitted function has a decay index of -0.0918 ± 0.0037 . The mean emission is fitted well up to $\sim 25''$ along the ejection, where the mean intensity shows enhanced emission above the exponential decay. The extracted velocity cross sections show the ejection emission is red-shifted above the O V limb. The Northern edge of the ejection shows a lower magnitude of red-shift, suggesting a velocity gradient across the width of the ejection due to rotation. The mean velocity profile shows a red-shift along the ejection of $\sim 25 \text{ km s}^{-1}$. The extracted line width cross sections show a mixed variation of widths within the ejection. The mean width profile does not reveal any significant structure within the errors.

CHAPTER 5. ACTIVE REGION STRUCTURE AND DYNAMICS

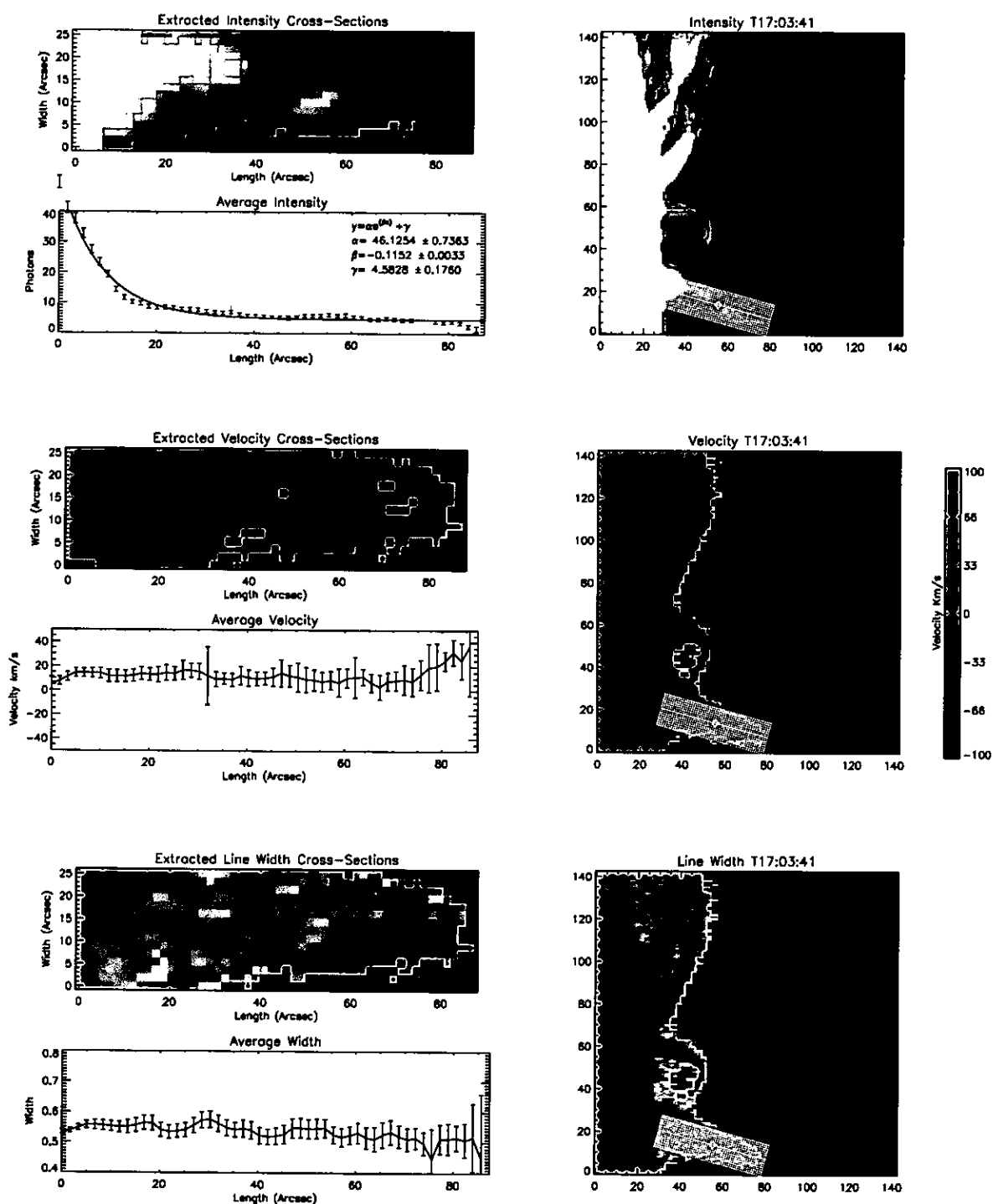


Figure 5.18: O V raster 0 line parameters along the ejection. Top: Context image of the extracted path in O V intensity, extracted 2-D intensity structure along the length of the ejection, average (mean) intensity profile as a function of length along the ejection. Middle: Context image of the extracted path in O V Doppler velocity, extracted 2-D velocity structure along the length of the ejection, average velocity profile as a function of length along the ejection. Bottom: Context image of the extracted path in O V line width, extracted 2-D line width structure along the length of the ejection, average line width profile as a function of length along the ejection.

CHAPTER 5. ACTIVE REGION STRUCTURE AND DYNAMICS

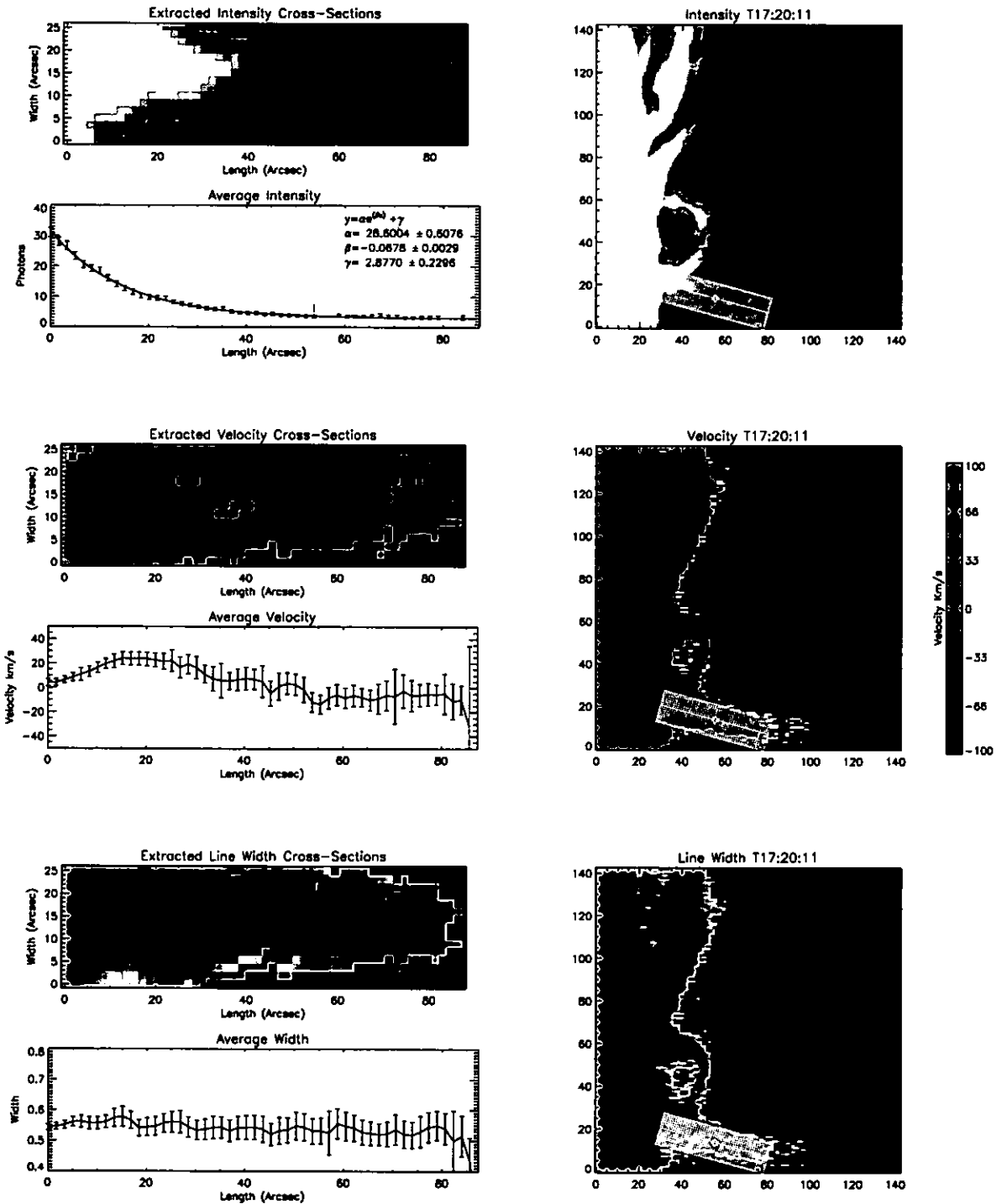


Figure 5.19: O V raster 1 line parameters along the ejection. Top: Context image of the extracted path in O V intensity, extracted 2-D intensity structure along the length of the ejection, average (mean) intensity profile as a function of length along the ejection. Middle: Context image of the extracted path in O V Doppler velocity, extracted 2-D velocity structure along the length of the ejection, average velocity profile as a function of length along the ejection. Bottom: Context image of the extracted path in O V line width, extracted 2-D line width structure along the length of the ejection, average line width profile as a function of length along the ejection.

CHAPTER 5. ACTIVE REGION STRUCTURE AND DYNAMICS

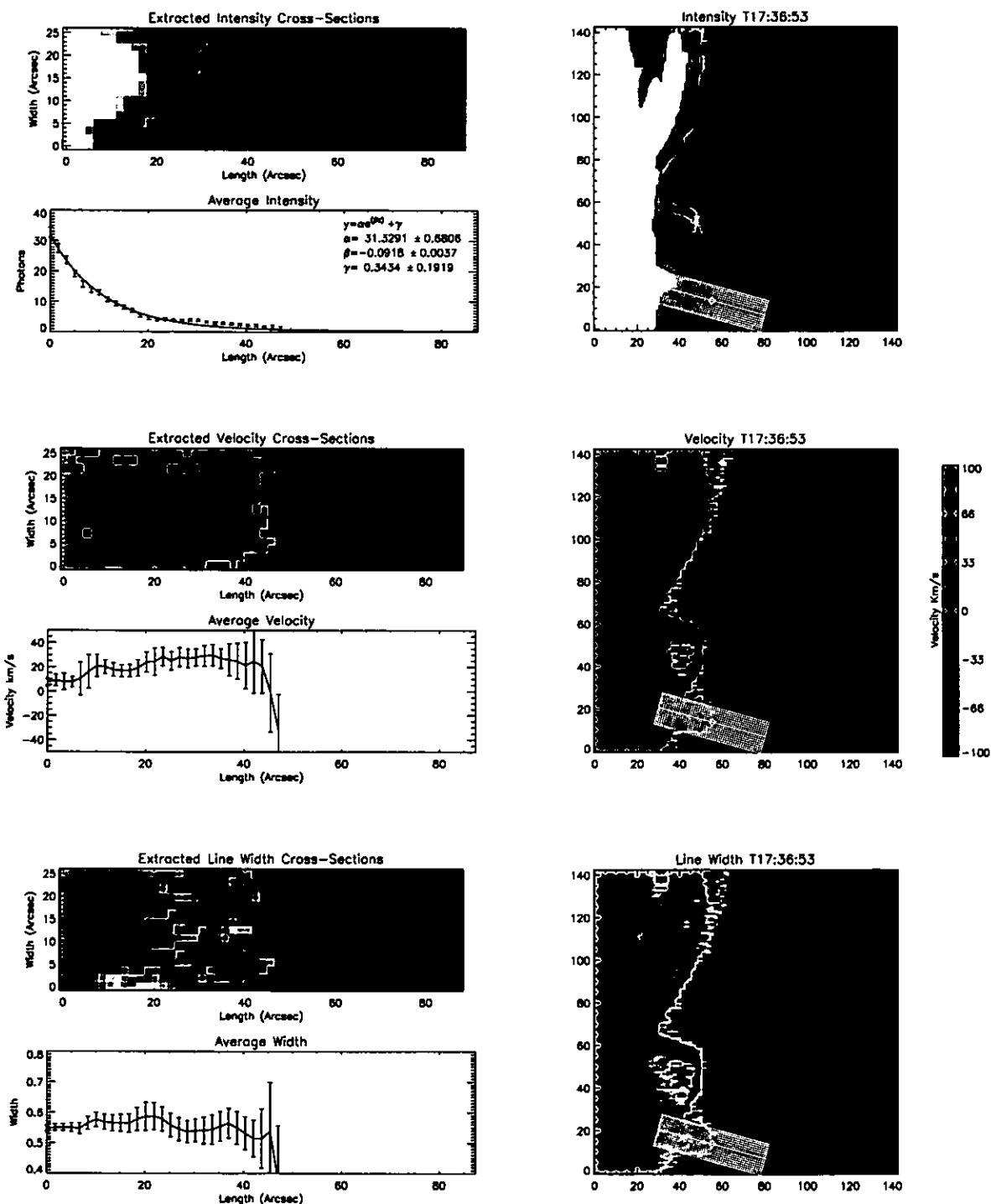


Figure 5.20: O V raster 2 line parameters along the ejection. Top: Context image of the extracted path in O V intensity, extracted 2-D intensity structure along the length of the ejection, average (mean) intensity profile as a function of length along the ejection. Middle: Context image of the extracted path in O V Doppler velocity, extracted 2-D velocity structure along the length of the ejection, average velocity profile as a function of length along the ejection. Bottom: Context image of the extracted path in O V line width, extracted 2-D line width structure along the length of the ejection, average line width profile as a function of length along the ejection.

		Emission scale length (km) [arcsec]	Density scale length (km)
He I	Raster 0	32,000 [44]	126,000
	Raster 1	8,000 [11]	12,000
	Raster 2	10,000 [14]	20,000
O V	Raster 0	7,000 [10]	13,000
	Raster 1	13,000 [18]	21,000
	Raster 2	8,000 [11]	16,000

Table 5.1: Ejection $\frac{1}{e}$ emission and density scale lengths in He I and O V for rasters 0–2

5.7.3 Active Region Ejection: Density Scale Heights

The literature reports the length of spicule/macrospicule structures by an estimation of the extent of the observed emission length. To form a more useful classification and comparison between different structures, the length of the ejection can be defined and measured by the $\frac{1}{e}$ emission decay length of the fitted exponential functions. If the ejection is assumed to have a uniform temperature, abundance and optical emission depth along its length and assuming $I \propto n_e^2$, the density scale height can then be measured along the length of the ejection perpendicular to the line of sight. The measured emission scale length and density scale lengths of the ejection in He I and O V are listed in Table 5.1, for rasters 0–2. It is clear to see that the ejection has a very different behaviour in He I and O V.

Considering He I, in raster 0 the ejection has an almost linear decay in emission, and so density along its length, resulting in large scale lengths. In raster 1 the scale lengths are much smaller before increasing again in raster 2. Considering O V, in raster 0 the scale lengths are much smaller than in He I, demonstrating the different structure between the two temperatures at the same time and apparent location. In raster 1, the scale lengths increase before reducing in raster 2. This shows an opposite behaviour to He I over the same time frame.

5.8 Active Region Ejection: Quantitative Width Structure

Section 5.7 investigated the mean emission line properties as a function of length along the ejection. To investigate these properties as a function of width, the same vector extraction method is used to extract the data parallel to the ejections axis. Eight cross sections are defined

along the ejections length at $\approx 11''$ spacing. Each cross section has a width of $\approx 7''$, over which the mean cross section profile is formed. Figures 5.21–5.26 show the cross section profiles along the ejection in He I and O V for rasters 0–2. In each figure the left column shows the context of the eight cross sections with respect to the emission structure and the corresponding mean emission profiles of each cross section. The middle column shows the results for the Doppler velocity, and the right column shows the results for the emission line width.

5.8.1 He I

Considering He I, Fig. 5.21 shows the cross section profiles for raster 0. The mean intensity profiles show a smooth, widely peaked, emission across the ejection. Flatter emission profiles are observed within the centre of the ejection in cross sections # 3, 4 and 5. The FWHM width of the ejection has a range of 18–13 arcsec from the base to its end. The mean velocity profiles suggests a negative gradient across the ejection with plasma blue-shifted towards the end of the cross sections. This red→blue-shifted velocity trend from the Southern→Northern edge of the ejection, respectively, suggests a possible rotation of the plasma. However, considering the errors, this trend only appears significant in cross sections 2, 3 and 7. The line width cross sections show a flat profile along the ejection, and do not show any significant structure across the width of the ejection within the errors.

Figure 5.22 shows the cross section profiles for raster 1. The mean emission profiles show a more peaked emission across the ejection. The peak in emission across the ejection has approximately the same location along the length of the ejection. This indicates that, at this time, the emission within the ejection is symmetrical about its axis. The FWHM width of the ejection has a range of 16'' at the base to 11'' at its end. The mean velocity profiles again show a negative velocity gradient across the ejection from South→North. The Southern edge of the ejection has a velocity of $\approx 0 \text{ km s}^{-1}$. The Northern edge has a significant blue-shift of $\approx -(20-50) \text{ km s}^{-1}$ across cross sections 2–5. The line width profiles do not show any significant structure within the errors.

Figure 5.23 shows the cross section profiles for raster 2. As described in Sect. 5.7.1 the emission extends over a much shorter length. The ejection emission is slightly inclined to the

CHAPTER 5. ACTIVE REGION STRUCTURE AND DYNAMICS

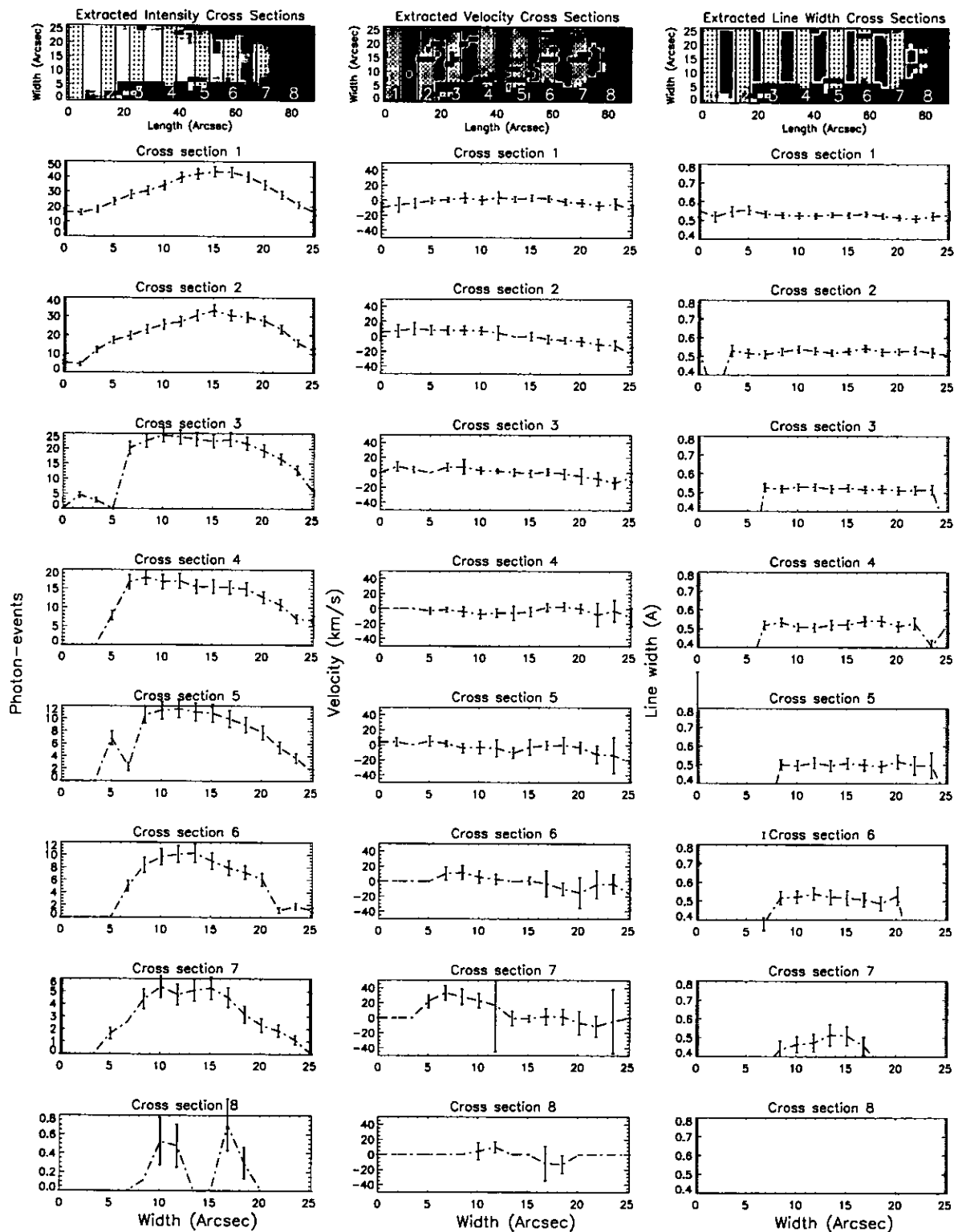


Figure 5.21: He I raster 0 line parameters across the width of the ejection. 8 cross sections are defined along the ejection. The left, middle and right columns indicate the location of the cross sections and their mean profiles in intensity, Doppler velocity and line width respectively.

CHAPTER 5. ACTIVE REGION STRUCTURE AND DYNAMICS

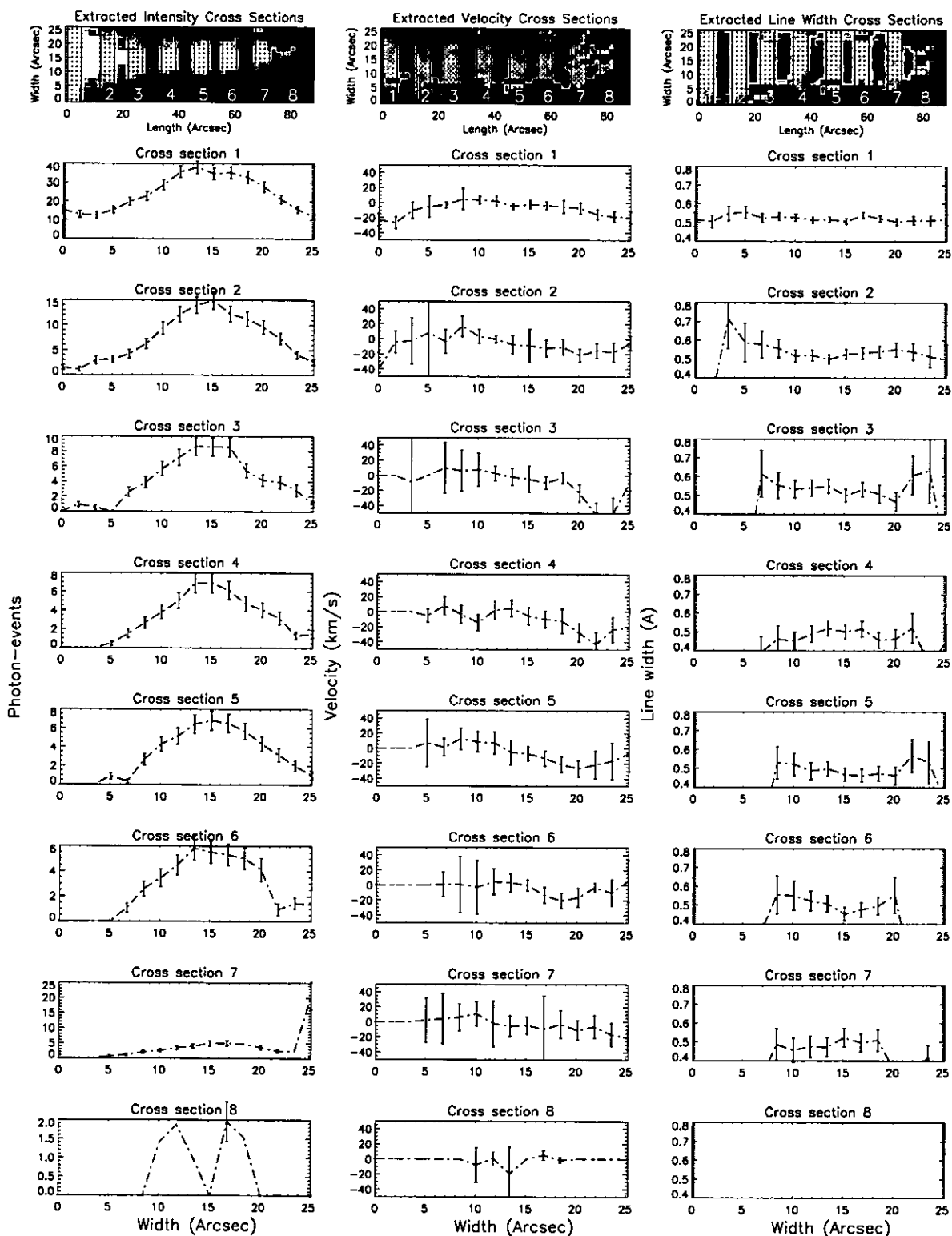


Figure 5.22: He I raster 1 line parameters across the width of the ejection. 8 cross sections are defined along the ejection. The left, middle and right columns indicate the location of the cross sections and their mean profiles in intensity, Doppler velocity and line width respectively.

CHAPTER 5. ACTIVE REGION STRUCTURE AND DYNAMICS

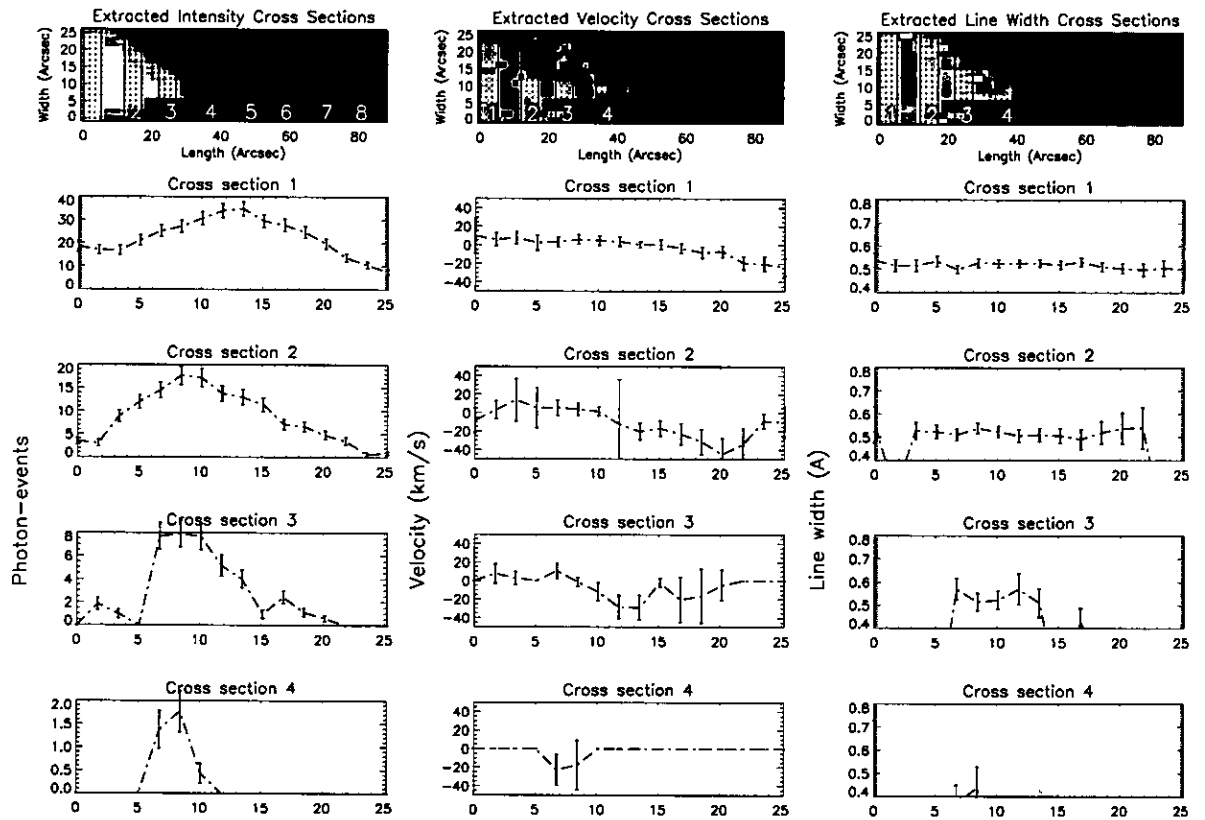


Figure 5.23: He I raster 2 line parameters across the width of the ejection. 8 cross sections are defined along the ejection. The left, middle and right columns indicate the location of the cross sections and their mean profiles in intensity, Doppler velocity and line width respectively.

South, indicated by the shift of the emission peak towards the beginning of the cross sections in the mean emission profiles. The FWHM width of the ejection has a range of 15–4 arcsec from the base to its end. Again a velocity trend is suggested across the ejection by the mean velocity profiles. Cross sections 1 and 2 show a negative velocity trend across the ejection. Particularly in cross section 2, which has a red-shift of $\approx 10 \text{ km s}^{-1}$ at the Southern edge of the ejection and a blue-shift of $\approx -40 \text{ km s}^{-1}$ at the Northern edge. The mean line width profiles do not reveal any significant structure within the errors.

5.8.2 O V

Considering O V, Fig. 5.24 shows the cross section profiles for raster 0. The ejection emission shows an asymmetric structure about its axis. This is indicated by the movement of the main emission peak towards the beginning of the cross sections, corresponding to the Southern edge of the ejection. The FWHM width of the ejection has a range of ≥ 25 –12 arcsec from the base to its end. The ejection shows a mixed velocity structure along its length. The mean velocity profiles do not show a significant structure within the errors, apart from cross sections 2 and 3 which show a trend from a red-shift of $\approx 30 \text{ km s}^{-1}$ and $\approx 40 \text{ km s}^{-1}$ at the Southern edge of the ejection to a velocity of $\approx 0 \text{ km s}^{-1}$ at the Northern edge. The mean line width profiles do not show any significant structure within the errors.

Figure 5.25 shows the cross section profiles for raster 1. The mean emission profiles show that in the first four cross sections the peak emission is concentrated within the Northern half of the ejection. The remaining cross sections show a more axisymmetric emission with the last three cross sections, towards the top of the ejection, having a flatter emission across the centre. The FWHM width of the ejection has a range of ≥ 25 –14 arcsec from the base to its end. The mean velocity profiles show a significant negative gradient across the ejection in cross sections 2–6. Cross section 4 has the largest trend from a red-shift of $\approx 50 \text{ km s}^{-1}$ at the Southern edge to a blue-shift of $\approx -20 \text{ km s}^{-1}$ at the Northern edge. These large gradients suggest a strong rotation of the plasma at the base of the ejection. Considering the mean line width profiles, cross section 2 shows an increase in the line width, located within the strongly red-shifted region, that is significant with respect to the errors and has a minimum increase of

$\sim 0.3 \text{ \AA}$ compared to the Northern edge.

Figure 5.26 shows the cross section profiles for raster 2. The mean emission profiles suggest a possible double peaked in the emission across the ejection at its top. The FWHM width of the ejection has a range of $\geq 25\text{--}21$ arcsec from the base to its end. The mean velocity profiles show that the majority of the plasma is red-shifted with a velocity around 40 km s^{-1} . Cross sections 2 and 3 show a significant drop in velocity to $\approx 0 \text{ km s}^{-1}$ at the Northern edge of the ejection. No significant structure can be observed within the mean line width profiles considering the errors.

5.9 Summary and Discussion

5.9.1 Active region loop

An active region loop is observed which appears to show oppositely directed flows in He I and O V intensity. He I appears to show plasma to be ejected, and fall, along one loop leg whilst a constant downward flow is present in the same loop leg due to a syphon-like flow. The intensity motions in O V combined with the Doppler shift pattern of the loop are used to attempt to imply the geometry of the loop. If the intensity motions are due to movement of the same plasma elements in each raster then a South→North directed syphon flow with the plane of the loop inclined away from the line of sight is the most likely geometry of the system. The quantitative analysis of the O V loop shows the dynamic nature of the plasma in emission and velocity over the cadence of the observations. The loop shows oppositely directed flows in each leg with an asymmetric mean velocity profile of up to $-20\rightarrow 40 \text{ km s}^{-1}$ (blue→red-shift) in the Northern and Southern legs respectively. However, these are line of sight velocities, as the precise geometry of the loop is not known, and cannot be derived without observations along two different lines of sight.

High velocity flows in a CDS O V active region loop system were first reported by Brekke et al. (1997). They observe a $>50 \text{ km s}^{-1}$ blue shift over a large fraction of an O V loop. They briefly comment on the possible flow mechanisms that might produce the observations, and, as in the analysis here, they find that the interpretation is strongly dependent on the loop

CHAPTER 5. ACTIVE REGION STRUCTURE AND DYNAMICS

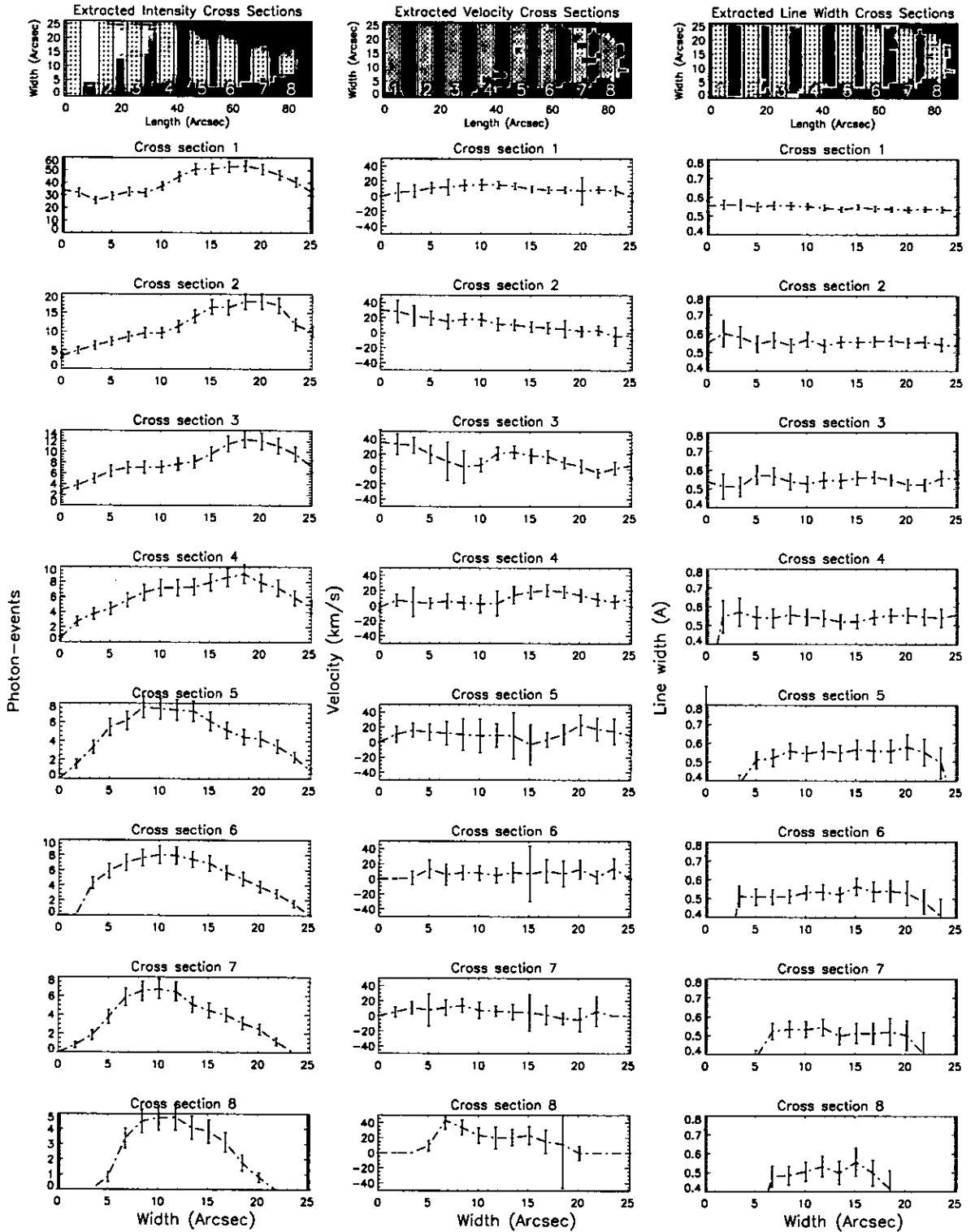


Figure 5.24: O V raster 0 line parameters across the width of the ejection. 8 cross sections are defined along the ejection. The left, middle and right columns indicate the location of the cross sections and their mean profiles in intensity, Doppler velocity and line width respectively.

CHAPTER 5. ACTIVE REGION STRUCTURE AND DYNAMICS

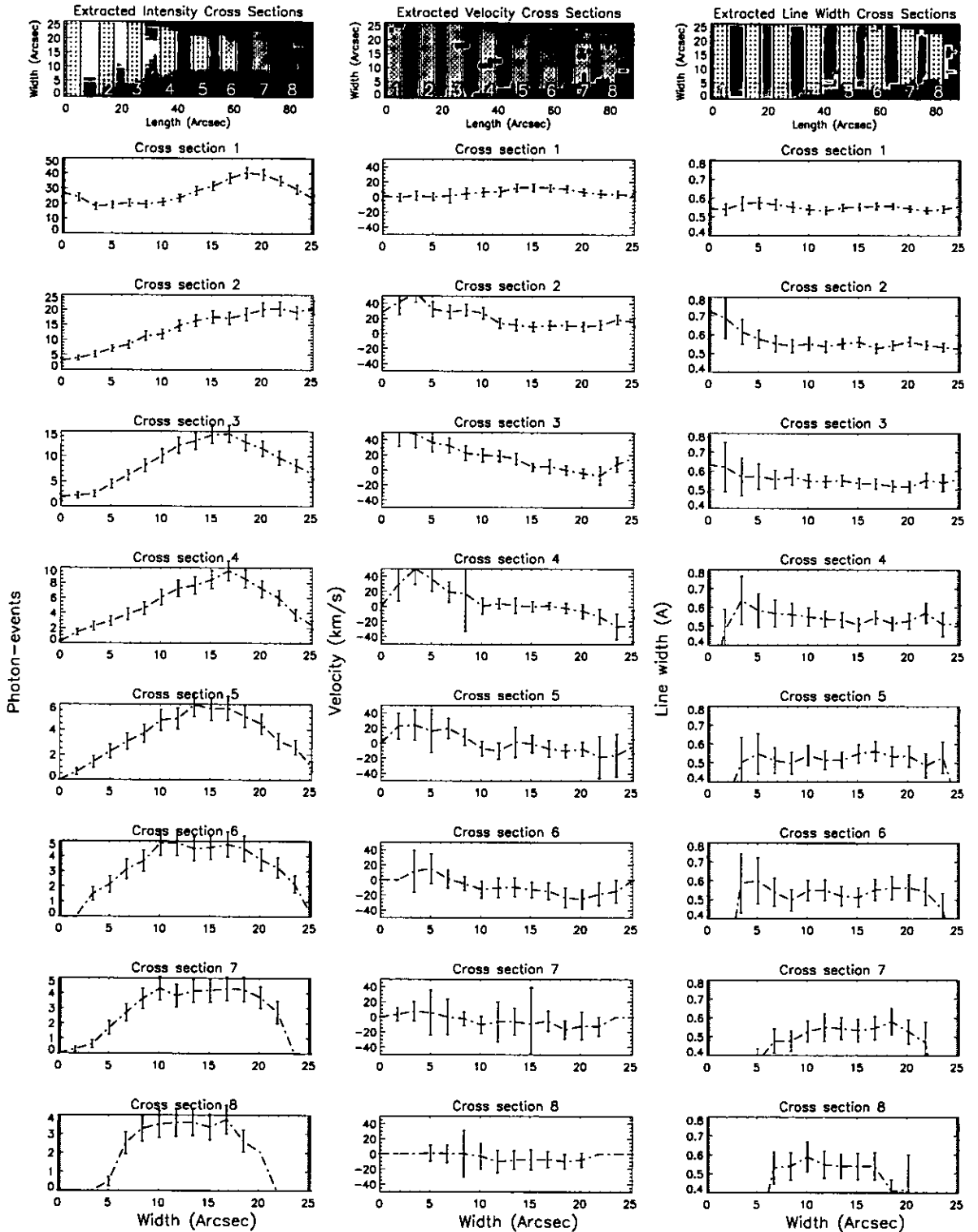


Figure 5.25: O V raster 1 line parameters across the width of the ejection. 8 cross sections are defined along the ejection. The left, middle and right columns indicate the location of the cross sections and their mean profiles in intensity, Doppler velocity and line width respectively.

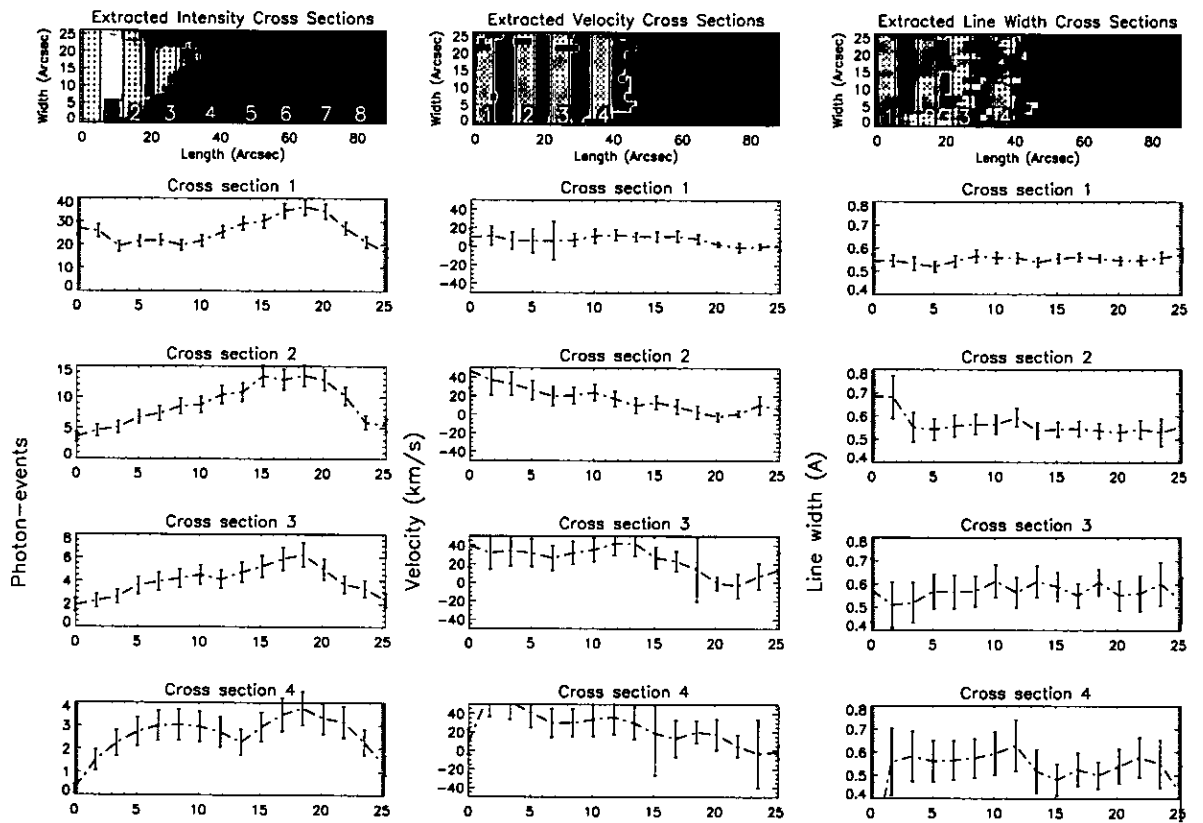


Figure 5.26: O V raster 2 line parameters across the width of the ejection. 8 cross sections are defined along the ejection. The left, middle and right columns indicate the location of the cross sections and their mean profiles in intensity, Doppler velocity and line width respectively.

CHAPTER 5. ACTIVE REGION STRUCTURE AND DYNAMICS

geometry. The possibility that the Doppler shifts may originate from wave processes is also mentioned.

Kjeldseth-Moe & Brekke (1998) report on the highly dynamic and time variable nature of loops observed at transition region temperatures. The emission in loops at these temperatures is found to vary dramatically on timescales <10 minutes, while coronal loops are found to be generally much more stable. O V Doppler shifts are observed within loops with typical velocities of $50\text{--}100\text{ km s}^{-1}$, and up to 300 km s^{-1} in some cases.

Similar work is described by Fredvik et al. (2002) who also investigate the variability and plasma dynamics of active region loops. They observe Doppler velocities within transition region loops, and suggest syphon flows may occur in some of the observed loops. The highest velocities are also observed where the intensities are weak, on the outer edges of the loops. A possible example of syphon flow is observed with red and blue Doppler shifts of $\pm 30\text{ km s}^{-1}$ found in opposite loop legs. No clear correlation between intensity and plasma velocity is found. Examples of individual loops are observed across a range of emission lines suggesting that the loops contain plasma over a range of temperatures.

Di Giorgio et al. (2003) observe a hot stable loop in coronal lines, and a transient dynamic loop in transition region lines. The transition region loop has blue-shifted upflow in O V at the foot point of the loop, thought to be the origin of the plasma flow.

Spadaro et al. (2000) observe an on-disk active region loop system with SUMER. Plasma flows up to 16 km s^{-1} are observed at the loop foot points. Red/blue-shifted velocities are observed in opposite footpoints, suggesting a syphon flow mechanism. Larger Doppler velocities are found in more compact loops at transition region temperatures. Observations of a compact transition region loop show a higher flow and non-thermal velocity at the rising footpoint. The loop legs supporting a downflow of plasma are usually found to be brighter than the upflow legs. This is believed to be the origin of the general red-shift observed at transition region temperatures in the sun and late type stars.

These observations of a higher flow and non-thermal velocity in the upflow loop leg are consistent with the observations and implied geometry presented here. Figures 5.9 and 5.11 show a clear syphon-like flow profile along the loop. Considering the implied South \rightarrow North

syphon flow geometry derived in Section 5.4, the Southern (upflow) loop leg shows the largest Doppler velocity, and the mean line width profile also suggests the possibility of an increase in line width, although this cannot be confirmed within the error levels. In these two rasters where a syphon flow pattern is visible, the Northern (downflow) loop leg also shows the greatest emission.

The exact interpretation of the velocity profiles in loop structures is not possible, as only the line of sight velocities are available. Observations from two different lines of sight are necessary to derive the full three dimensional vectors of the loop and flow geometries. Only then will it be possible to determine the energetics of loop structures, and allow theoretical loop models and their heating mechanisms to be tested. The data provided by the future STEREO mission will allow dynamic structures such as these to be observed for the first time in three dimensions. However, the imaging will not be complimented by spectroscopic data.

5.9.2 Active region ejection

The results from the qualitative analysis of the ejection are summarised in Table 5.2 below. The table shows estimated values for the ejection of the width, length and instantaneous velocity between consecutive rasters in He I and O V over rasters 0–2. The fact that the ejection is observed as emission in He I and O V, and as absorption in the coronal Mg IX, Si X and Fe XVI lines suggests that the ejection is composed of plasma with a temperature range between $\text{Log } T=4.4 \rightarrow \text{Log } T=6.0$

Table 5.2: Summary of qualitative analysis results

Raster	He I			O V		
	Width (")	Length (")	Velocity (km s ⁻¹)	Width (")	Length (")	Velocity (km s ⁻¹)
0	30	75	16	25	80	20
1	15	100	-46	20	110	-46
2	20	30	-19	25	50	-15

The results from the quantitative analysis of the ejection are summarised in Table 5.3 below. The table lists the range of the FWHM width from the base to the end of the ejection and the $\frac{1}{e}$ emission scale length of the fitted exponential functions in He I and O V over rasters 0–2. The FWHM width and emission scale length measured here are more instructive methods

CHAPTER 5. ACTIVE REGION STRUCTURE AND DYNAMICS

of classifying this kind of structure as they provide non-subjective parameters of the ejection, and convey information about the spatial structure. Often these kind of ejecta are classified in the observational literature by a visual estimation of the extent of their width and length. The theoretical models described in the literature are then tested by their ability to reproduce these limits, without reproducing the spatial distribution of these parameters either in emission or density. A full treatment should reproduce the observed spatial profiles, obtained using a method similar to that applied here.

Table 5.3: Summary of quantitative analysis results

Raster	He I		O V	
	Width (")	Length (")	Width (")	Length (")
0	18–13	44	≥ 25 –12	10
1	16–11	11	≥ 25 –14	18
2	15–4	14	≥ 25 –21	11

There are many examples of dynamic ejection events described within the literature such as spicules, macrospicules, surges, X-ray jets, etc. Recorded observations of spicules date back to the nineteenth century and are described by Lyot (1945) and Roberts (1945). Sterling (2000) gives a review of spicule models and describes the following typical spicule properties:

Typical spicule properties

Height: 10–18 arcsec

Width: ≤ 0.5 –2 arcsec

Lifetime: 1–10 mins

Upward velocity: 25 km s⁻¹

Temperature: 5,000–15,000 K

Macrospicules were first discovered in Skylab He II 304Å observations (Bohlin et al. 1975), and are observed in a number of other EUV lines (Withbroe et al. 1976). Labonte (1979) observe macrospicules in H α and Sodium D₃ lines. Observations of macrospicules in the UV, made during the Spacelab 2 mission, are described by Dere et al. (1989b). Recently Yamauchi et al. (2004) observe a sample of H α macrospicules. Typical properties of macrospicules derived from the above papers are listed below.

Typical macrospicule properties

Height: 10–60 arcsec
 Width: 5–30 arcsec
 Lifetime: 3–45 mins
 Upward velocity: $42 \pm 19 \text{ km s}^{-1}$
 Temperature: 50,000–300,000 K

Habbal & Gonzalez (1991) observe macrospicules at radio wavelengths and derive an empirical model of the spicules consisting of a $8 \times 10^3 \text{ K}$ core surrounded by a lower density $1\text{--}2 \times 10^5 \text{ K}$ outer sheath. Pike & Mason (1998) observe rotating transition region structures, consistent with macrospicules, in O V with CDS, termed solar tornadoes. They observe blue/red-shifted emission on either side of an axis, located above the limb. The velocity is observed to increase with height on either side of the axis, reaching a peak magnitude of $\pm 30 \text{ km s}^{-1}$ approximately $30''$ above the footpoints.

Pike & Harrison (1997) observe a macrospicule within a Southern polar coronal hole region with CDS. They observe an acceleration of the plasma up to 20–25 arcsec above the footpoint, above which the velocity tends to a constant $\sim 150 \text{ km s}^{-1}$ in O V. This is interpreted as a non-radial open structure overlying a loop system with a possible outflow into the solar wind. They also state that the EUV characteristics of the macrospicule are consistent with observations of X-ray jets.

Harrison et al. (2001) describe jet-like eruptive activity on the limb observed with CDS. The jets have lengths $\sim 150''$, greater than typical spicule/macrospicule lengths, and lifetimes $\sim 30\text{--}100$ mins. They also note the presence of a small loop, or intensity enhancements at the base, which are only observed in conjunction with the jets. One of the observed jets shows a rotation from the Doppler velocity which accelerates with distance above the limb reaching a peak red/blue-shift of $380/190 \text{ km s}^{-1}$ respectively. The similarity in the dimensions and velocities of the jets to X-ray jets is mentioned; however, these EUV jets are not observed at coronal temperatures. They suggest that the jets can be explained by the reconnection of a small loop and open field, with a magnetic accretion model.

Sterling (2000) reviews recent models of spicules with the numerical models all consisting of an energy deposition in the photosphere or chromosphere within a flux tube extending to coronal heights. These models are classified by a velocity/pressure pulse in the photosphere, a

CHAPTER 5. ACTIVE REGION STRUCTURE AND DYNAMICS

pressure pulse in the chromosphere, or generation of Alfvén waves. It is not known if ejection structures such as spicules, macrospicules, surges, X-ray jets, etc, are manifestations of the same mechanism on differing scales, or are caused by different mechanisms. However, the similarity of the different structures suggests that there may be a close relationship between them. It appears that the observed structures may, primarily, be dependent on the observation wavelength/temperature. A thorough program including $H\alpha$, UV, EUV and X-ray observations is necessary to determine any relationship.

The ejection observed in this chapter is consistent with the observed properties of a macrospicule. Observations of macrospicules tend to be associated with coronal hole regions; however, the macrospicule observed here is associated with AR 8015 located on the Western limb, just North of the solar equator. However, EIT 171 Å observations of the region a few days before show a small coronal hole region located to the East, directly adjacent to the active region. The macrospicule and the active region loop at its base appear to share the same foot-point region. Both structures are only visible in conjunction with one another. This geometry has a striking similarities with the observations of Harrison et al. (2001). They interpret their observations in terms of a magnetic accretion model, whereby a small closed loop impinges on an open field region driving reconnection. This produces a kink in the open field causing a vertical velocity flow with a bulk rotation. Thus, the macrospicule presented here may be interpreted as being driven by reconnection between open field and a small loop region. This would also deposit energy in the Southern leg of the loop driving the observed flow geometry in conjunction with the presence of the macrospicule.

Chapter 6

JOP 83 Observations of Propagating Loop Oscillations with CDS and TRACE

6.1 Introduction

In this chapter, Joint Observing Program (JOP) 83 Solar and Heliospheric Observatory/Coronal Diagnostic Spectrometer (SOHO/CDS) and Transition Region and Coronal Explorer (TRACE) data is analysed for evidence of propagating intensity oscillations along loop structures in the solar corona. A propagating intensity oscillation with a minimum estimated speed of 50–195 km s⁻¹ is observed within a TRACE 171 Å coronal loop using a running difference method. Co-spatial and co-temporal CDS and TRACE observations of this loop are analysed using a wavelet analysis method. The TRACE data shows a propagating oscillation with a period of ≈ 300 s. This period is also observed with CDS suggesting propagating oscillations at chromospheric, transition region and coronal temperatures in the He I, O V and Mg IX lines.

De Moortel et al. (2002c,a) give an overview of propagating intensity oscillations in coronal loops observed with TRACE. JOP 83 and JOP 144 TRACE 171 Å data is analysed using running difference and wavelet analysis methods. They find oscillations in the footpoints of large diffuse coronal loops that emerge from active regions. The oscillations are observed

as periodic intensity propagations which travel upwards along the base of the coronal loop structures. These oscillations are interpreted as slow magneto-acoustic waves with propagation speeds in the range $70\text{--}235\text{ km s}^{-1}$ with periods of $282 \pm 93\text{ s}$ that are damped very quickly along the loop (within $8.9 \pm 4.4\text{ Mm}$). De Moortel et al. (2002b) comment on the relation between 3 minute oscillations found in TRACE coronal loops situated above sunspot regions and 5 minute oscillations found in “non-sunspot” loops.

Brynildsen et al. (2002, 2004) and O’Shea et al. (2002) discuss the 3 minute oscillations above sunspots using TRACE and CDS. They find that the oscillation amplitude above the umbra increases with temperature, reaches a maximum for lines formed close to $1\text{--}2 \times 10^5\text{ K}$, and decreases at higher temperatures. It is suggested that waves propagate from the footpoints of coronal loops along the magnetic field into the corona.

In this chapter part of the same data set used by De Moortel et al. (2002c) is investigated. The CDS observations that form part of the JOP 83 observations, obtained over the 7th–9th April 2000, are analysed, along with the TRACE 171 \AA observations. A 5 minute oscillation in a “non-sunspot” coronal loop is observed on 7th April 2000 using TRACE and CDS. Results are presented which suggest that a propagating disturbance observed in TRACE at coronal temperatures is also present in co-spatial/co-temporal CDS-NIS observations at chromospheric, transition region and coronal temperatures. Note that this work has been published in Marsh et al. (2003).

6.2 Observations

The observations are taken as part of the JOP 83 - “High Cadence Activity Studies and the Heating of Coronal Loops”, performed on 7th–9th April 2000. The aim of this JOP was to investigate the rapid time variation in and around a target coronal loop system. The observations consist of co-temporal TRACE and CDS data with the position of the CDS slit located within the TRACE field of view. Table 6.1 lists the TRACE observing sequences analysed over the three days of observations; Table 6.2 lists the CDS observing sequences. The TRACE observations consist of $512'' \times 512''$ and $768'' \times 768''$ images taken in the 171 \AA passband at $1''$ and $0.5''$ resolution. The CDS data uses two observing sequences performed with NIS,

LARGEBP2 and LOOPS_5. LARGEBP2 uses the $2'' \times 240''$ slit at 120 locations to produce a $240'' \times 240''$ context image in 16 spectral windows. LOOPS_5 uses the $2'' \times 240''$ slit at one location to take data in the following lines: He I 584 Å, O V 639 Å, WW 558.30 Å (wavelength band), and Mg IX 368 Å.

Table 6.1: Summary of JOP 83 TRACE observations analysed for 7th–9th April.

	Date	Time	Exp (s)	Nx × Ny	X cen (arcsec)	Y cen (arcsec)
#1	7 th April 2000	11:08–11:40	23.2	768	474	440
#2	–	11:51–12:12	6.9	512	–	–
	–	12:19–12:29	23.2	768	–	–
#3	–	12:42–13:01	6.9	512	–	–
	–	13:08–13:17	23.2	768	–	–
#4	–	13:28–13:49	6.9	512	492	423
#5,6	–	14:17–14:38	6.9	512	–	–
#7	–	14:47–15:44	27.6	768	–	–
	8 th April 2000	10:27–10:48	6.9	512	583	418
#8	–	11:24–11:55	27.6	768	–	–
#9	–	12:05–12:27	6.9	512	–	–
#10	–	12:33–12:46	23.2	768	–	–
#11	–	12:57–13:18	6.9	512	–	–
	–	13:28–13:39	23.2	768	–	–
#12	–	13:46–14:11	6.9	512	–	–
#13	–	14:31–14:53	6.9	512	–	–
	9 th April 2000	12:47–12:58	23.2	768	758	424
#14	–	13:07–13:22	5.8	512	–	–
#14	–	13:22–13:30	6.9	512	–	–
#15	–	13:54–14:19	6.9	512	755	398
#16	–	14:46–15:08	6.9	512	–	–
#17,18	–	15:21–16:07	23.2	768	–	–

indicates observations coincident with CDS.

6.3 Calibration of the data

The CDS data must be cleaned and calibrated to correct a number of effects before the data can be analysed. The data is cleaned for cosmic ray spikes and corrected for detector bias and flat field. The CDS pointing is updated from an OPS calibration database. The dispersion direction in NIS data is not parallel to the CCD pixel rows; this “rotation” effect is due to a misalignment between the grating and detector. Also, the spectral lines are not perpendicular to the dispersion direction; this “tilt” effect is due to a misalignment between the grating and slit.

CHAPTER 6. PROPAGATING LOOP OSCILLATIONS WITH CDS AND TRACE

Table 6.2: Summary of JOP 83 CDS observations analysed for 7th–9th April.

	Date	Study N ^o	Study	Time	Duration	X cen (arcsec)	Y cen (arcsec)
	7 th April 2000	s19254r00	LARGEBP2	09:20	1:47	555	356
#1	–	s19255r00	LOOPS_5	11:24	29.36	533	386
#2	–	s19255r01	LOOPS_5	11:54	29.41	–	–
	–	s19255r02	LOOPS_5	12:24	29.33	–	–
#3	–	s19255r03	LOOPS_5	12:53	29.36	–	–
#4	–	s19256r00	LOOPS_5	13:29	29.36	322	532
#5	–	s19256r01	LOOPS_5	13:59	29.38	–	–
#6	–	s19256r02	LOOPS_5	14:28	29.40	–	–
#7	–	s19256r03	LOOPS_5	14:58	29.40	–	–
	8 th April 2000	s19277r00	LARGEBP2	08:47	1:47	706	408
	–	s19278r00	LOOPS_5	10:48	31.48	697	397
#8	–	s19278r01	LOOPS_5	11:19	31.51	–	–
#9	–	s19278r02	LOOPS_5	11:51	31.52	–	–
#10	–	s19278r03	LOOPS_5	12:23	31.51	–	–
#11	–	s19279r00	LOOPS_5	13:05	31.50	521	533
#12	–	s19279r01	LOOPS_5	13:37	31.51	–	–
#13	–	s19279r02	LOOPS_5	14:09	31.51	–	–
	–	s19280r00	LARGEBP2	14:57	1:47	525	535
	9 th April 2000	s19290r00	LARGEBP2	10:57	1:47	826	389
#14	–	s19291r00	LOOPS_5	12:58	31.50	804	386
	–	s19291r01	LOOPS_5	13:30	31.53	–	–
#15	–	s19291r02	LOOPS_5	14:02	31.52	–	–
#16	–	s19291r03	LOOPS_5	14:34	31.52	–	–
#17	–	s19291r04	LOOPS_5	15:06	31.53	–	–
#18	–	s19291r05	LOOPS_5	15:38	31.52	–	–

indicates observations coincident with TRACE.

The rotation and tilt corrections are applied to the spectra and the mis-alignment between NIS-1 and NIS-2 is corrected. These corrections are applied using CDS_NEW_SPIKE, VDS_CALIB, UPD_CDS_POINT, NIS_ROTATE and relevant keywords. Since the loss of SOHO, NIS-1 has shown a decrease in responsivity. We use a reasonable estimate for the correction factor of 1.8 for NIS-1 (Thompson 2003).

Standard corrections and preparations are applied to the TRACE data using TRACE_PREP and appropriate keywords. The pointings of the various bandpasses used by TRACE are offset from the white light values used in the TRACE index structure (Handy et al. 1999). This offset is due to changes of the best focus position, and tilts between the different channel filters. The offset is of the order 2.15'' E 3.60'' N for the EUV channels and is corrected. The data

is cleaned for cosmic ray spikes and streaks, the ADC offset and the background diffraction pattern are removed.

6.4 Pointing discrepancy and correlation of the data

When the LARGEBP2 images produced by CDS in a coronal temperature line such as Mg IX are compared to the TRACE images it is evident that within this dataset there is a difference in the pointing between the two instruments. This is apparent in the different location of features visible in both images, even when the pointings are corrected for solar rotation. Since we are trying to observe the sun at the same location with the two different instruments simultaneously, it is important that we find a satisfactory method of relating the pointing.

To achieve this, a 2-D cross correlation technique is used. The area in the TRACE image that corresponds to the position of the LARGEBP2 image field of view is selected, and normalised to have the same mean intensity as the LARGEBP2 image. A 2-D cross correlation method is then applied, to determine the offset between the two images. In the data from the 7th listed as #2 in Tables 6.1 and 6.2, the first TRACE image is offset 10.2'' E and 3.6'' N relative to the CDS LARGEBP2 image, after taking account of solar rotation. The pointings in the TRACE index structure are then corrected by these offset values, and the above process is repeated. A data cube is then extracted from the TRACE data that has the corrected coincident pointing with CDS. Figure 6.1 shows the CDS LARGEBP2 and TRACE 171 Å data for the 7th after coalignment. These are plotted with bilinear interpolation applied to increase image clarity.

6.5 Data analysis

Tables 6.1 and 6.2 list the whole of the TRACE and CDS data included in this analysis. Approximately 8 hours of TRACE data, and 17 hours of CDS data are analysed over the three days. The first column of numbers in Tables 6.1 & 6.2 indicates the respective co-temporal TRACE and CDS observing sequences.

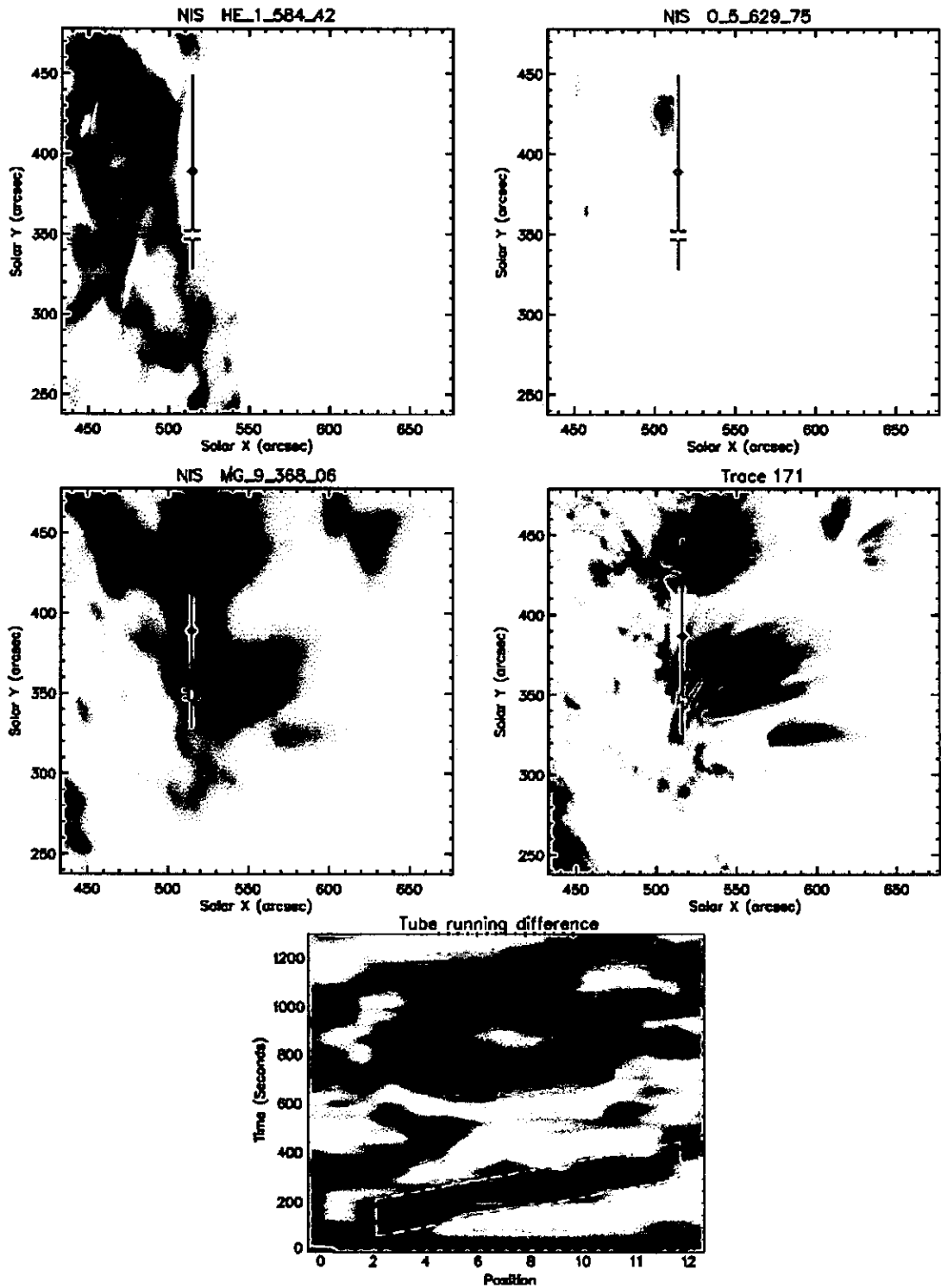


Figure 6.1: Context images for NIS (He I, O V and Mg IX) and TRACE 171 Å. Each indicates the position of the CDS slit (black line), and the pixels that form the CDS time series (white line). The TRACE 171 context image shows the CDS slit, tube (black arcs) defined for TRACE analysis, and the cross section used to form the TRACE time series at position 4 along the tube (white band). The bottom image shows the running difference image formed from the tube in the TRACE context image, the dashed box outlines a dark band indicating propagation along the tube.

6.5.1 CDS data analysis

To form a time series from the LOOPS_5 data, 3 pixels ($\approx 5''$) are summed along the CDS slit to increase the signal to noise ratio. A running summed time series is formed, for each pixel along the CDS slit, for each of the LOOPS_5 studies analysed. The wavelet transform is then calculated for each of the time series. The CDS wavelet power spectra are compared to the power spectra from the TRACE analysis, to investigate any coincident oscillations. The CDS images in Fig. 6.1 indicate the location of the time series from data on the 7th. The selected pixels are coloured white and are bounded by two horizontal lines crossing the slit. These pixels overlies the position of the tube cross section used to form the TRACE time series.

6.5.2 TRACE data analysis

The position of the LOOPS_5 slit can be seen in the context of the CDS LARGE BP2 He I 584 Å, O V 629 Å, Mg IX 368 Å and TRACE 171 Å observations (Fig. 6.1). Considering the TRACE data, a tube is defined that overlies a coronal loop structure and the position of the CDS slit. Using the same code as De Moortel et al. (2002c) (courtesy of J. Ireland), the length of the tube sides are normalised and cross sections are formed along the tube of 2'' width. The pixels are summed across a selected cross section, to form a time series from the TRACE data. The TRACE image in Fig. 6.1 shows the defined tube as two black curves. The white band connecting these indicates the location of the selected tube cross section. This cross section is located close to the bottom of a coronal loop structure.

To investigate any propagating intensity oscillations we use a running difference method as in De Moortel et al. (2002c). A running difference image was formed by using the integrated intensity profile of the tube along its length and subtracting the profile of the tube 90 s earlier. Thus any propagating oscillation should appear as diagonal light and dark bands in the difference image.

6.5.3 Wavelet analysis

The period of any oscillations within the TRACE and CDS time series are investigated using a wavelet analysis method. For a more detailed description of the wavelet analysis method see

CHAPTER 6. PROPAGATING LOOP OSCILLATIONS WITH CDS AND TRACE

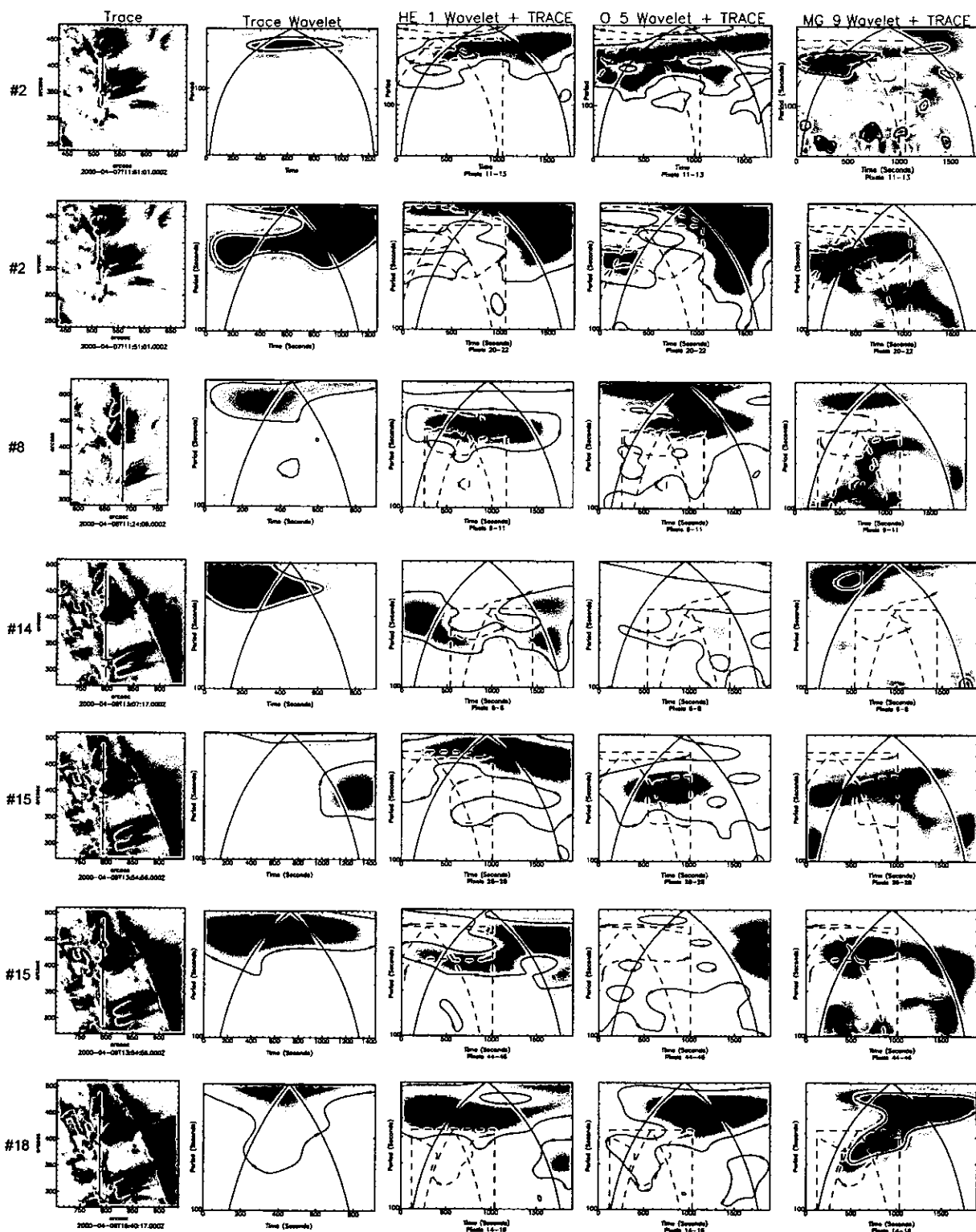


Figure 6.2: Results for possible coincident TRACE and CDS oscillations. Row # indicates the respective data from Tables 6.1 & 6.2. *First column:* TRACE context image, *second column:* TRACE wavelet power spectrum, *third column:* He I power spectrum + TRACE power spectrum contours, *fourth column:* O V power spectrum + TRACE contours, *fifth column:* Mg IX power spectrum + TRACE contours.

Chapter 3. The wavelet function and time series are finite, so the wavelet power spectrum suffers edge effects that are proportional to wavelet scale (wavelet scale is converted to equivalent Fourier period using a small correction factor). The cone shaped line in Fig. 6.3a for example is the cone of influence (COI) which marks the limit of these edge effects. The area beneath the COI and the x -axis can be considered free from these effects. The shaded regions in this figure indicate wavelet power of period p occurring at time t . To place an error estimate on the analysis, the wavelet power spectrum is compared to what would be expected from the appropriate noise distribution for each instrument. TRACE is assumed to have Poisson distributed noise; sigma is then equal to the square root of the mean intensity $\sigma = \sqrt{I}$. CDS is assumed to have Poisson distributed noise, plus an instrumental contribution, as described in Thompson (2000); then $\sigma = \sqrt{2I + R^2n}$ where I is the number of photon-events, R is the readout noise per pixel and n is the number of pixels summed over. A conservative value of $R=1$ photon-event/pixel is used here. A significance level is chosen representing the probability that the power can be considered as being due to a real oscillation. A significance level of 99% is used here, and any significant wavelet power is enclosed by a contour of significance.

6.6 Results

It is found that the observations are limited by a number of factors. Primarily, to produce useful data, the narrow 2'' CDS slit must be pointed accurately at the base of the coronal loop structures. As described by De Moortel et al. (2002c) the observed loop propagations are damped rapidly along the base of the loop. The CDS slit must be located close to the loop base to ensure that the oscillations have a sufficient amplitude to enable detection above the noise level. Also, with respect to the period of the oscillation, the overlap of the CDS and TRACE observation times must have a sufficient duration to allow a successful observation within the wavelet analysis cone of influence. Figure 6.2 shows the results for a number of data that indicate the possibility of coincident oscillations within CDS and TRACE. Each row # represents the respective data from Tables 6.1 & 6.2. The first column shows the TRACE context image; the white pixels indicate the location where the respective time series are formed. The second column shows the wavelet power spectrum of the TRACE time series. The third, fourth and fifth

columns show the power spectrum for the He I, O V and Mg IX time series respectively, overlaid with the contours of the TRACE power spectrum. All these data display an indication of a coincident oscillation in TRACE, and at least one of the CDS lines; with the exception of #2, these data are all effected too greatly by the above limiting factors.

The results presented in this section show the best example of a propagating TRACE oscillation observed with CDS over the three days of observations. The data observes NOAA active region 8940 on the 7th April 2000, and is listed as #2 in Tables 6.1 & 6.2 and Fig. 6.2. The TRACE observations analysed are $512'' \times 512''$ images taken in the 171 Å passband at $1''$ resolution and run from 11:51–12:12 UT at a cadence of 9 s. The CDS observations run from 11:54–12:24 UT at a cadence of 15 s.

Fig. 6.1 shows the LARGE BP2 context image for the 7th in the Mg IX 368 Å line formed at a temperature of $\log T_e = 6.01$, Fig. 6.1 also shows the TRACE context image from the bandpass dominated by Fe IX 171 Å formed at $\log T_e = 5.99$. We can see the same coronal loop and moss structures with both instruments. The TRACE image shows clearly the context of the observations revealing the fine scale structure visible at $1'' \times 1''$ resolution compared to the $2.03'' \times 1.68''$ resolution of CDS. As described in Sect. 6.5.2, the location from where the time series are extracted is indicated. We can see that this section is located at the base of a complex coronal loop configuration which is surrounded by moss.

The cross section of the tube chosen is approximately perpendicular to the filamentary structure of the loop, and provides a good intersection with the CDS slit. This cross section is located at position 4 along the defined tube, and can be located in the running difference image (Fig. 6.1). The running difference image suggests that there are intensity propagations along the tube. This can be seen as a series of light and dark bands with a positive gradient. These bands appear to start before position 4 along the tube suggesting that the time series is located very close to the footpoint of the coronal loop, or at least very close to the origin where the oscillations are generated. Each position unit along the tube has a width of $2''$ (≈ 1440 km). The band outlined by a dashed box in Fig. 6.1 was chosen as it represents the clearest example of a propagation. The gradient of this band gives a minimum estimate (due to projection effects) of the propagation speed. As an estimate of the uncertainty of the speed the

gradient of the diagonals of the dashed box give maximum and minimum speeds in the range 50–195 km s⁻¹. This overlaps with the range of speeds reported in De Moortel et al. (2002c).

Figure 6.3a shows the wavelet power spectrum for the TRACE time series. The number of cycles within the COI is limited by the period of interest and the length of the time series. Due to edge effects we can only comment reliably on the period within the COI. The power spectrum shows a clear band of wavelet power above the confidence level, within the COI and centred around 300 s. The COI limits us to reliably observing ≈ 1.3 cycles. This could be increased by extending the duration of future similar observations.

Figures 6.3b,c,d show the wavelet power spectra for the CDS time series, and have the same start time. Fig. 6.3a shows the TRACE power spectrum which begins 209 s before the CDS time series. Figure 6.3b shows the wavelet power spectrum for the CDS He I time series. The dashed lines plotted over this are taken from the TRACE wavelet power spectrum and indicate: the boundaries of the spectrum, the COI and the significance contour of the ≈ 300 s period. He I has significant power at periods between ≈ 250 –450 s and overlaps with the period found in TRACE. The centre of this band of power in He I appears to have a slightly longer period than in TRACE 171 Å. Figure 6.3c shows the wavelet power spectrum in O V. There is a band of significant power present at periods between ≈ 200 –500 s. The region of maximum wavelet power forms a band with ≈ 3 cycles present within the COI. The significant power in TRACE overlaps the power within the O V 99% confidence level very well. Figure 6.3c shows the wavelet power spectrum produced by Mg IX. Significant power is observed between ≈ 200 –350 s, but with only ≈ 1 cycle present within the CDS COI. Again the power overlaps well with that found in TRACE with the centre of this power appearing to have a slightly lower period in Mg IX than in TRACE 171 Å. The WW wavelength band was also analysed, and power was found at a similar period. However, this power was only found at a confidence level of 95%.

The amplitude of the oscillations in He I, O V and Mg IX can be estimated using the deviation of the time series as a percentage of its mean intensity. Fig. 6.4 shows the time series for each line. The amplitude is determined by dividing the time series by its mean value and subtracting one $\frac{I(t)}{\bar{I}} - 1$. This gives the percentage deviation of the time series from the mean value of intensity. We find amplitudes of 9.8 ± 3.1 % for He I, 12.4 ± 2.1 % for O V and 8.6

CHAPTER 6. PROPAGATING LOOP OSCILLATIONS WITH CDS AND TRACE

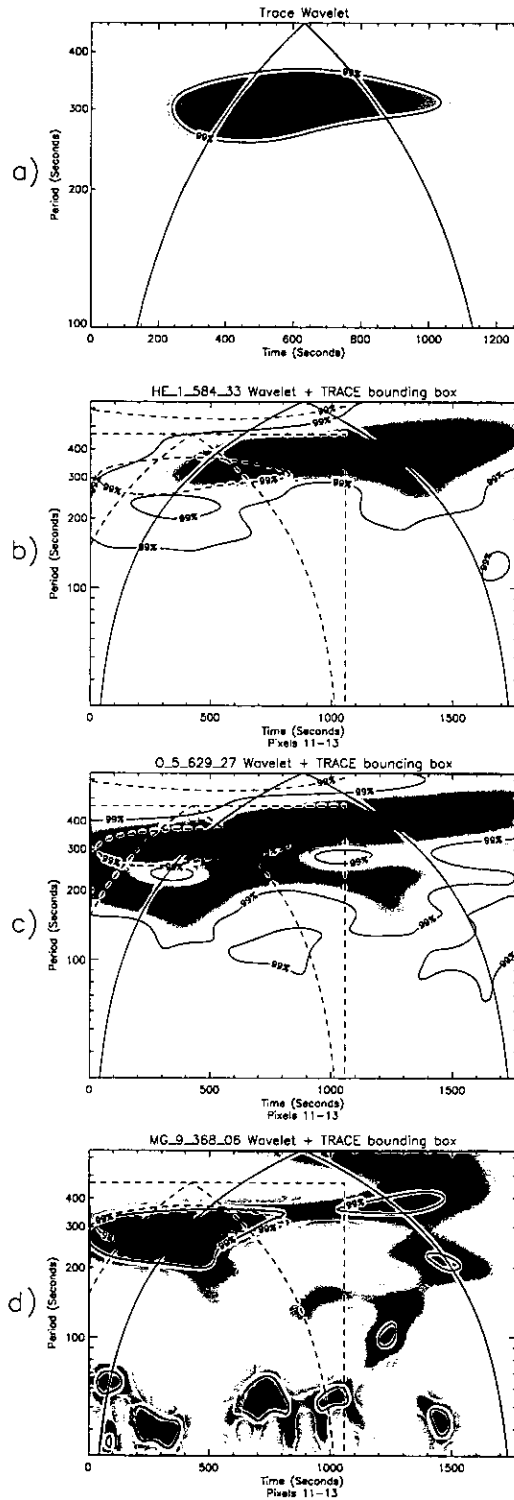


Figure 6.3: Wavelet power spectra: a) for TRACE time series produced by the cross section indicated in Fig. 6.1b; b) for CDS He I time series from the pixels indicated in Fig. 6.1a with the position of the TRACE power spectrum (dashed lines) positioned relative to the timing of the CDS observations; c) as b) but indicating power for the CDS O V time series; d) as above but indicating power for the CDS Mg IX time series.

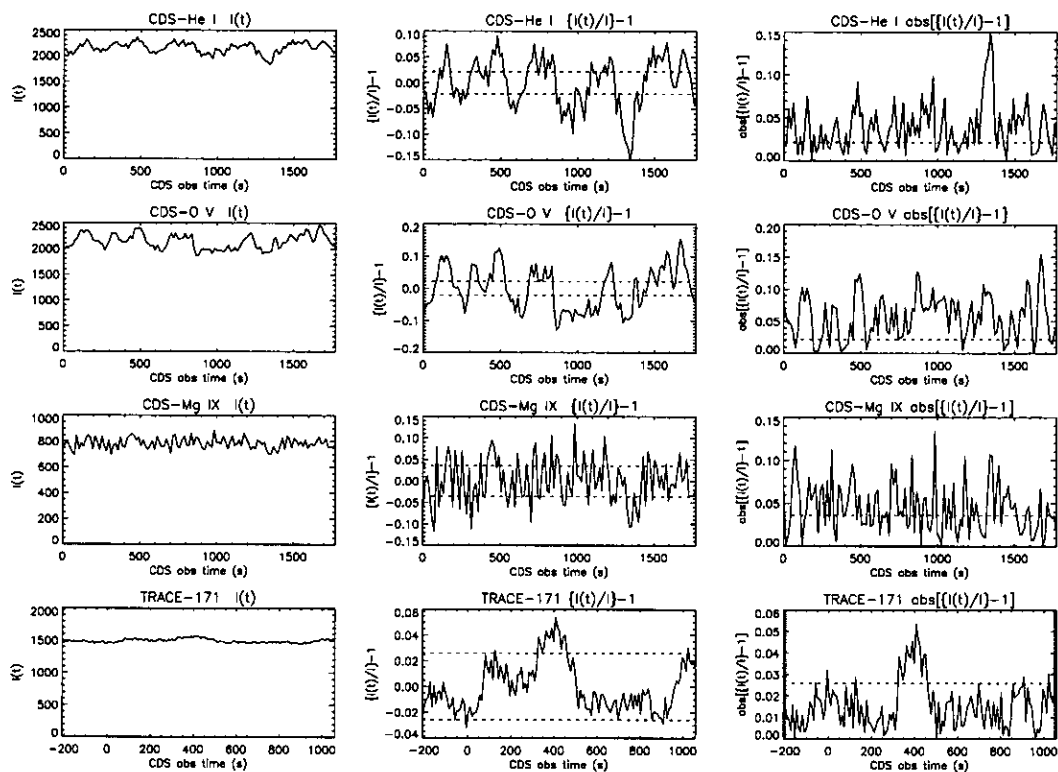


Figure 6.4: Time series for He I, O V, Mg IX and TRACE 171 along each respective row. *First column:* Time series for each line. *Second column:* Time series divided by its mean value minus 1. *Third column:* Absolute value of second column. Dotted lines indicate appropriate noise level i.e. Any data below dotted line in the third column is expected to be due to noise.

$\pm 1.2\%$ for Mg IX. Brynildsen et al. (2002) present four observations above sunspot regions and find similar amplitudes ranging from 2.5–6% for He I, 7–16% for O V and 3–5% for Mg IX.

6.7 Conclusions

Evidence of a propagating longitudinal intensity oscillation in a TRACE 171 Å coronal loop structure is observed. A running difference method gives a minimum estimate of the propagation speed of 50–195 km s⁻¹. A wavelet analysis shows this to have a period of ≈ 300 seconds. The TRACE bandpass is dominated by emission from Fe IX 171 Å formed at $\log T_e = 5.99$. Wavelet analysis of co-spatial, co-temporal CDS-NIS data reveals a coincident period present in He I 584 Å ($\log T_e = 4.54$), O V 629 Å ($\log T_e = 5.4$) and Mg IX 368 Å ($\log T_e = 6.0$).

CHAPTER 6. PROPAGATING LOOP OSCILLATIONS WITH CDS AND TRACE

The three CDS lines show a coincident period with the coronal TRACE data. O V formed at transition region temperatures appears to be better correlated with the TRACE 171 Å result than the He I (chromospheric) and Mg IX (coronal) lines.

The estimated amplitudes of the oscillations in He I, O V and Mg IX are of the same order as those reported by Brynildsen et al. (2002). It is also found that O V has the largest amplitude in agreement with their observation that the amplitude peaks in O V. However, also in sunspot regions, O'Shea et al. (2002) found that the amplitude peaked in O III in the majority of cases.

As in De Moortel et al. (2002c) the propagating intensity oscillation observed in TRACE 171 Å is consistent with the interpretation of a slow magneto-acoustic wave. It should also be noted that Cooper et al. (2003) state that line of sight effects may allow kink modes to be observed as propagating disturbances in emission intensity. The results from the CDS data imply that this oscillation is also present at chromospheric, transition region and coronal temperatures. The observed period also coincides with the photospheric 5-min period. *These combined factors suggest that there is a coupling and propagation of slow magneto-acoustic/kink waves at photospheric, chromospheric, transition region and coronal temperatures at the same location.*

It has been questioned whether it is valid to assume that lines such as Fe IX and Mg IX are formed at coronal temperatures (Doyle & Madjarska 2003). They find that when the sunspot plume emission measure distribution is used, the contribution function for lines formed just below 1×10^6 K are shifted to lower temperatures. They also state that temperature gradients and particle concentration can lead to a non-Maxwellian electron temperature distribution. Fe IX 171 Å and Mg IX 368 Å can then be formed at temperatures down to 5×10^5 K. It is then questioned whether oscillations above sunspots can be observed at coronal temperatures with these lines. Since the coronal loops analysed here are not associated with a sunspot region the TRACE 171 Å and Mg IX emission can be considered to originate at coronal temperatures.

Considering the results from the TRACE analysis, Figure 6.1 shows the tube we have defined for the analysis, bounding the coronal loop structure that crosses the CDS slit. We see that the CDS slit also crosses loop structures towards the top of the slit, emerging from active region AR 8939. These loops do show some propagation in their TRACE running difference

CHAPTER 6. PROPAGATING LOOP OSCILLATIONS WITH CDS AND TRACE

images. However, they are quickly damped and do not show any oscillation above the wavelet analysis confidence level at the position of the CDS slit. This indicates the need for accurate pointing to position the CDS slit close to the loop footpoints.

Three days of JOP 83 data were analysed on the 7th, 8th and 9th of April 2000 during this work. The CDS and TRACE data were analysed at 70 positions overlying the CDS slit over this period. The example presented here represents the best example of a coincident period within CDS and TRACE. The paucity of examples is likely due to undesirable pointing of CDS with respect to the coronal loop structures, combined with mistimed observations.

As described above, the TRACE oscillations seen in coronal loops are quickly damped, and so positioning of the CDS slit close to the loop footpoint is critical in observing the oscillations in both CDS and TRACE. The amount of overlap between the COI of the CDS and TRACE time series is limited by the duration and relative timing of the CDS and TRACE observations. The timing of the observations is then also a vital factor in the ability to observe coincident oscillations in CDS and TRACE.

6.7.1 Further progress

The natural progression of the results presented here is the need to image the TRACE propagations at chromospheric, transition region and coronal temperatures using CDS over large spatial scales. This is not possible with previous observations using CDS which produce 1-D spatial data. Thus, any propagation can only be suggested, not observed. Marsh and Walsh defined the LOOP2D rasters in an attempt to observe these coronal loop structures using CDS as an imaging spectrometer (see Chapter 8 - "Conclusions and further work"). The LOOP2D_V raster produces 10"x120" images at 52s cadence in He I, O V and Mg IX to try and observe any propagation. However, these observations are severely limited by their restricted spatial coverage and low cadence relative to the periods being investigated.

CDS has the potential to produce ideal observations of this nature using the wide slit. This can produce 90"x240" intensity images in He I, O V and Mg IX at ≈ 30 s cadence. These observations would allow coronal loop regions to be imaged over a large area. This gives the possibility that the propagating oscillations, imaged co-temporally with TRACE, could

CHAPTER 6. PROPAGATING LOOP OSCILLATIONS WITH CDS AND TRACE

be observed and their properties determined at chromospheric, transition region and coronal temperatures.

Thus, as a result of the work outlined in this chapter, a coordinated observing campaign using the CDS wide slit and TRACE was designed and carried out. The following chapter details the extension of this work, and the new results obtained as a result of that campaign.

Chapter 7

Joint Observations of Active Region Dynamics with the CDS Wide Slit, TRACE and MDI

7.1 Introduction

This chapter presents results from a coordinated observing campaign using CDS and TRACE, with supporting MDI observations. We observe a sunspot active region and its emerging coronal loops. The observations show 3-min oscillations above the sunspot umbra at chromospheric and transition region temperatures, and simultaneous periodic 3-min propagations along the TRACE coronal loops. A primary goal of this campaign was to overcome the limitations found in the JOP 83 analysis (Chapter 6) when searching for the chromospheric/transition region signatures of the loop propagations observed with TRACE.

The loop variability campaign (SOHO campaign #7024), designed by M. Marsh, was run during 2–15th March 2004. The campaign was designed to investigate the structure and dynamics in and around the TRACE coronal loop structures at chromospheric, transition region and coronal temperatures. To achieve this the campaign consists of observations from the TRACE and SOHO spacecraft utilising a number of instruments. The range of instruments employed allows large spatial, temporal and temperature coverage of the observed regions.

Table 7.1: Summary of loop variability campaign observations on 13th March 2004.

Program	CDS		TRACE		MDI	
	Study	Time (UT)	Sequence	Time (UT)	Sequence	Time (UT)
EJECT_V3	s29738r00	06:30–06:47				
UCLAN_MV	s29739r00–04	07:08–07:52	171 @ 30s	00:00–14:00	FD I, M, V	Daily
EJECT_V3	s29740r00–02	07:52–08:40	171/1600 @ 30s	07:00–08:00	HR I, M, V	06:00–08:00
LOOP2D_5	s29741r00–199	08:40–11:44				
EJECT_V3	s29742r00–01	11:44–12:16				

The campaign consists of CDS, MDI, EIT and TRACE observations. The typical wavelengths employed and exposure cadence achieved are summarised in Table B.1 in Appendix B. The table lists the date of observation and the target NOAA active region number. The different observing sequences and observation times are also listed for the CDS, TRACE and MDI observations. This campaign forms a large dataset with great potential for investigating the structure and dynamics of the outer solar atmosphere. This thesis chapter presents only a partial analysis of the data, as time has allowed for, from the observations gathered on the 13th March 2004. These observations are summarised in Table 7.1. The analysis here consists of UCLAN_MV, EJECT_V3, TRACE 171 Å and MDI data.

7.2 CDS Studies

The CDS observations within the campaign use three main NIS rasters, UCLAN_MV, LOOP2D_5 and EJECT_V3 as summarised in Table 7.2 and described below.

7.2.1 UCLAN_MV

UCLAN_MV was designed by M. Marsh and uses the $90'' \times 240''$ CDS wide slit to produce direct images in He I, O V and Mg IX. This allows a large spatial area to be observed at high cadence over chromospheric, transition region and coronal temperatures. A relatively high cadence of 26s (with an exposure of 20s) is employed to allow dynamic events to be observed over short timescales, and maximise the signal to noise ratio in the weaker Mg IX line. This raster was designed specifically to provide large-scale, co-spatial, and co-temporal *imaging* of the coronal loops observed with TRACE, at chromospheric and transition region temperatures

CHAPTER 7. CDS WIDE SLIT & TRACE ACTIVE REGION DYNAMICS

using CDS. The main purpose of the UCLAN_MV raster was to overcome the limitations of narrow slit observations described in Chapter 6, in the investigation of active region loop propagations. The spatially resolved nature of the observations over a large area ensures that the target TRACE loops are observed with CDS. This then allows the effect of the TRACE propagations to be observed simultaneously with the wider temperature range available using CDS.

7.2.2 LOOP2D_5

LOOP2D_5 was designed by M. Marsh to produce spatially resolved spectral data at as high cadence as possible whilst retaining reasonable signal to noise. The raster uses 5s exposures of the $4'' \times 240''$ slit at 5 positions to produce $20'' \times 120''$ rastered images in He I, O V and Mg IX, with a total cadence of 55s. This has the advantage in producing spatially resolved data over a moderate area as compared to narrow slit sit-and-stare studies. The cadence and exposure time are limited by instrument overheads due to movement of the spectrometer slit. This raster was designed to be pointed at the base of loops observed with TRACE. The spectroscopic data allows the effects on the line profiles to be investigated due to Doppler shift and non-thermal broadening. It is hoped that this raster may allow the intensity, velocity and possibly the line width signatures of the propagations to be observed in He I, O V, and Mg IX within intensely bright regions.

7.2.3 EJECT_V3

EJECT_V3 v18 was used to provide spectroscopic context images over a large field of view. EJECT_V3 is a standard NIS raster normally used in the long term CME onset monitoring program. The raster uses 60 positions of the $4'' \times 240''$ slit to form $240'' \times 240''$ rastered images in He I, O V, Mg IX, Fe XVI and two Si X lines, with a total duration of 16 minutes. The EJECT_V3 raster allows the UCLAN_MV and LOOP2D_5 rasters to be placed in context within the structure of the surrounding region, across a large range of temperatures. EJECT_V3 allows the emission, velocity and line width structure to be observed over the target active region.

Table 7.2: Summary of loop variability CDS rasters.

	UCLAN_MV	LOOP2D_5	EJECT_V3
FOV	90'' \times 240''	20'' \times 120	240'' \times 240
Lines	He I, O V, Mg IX	He I, O V, Mg IX	He I, O V, Mg IX, Si X, Si X, Fe XVI
Cadence	26s	55s	16m10s
Exposure	20s	5s	10s
Method	Wide slit image	Rastered image	Rastered image

7.2.4 Active Regions with the CDS Wide Slit

The wide slit rasters form part of a carefully designed program of observations to investigate active region dynamic phenomena. Ordinarily, observations of active regions with the CDS wide slit are not permitted. The NIS detector system (See Chapter 2) uses a microchannel-plate (MCP) to produce and amplify EUV photoelectrons which pass through a phosphor converter and are detected by a CCD. The NIS optics disperse the spectral lines to a fixed position on the MCP. Exposure of the MCP to EUV reduces its responsivity in relation to the number of photons detected. This ‘burn-in’ effect is greatest in the most intense spectral lines. The wide slit is used to calibrate the burn-in effect of the narrow 2'' or 4'' slits on the MCP. A more detailed description of the burn-in effect, and the restrictions on observing active regions with the wide slit is given in Chapter 2 Sect. 2.2.1. A proposal stating the scientific case for using the wide slit on quiescent active regions was submitted to the CDS instrument team in May 2003. Following a study by W.T. Thompson of the burn-in effects due to wide slit exposure on an active region, the proposal was accepted in October 2003. The observations were approved for quiescent active regions with a low probability of flaring and limited to five 45 minute runs of the UCLAN_MV raster. One of these runs was performed in November 2003 as a test of the raster; four runs form part of the campaign outlined here.

7.3 CDS data reduction

The CDS data is cleaned and calibrated to correct a number of detector effects before the data can be analysed. The data is corrected for cosmic ray spikes, detector bias and flat

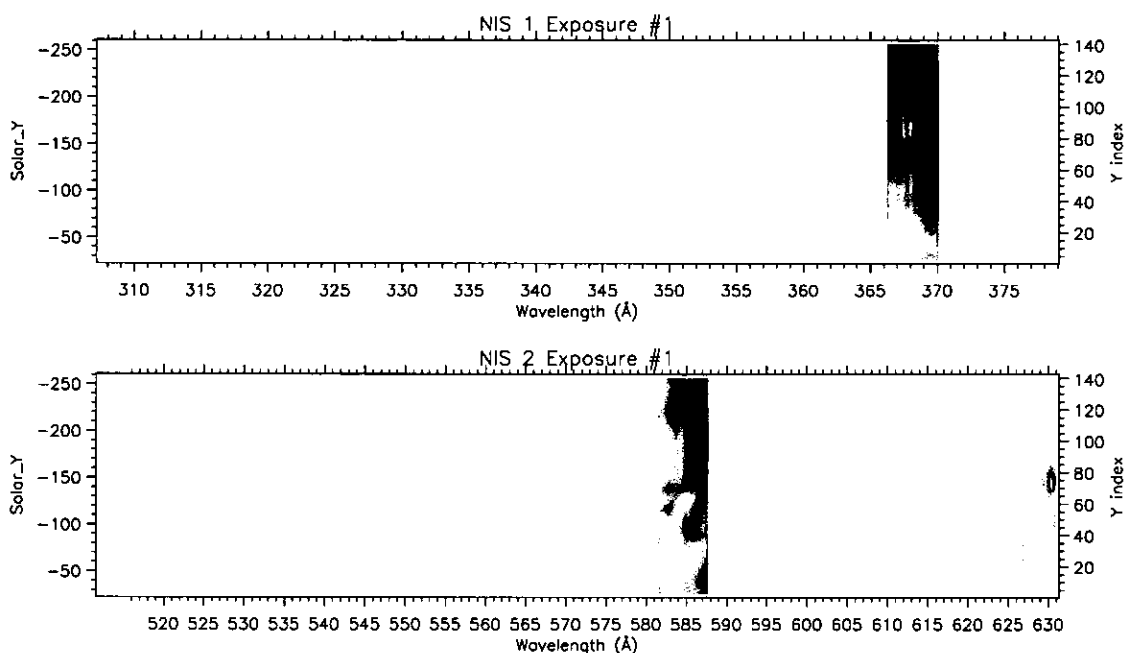


Figure 7.1: Images of the CDS wide slit are dispersed onto the NIS detectors at the corresponding position of each spectral line. The UCLAN_MV data uses the bright He I 584 Å, O V 629 Å and Mg IX 368 Å lines. Note the O V image is dispersed to the edge of NIS 2.

field. The CDS pointing is updated from the OPS calibration database. The standard rotation and tilt corrections are applied to the spectra and the mis-alignment between NIS-1 and NIS-2 is corrected. These corrections are applied using CDS_NEW_SPIKE, VDS_CALIB, UPD_CDS_POINT, NIS_ROTATE and relevant keywords available in the CDS branch of the *SolarSoft* software tree. Since the loss of SOHO, NIS-1 has shown a decrease in responsivity. We use a reasonable estimate for the correction factor of 1.8 for NIS-1 (Thompson 2003).

7.3.1 UCLAN_MV

As mentioned previously, the CDS wide slit produces $90'' \times 240''$ images. The images of the wide slit are dispersed onto the detector at the corresponding position of each spectral line (Fig. 7.1). In principle, images from any NIS line may be included within the raster; we use the He I, O V and Mg IX lines. These lines are used as they are the brightest lines at their respective temperatures, and they are isolated from other bright lines which could contaminate the images. On the detector the images have dimensions of 55 pixels in the x or horizontal direction (normally the spectral dispersion direction), and 143 pixels in the y or vertical direction. The

O V line is located at the edge of the NIS 2 detector, and part of the O V image is dispersed off the detector. The resulting O V images consist of 41 pixels in the x direction; when SOHO has a normal orientation, the right hand edge of the wide slit image is missing.

It is found that when CDS is operated using the wide slit, an incorrect x pixel scale is given in the study header structure. This is calculated incorrectly using an x pixel scale derived from re-pointing the $2''$ slit to form a rastered image using the CDS plate scale and pixel size of $12.5 \mu\text{m}/\text{arcsec}$ and $21 \mu\text{m}$ respectively. Since the NIS detector has square pixels, this error is corrected by setting the x scale equal to the y scale.

7.3.2 EJECT_V3

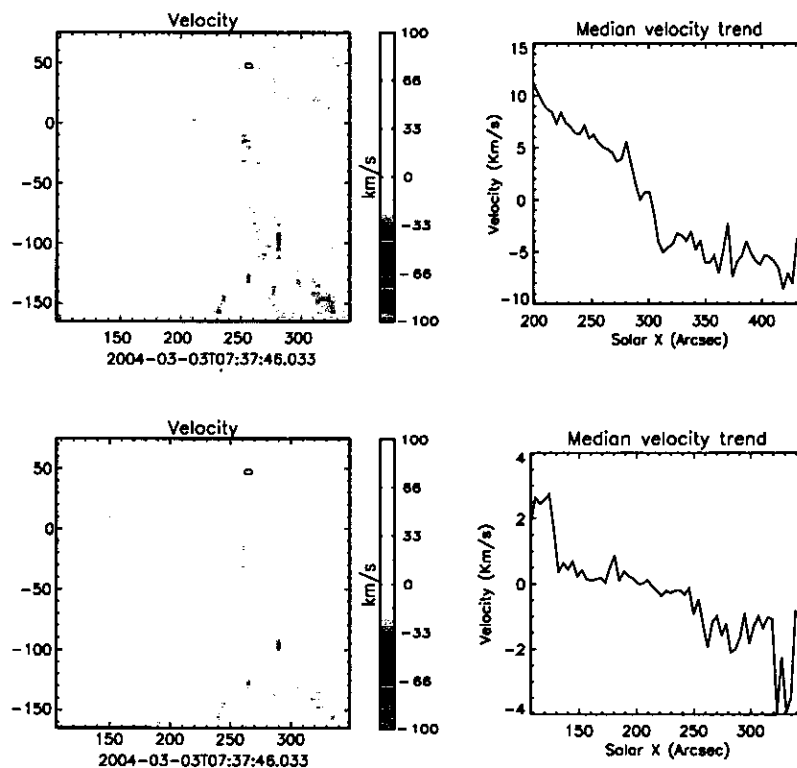


Figure 7.2: Top: Doppler velocity map of EJECT_V3 O V data from 3rd March, displaying the East-West trend in the line position and median trend in the x direction. Bottom: Doppler map with trend subtracted, and re-calculated trend.

The spectral data of EJECT_V3 is fitted with broadened Gaussian profiles (see Thompson 1999), found in post-recovery data, using the *SolarSoft* Component Fitting System (CFIT) program (Haugan 1997). The data for the He I, O V, Mg IX, Fe XVI and two Si X lines are

fitted by defining fit structures for each of the lines. The efficiency of using the maximum and median intensity pixels to define the fit structures is tested on a number of EJECT_V3 data. It is found that using the maximum intensity pixel to define the fit structures reduces the number of badly fitted pixels. The fit structures are defined using the s29740r00 study with the brightest pixel in each respective line.

It is found that, in certain regions, the Mg IX line shows a significant blend with Mg VII. The Mg IX data is therefore fitted with two Gaussian profiles. The number of badly fitted pixels is minimised by using appropriate limits on the component positions and widths.

The routine NIS_ROTATE corrects for the instrumental rotation and tilt effects. However, it is found that the spectral tilt can vary over time and is affected by temperature, pointing and mirror position (Bewsher 2002). The EJECT_V3 images of the fitted line position in He I and O V show an instrumental trend in the x direction, Fig. 7.2 shows a typical example. It is likely this East-West trend is due to the dependence of the tilt on the slit position. This effect is corrected by subtracting the trend from the maps of Doppler velocity. This is done by averaging the pixels in the y direction to find the median trend in the x direction. The limits of the velocity trend are of the order $\pm 10 \text{ km s}^{-1}$; the median is formed from pixels having velocities between $\pm 15 \text{ km s}^{-1}$ to exclude real physical velocity structure. The median trend is then subtracted from the Doppler maps to significantly reduce the velocity trend (Fig. 7.2). Figure 7.2 shows the EJECT_V3 data after the trend correction and the re-calculated median velocity trend. The velocity trend appears to be a quadratic function across the raster in the x direction. In future work, it may be desirable to subtract these fitted functions to correct the data. This will also assist in investigating the nature and variability of these spectral tilt effects.

Doppler velocity maps are formed from the fitted line position in each raster. A completely accurate wavelength calibration, with respect to time, is not available for CDS; this means it is not possible to measure accurate absolute velocities. However, the velocity can be measured relative to the distribution of velocities within the raster. To calculate Doppler velocity maps, the Doppler shift of the fitted line profiles are measured relative to the median line position within the raster. It is assumed that this median line position can be approximated to the rest wavelength of the line. Doppler velocity maps are then calculated indicating the relative

velocity of plasma within the raster.

7.4 TRACE Sequences

The TRACE contribution to the campaign was designed to provide high cadence observations over a large area, using primarily the 171 Å filter. The TRACE observations allow the quiescent loop structures emerging from active regions and the surrounding structure to be observed. Thus, this allows dynamic events within the corona such as loop propagations, plasma flows, eruptive activity and restructuring of the large scale magnetic field to be investigated in detail. The 171 Å data has either a pixel size of 0.5'' and field of view of 512''×512'', or uses 2×2 binning to give a pixel size of 1'' again with a 512''×512'' field of view. All the TRACE observations have a cadence of ≈30s. In addition to the continuous 171 Å observations, a number of sequences are defined which alternate 171 with another filter quadrant. These sequences are limited to a one hour duration as the TRACE onboard software restricts the number of quadrant shutter failures before the observing sequence is terminated.

The sequences alternate the 171 quadrant with another selected quadrant still at ≈30s cadence. The alternating filters defined are 171/WL, 171/1600 and 171/1550. The alternating white light sequence allows the structure and dynamics in the photosphere and corona to be related. The alternating 171/1600 and 171/1550 sequences allow the dynamic structure of the lower chromosphere to be related to that of the corona. These dual temperature, high resolution observations, combined with the observations by the other instruments allow structure and events to be observed over large spatial and temperature scales. This provides a very useful and unique dataset, particularly for the investigation of the TRACE loop propagations at multiple temperatures. The nature of this large scale imaging data is also particularly important in interpreting the more spatially confined CDS observations.

7.4.1 TRACE data reduction

Standard corrections and calibrations are applied to the TRACE data using TRACE.PREP and appropriate keywords. The pointings of the various bandpasses used by TRACE are offset from the white light values used in the TRACE index structure (Handy et al. 1999). This offset

is of the order $2.1''$ W $4.35''$ S for the EUV channels on the 13^{th} and is corrected. The data is cleaned for cosmic ray spikes and streaks, the ADC offset and the background diffraction pattern are removed.

7.5 MDI Sequences

As part of the MDI Solar Oscillations Investigation (SOI) daily real time images and magnetic program, MDI routinely performs full disk (FD) white light continuum intensity (I), magnetogram observations (M) along with Dopplergrams (V). The FD observations have a $34' \times 34'$ field of view at $4''$ resolution. These allow context observations of the global solar intensity, magnetic field and velocity structure. During the campaign MDI performed a number of high resolution (HR) observations. The MDI HR mode has a $11' \times 11'$ field of view at $1.25''$ resolution. The HR observations acquired during this campaign consist of simultaneous high resolution continuum intensity, magnetogram, and Dopplergram sequences at 1 minute cadence. These sequences allow high spatial and temporal resolution observations of the structure and dynamics in the photosphere. Dynamic photospheric phenomena such as oscillations, flows and convection can be observed along with their driving effect on the higher temperature structures observed with the other instruments. In particular the aim is to observe the photospheric origin of the chromospheric, transition region and coronal phenomena such as the active region loop propagations.

7.5.1 MDI data reduction

The MDI data is calibrated by the MDI Solar Oscillations Investigation team to produce data in physical units (Scherrer et al. 1995). The data consists of level 1.8 calibrated data consisting of: intensitygrams, Dopplergrams and magnetograms.

The calibrated Dopplergrams display the velocity trend due to solar rotation. As we move outwards from the centre of the solar disk, the velocity becomes increasingly blue/red shifted towards the Eastern/Western solar limb respectively. To perform an analysis on the HR Dopplergrams the Doppler trend caused by solar rotation is subtracted. This is done by calculating the mean velocity along the x direction. This mean is taken over all data frames within the

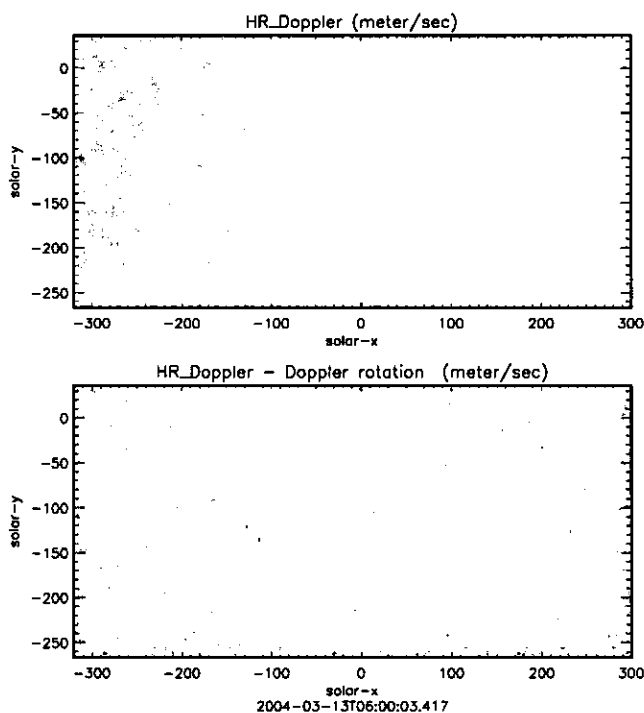


Figure 7.3: Top: MDI high resolution Dopplergram displaying East-West velocity trend due to solar rotation. Bottom: Dopplergram corrected with mean rotation trend subtraction.

time series, averaged over the lower pixels 0–150 in the y direction and subtracted from the data in each frame. This is a reliable method of correcting the rotational Doppler effect on the condition that no long-lived velocity structures are present in the region where the velocity trend is calculated. Crucial to this method's success is the fact that the duration of the observations is much greater than the granulation time scale. The Doppler velocity fluctuations due to granulation cancel out over time and the spatially averaged y direction. This leaves the residual Doppler velocity trend due to solar rotation. Figure 7.3 shows an example of MDI HR data before and after correction.

7.6 Spatial solar rotation correction

Once the CDS wide slit, TRACE and MDI data is cleaned/calibrated it must be corrected for spatial solar rotation to perform time series analysis. Solar rotation is removed by calculating the offset of each image from the first in the time series. The data is then aligned by applying cubic convolution interpolation to the translation of each frame by its negative offset. The

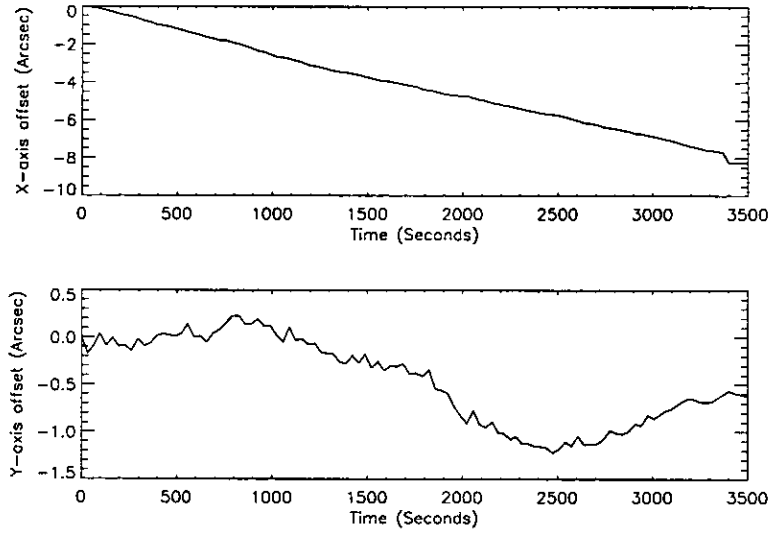


Figure 7.4: Top: TRACE 1600 Å data solar x offset measured using 2-D cross correlation. Solar x shows linear offset due to solar rotation. Bottom: Solar y offset displays possible orbital variation combined with high frequency variation due to quadrant shutter changes.

resulting 3-D data cube is then co-aligned to sub pixel accuracy.

The offset values of the CDS wide slit and MDI data are calculated using the solar rotation rate at the coordinates of the centre of the first image.

TRACE is located in a polar orbit and displays an orbitally effected pointing variation, possibly due to thermal effects (Handy et al. 1999). We use a 2-D cross correlation method between each TRACE image and the first image in the time series, to calculate the combined offset produced by the orbital variation and solar rotation in the TRACE data. Figure 7.4 displays the measured offsets of the x and y axes for the TRACE 1600 Å data from 13/3/04. We find in this data, a possible orbital variation with a peak to peak amplitude of approximately 1.4'' in the solar y direction; the x axis has a linear offset as expected, due to solar rotation. Vibrations due to shutter quadrant changes can cause an additional pointing error of the order 0.1'' (Handy et al. 1999). The high frequency variation present within the y axis offsets in Fig. 7.4 appears to be due to the quadrant shutter changes in this alternating 171/1600 observing sequence.

7.7 SOHO keyhole correction

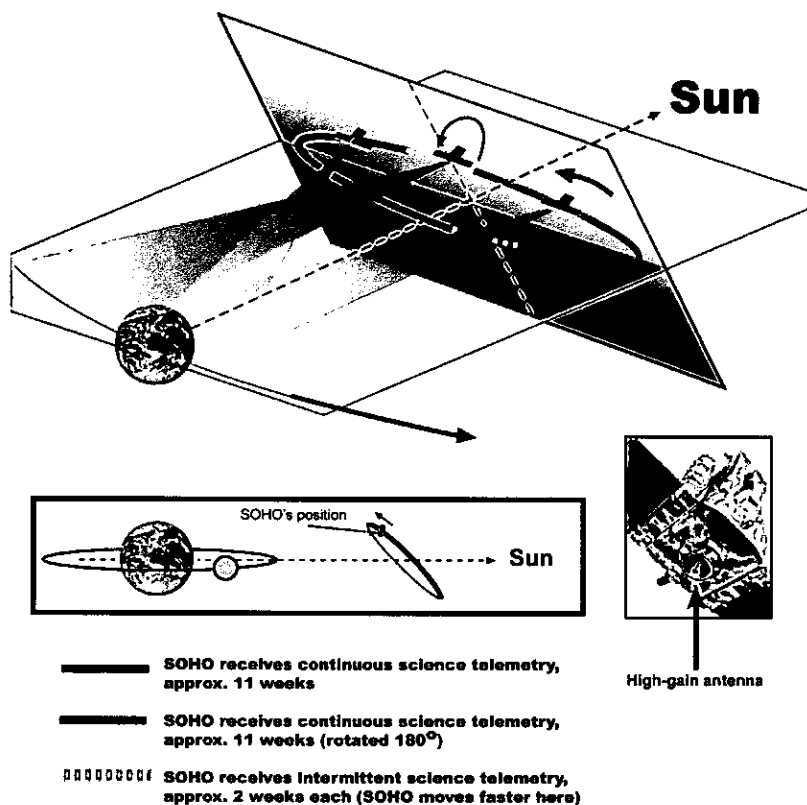


Figure 7.5: Schematic diagram of SOHO's L1 orbit indicating periods of normal operation and SOHO keyhole periods, relative to the geometry of the high gain antenna. Courtesy ESA/NASA.

During May 2003, SOHO experienced problems with the pointing mechanism of the high gain antenna. Currently this antenna is fixed in the optimum position for telemetry to Earth during half of SOHO's orbit around the L1 Lagrangian point. SOHO is inverted 180° during the other half of the orbit to maximise the availability of high rate data. During the two periods between each half of the orbit the pointing offset of the high gain antenna is too great to receive telemetry at Earth, and normal science operations are interrupted. These periods are termed "keyholes" and occur approximately every three months during SOHO's ~6 month L1 orbit (see Fig. 7.5).

The observations investigated here were performed when SOHO's orientation was 180°; this must be corrected before the data is analysed. The official CDS correction for the keyhole

orientation is handled by the routine UPD_CDS_POINT, called by READCDSFITS. This official correction method changes the values of the XCEN and YCEN pointing and the x scale and y scale spacing by multiplying by -1. A complete correction is applied to the data analysed here and the data is returned to the 0° normal orientation. It is extremely important that account is taken of SOHO's orientation when analysing CDS data. It should be noted that in the inverted orientation the sun appears to rotate in the *opposite direction*, and the CDS slit *rasters* in the *East-West* direction as opposed to the normal *West-East* direction.

7.8 Observational Outline – 13th March 2004

The observations were taken as part of a coordinated 'Loop Variability Study' campaign. The campaign utilises simultaneous CDS and TRACE observations of quiescent active region loop structures to study waves/flows. The campaign was designed to make the first coordinated observations of active regions using the CDS wide slit combined with co-temporal TRACE observations. The primary aim of these observations was to progress the work of Marsh et al. (2003) and Chapter 6, and observe directly the manifestation of the TRACE 171 Å propagations at corresponding chromospheric and transition region temperatures using CDS.

The CDS wide slit produces large scale intensity images (without rastering) in He I, O V and Mg IX at high cadence. Essentially, for the first time we use CDS as a chromospheric and transition region imager of active regions coordinated with TRACE. The wide slit observations have a duration of 44 mins (07:08–07:52 UT) and consist of $90'' \times 240''$ intensity images with a pixel size of $1.68''$ in He I 584 Å, O V 629 Å and Mg IX 368 Å with an exposure of 20 s and cadence of 26 s. The Mg IX 368 Å line is blended with the Mg VII 367.659 and 367.672 Å lines which have peak formation temperatures of $\text{Log } T=5.9$ using the CHIANTI v4.2 atomic database active region differential emission measure (Dere et al. 1997; Young et al. 2003). The EJECT_V3 observations above the sunspot plume region show that the Mg VII contributions are of the same order, or in places greater than the Mg IX line profile (Fig. 7.6). For simplicity, hereafter, this blend will be referred to as Mg IX/VII. In this dataset we find the signal to noise ratio of Mg IX/VII is too low to be included in the analysis of Sect. 7.9, and use it for context only. The peak line formation temperatures of He I, O V, Mg IX and Fe IX

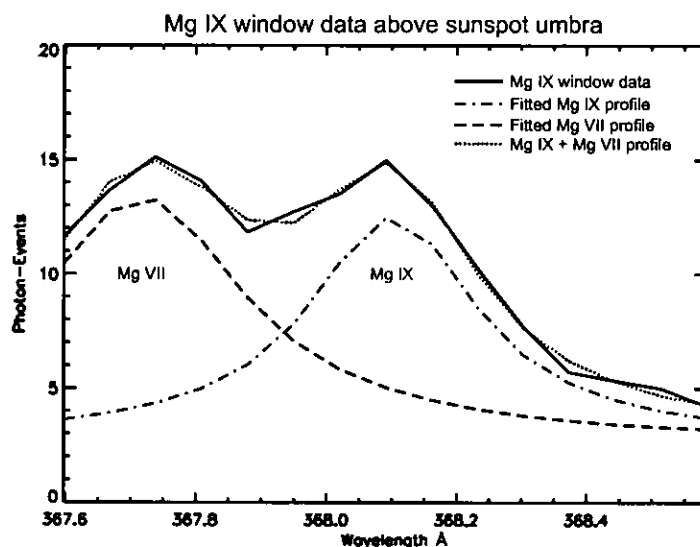


Figure 7.6: Mg VII/IX blend above the western sunspot region of AR 10570 shown in Fig. 7.7. Above the umbra the Mg IX window data displays emission from the Mg VII line is comparable to Mg IX.

(dominant in the TRACE 171 Å bandpass) are Log T=4.4, Log T=5.4, Log T=6.0 and Log T=6.0 respectively. The TRACE observations analysed are $512'' \times 512''$ images in the 171 Å passband at $1''$ resolution with an exposure of 23 s and ≈ 30 s cadence taken during the hour 07:00–08:00 UT.

NOAA active region 10570 is observed on the 13th March 2004 near disk centre. While the active region consists of two clear sunspot regions, here we concentrate on the westerly sunspot region located at $[315'', -120'']$ in solar coordinates. Fig. 7.7 shows the sunspot active region viewed with MDI (magnetogram and white light), CDS wide slit (He I, O V, and Mg IX) and TRACE (171 Å). The field of view of the CDS wide slit for each instrument is plotted. The MDI white light contours are over-plotted indicating the sunspot umbral and penumbral regions. The magnetogram shows the intense negative magnetic field of the sunspot surrounded by a number of small bipolar magnetic fragments.

In He I we observe relatively uniform emission above the sunspot with a number of emitting structures in the surroundings. Using coordinates where East and West are to the left and right of sun centre respectively; to the South-East of the sunspot there is intense emission in He I caused by small eruptive activity visible in TRACE 1600 Å observations. There is also

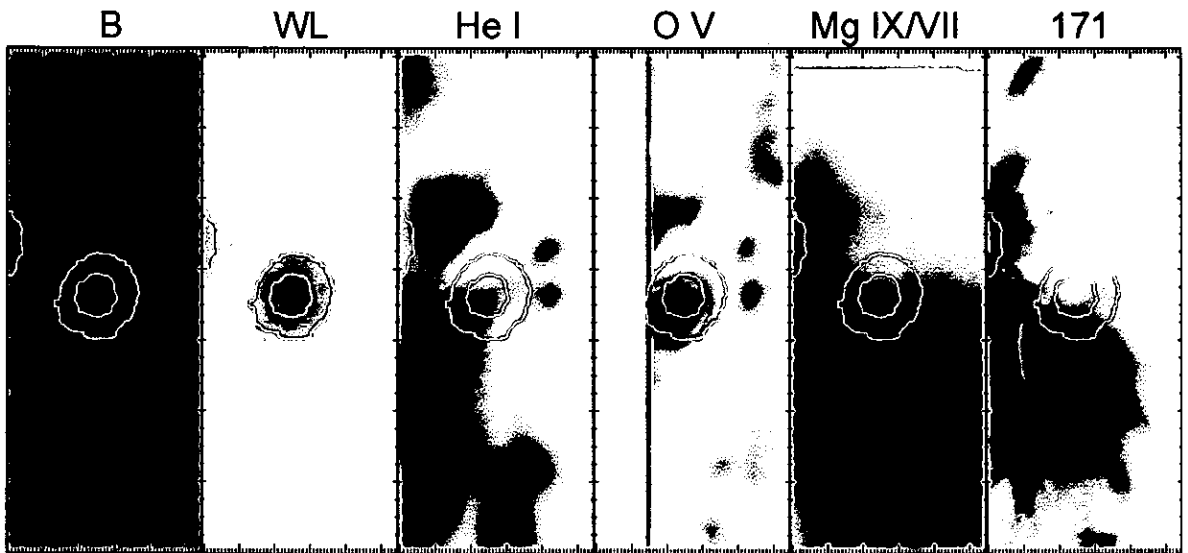


Figure 7.7: The western sunspot region of AR 10570 observed in MDI: magnetogram and white light, CDS wide slit: He I, O V, Mg IX/VII, and TRACE: 171 Å. MDI white light contours are over-plotted indicating the location of the umbra and penumbra.

emission towards the North-East and West of the sunspot associated with bipolar regions in the magnetogram.

The transition region temperature of O V shows similar emission structures to He I around the sunspot. There is a significant difference in structure above the sunspot, however; here we observe the intense emission of the sunspot plume located above the umbra and South-Eastern penumbra. The missing data on the left of the O V image is due to the fact that the O V line is dispersed onto the edge of the detector. In Mg IX/VII and TRACE 171 Å, we observe the coronal loop structures associated with the sunspot region. These loops outline the magnetic field emerging from the sunspot which is embedded within plasma emitting at coronal temperatures.

Figure 7.8 shows the EJECT_V3 observations of AR 10570. Running from left to right the top row of images shows the He I line intensity, Doppler velocity and line width. The middle row shows O V intensity, Doppler velocity and line width. The bottom row shows the Mg VII and Mg IX line intensity. The signal to noise ratio is too low within the Mg lines to fit the line position and width accurately. Overplotted within each image are the field of view of the wide slit data and the MDI white light intensity contours. The structures shown in Fig. 7.7 are

CHAPTER 7. CDS WIDE SLIT & TRACE ACTIVE REGION DYNAMICS

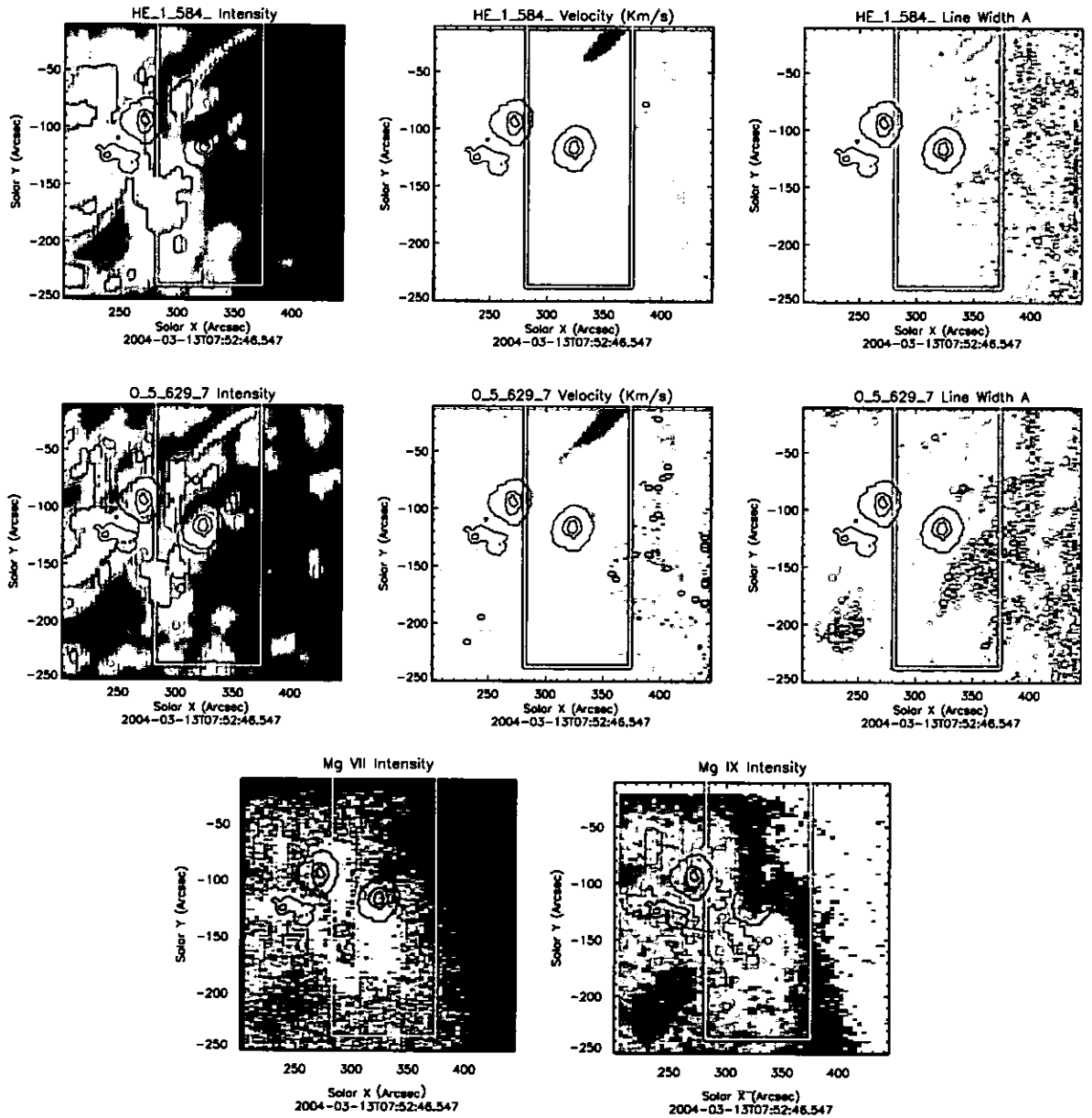


Figure 7.8: EJECT_V3 s29740r00 observations of AR 10570. Top row: He I line intensity, relative Doppler velocity and line width. Middle row: O V intensity, Doppler velocity and line width. Bottom row: Mg VII and Mg IX intensity. In each image: white box indicates field of view of wide slit data, and MDI white light intensity contours indicate the location of sunspots.

visible within the wide slit field of view.

In Fig. 7.8 towards the top of the wide slit field of view is a channel of plasma emission, visible in both He I and O V. In the corresponding Doppler maps, we can see that this channel appears to be a flow of plasma. This velocity of this flow channel is blue shifted, appearing to increase with altitude. The channel has a peak velocity of the order -150 km s^{-1} in its upper region. The wide slit movies on the CD-ROM for the 12th and 13th March show the dynamic nature of the plasma flow. The movies show sporadic ejections of plasma along the path of the channel, on time-scales down to the observation cadence, rather than a homogeneous fluid flow. This is illustrated by the fact that we cannot see a clear flow channel in the wide slit frame in Fig. 7.7, but it is observed in other frames (see the movies on the CD-ROM). The wide slit observations were made just before the EJECT_V3 data presented in Fig. 7.8. These observations reveal that the apparently steady flow observed with EJECT_V3 is actually formed by intermittent ejections of plasma, along the same path, over the duration of the raster. This unique combination of 2-D spectral imaging and spectroscopic data is required to obtain a full view of the processes at work. The maps of line width show that the line width increases at the top end of the channel. This suggests an increase in the non-thermal velocity, possibly due to turbulence within the plasma flow. Doyle & Madjarska (2003) describe a reduction in line width located above sunspot umbrae, and associated with sunspot plume regions; an indication of this effect is observed here, particularly in O V.

Comparing the Mg VII and Mg IX emission in Fig. 7.8 with the TRACE 171 Å emission in Fig. 7.7, reveals the emission within the wide slit f.o.v. from the Mg VII contribution more closely resembles the emission from the loop structures in TRACE 171 Å than the emission contribution from Mg IX. This suggests that the TRACE 171 Å emission originates from plasma at a temperature closer to the formation temperature of Mg VII than Mg IX. The emission temperature of Mg VII is $\text{Log } T=5.9$ using the active region DEM within the Chianti database. To explain this different emission structure, further work is required to determine a valid DEM for these types of region.

7.9 Data analysis techniques – 13th March 2004

7.9.1 CDS wide slit

To investigate any oscillations within the wide slit data we form maps of Fourier power, where the Fast Fourier Transform (FFT) of the time series at each pixel location is calculated. The resulting 3-D data cube contains the Fourier power with frequency for each pixel. To test the significance of power within the data cube we use a randomisation method (see following Sect. 7.9.2). Briefly, the method is applied as follows.

The time series at each pixel location is randomised and its FFT calculated. The FFT is calculated for M randomised permutations of the original time series. The power at each frequency is then compared to the power produced by the original time series. Only power in the original time series having a magnitude greater than that occurring in percentage S of permutations is considered significant. Here we use a significance level S of 95% and power at frequencies occurring below this level is set equal to zero. We then use the maps of significant Fourier power to observe the spatial distribution of oscillations at different frequencies. The time series at locations showing oscillating structures can then be investigated. The frequencies/periods of oscillations within these structures are determined using a Fourier analysis. Fourier analysis is used to test the presence of frequencies statistically, rather than investigate their time dependence using a method such as wavelet analysis.

7.9.2 Randomisation Significance Test

To test the significance of power within the Fourier transform, a randomisation method is used following Linnell Nemeč & Nemeč (1985). The null hypothesis that Fourier power P at a particular frequency ν is caused by chance is tested, compared to the positive hypothesis that the power is caused by a periodic signal within the time series. The method is based on the principal that, under the null hypothesis, the measured order of the time series data points is one of the possible, equally likely, permutations of the order. If there is no periodicity within the time series then the measured values $y_1, y_2, y_3, \dots, y_n$ can be randomly rearranged $y_{r(1)}, y_{r(2)}, y_{r(3)}, \dots, y_{r(n)}$ without affecting the distribution of Fourier power for large

n , where $r(1), r(2), r(3), \dots, r(n)$ is a random permutation of the data point subscripts. To test the hypothesis that the power $P(\nu)$ is due to chance, the power at ν can be calculated for the $n!$ possible permutations of the time series. The value p is the fraction of permutations that produce less power than the original time series at frequency ν .

Practically, $n!$ permutations is too large to calculate for long, or large numbers of time series, and thus the value of p can be estimated by calculating $P(\nu)$ for $m \ll n$ random permutations of the time series. The fraction of permutations s that produce a lower value of $P(\nu)$ than the original time series gives an estimate of the value of p . The quantity $1 - s$ then gives an estimate of the probability that $P(\nu)$ is due to chance. Then s gives an estimate of the probability that $P(\nu)$ is due to a periodic signal within the time series; following Linnell Nemeč & Nemeč (1985) s then has a standard error equal to $[s(1 - s)/m]^{\frac{1}{2}}$. The significance level S can then be defined as the level above which power is assumed to be due to real periodicity. A significance level of 95% is used here.

7.9.3 TRACE

To investigate any propagating intensity oscillations in the TRACE data we use a running difference method as in Chapter 6. A tube is defined overlying a coronal loop structure. Cross sections are formed along the tube of $2''$ width. A running difference is formed by using the integrated intensity profile of the tube along its length and subtracting the profile of the tube ≈ 90 s earlier. Thus any propagating oscillations should appear as diagonal light and dark bands in the difference image. The gradient of these bands can then be used as an indication of the propagation velocity of the oscillations. The periodicity of the propagating oscillations is investigated using a Fourier analysis of time series formed from cross-sections along the defined tube. Low frequency trends within all data are removed using a third order polynomial subtraction.

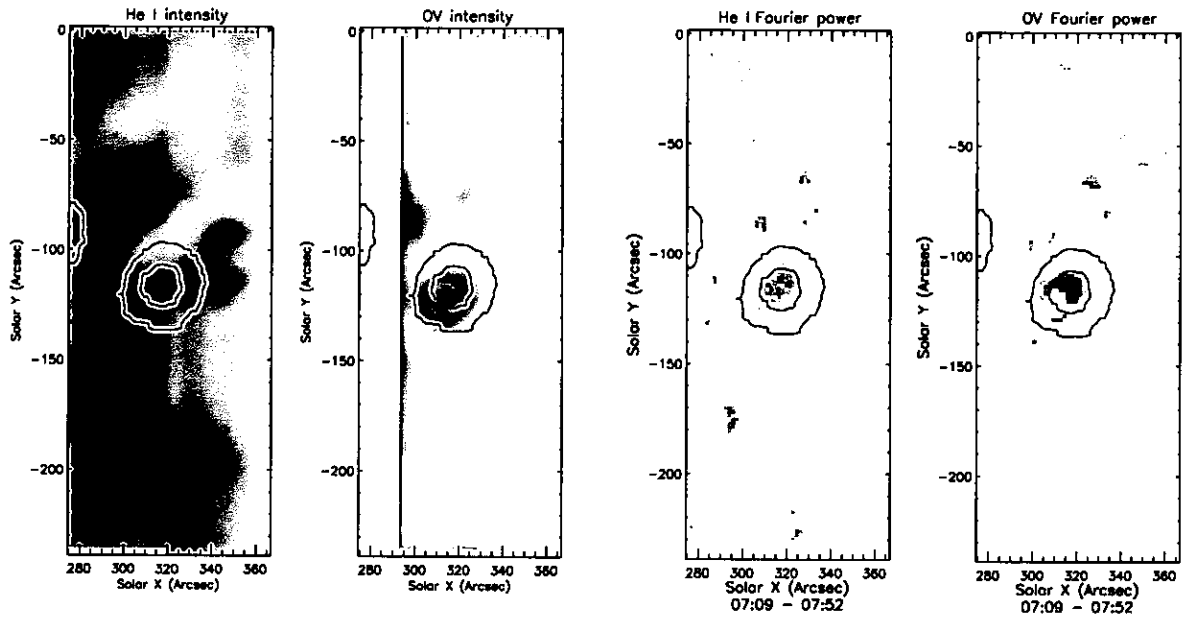


Figure 7.9: Intensity and Fourier power maps for the CDS wide slit data in He I and O V overplotted with MDI WL contours. Within the power maps the shaded regions indicate 95% significant power within the frequency range 4.7–6.6 mHz (150–210 s)

7.10 Observational Results – 13th March 2004

7.10.1 CDS wide slit

Fig. 7.9 shows the intensity and Fourier power maps for He I and O V significant to the 95% level within the ~ 3 -min frequency range 4.7–6.6 mHz (150–210 s) over the entire dataset. The region above the sunspot appears quite uniform in He I intensity. However, the power map for He I shows significant 3-min power confined above the sunspot umbral region as indicated by the contour. This suggests the region above the sunspot umbra is not quiescent and supports a dynamic oscillating structure at the temperature of He I.

The power map for O V shows greater significant power than He I above the umbral region. The increase in the magnitude of power suggests a greater oscillation amplitude in the transition region temperature of O V. The 3-min power is located above the umbra in the region of intense emission of the sunspot plume. In the O V intensity map, the sunspot plume also extends over the South-Eastern penumbral region. However, in this location, the intensity becomes so large that the detector becomes saturated. Therefore, in the O V power map we are not able to observe the oscillation in this region of greatest intensity. The Mg IX/VII blend is too weak in

this dataset to observe any significant oscillation above the noise level and so is not included in this analysis.

To investigate the periodicity of oscillations in the intensity time series of He I and O V, we use a binary mask method to sum all the pixels above the sunspot containing the significant 3-min oscillations. The FFT is applied to these time series to determine the frequency distribution of power within the 3-min band. The upper row of plots in Fig. 7.10 show the He I time series with a cadence of 26 s; the relative amplitude of the 3-min oscillation to the mean intensity of the times series $\frac{I(t)}{\bar{I}} - 1$ and the FFT of that time series. The time series shows a clear oscillation present throughout the duration of the observations. The relative amplitude indicates that the oscillation has an amplitude of $\approx 2\%$. The FFT reveals that the oscillation is not a single frequency but consists of two dominant frequencies within the 3-min band. These frequencies are centred around 6.1 and 7.1 mHz (164 and 141 s).

The second row of plots in Fig. 7.10 display the results for the O V time series. Comparing the two time series, it is clear to see that the oscillation amplitude is greater in O V. The estimated relative amplitude of the oscillation to the mean intensity is $\approx 4\%$ in the range 2–8%. As in He I, the FFT of the O V time series displays that the oscillation is not composed of a single frequency, but consists of two dominant frequencies. In the O V data these frequencies are centred around 5.9 and 7.3 mHz (169 and 137 s).

To isolate the two dominant frequencies we filter the time series by setting all power outside the 3-min band equal to zero, and take the inverse Fourier transform. The third and fourth rows in Fig. 7.10 show the results for the filtered He I and O V time series respectively. The filtered time series plots show the beat oscillation of the two frequencies. If we compare the filtered time series to the original time series we observe the beat oscillation of the two frequencies within the original time series, suggesting that both frequencies are present throughout. A wavelet analysis is also applied to the original and filtered time series to investigate the possible time dependence of the frequencies. The wavelet analysis power spectra are presented in the Loop Variability Appendix (Appendix B Figs. B.11). It is difficult to isolate and interpret such closely separated periods within the wavelet power spectra, due to the time/frequency uncertainty in the wavelet analysis method. Increasing the angular frequency of the mother

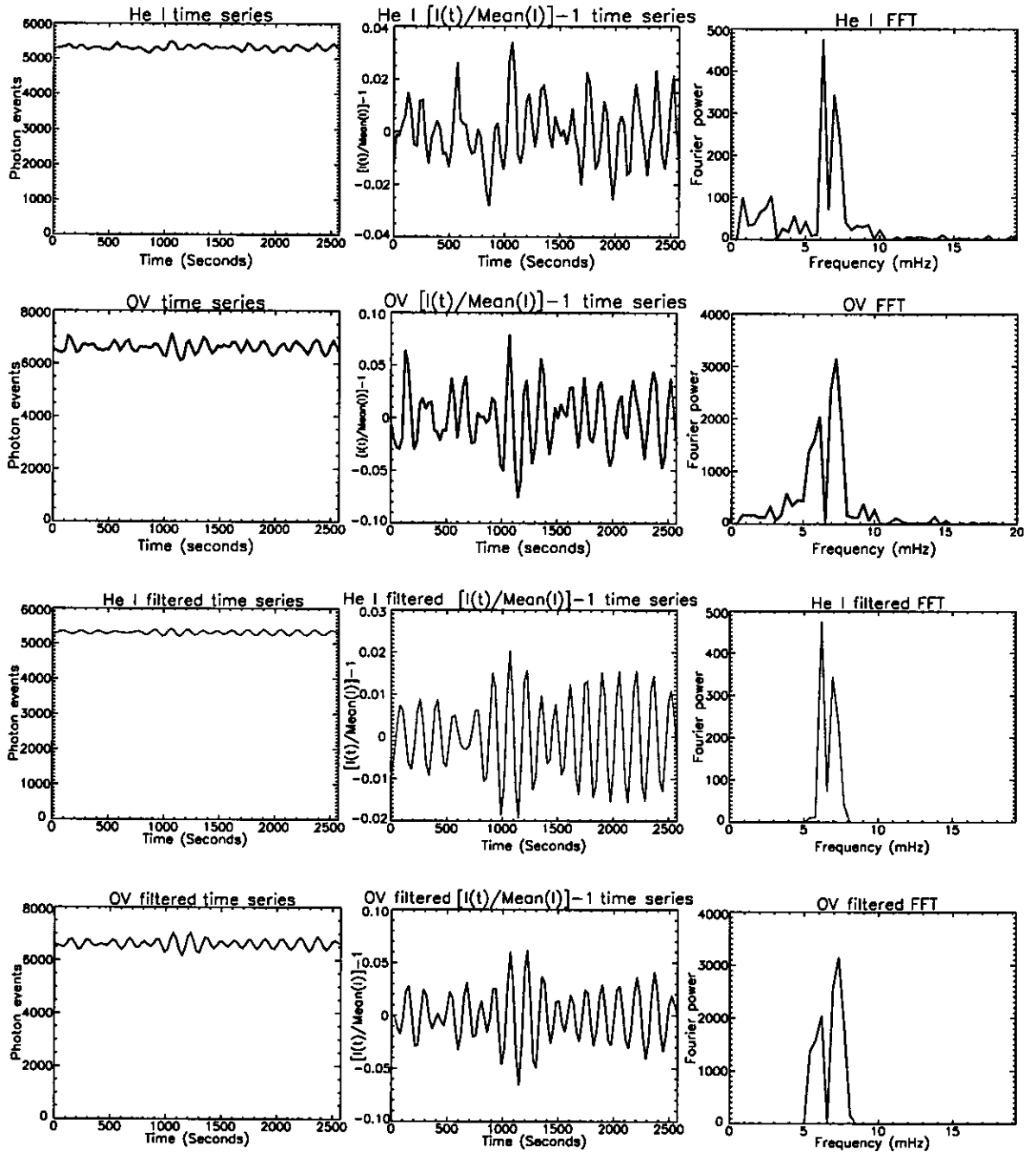


Figure 7.10: Left: The He I and O V time series for the summed pixels above the sunspot umbra showing significant 3-min power. Middle: The relative amplitude to the mean intensity for the He I and O V time series. Right: The FFT for the He I and O V time series. The third and fourth rows show the results for the filtered time series within the 3-min band.

wavelet function will increase the frequency resolution within the power spectra, and may assist in separating the two frequencies with a loss of temporal resolution.

Figure 7.11 shows the correlation between the He I and O V time series. Running from left to right, the top row shows the He I and O V time series for the significant 3-min oscillating region above the sunspot umbra, the relative amplitude to the mean intensity of the time series and the time series normalised to their peak intensity. The second row displays the cross correlation coefficient of the He I and O V time series as a function of the lag in seconds between the two time series, the cross correlation for the first half of the time series and the cross correlation for the second half of the time series. The beginning of the time series appears to be less correlated than the rest of the time series generally. Since this will lower the cross correlation coefficient of the time series as a whole, both halves of the time series are tested. The third row shows: the He I and O V Fourier filtered time series, the relative amplitude of the filtered time series, and the filtered time series normalised to their peak intensity. The bottom row shows: the cross correlation of the filtered time series, the cross correlation of the first half of the filtered time series, and the cross correlation of the second half of the filtered time series.

Considering the plots of the original time series data in Fig.7.11, it is clear to see that the two time series show a high degree of correlation. The plots of the relative and normalised amplitude show this correlation more clearly, particularly in the second half of the time series. The correlation for the whole of the original time series shows a maximum cross correlation coefficient of 0.67 for zero time lag. Visually there appears to be much less correlation in the first 900 s of the time series. The cross correlation of the first half of the time series confirm this with a maximum correlation coefficient of 0.54 with zero lag. After 900 s the time series appear to become very well correlated; the second half of the time series has a maximum cross correlation coefficient of 0.81.

Considering the plots of the filtered time series data in Fig.7.11; the correlation between the time series can be observed more clearly. The plot of the relative amplitudes shows a very good correlation between the time series. The cross correlation for the whole of the filtered time series has a maximum correlation coefficient of 0.75, again with zero time lag. The first half of the filtered time series shows a better correlation than the original time series, and has

CHAPTER 7. CDS WIDE SLIT & TRACE ACTIVE REGION DYNAMICS

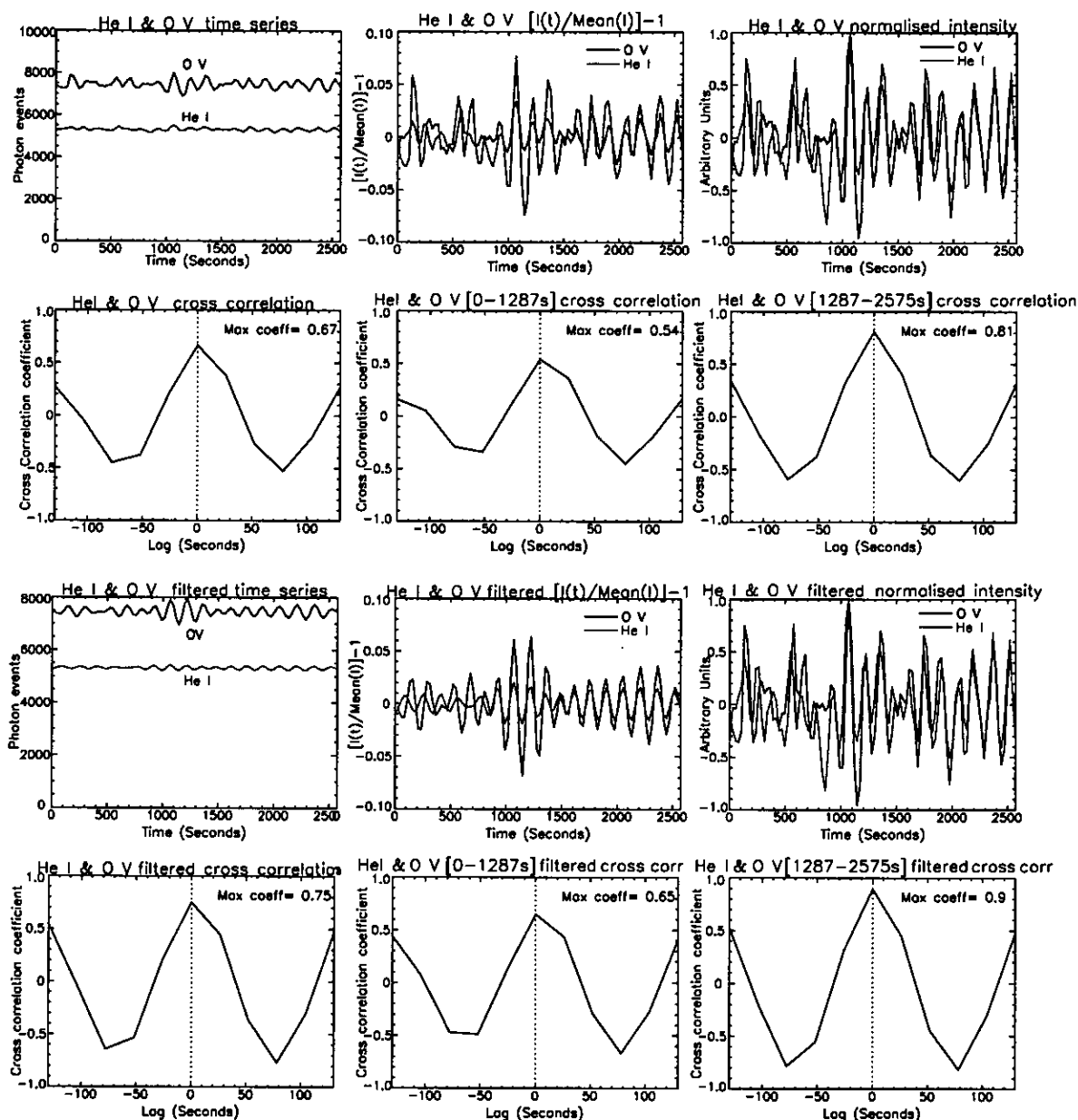


Figure 7.11: He I & O V time series correlation. Top row: The He I & O V time series, He I & O V time series relative amplitude, He I & O V time series normalised amplitude. Second row: Cross correlation coefficient of the He I & O V time series as a function time lag, cross correlation for the first half of the He I & O V time series, cross correlation for the second half of the He I & O V time series. Third row: Filtered He I & O V time series, Filtered He I & O V time series relative amplitude, and Filtered He I & O V time series normalised amplitude. Fourth row: Cross correlation of the filtered He I & O V time series, cross correlation for the first half of the filtered He I & O V time series, cross correlation for the second half of the filtered He I & O V time series.

CHAPTER 7. CDS WIDE SLIT & TRACE ACTIVE REGION DYNAMICS

a maximum correlation coefficient of 0.65 with zero lag. The correlation for the second half of the filtered time series shows an excellent correlation, with a cross correlation coefficient of 0.9 at zero lag. The first half of the time series is less well correlated in the original and filtered time series, suggesting this is not due to the superposition of other frequencies. It is possible that the cause is quasi-periodicity or time dependence within the frequencies.

It is difficult to reliably interpret the results from either the Fourier analysis or wavelet method alone. A more instructive approach is to utilise both methods to interpret the entire time series dataset. Filtering the signal, as has been applied here, is a useful method to gain more information on the modes present. Much of the work in the literature neglects to do this and characterise time series as a whole. In complex time series, power at other frequencies interfere with the dominant mode present, and relative amplitudes are then quoted as an estimated average of the beat amplitude. A more accurate method is to filter the time series as applied here. Even so, in future work a more thorough approach could be adopted to filter and analyse each frequency separately. Decomposing the time series in this way will allow any time dependence of the amplitude or frequency to be observed more clearly. It should be remembered that the data analysed here is integrated over the spatial region above the sunspot umbra; therefore, time dependence may be linked to spatial variations.

The cross correlation of the time series doesn't show any significant lag between He I and O V. We may expect to observe a lag assuming that the observed oscillations are caused by upwardly propagating waves, and that He I is formed at a lower altitude than O V. However, the cross correlation coefficients are calculated for lags of integer factors of the data cadence (~ 26 s). If the phase difference between He I and O V produces a lag that is smaller than the time series cadence then this phase difference will not be observable. To investigate this, the time series are linearly interpolated to a cadence of 1 s, and the cross correlation analysis is repeated. Figure 7.12 shows the results for the interpolated original and filtered time series. The interpolated time series have a maximum cross correlation coefficient of 0.64 at a lag of 3 s. The filtered and interpolated time series have a maximum coefficient of 0.75, also at 3 s lag. This suggests that the He I oscillation leads the O V oscillation by 3 seconds. Using the above assumptions about the formation height of the two lines, this result implies the oscillations

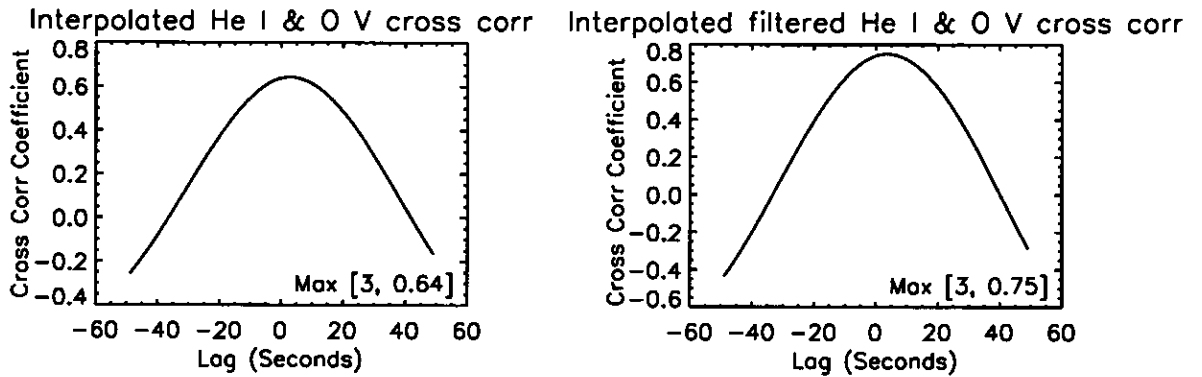


Figure 7.12: Cross correlation of He I & O V time series linearly interpolated to 1 s cadence. Left: Cross correlation of interpolated time series. Right: Cross correlation of filtered and interpolated time series.

in He I and O V are caused by upwardly propagating waves. This is not an ideal method to demonstrate that this 3 s lag is valid, but is used as an indication of its presence. Again, in further work the time series should be decomposed into their component frequencies. These single frequencies can then be fitted with sinusoidal functions, assuming a constant frequency over time; phase shifts could then be observed more clearly between different lines.

7.10.2 TRACE

The TRACE data displays propagating oscillations present in many of the loop structures emerging from the sunspot. Figure B.10 in the Loop Variability Appendix shows the running difference images for a number of the loop structures. The majority of the loop structures emerging to the West of the sunspot show periodic propagations in their corresponding running difference image. We select one of the loop structures that appears to be rooted in the umbra where we observe significant oscillations with the CDS wide slit. Fig. 7.13 shows the TRACE 171 Å context image of the CDS wide slit field of view. Over-plotted are the MDI white light contours of the sunspot umbra and penumbra along with the tube outlining the loop structures selected to form the running difference image. The running difference image in Fig. 7.13 clearly shows the light and dark diagonal bands that indicate intensity propagations along the loop structure. The regular spacing of the bands suggests that the propagations have a periodic nature over the duration of the observations with a period of ≈ 180 s. The positive gradient

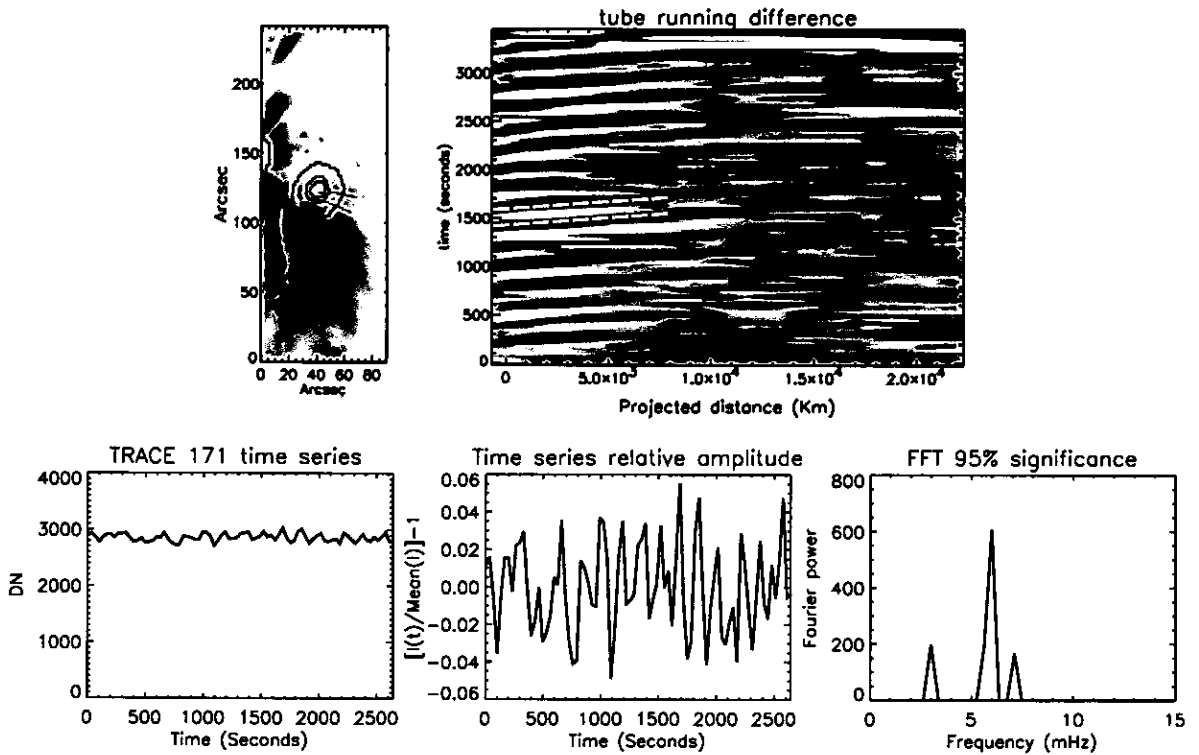


Figure 7.13: Top: TRACE 171 Å context image indicating the location of sunspot umbra/penumbra and running difference tube. Running difference image indicates outward intensity propagations along the length of the loops. Dashed yellow lines outline one of the propagations and give an estimated velocity of 80 km s^{-1} . Bottom: TRACE time series formed from the cross section at the base of the tube, relative amplitude to the mean intensity and time series FFT.

of the bands indicates that the propagations originate at the base of the loops and propagate outwards along their length. The gradient of the dashed yellow lines in the running difference image gives an estimate of the propagation velocity perpendicular to the line of sight of 80 km s^{-1} .

To analyse the periodicity of the TRACE propagations, we select the cross section at the base of the defined tube above the sunspot umbra. The pixels of this cross section are summed to form the TRACE time series. The FFT is then applied to the time series to determine the oscillation frequencies of the TRACE propagations. The lower plots in Fig. 7.13 show the time series, the relative amplitude of the propagating oscillations, and the FFT of the time series with power significant to the 95% level. The time series shows that the oscillation at the base of the loops is caused by the periodic propagations. The relative amplitude to the mean

intensity indicates that the propagating oscillations have amplitudes of $\approx 3\%$. As in He I and O V, the FFT shows that in the 3-min band the TRACE propagating oscillations, at the base of the loops, consist of two dominant frequencies. These frequencies are centred around 5.9 and 7.3 mHz (169 and 137 s), as in O V. We also observe power at ≈ 3 mHz (330 s) coincident with the 5-min p-mode oscillation.

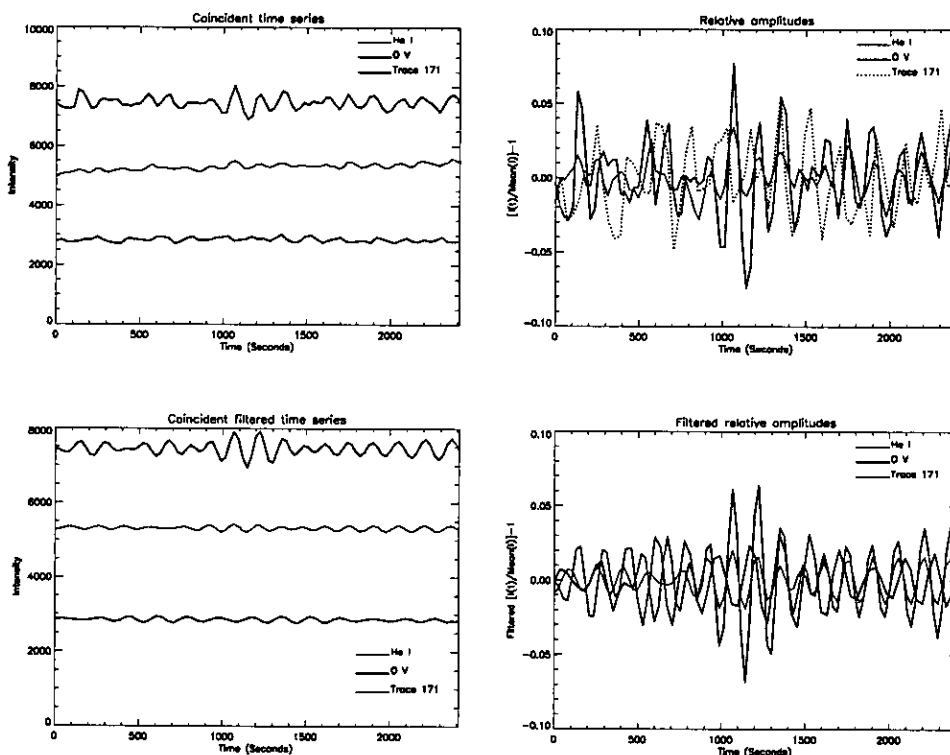


Figure 7.14: Time series for He I, O V and TRACE shifted to share the same origin in time. Top row: The intensity and relative amplitude for all time series. Bottom row: The intensity and relative amplitude for all filtered time series.

Figure 7.14 shows the He I, O V and TRACE 171 Å time series corrected to be coincident in time. The top left plot shows the three time series, and indicates the relative intensity in each line. Top right shows the relative intensity, as in Fig. 7.11 the He I and O V time series show a good correlation. It is difficult to observe any close correlation with the TRACE time series. To compare the time series more clearly the bottom plots show the results for the time series filtered in the 3-min band. Bottom left shows the filtered time series; the beat oscillation of the two frequencies can be seen more easily in all the time series. Bottom right shows the relative amplitude of all three filtered time series. Again He I and O V show an excellent correlation,

particularly towards the second half of the time series. The TRACE time series doesn't show any apparent close correlation with He I and O V. This may be due to spatial variations in the oscillations at the footpoints of the field lines used to form the time series. It is also possible that changing physical conditions such as density, temperature and magnetic field affects the oscillation between the temperature of O V and TRACE 171 Å.

7.11 Acoustic wave energy flux

The observations presented here reveal a periodic, propagating, intensity oscillation from the chromosphere to the corona. The combined propagation, and oscillation in intensity imply a longitudinal, compressive, wave mechanism, such as acoustic or magnetoacoustic waves. Brynildsen et al. (2004) find an $\approx 180^\circ$ phase difference between the intensity and velocity oscillations in He I, O IV and O V above a sunspot umbra, in agreement with the acoustic wave interpretation.

To estimate the energy flux carried by the observed oscillations under the acoustic wave interpretation the following method is applied. Considering the wave as perturbations to a constant velocity and pressure, the velocity V and pressure P of the wave are given by

$$V = V_o + V' \qquad P = P_o + P'$$

where V_o and P_o are the constant background flow velocity and pressure, and V' and P' are the velocity and pressure perturbations of the wave given by

$$V' = \Delta V e^{i(\omega t - kx)} \qquad P' = \Delta P e^{i(\omega t - kx)}.$$

Applying the equation of motion gives

$$\rho \frac{\delta V}{\delta t} = -\nabla P$$

$$i\rho\omega\Delta V = ik\Delta P$$

CHAPTER 7. CDS WIDE SLIT & TRACE ACTIVE REGION DYNAMICS

$$\Delta V = \frac{\Delta P k}{\rho \omega} \quad C_s = \frac{\omega}{k}$$

$$\Rightarrow \Delta V = \frac{\Delta P}{\rho C_s} \quad (7.1)$$

where ρ and C_s are the plasma density and acoustic velocity respectively. The acoustic velocity is given by

$$C_s^2 = \frac{\gamma P}{\rho}, \quad (7.2)$$

$$\Rightarrow \Delta P = \frac{C_s^2 \Delta \rho}{\gamma}. \quad (7.3)$$

Combining equations 7.1 and 7.3 gives,

$$\Delta V = \frac{C_s \Delta \rho}{\gamma \rho}. \quad (7.4)$$

The energy flux of the wave ϵ is given by,

$$\epsilon = \frac{1}{2} \rho (\Delta V)^2 V.$$

$V \approx C_s$, and substituting equation 7.4 gives,

$$\Rightarrow \epsilon = \frac{C_s^3 \rho}{2\gamma^2} \left(\frac{\Delta \rho}{\rho} \right)^2.$$

Assuming optically thin emission then the intensity $I \propto \rho^2$.

$$\Rightarrow I_1 \propto (\rho + \Delta \rho)^2 \quad \Delta I = I_1 - I$$

$$\Rightarrow \Delta I \propto (\rho + \Delta \rho)^2 - \rho^2$$

Neglecting $\Delta \rho^2$ as a small term,

$$\Rightarrow \Delta I \propto 2\rho\Delta\rho$$

$$\Rightarrow \frac{\Delta I}{I} = \frac{2\Delta\rho}{\rho}$$

Then,

$$\epsilon = \frac{C_s^3 \rho}{8\gamma^2} \left(\frac{\Delta I}{I} \right)^2 \quad (7.5)$$

Substituting equation 7.2,

$$\Rightarrow \epsilon = \frac{1}{8} \sqrt{\frac{P^3}{\gamma\rho}} \left(\frac{\Delta I}{I} \right)^2.$$

Making the ideal gas approximation then $P = NkT$

$$\Rightarrow \epsilon = \frac{1}{8} \sqrt{\frac{N^3 k^3 T^3}{\gamma\rho}} \left(\frac{\Delta I}{I} \right)^2$$

$\frac{N}{\rho} = \frac{1}{\bar{m}}$ where \bar{m} is the mean particle mass. The acoustic energy flux is then given by,

$$\epsilon = \left(\frac{N^2 k^3 T^3}{64\gamma\bar{m}} \right)^{\frac{1}{2}} \left(\frac{\Delta I}{I} \right)^2 \quad (7.6)$$

Where,

N = the plasma particle number density

k = the Boltzmann constant

T = the plasma temperature

γ = the ratio of the specific heats of constant pressure to constant volume

\bar{m} = the mean particle mass

$\frac{\Delta I}{I}$ = the intensity amplitude of the plasma emission due to the compression of the wave.

7.11.1 Plasma particle number density

To estimate the energy flux, the plasma particle number density must be derived. Assuming the complete ionisation of Hydrogen and Helium within the plasma, the electron density of

CHAPTER 7. CDS WIDE SLIT & TRACE ACTIVE REGION DYNAMICS

the plasma N_e is dominated by the electron density due to Hydrogen ($N_{e(H)}$), and the electron density due to Helium ($N_{e(He)}$). The contribution of electrons from the metals can be neglected, and the plasma can be approximated by a composition of Hydrogen and Helium of relative abundances X and Y , where $X \approx 0.9$ and $Y \approx 0.1$ for coronal abundances.

The plasma electron density is then,

$$N_e = NX + 2NY$$

where N = the total plasma particle density.

$$\Rightarrow \frac{N_e}{N} = X + 2Y$$

and

$$\frac{N_{e(H)}}{N} = X \quad \frac{N_{e(He)}}{N} = 2Y$$

then

$$\frac{N_{e(H)}}{N_e} = \frac{X}{X + 2Y} \quad \frac{N_{e(He)}}{N_e} = \frac{2Y}{X + 2Y}$$

$$N_H = \left(\frac{X}{X + 2Y} \right) N_e \quad N_{He} = \left(\frac{2Y}{X + 2Y} \right) \frac{N_e}{2}$$

where N_H = the particle density of Hydrogen and N_{He} = the particle density of Helium.

Considering the ideal gas approximation the contribution of the electrons is neglected. The total plasma particle number density is then given by,

$$N = N_H + N_{He} \tag{7.7}$$

$$N = N_e \left[\left(\frac{X}{X + 2Y} \right) + \left(\frac{2Y}{X + 2Y} \right) \frac{1}{2} \right] \tag{7.8}$$

$$N = N_e (0.82 + 0.09) \tag{7.9}$$

Table 7.3: Estimated plasma particle densities at He I, O V and TRACE 171 Å temperatures

	Log T (K)	Log N_e (cm^{-3})	Log N (cm^{-3})
He I	4.5	11	10.959
O V	5.4	9.9	9.859
Fe IX/171 Å	6.0	9.3	9.259

$$\Rightarrow N \approx 0.91N_e \quad (7.10)$$

To estimate the energy flux of acoustic waves within the loop structures above sunspots the electron density must be measured at the observed temperatures. He I has a peak formation temperature of $\text{Log } T=4.5$. In these structures the electron density is estimated as $\text{Log } N_e=11 \text{ cm}^{-3}$. Doyle & Madjarska (2003) derive the electron density within a sunspot plume using O V lines. They observe a reduction in density within the plume compared to the surrounding region, and derive a mean electron density within the plume of $\text{Log } N_e=9.9 \text{ cm}^{-3}$. They also suggest that the agreement with previous observations may suggest that all sunspot plumes have similar electron densities at transition region temperatures. Del Zanna & Mason (2003) apply spectroscopic diagnostics to quiescent coronal loops. Del Zanna (2003) focuses on the diagnostics in the footpoint regions of these loop structures; also, where the propagating oscillations are observed with TRACE. Using a Mg VII diagnostic, electron densities of $\text{Log } N_e \simeq 9.3 \text{ cm}^{-3}$ are derived. Using these derived electron densities and equation 7.10, Table 7.3 lists the estimated plasma particle densities at the temperatures of He I, O V and TRACE Fe IX/171 Å.

7.11.2 Plasma mean particle mass

The mean particle mass of the plasma \bar{m} is given by,

$$\bar{m} = \frac{\rho}{N}. \quad (7.11)$$

Equations 7.7–7.9 give

$$\rho = N_e (0.82m_p + 0.09m_\alpha) \quad (7.12)$$

where m_p , m_α and m_e are the masses of the proton and Helium nuclei. $m_p=1.67\times 10^{-27}$ kg and $m_\alpha=6.64\times 10^{-27}$ kg. Substituting equations 7.10 and 7.12 in 7.11

$$\Rightarrow \bar{m} = 1.29m_p \quad (7.13)$$

7.11.3 Acoustic wave flux in He I, O V and TRACE 171 Å

Using equations 7.6, 7.10 and 7.13, Table 7.4 lists the estimated energy flux carried by the observed oscillations in He I, O V and TRACE 171 Å, assuming an acoustic wave mechanism. Due to the high conductivity of the plasma an isothermal wave assumption is made such that $\gamma=1$.

Table 7.4: Estimated acoustic wave energy flux of the He I, O V and TRACE 171 Å oscillations.

	Log T (K)	Log N (cm ⁻³)	$\frac{\Delta I}{I}$	ϵ (erg cm ⁻² s ⁻¹)
He I	4.5	10.959	0.02	28.3
O V	5.4	9.859	0.04	201.0
Fe IX/171 Å	6.0	9.259	0.03	225.6

The energy flux estimated using the described method, and assumptions, suggests an increase in the energy flux as the wave propagates along the loop. This arises, from equation 7.6, as the energy flux is dominated by the increase in temperature compared to the measured density stratification.

7.12 Summary and discussion

A sunspot active region and its associated quiescent coronal loops are observed with spatially resolved, high cadence observations using CDS, TRACE, and MDI. Spectroscopic rastered CDS observations above the sunspot umbra show the emission from Mg VII becomes of the same order or more dominant than Mg IX. The structure of the Mg VII emission appears match the emission in TRACE 171 Å more closely than the Mg IX emission. This may represent a separation of the formation temperatures of Mg IX and TRACE 171. If so, this could question the dominant emission temperature within the TRACE 171 Å bandpass.

The unique CDS wide slit observations reveal highly dynamic structures at chromospheric

and transition region temperatures such as flows, dynamic brightenings and oscillations, whilst the TRACE 171 Å observations show the region to be quiescent at coronal temperatures. Spectroscopic CDS data shows a high velocity plasma flow in He I and O V. The flow has a peak line of sight velocity of the order 150 km s^{-1} and indicates an increase in non-thermal velocity with height. The spatially resolved, high cadence wide slit data reveals that this plasma flow consists of intermittent ejections of plasma along the same path. Spectroscopic imaging data is essential to observe such spatially and temporally dynamic structures.

The 3-min sunspot oscillations in CDS wide slit data at the chromospheric and transition region temperatures of He I (Log T=4.4) and O V (Log T=5.4) are observed. Fourier power maps indicate that the oscillations are confined above the umbra in He I, whilst in O V the oscillations appear to be coincident with the emission from the sunspot plume. We are limited from observing oscillations in the most intense region of the plume due to saturation of the detector. However, it is possible that the whole of the plume emission oscillates in this manner. In coordinated TRACE 171 Å observations of the coronal loops emerging from the sunspot we observe periodic intensity propagations concurrent with the He I and O V oscillations. The propagations have a velocity perpendicular to the line of sight of $\sim 80 \text{ km s}^{-1}$ (cf. Robbrecht et al. 2001; De Moortel et al. 2002c).

The FFTs of the He I, O V and TRACE time series, formed above the umbra, indicate the 3-min band contains two distinct frequencies. In He I we observe the two frequencies around 6.1 and 7.1 mHz (164 and 141 s) with the lower frequency having the greatest peak power. In O V the two frequencies are observed around 5.9 and 7.3 mHz (169 and 137 s) with the higher frequency having the greater peak power. Using a cross correlation analysis of the interpolated He I and O V time series, we find an indication that the O V oscillation lags the He I oscillation by 3 s. Assuming that the O V sunspot plume emission is formed at a greater altitude than the He I emission; this suggests that the 3-min oscillations propagate upwards through the solar atmosphere. In TRACE we observe the two frequencies around 5.9 and 7.3 mHz (169 and 137 s) as in O V, but with the lower frequency having the greater peak power. We also observe an indication of a 5-min oscillation at the base of the loops. More examples within this dataset need to be analysed to determine the cause of the change in the dominant frequency and the

origin of the 5-min oscillation. The relative oscillation amplitudes of the time series are He I $\simeq 2\%$ (in the range 1–3%), O V $\simeq 4\%$ (in the range 2–8%) and TRACE $\simeq 3\%$ (in the range 1–5%). This agrees with the observations of Fludra (2001); Brynildsen et al. (2002); O’Shea et al. (2002) who find the oscillation amplitude peaks at transition region temperatures.

If the oscillations are interpreted as acoustic waves, assuming isothermal waves, ideal gas and composition of completely ionised H and He, then the acoustic energy flux increases with temperature along the loop structure. The estimated energy flux at the temperatures of He I $\epsilon=28.3 \text{ erg cm}^{-2} \text{ s}^{-1}$, O V $\epsilon=201.0 \text{ erg cm}^{-2} \text{ s}^{-1}$ and TRACE 171 Å $\epsilon=225.6 \text{ erg cm}^{-2} \text{ s}^{-1}$. De Moortel et al. (2002c) calculate an energy flux of $346 \text{ erg cm}^{-2} \text{ s}^{-1}$ in their observations of TRACE loop propagations. If the total energy required to heat active region loops is of the order $10^6 \text{ erg cm}^{-2} \text{ s}^{-1}$ (Priest 1982) then the energy flux of the waves derived here does not represent a significant contribution to this energy balance. Here, the estimation of the energy flux considers the superposition of the two observed frequencies; it may be more appropriate to decompose the oscillation into its two modes, and consider the combined energy flux of each mode (if it could be assumed that the two oscillation modes are co-temporal). Considering this, and that oscillation modes of higher/lower frequency may exist, but cannot be observed due to the limited observation cadence/duration; the dissipation of these waves may represent a more significant contribution to coronal heating.

The energy fluxes estimated here suggest an increase in the energy flux of the waves with temperature and, by implication, height. This counterintuitive increase in the energy flux with height may suggest that some of the assumptions made do not apply or, perhaps less likely, that an additional process is present that supplies energy to the compression of the plasma.

It was suggested by De Moortel et al. (2002a) that there may be a relation between their observations of ~ 3 -min propagations in TRACE loops and the 3-min oscillations above sunspots observed by Brynildsen et al. (2002). This thesis chapter presents the first observations that the long observed 3-min oscillations above sunspots in the chromosphere and transition region are directly connected to the 3-min propagations along the TRACE loops. This work shows that the oscillations in the chromosphere and transition region, and the propagations along the coronal loops are consistent with the same wave phenomena.

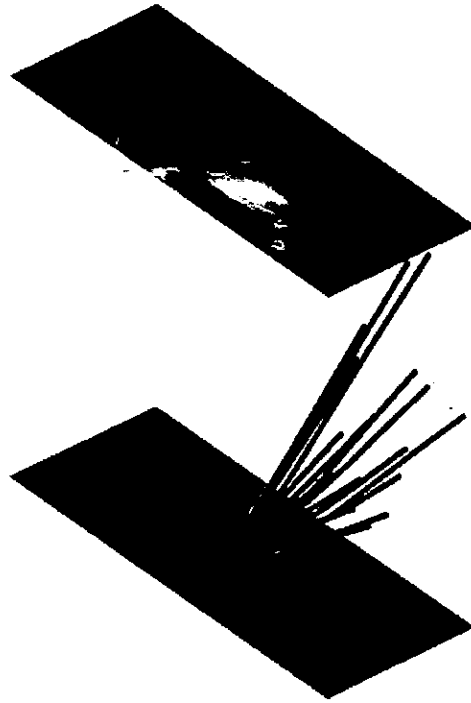


Figure 7.15: Magnetic field extrapolated using linear force-free code, courtesy D.S. Brown.

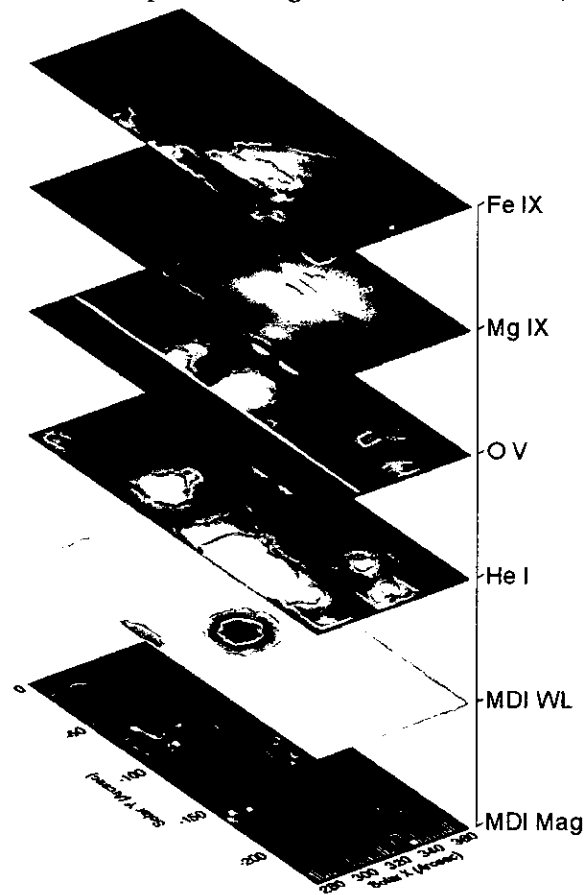


Figure 7.16: Atmospheric structure above the sunspot with increasing temperature.

The temperature scale heights are relatively small for He I and O V formation temperatures in the magnetic structure above sunspots. Thus, emission from these lines is located in regions at low altitudes above the photosphere where the umbral magnetic field is almost vertical. Thus, we only observe an oscillation at chromospheric and transition region temperatures. At the coronal temperatures of the TRACE loops the temperature scale height is much larger and the emitting region extends a greater distance along the loop magnetic field. At these altitudes the plasma β decreases and the magnetic field diverges becoming inclined significantly to the vertical. Thus, we are then able to observe the propagation perpendicular to the line of sight. Figure 7.15 shows the magnetic field above the sunspot extrapolated using a constant α linear force-free code (courtesy of D.S. Brown; the code is described by Carcedo et al. (2003) and uses the original method of Chiu & Hilton (1977)). This illustrates the line of sight effects involved in observing the propagating waves as either oscillations or propagations in the different temperature regions, considering the temperature scale heights of the different regions combined with the magnetic field geometry of the sunspot. Figure 7.16 shows the changing emission structure above the sunspot with increasing temperature. Above the sunspot umbra, the magnetic field is predominantly vertical through the photospheric, chromospheric and transition regions of MDI, He I, and O V which are formed close to the photosphere. The emission structure of the coronal loops outlining magnetic field indicates that, in the corona, the magnetic field becomes significantly inclined at the temperatures of Mg IX/VII and TRACE 171 Å;

There have been many observations of multiple frequencies within the 3-min band above sunspots e.g. Beckers & Tallant (1969); Beckers & Schultz (1972); Gurman et al. (1982); Lites (1984) and more recently by Fludra (2001); O'Shea et al. (2002); Christopoulou et al. (2003). Resonant theory predicts the formation of closely spaced oscillation frequencies within the 3-min band (see Zhukov 2005; Settele et al. 2001, and references within). However, using sit and stare CDS observations Brynildsen et al. (2002) find only one dominant frequency in the 3-min band in contrast to the other observations. Doyle et al. (1998) discuss the qualitative effect of sit and stare observations on power spectra. They find that the effect of solar rotation on oscillating structures broadens the distribution of power around the frequencies within the power spectra. To limit the spatial drift of the slit Brynildsen et al. (2002) limit the duration of the analysed

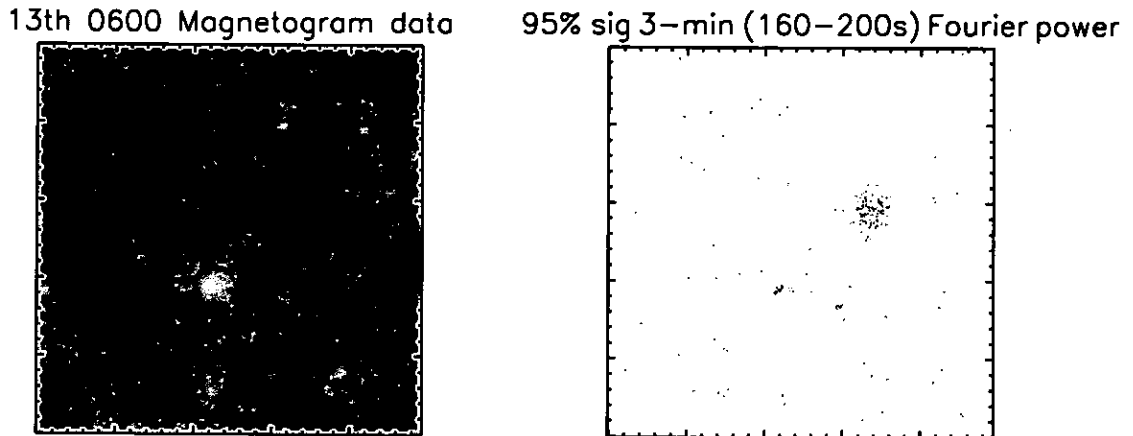


Figure 7.17: Left: MDI high resolution magnetogram. Right: Corresponding Fourier power map. Power is significant to the 95% level and filtered in the 3-min band (160–200s). Significant power is indicated by grey scales. Significant 3-min power is concentrated above the sunspot umbra and bipolar region.

time series to 20 min. Limiting the duration of the time series restricts the information that can be gained about the beat frequency of possible multiple frequencies. Two frequencies separated by 1 mHz produce a beat oscillation period of ~ 16 mins for example; this is of the order of their time series duration. This also broadens the distribution of power around the oscillation frequencies. It is suggested here that the combination of these solar rotation and time series duration effects can explain the single frequency observed by Brynildsen et al. (2002).

There is evidence that the 3-min sunspot umbra oscillations in $H\alpha$ are variable spatially, and are coherent over $\sim 2''$ scales (Kobanov & Makarchik 2004). Future work should investigate the spatial distribution of these oscillations from the photosphere, chromosphere, transition region and their propagation into, and along, the coronal loops. Figures B.8 & B.9 in Appendix B show preliminary investigations of this using the wide slit data to determine the oscillation frequencies at different spatial locations.

This work shows the connection between the oscillations in the chromosphere and transition region, and the propagation along the coronal loops, caused by propagating waves. Direct observations of the source of the waves have not yet been made. A complete set of observations, at photospheric to coronal temperatures, are needed to discover the photospheric signature of these waves. This will allow the propagation along the magnetic field and coupling through the atmosphere to be quantified.

Figure 7.17 shows a preliminary analysis of the high resolution MDI magnetogram data. The context image shows the Eastern sunspot region of AR 10570. The Fourier power map of this region shows oscillations of the magnetic field data within the 3-min band at 95% significance. This could represent the observation of the magnetic oscillation component associated with the wave propagation upwards along the magnetic field. However, to determine this conclusively, a complete investigation of the possible effect of cross-talk from other line parameters on the observational method used by MDI to calculate B needs to be made. Inconclusive observations of magnetic field oscillations have been made previously. Using MDI, Settele et al. (2002) are unable to produce their magnetic oscillation from cross-talk alone. Rüedi & Cally (2003) state that a full simulation of the observing procedure is necessary to interpret the magnetic oscillation signal correctly. Complete spatially resolved high cadence observations at all temperatures above the active region are required, including magnetograms, Dopplergrams, the chromosphere, transition region and corona.

In future analysis, these kind of time series data should be investigated using a more detailed approach of decomposing the time series into its component frequencies. This may be done by filtering, or the recently developed method of empirical mode decomposition (Huang et al. 1998) has great potential for analysis of this nature. Decomposing the time series into its component frequencies in this way allows the parameters of each frequency to be measured individually. The relative amplitude and phase relationship of each frequency can then be determined, along with their time dependent properties. These parameters can then be directly related to the physical properties and structure of the observed atmospheric regions above the photosphere. An accurate and consistent approach such as this will then allow the study of solar atmospheric seismology across a complete temperature range.

Chapter 8

Conclusions and Further Work

8.1 Loop Variability Campaign

The loop variability campaign was performed during 3-15 March 2004 consisting of joint observations of quiescent active regions (10567, 10569, 10570) using CDS, TRACE and MDI. Proposed further research will consist of an in-depth analysis of this campaign data-set. The principal aim of this research is to characterise the nature of the TRACE propagations at photospheric, chromospheric, transition region and coronal temperatures. The different phases of research can be summarised as follows:

Connection of He I & O V oscillations to TRACE loop propagations

The results described in Chapters 6 & 7 suggest that the propagations observed in coronal TRACE loops can be observed as intensity oscillations in the chromosphere and transition region. If these oscillations are caused by wave activity then a velocity oscillation will also be observable. Since TRACE is a bandpass imager it cannot supply any spectroscopic information. This was the motivation for the spatially resolved spectral rasters within the campaign. As far as the author is aware, the work presented in Chapters 6 & 7 are the only attempts to relate the TRACE propagations to structure and dynamics at chromospheric and transition region temperatures. The results in Chapter 7 show that the 3-min oscillations above sunspot umbrae are in fact connected to the 3-min TRACE propagations. More examples exist that are yet to

CHAPTER 8. CONCLUSIONS AND FURTHER WORK

be analysed. Further work needs to be done to determine the coherence and phase of the oscillations in the different temperature observations. The spectral data of this dataset may allow the Doppler signature and line width of the oscillations/propagations to be determined. These can be used to indicate the presence of wave/flow processes, and the relation to the TRACE propagations.

Large scale plasma properties of the active regions

The active regions observed by this campaign show quiescent loop structures at the coronal temperatures of TRACE 171 . The spatially resolved wide slit data at chromospheric and transition region temperatures reveal regions that are extremely dynamic by comparison. A number of eruptions and transient brightenings are observed along with apparent high velocity plasma flows. A preliminary examination using a large scale CDS context raster confirms a plasma flow which shows a line of sight velocity $v \approx 150 \text{ km s}^{-1}$, with an increase of non-thermal line broadening along its length. Analysis of these large scale spectroscopic rasters will allow the physical structures observed in the wide slit data and small scale spectroscopic rasters to be understood more clearly. Analysis of the magnetogram and wide slit data may allow the energetics and dynamics of these transient events to be related to magnetic reconnection processes.

Connection of TRACE WL/UV oscillations to TRACE 171 propagations

Observations have been made of oscillatory power in sunspot penumbra, plage and network regions in TRACE UV data (Muglach 2003). There is no published research investigating any connection between oscillations in the photosphere/temperature-minimum region and TRACE 171 propagations. The co-temporal TRACE WL/UV and 171 data obtained during this campaign could be used to determine if the propagations along the 171 magnetic loops can be related to oscillations/dynamics at their footpoints in the WL/UV data.

Connection of MDI oscillations to TRACE propagations

Co-temporal TRACE and MDI high resolution WL continuum, Dopplergram and magnetogram data was available during this campaign. As above, the combination of these data

allow the TRACE loop propagations to be related to their footpoints in the MDI photospheric intensity, Doppler and magnetogram fields. Hence, the photospheric p-mode signatures could be assessed as a possible driver of the TRACE/CDS propagations/oscillations. Oscillations have been observed in magnetic data in sunspot umbrae (see Settele et al. 2002, and references within). It has been suggested that these oscillations may be observable in MDI magnetogram data (Norton & Settele 2003). It is not conclusive that the oscillations in the magnetic data are physical oscillations of the magnetic field vector and distinct from instrumental effects. The connection between the TRACE/CDS propagations/oscillations and possible magnetic oscillations should be investigated. An observed relationship would be a very significant result, indicating a direct coupling and transfer of energy through the atmosphere from the photosphere to the corona.

8.2 The Atmospheric Seismology Joint Observing Program

A new SOHO joint observing program is proposed to utilise the experience already gained from the Loop Variability campaign to obtain new observations covering the complete temperature range of the solar atmosphere available with current instrumentation, using simultaneous spectroscopic and imaging data from SOHO/CDS, SOHO/MDI, SOHO/EIT, TRACE and high resolution ground based visible, vector magnetogram and polarimetry observations. In addition, newly available data from the Solar and Terrestrial Relations Observatory (STEREO) and Solar-B will also be exploited.

The proposed observing program will allow the propagation of MHD waves to be followed from the photosphere to the corona.

Photospheric MDI waves

The photospheric p-mode signatures will be assessed as a possible driver of the TRACE/CDS propagations/oscillations. The nature of the connectivity between the photosphere and corona has not been established thus far. The connection between the TRACE/CDS propagations/oscillations and photospheric intensity, photospheric Doppler velocity and possible photospheric magnetic oscillations will be investigated. An observed relationship would indicate a direct coupling and

CHAPTER 8. CONCLUSIONS AND FURTHER WORK

transfer of energy through the atmosphere from the photosphere to the corona.

Achieved by: MDI high resolution photospheric WL continuum, Doppler velocity and magnetogram observations.

Photospheric/low chromospheric TRACE WL/UV waves

Co-temporal TRACE WL/UV and 171 data will be used to determine the relation between the propagations along the 171 magnetic loops, and the driving oscillations/dynamics at their footpoints in the WL/UV data.

Achieved by: Co-temporal, high spatial/time resolution TRACE observations in the white light (photosphere), UV (low chromosphere/temperature minimum) and 171 (coronal) channels.

Photospheric/chromospheric ground based waves

The very high spatial and temporal resolution available using ground based visible band, $H\alpha$, Ca II, Ba II, vector magnetogram and polarimetry observations of the photosphere, chromosphere and magnetic field structure will allow the nature of the waves to be examined in great detail.

Achieved by: Very high spatial/time resolution observations using ground based observatories such as the Dutch Open Telescope (Rutten et al. 2004), Swedish Solar Telescope and National Solar Observatory facilities.

Chromospheric, transition region and coronal CDS & TRACE waves

The work presented in Chapter 7 is the first to show directly that the 3-min sunspot transition region oscillations and the 3-min propagating TRACE waves are the same phenomenon. The work presented in Chapter 6 suggests that the 5-min plage propagating TRACE waves can also be observed in the chromosphere/transition region. Further analysis using the CDS wide slit will greatly enhance the understanding of these 3 & 5 minute waves in sunspot and plage regions.

CHAPTER 8. CONCLUSIONS AND FURTHER WORK

Achieved by: Using SOHO/CDS to spectroscopically image the chromosphere, transition region and corona of active regions using the CDS wide slit. The CDS wide slit can produce 90"x240" intensity images in He I (Log T=4.5), O V (Log T=5.4) and Mg IX (Log T=6.0) at 30s cadence. Combined with co-temporal TRACE observations and high cadence CDS spectroscopic data, this allows the waves to be imaged and their propagation followed through the chromosphere, transition region and corona.

Upcoming STEREO & Solar-B waves

The soon to be launched STEREO mission (see Sect. 8.3) will carry an EUV imager as part of the Sun Earth Connection Coronal and Heliospheric Investigation (SECCHI) instrument package. This will produce observations in four passbands, similar to EIT, from two different view-points. This will allow the 3-D structure of active region loops to be derived, allowing the true velocity vector of propagating waves to be determined. This will permit direct measurement of the propagation speed allowing inferences of the density, temperature and pressure to be made.

The Solar-B mission will carry an EUV Imaging Spectrometer (EIS, see Sect. 8.3) that will allow spectroscopy and imaging, similar to CDS, but with high spatial/temporal/spectral resolution. The increased resolution will allow a precise investigation of the wave mode Doppler/non-thermal velocities, important in identifying specific wave modes. Solar-B will also carry the Solar Optical Telescope (SOT) producing photospheric intensity, Dopplergrams and photospheric vector magnetograms at high spatial resolution.

The proposed future research would exploit the availability of these new data to further enhance the understanding of MHD wave propagation through the atmosphere, and its applications to solar atmospheric seismology.

8.3 Future missions

Solar-B/EIS

The Solar-B mission is due to be launched in September 2006. A further progression of the results from Chapters 6 & 7 will be to observe the TRACE propagations at different temperatures using the kind of data provided by the EUV Imaging Spectrometer (EIS) on Solar-B. A future study using EIS has been proposed “Coronal Loop Variability - Propagating Oscillations”. The characteristics of these propagating waves could be observed with EIS utilising the high time resolution in a number of different lines. Observations using the EIS slots in different temperature lines will provide the ideal data set to advance the CDS wide slit/TRACE observations and allow these propagations to be characterised at different temperatures, at a much higher cadence and spatial resolution.

Another proposed possible study “Coronal Loop Variability - Time dependent diagnostics” intends to use high time resolution spectroscopic observations of coronal loops. These observations would yield *high cadence/time dependent plasma diagnostics* within coronal loops. These data will finally allow the physical properties of the oscillations to be determined. This will indicate the correct theoretical model for these waves allowing their dissipation to be described and placed in the context of coronal heating.

STEREO

The Solar Terrestrial Relations Observatory (STEREO) is due to be launched in February 2006. The STEREO mission consists of two identical spacecraft that will observe the Sun from Lagrange points ahead and behind the Earth’s orbit. In addition to coronagraphs the spacecraft will each carry an Extreme Ultra-Violet Imager (EUVI). These will allow solar structures, such as active region loops, to be observed in three dimensions for the first time, removing the projection effects from the propagating oscillations.

CHAPTER 8. CONCLUSIONS AND FURTHER WORK

SDO

The Solar Dynamics Observatory (SDO) is scheduled to be launched in 2008. SDO will carry instruments that improve upon the ones currently in operation, such as MDI and TRACE. An extreme ultra-violet imager will produce full disk observations of the Sun at a similar resolution to TRACE in a number of bandpasses simultaneously, so as to observe at a range of temperatures rather than 171 Å alone.

Solar Orbiter

Solar orbiter is scheduled for launch in 2013, and will use close approach orbit of the Sun to produce in-situ measurements of the temperature, density and magnetic field in the corona. The proximity to the Sun will allow a very high spatial resolution to be achieved allowing a detailed investigation of dynamic phenomena. This may allow the sausage and torsional MHD wave modes within magnetic structures to be observed for the first time.

Appendix A

Active Region Structure and Dynamics

A.1 Vector Path Extraction Method

To simplify the analysis of observed solar structures, a coordinate system that is parallel to the axis of the structure is used. This is achieved by extracting data along a defined path along the length of the structure; for example a path can be defined along a curved loop. The extracted intensity, velocity, or line width data can then be analysed as a linear function of distance along the feature.

The rastered CDS data analysed here are formed by rastering the 4'' slit. Therefore, the data pixels are not square, and have a scale of $4.06'' \times 1.68''$. To ensure the extracted vectors have the same component scale in all orientations, the data is resampled to form a square array. The data is resampled to a square pixel scale of $1.68''$ using nearest neighbour resampling.

In the case of a loop, the path is defined by selecting a number of points to form sections along the axis of the structure. Consecutive pairs of points define a section vector \bar{v} . Perpendicular vectors \bar{p} are calculated, and used to extract the data along the length of \bar{v} (Fig. A.1). The process is repeated for the next set of consecutive points to extract the data for each section along the total length of the defined path.

\bar{p} is calculated as follows: \bar{v} and \bar{p} are perpendicular

$$\bar{v} \cdot \bar{p} = 0$$

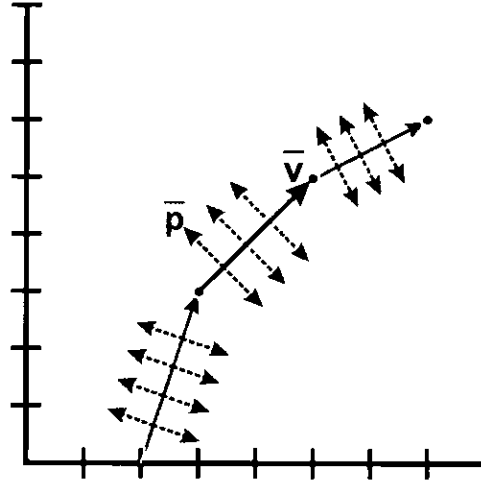


Figure A.1: Data is extracted along a defined path by selecting points which define section vectors \bar{v} . Perpendicular vectors \bar{p} are calculated to divide each section vector into cross-sections. The data in each cross-section is extracted to produce data in an orthogonal coordinate system along the length of the defined path.

$$\Rightarrow \bar{v}_x \bar{p}_x + \bar{v}_y \bar{p}_y = 0$$

where $\bar{v}_x, \bar{p}_x, \bar{v}_y, \bar{p}_y$ are the x and y components of \bar{v} and \bar{p} . Then

$$\bar{p}_x = \frac{-\bar{v}_y \bar{p}_y}{\bar{v}_x}.$$

Since \bar{v}_x and \bar{v}_y are known, an arbitrary value of \bar{p}_y can be chosen to calculate \bar{p}_x .

Given unit vector $\hat{p} = \frac{\bar{p}}{|\bar{p}|}$, any point along \bar{p} is then given by

$$p_{(x,y)} = p_{(x_i,y_i)} + \lambda \hat{p}$$

where $p_{(x_i,y_i)}$ is the point lying on the vectors \bar{p} and \bar{v} , and λ defines the length of \bar{p} . The vectors \bar{p} and $-\bar{p}$ divide \bar{v} into cross sections of length 2λ and extract the data at each point along \bar{v} . No check is made for repeated pixels in each cross-section; therefore, highly curved paths will include repeated pixels along the inner edge of curvature.

A.2 Errors of fitted Gaussian parameters

The errors for the fitted Gaussian amplitude, position and width parameters are the sigma values returned by the routine CFIT_ERROR.

A.3 Calculation of errors for fitted line intensity

The fitted line width returned by the program CFIT is the full-width-half-maximum (FWHM) of the fitted Gaussian. The error in the fitted line intensity is calculated as follows (see Thompson 2000). The integrated intensity of a Gaussian is given by

$$I = \frac{1}{2} \sqrt{\frac{\pi}{\ln 2}} A w_f$$

where I is the line intensity, A is the amplitude of the Gaussian and w_f is the Gaussian FWHM. The calculated error in the fitted line intensity is therefore

$$\left(\frac{\sigma_I}{I}\right)^2 = \frac{1}{2} \left[\left(\frac{\sigma_A}{A}\right)^2 + \left(\frac{\sigma_w}{w}\right)^2 \right]$$

where σ_I is the value of sigma for intensity, σ_A is the value of sigma for the fitted line amplitude returned by CFIT, and σ_w is the value of sigma for the fitted line width returned by CFIT.

A.4 Calculation of errors for measured Doppler velocity

The errors in the calculated Doppler velocity are calculated as follows. The Doppler velocity is given by

$$V = \frac{d\lambda}{\lambda_0} c$$

Therefore,

$$\left(\frac{\Delta V}{V}\right)^2 \equiv \left(\frac{\Delta d\lambda}{d\lambda}\right)^2 + \left(\frac{\Delta \lambda_0}{\lambda_0}\right)^2$$

where $d\lambda = \lambda_1 - \lambda_0$

APPENDIX A. ACTIVE REGION STRUCTURE AND DYNAMICS

$$\Rightarrow \Delta d\lambda = (\Delta\lambda_1^2 + \Delta\lambda_0^2)^{\frac{1}{2}}$$

λ_1 = Fitted Gaussian position

λ_0 = Rest wavelength position

$\Delta\lambda_1$ = Sigma of fitted Gaussian position

$\Delta\lambda_0$ = Sigma of fitted Gaussian positions used to calculate mean rest wavelength position

A.5 Calculation of errors for average extracted profile

Once the data has been extracted, the data is in the form of a 2-D array of cross sections extracted along the length of the path. To quantify properties such as intensity, velocity, and line width as a function of length, the mean value of each cross section is calculated to form the mean profile as a function of path length. Certain pixels within the data are marked as missing due to, for example, a poor line fit or missing data. These pixels are not included when calculating the mean of each cross section. The mean of each cross section is given by

$$M_i = \frac{1}{n} \sum_{j=0}^{n-1} P_{i,j}$$

where i = index of each cross section

j = index of the pixels in each cross section

n = total number of finite value pixels in each cross section

M_i = mean value of the cross section i

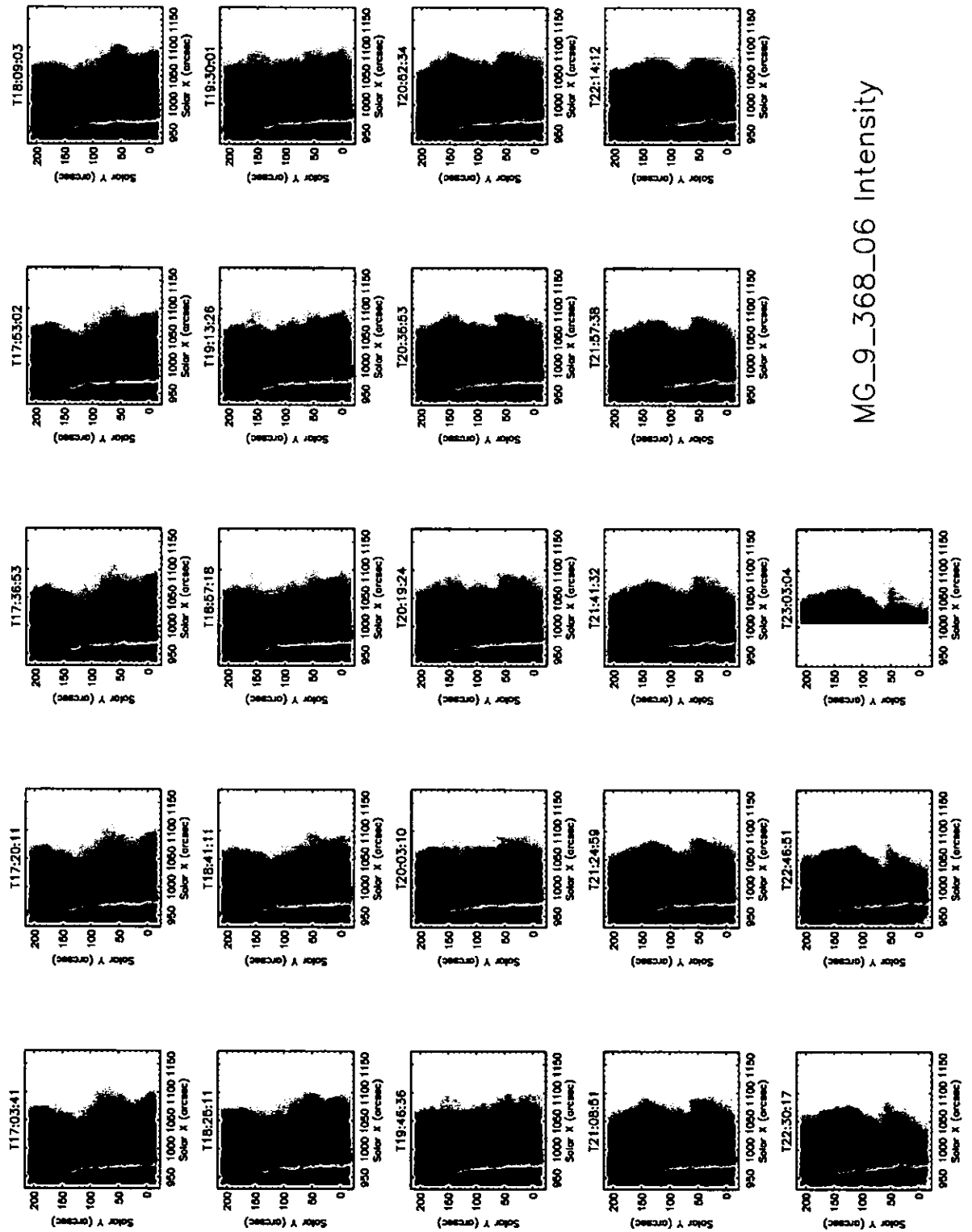
$P_{i,j}$ = value at pixel j in cross section i

The error in the mean of each cross section is calculated as

$$\Delta M_i = \frac{1}{n} \left(\sum_{j=0}^{n-1} \Delta P_{i,j}^2 \right)^{\frac{1}{2}}$$

where ΔM_i = error in the average value, and $\Delta P_{i,j}$ = sigma of the value at pixel j in cross section i

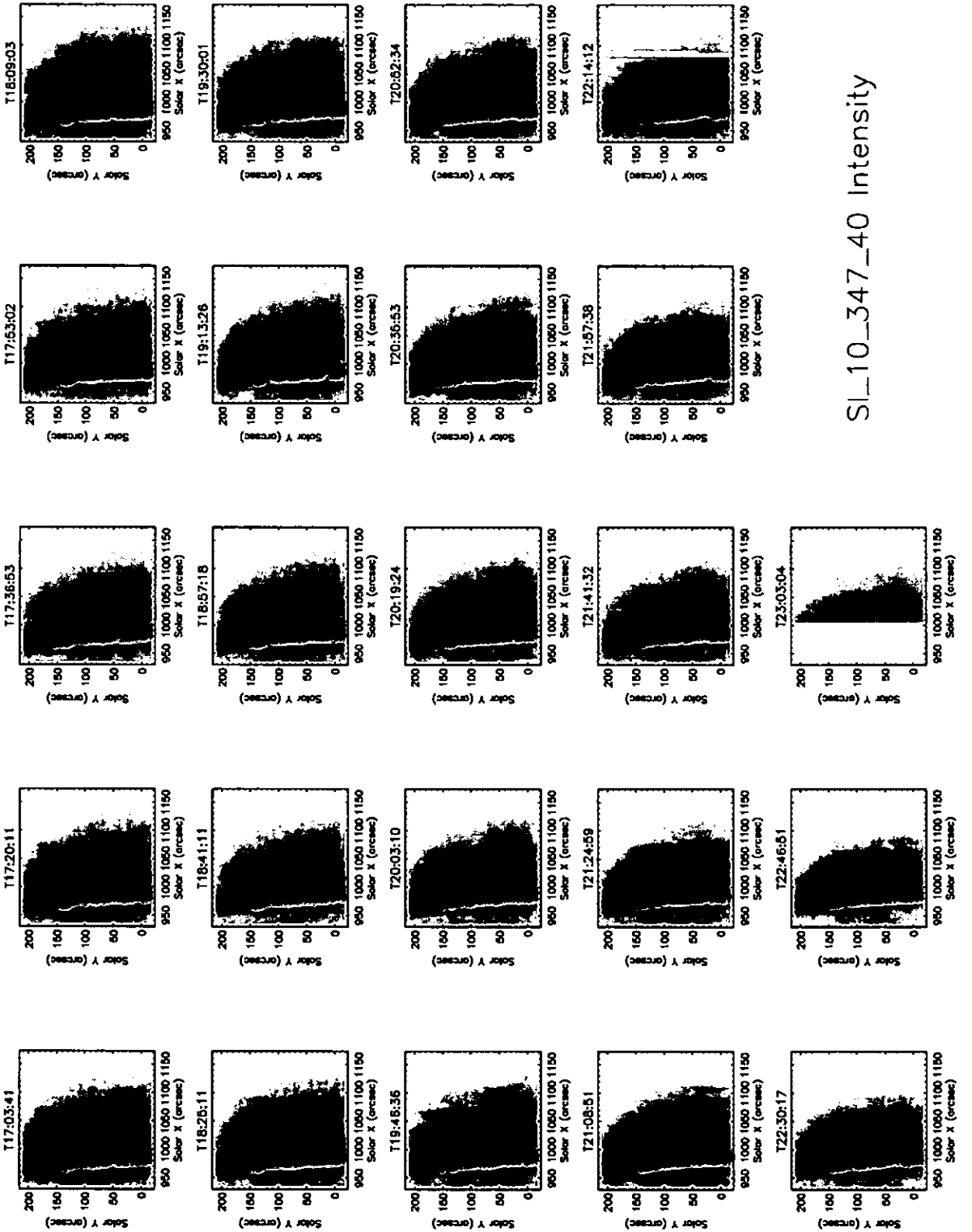
APPENDIX A. ACTIVE REGION STRUCTURE AND DYNAMICS



MG_9_368_06 Intensity

Figure A.3: Mg IX 368 Å negative context images for all rasters.

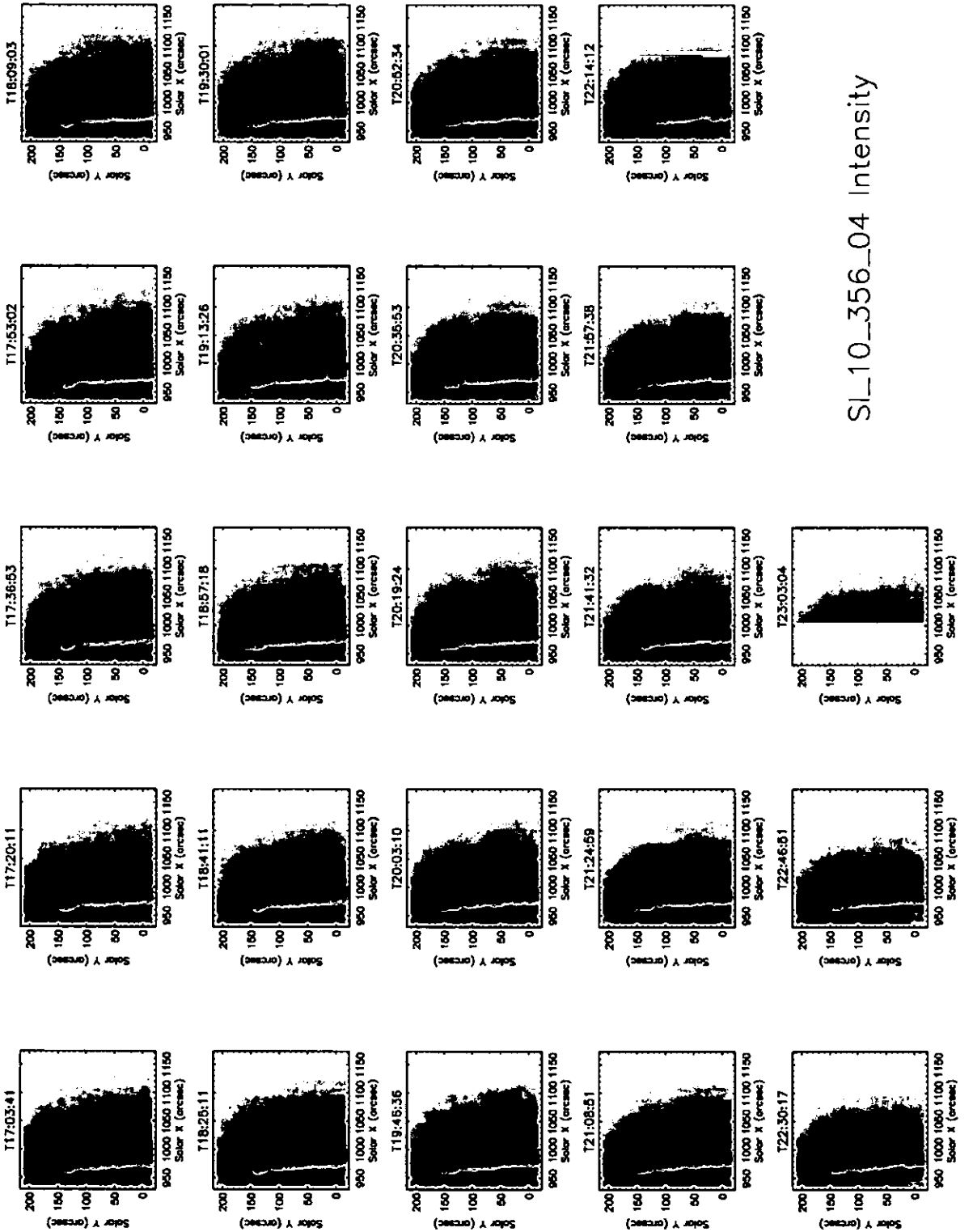
APPENDIX A. ACTIVE REGION STRUCTURE AND DYNAMICS



SI_10_347_40 Intensity

Figure A.4: Si X 347 Å negative context images for all rasters.

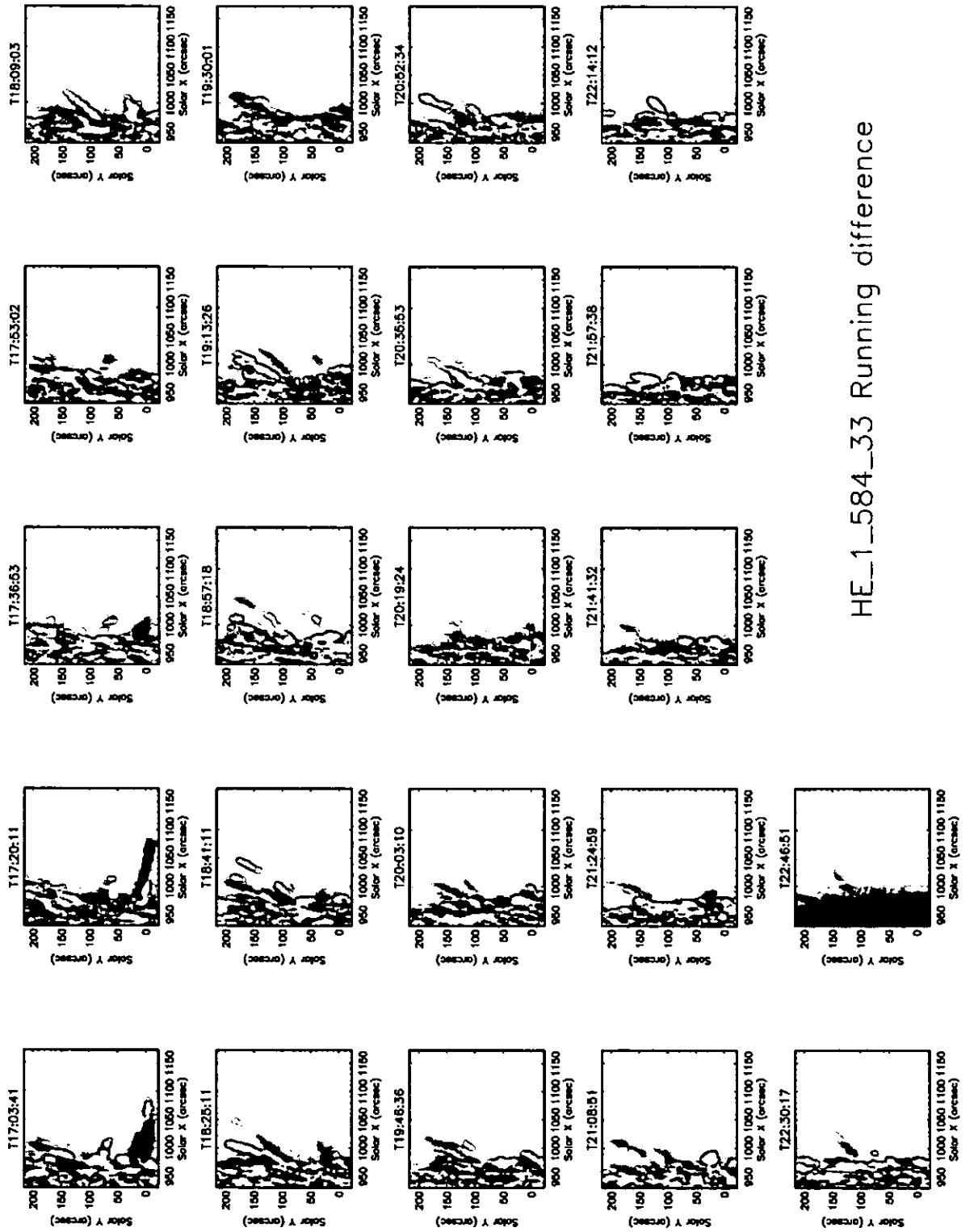
APPENDIX A. ACTIVE REGION STRUCTURE AND DYNAMICS



SL10_356_04 Intensity

Figure A.5: Si X 356 Å negative context images for all rasters.

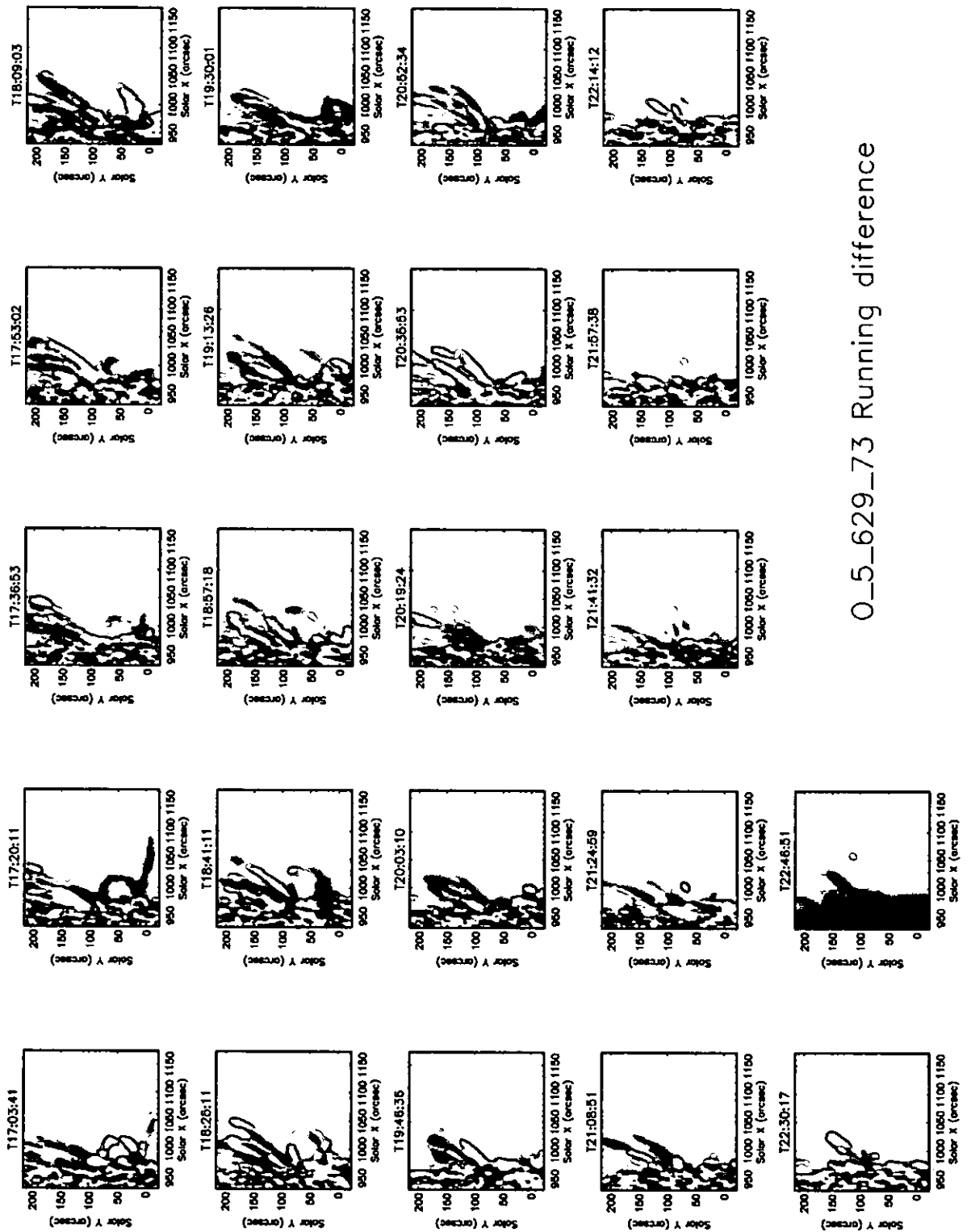
APPENDIX A. ACTIVE REGION STRUCTURE AND DYNAMICS



HE_1_584_33 Running difference

Figure A.6: He I 584 Å running difference images.

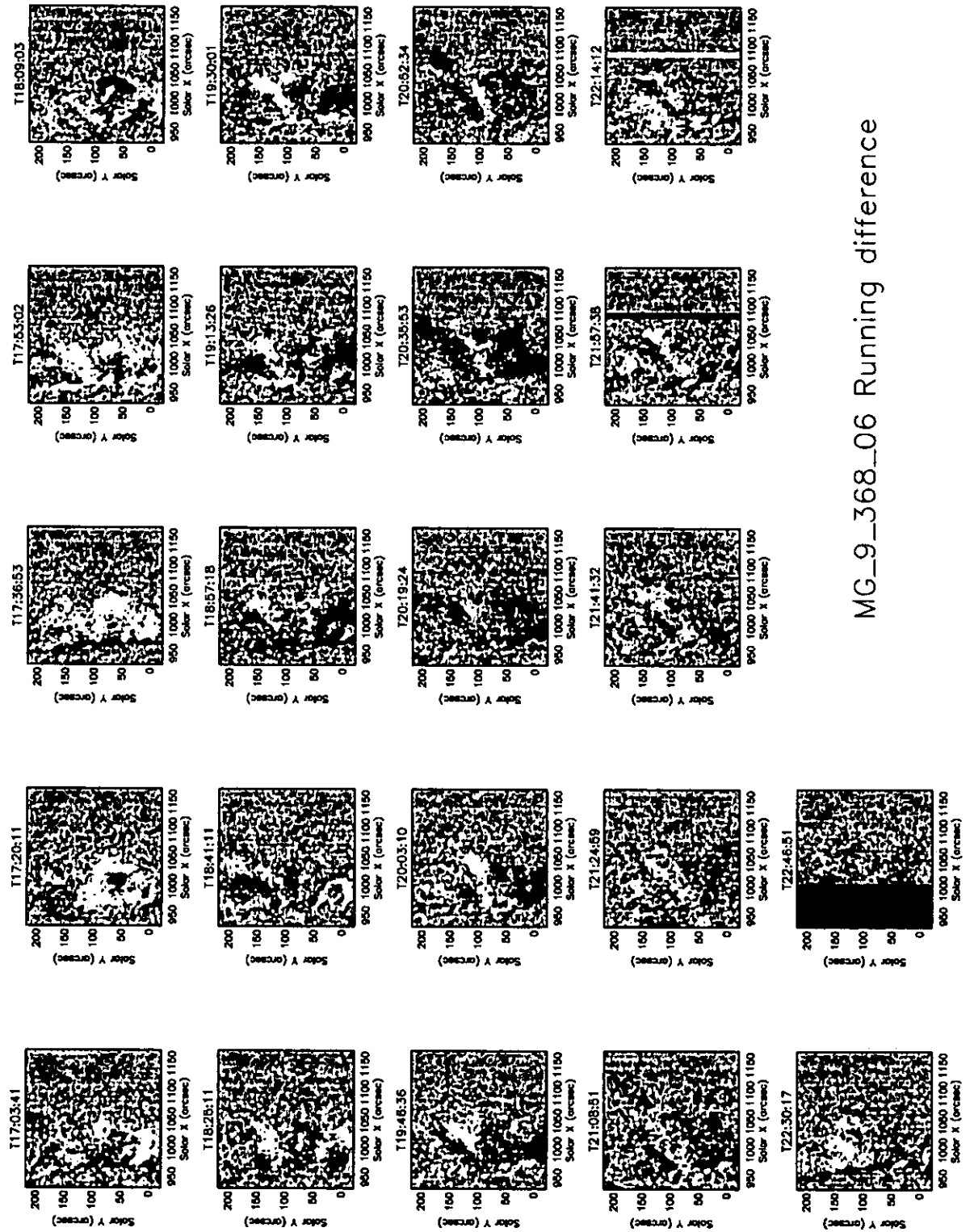
APPENDIX A. ACTIVE REGION STRUCTURE AND DYNAMICS



0_5_629_73 Running difference

Figure A.7: O V 629 Å running difference images.

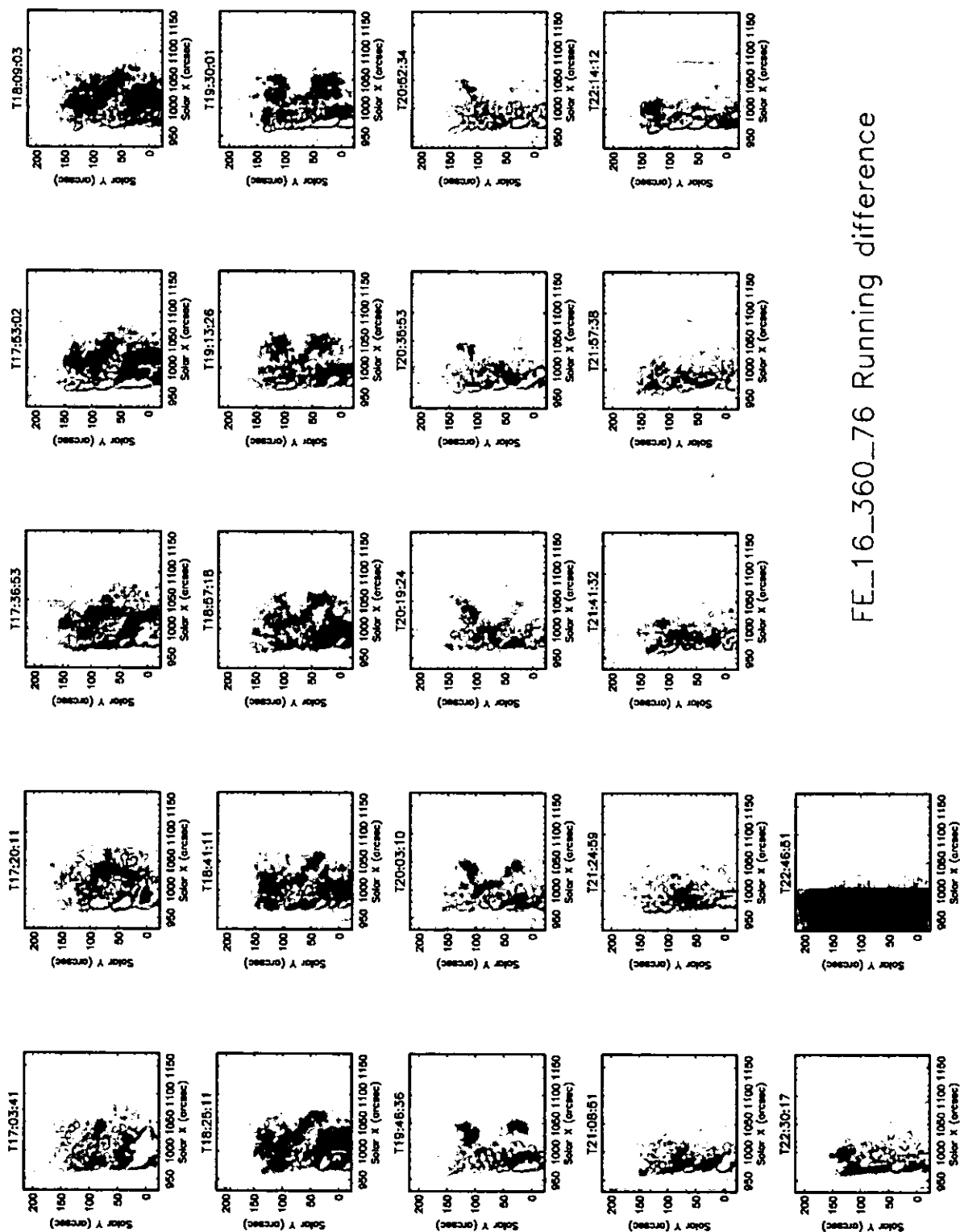
APPENDIX A. ACTIVE REGION STRUCTURE AND DYNAMICS



MG_9_368_06 Running difference

Figure A.8: Mg IX 368 Å running difference images.

APPENDIX A. ACTIVE REGION STRUCTURE AND DYNAMICS



FE_16_360_76 Running difference

Figure A.9: Fe XVI 360 Å running difference images.

APPENDIX A. ACTIVE REGION STRUCTURE AND DYNAMICS

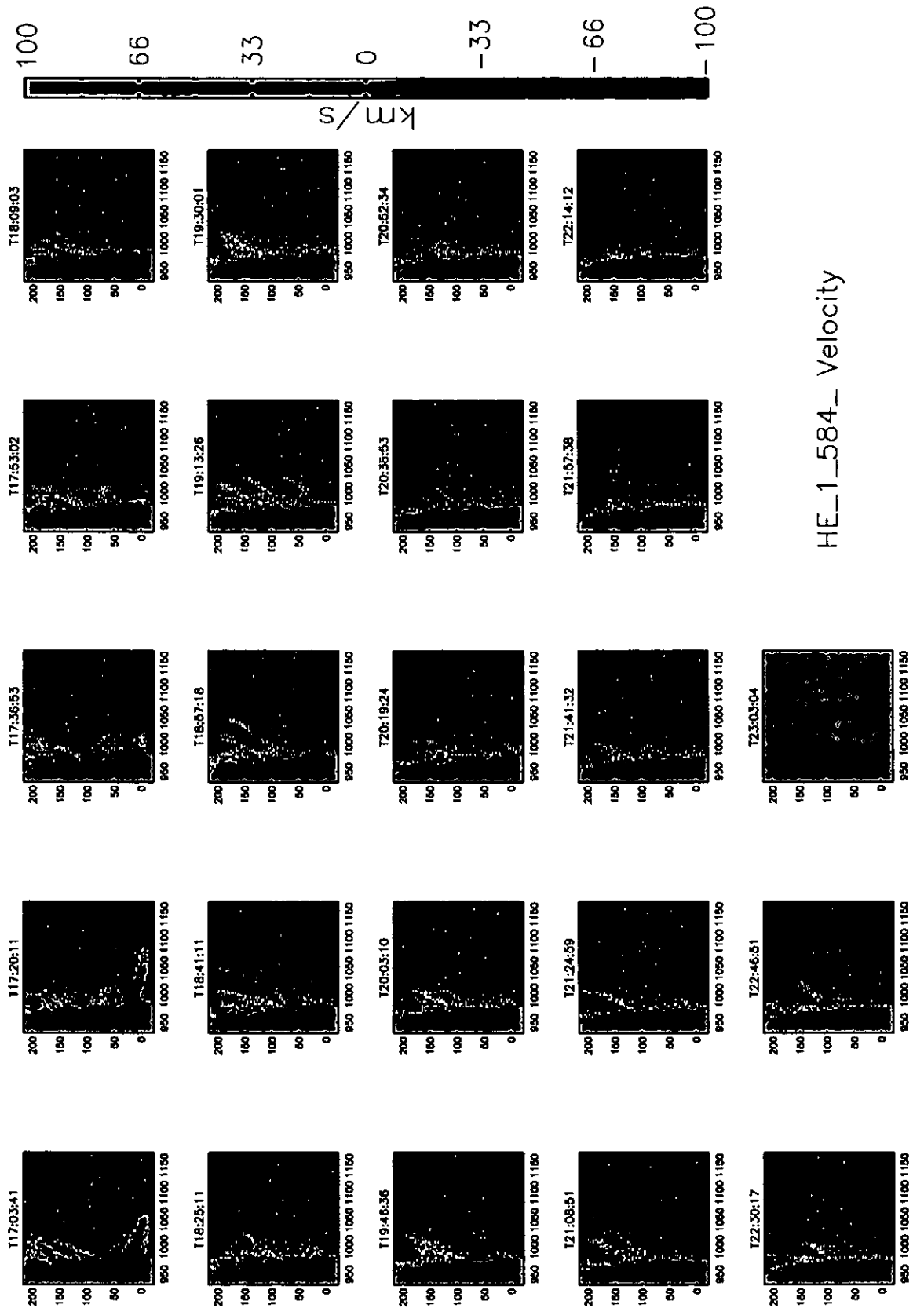


Figure A.10: He I 584 Å Doppler velocity maps.

APPENDIX A. ACTIVE REGION STRUCTURE AND DYNAMICS

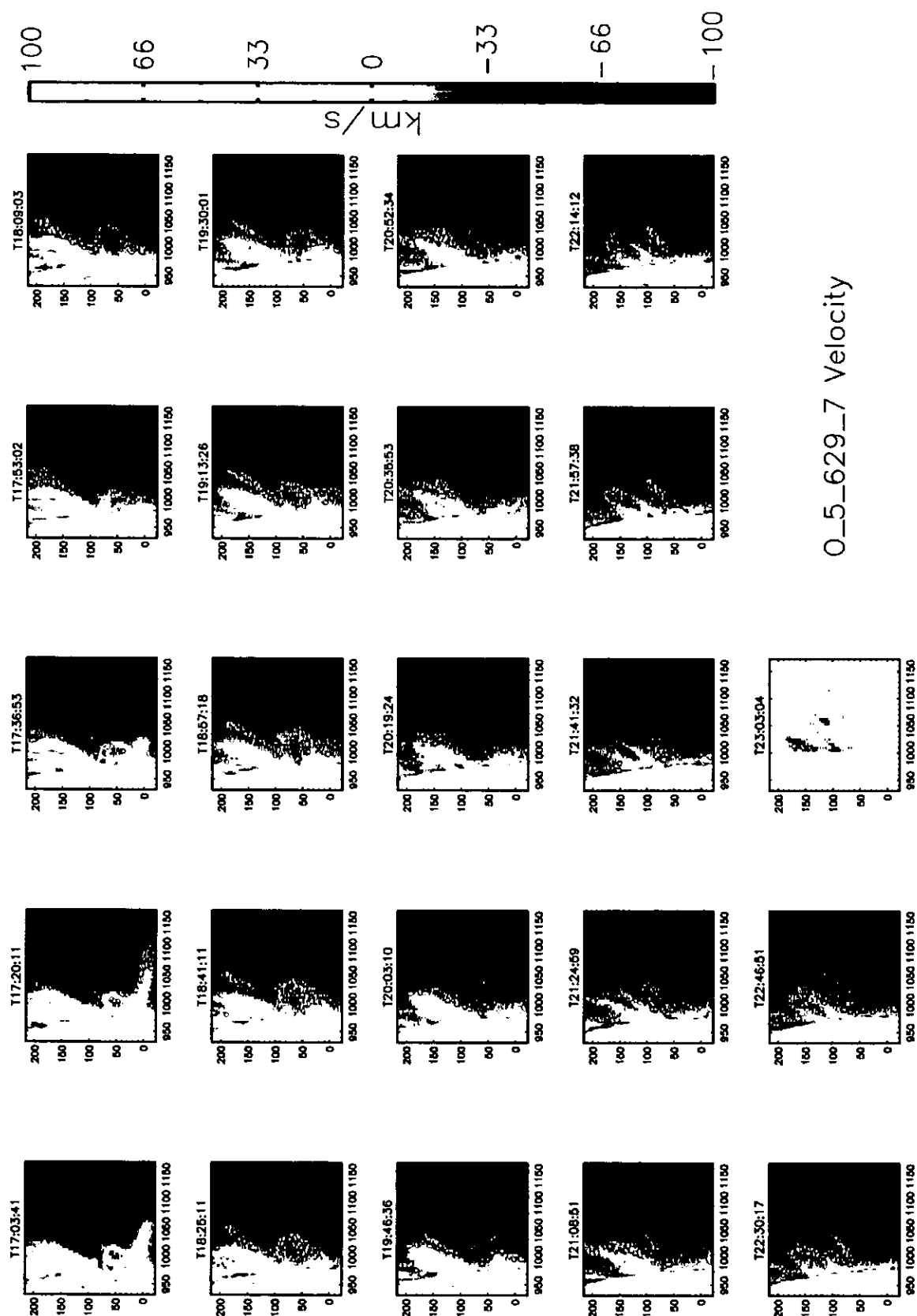


Figure A.11: O V 629 Å Doppler velocity maps.

APPENDIX A. ACTIVE REGION STRUCTURE AND DYNAMICS

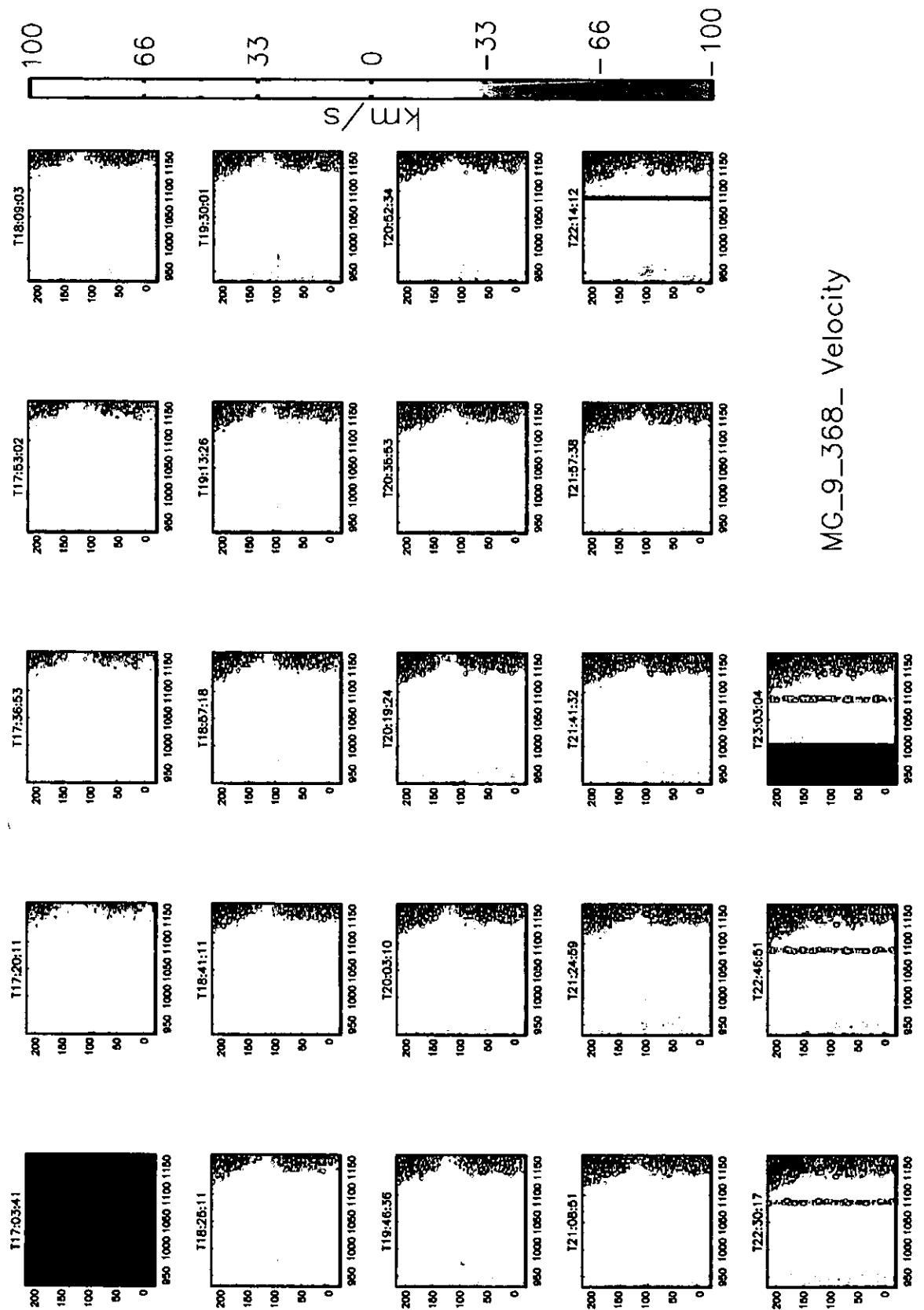
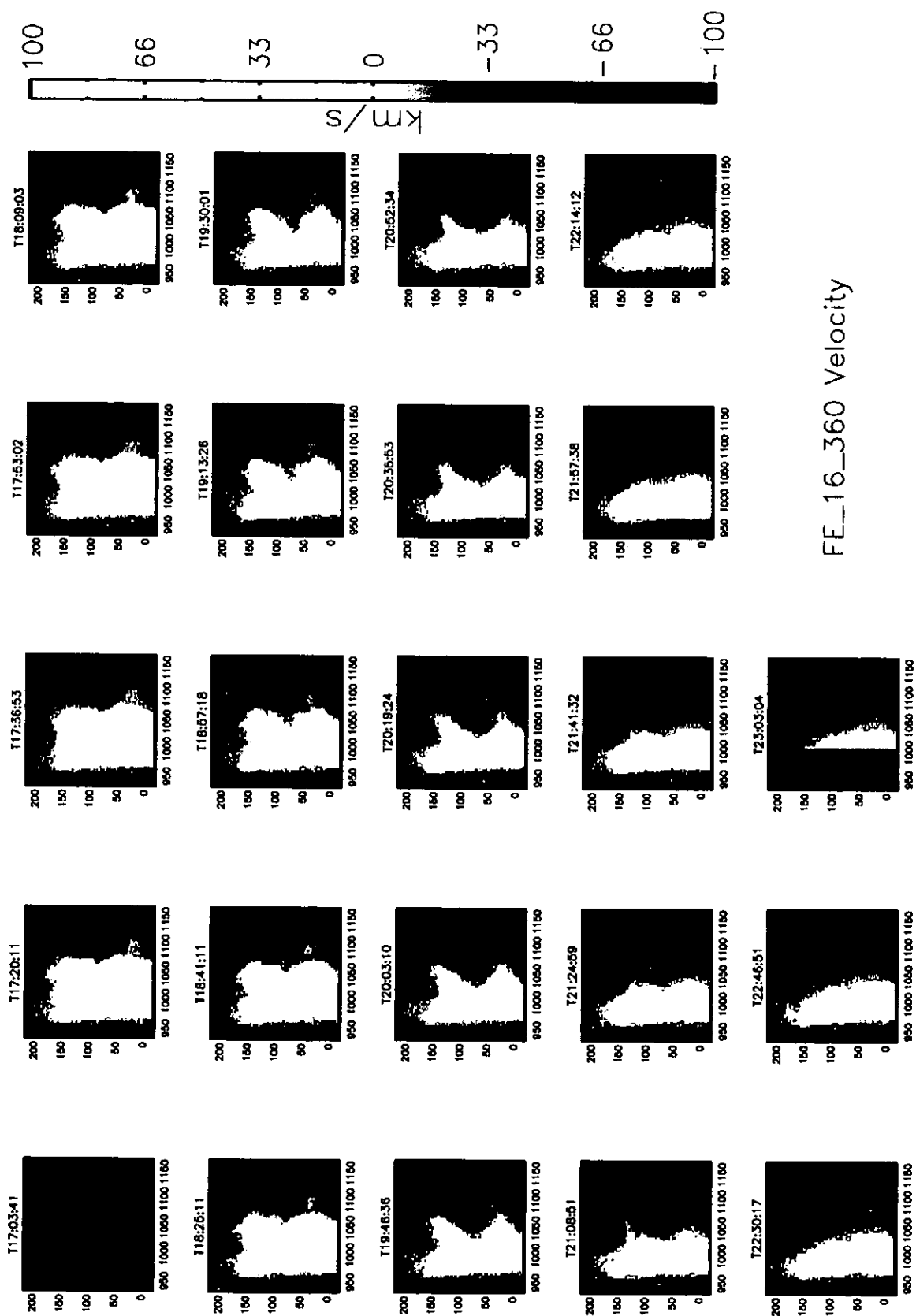


Figure A.12: Mg IX 368 Å Doppler velocity maps.

APPENDIX A. ACTIVE REGION STRUCTURE AND DYNAMICS



FE_16_360 Velocity

Figure A.13: Fe XVI 360 Å Doppler velocity maps

Table B.1: Summary of loop variability campaign observations

Date	Target	CDS			TRACE		MDI	
		Program	Study	Time (UT)	Sequence	Time (UT)	Sequence	Time (UT)
2/3/04	AR 10567	GENE	s29633r00-03	08:17-10:09	171 @ 30s	Whole day	FD I, M, V	Daily
		UCLAN_MV	s29634r00-04	10:09-10:53				
		LOOP2D_5	s29635r00-299	10:53-15-28				
		GENE	s29636r00-03	16:02-17:54				
		LOOP2D_5	s29637r00-299	17:54-22:29				
GENE	s29638r00-03	22:29-00:21 ⁺¹						
3/3/04	AR 10567	EJECT_V3	s29640r00-03	07:35-08:42	171 @ 30s	Whole day	FD I, M, V HR I, M	Daily 09:00-10:00
		LOOP2D_5	s29641r00-400	08:42-14:49				
		EJECT_V3	s29642r00-01	15:23-15:56				
		LOOP2D_5	s29643r00-150	15:56-18:13				
LOOP2D_5	s29644r00-199	18:13-21:17						
4/3/04	AR 10567	EJECT_V3	s29647r00-03	07:45-08:53	171 @ 30s	00:00-14:00	FD I, M, V	Daily
		LOOP2D_5	s29648r00-300	08:53-13:28				
5/3/04	AR 10567	EJECT_V3	s29654r00-03	07:11-08:18	171 @ 30s	00:00-14:00	FD I, M, V	Daily
		LOOP2D_5	s29655r00-109	08:18-09:59				
6/3/04	AR 10569	EJECT_V3	s29665r00	07:29-07:46	171 @ 30s	00:00-14:00	FD I, M, V HR I, M, V	Daily 07:00-08:00
		UCLAN_MV	s29666r00-04	07:46-08:30				
		LOOP2D_5	s29667r00-209	08:30-11:43				
		EJECT_V3	s29668r00	11:43-11:59				
8/3/04	AR 10569	EJECT_V3	s29687r00	06:51-07:08	171 @ 30s	00:00-14:00	FD I, M, V HR I, M	Daily 11:00-12:00
		LOOP2D_5	s29688r00-419	07:29-13:54				
		EJECT_V3	s29689r00	13:54-14:10				
9/3/04	AR 10570	EJECT_V3	s29693r00	06:47-07:05	171 @ 30s	00:00-14:00	FD I, M, V	Daily
		LOOP2D_5	s29694r00-249	07:05-10:54				
		LOOP2D_5	s29695r00-49	10:54-11:40				
		LOOP2D_5	s29696r00-294	11:40-16:11				
10/3/04	AR 10570	EJECT_V3	s29709r00	06:29-06:47	171 @ 30s	00:00-14:00	FD I, M, V	Daily
		LOOP2D_5	s29710r00-189	06:47-09:41	171/1550 @ 30s	10:00-11:00		
		LOOP2D_5	s29711r00-234	10:00-13:35				
		EJECT_V3	s29712r00	13:35-13:51				
11/3/04	AR 10570	EJECT_V3	s29721r00	06:49-07:07	171 @ 30s	00:00-14:00	FD I, M, V	Daily
		LOOP2D_5	s29722r00-429	07:07-13:41	171/WL @ 30s	10:00-11:00		
		EJECT_V3	s29723r00	13:41-13:57				
12/3/04	AR 10570	EJECT_V3	s29727r00	06:49-07:07	171 @ 30s 171/1600 @ 30s	00:00-14:00 12:00-13:00	FD I, M, V HR I, M, V	Daily 14:00-15:00
		EJECT_V3	s29729r00	07:07-11:32				
		UCLAN_MV	s29730r00-04	12:05-12:48				
		LOOP2D_5	s29732r00-199	12:49-15:52				
		EJECT_V3	s29733r00-01	unrecoverable				
13/3/04	AR 10570	EJECT_V3	s29738r00	06:30-06:47	171 @ 30s 171/1600 @ 30s	00:00-14:00 07:00-08:00	FD I, M, V HR I, M, V	Daily 06:00-08:00
		UCLAN_MV	s29739r00-04	07:08-07:52				
		EJECT_V3	s29740r00-02	07:52-08:40				
		LOOP2D_5	s29741r00-199	08:40-11:44				
		EJECT_V3	s29742r00-01	11:44-12:16				

APPENDIX B. CDS WIDE SLIT & TRACE ACTIVE REGION DYNAMICS

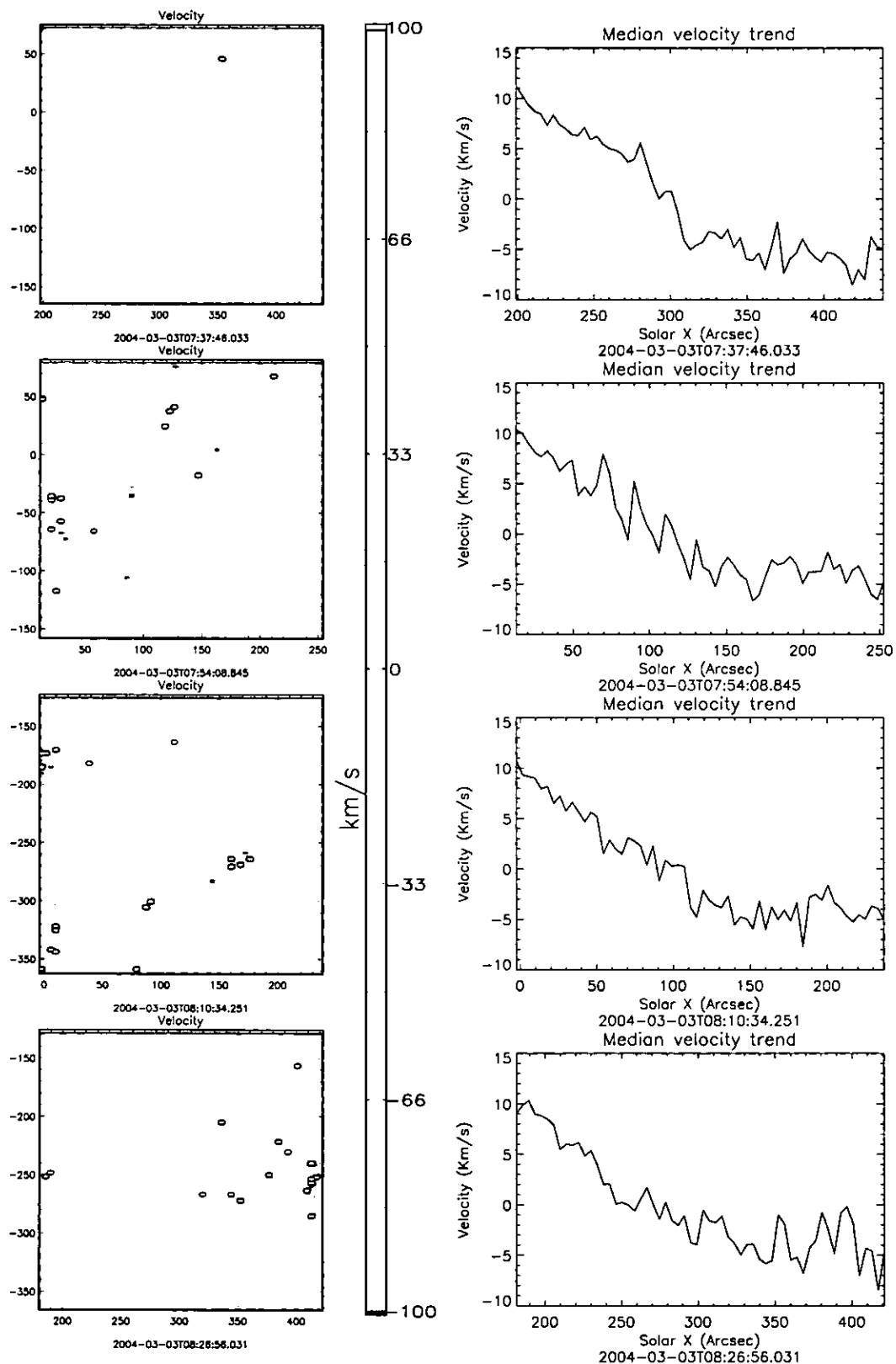


Figure B.1: EJECT_V3 s29640r00-03 spectral tilt. Left: E-W line position trend is visible in raster Doppler maps. Right: Median Doppler velocity trend in the E-W direction.

APPENDIX B. CDS WIDE SLIT & TRACE ACTIVE REGION DYNAMICS

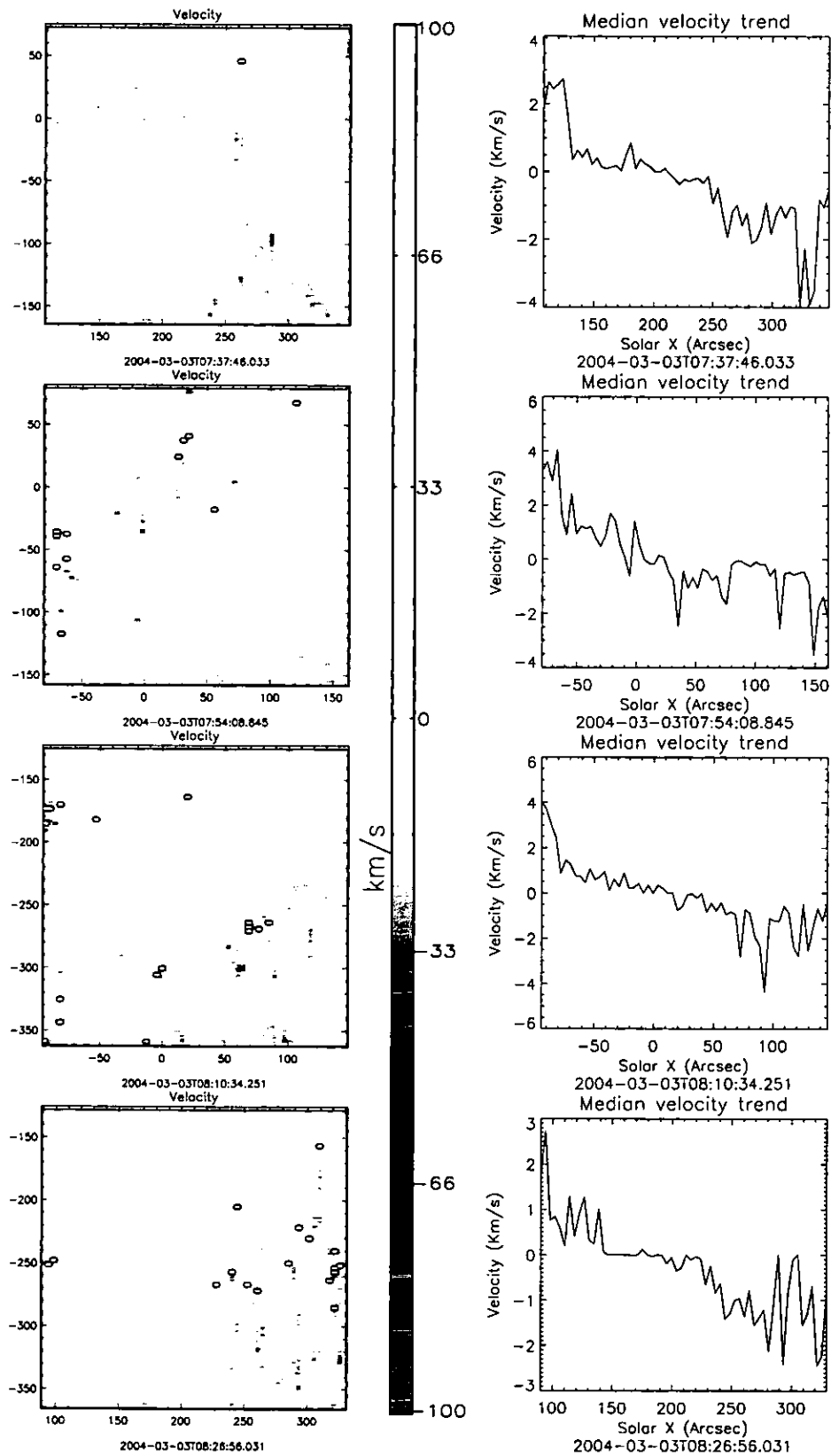


Figure B.2: EJECT_V3 s29640r00-03 corrected spectral tilt. Left: Raster Doppler maps after median trend subtraction. Right: Doppler velocity trend in the E-W direction recalculated after median trend subtraction.

APPENDIX B. CDS WIDE SLIT & TRACE ACTIVE REGION DYNAMICS

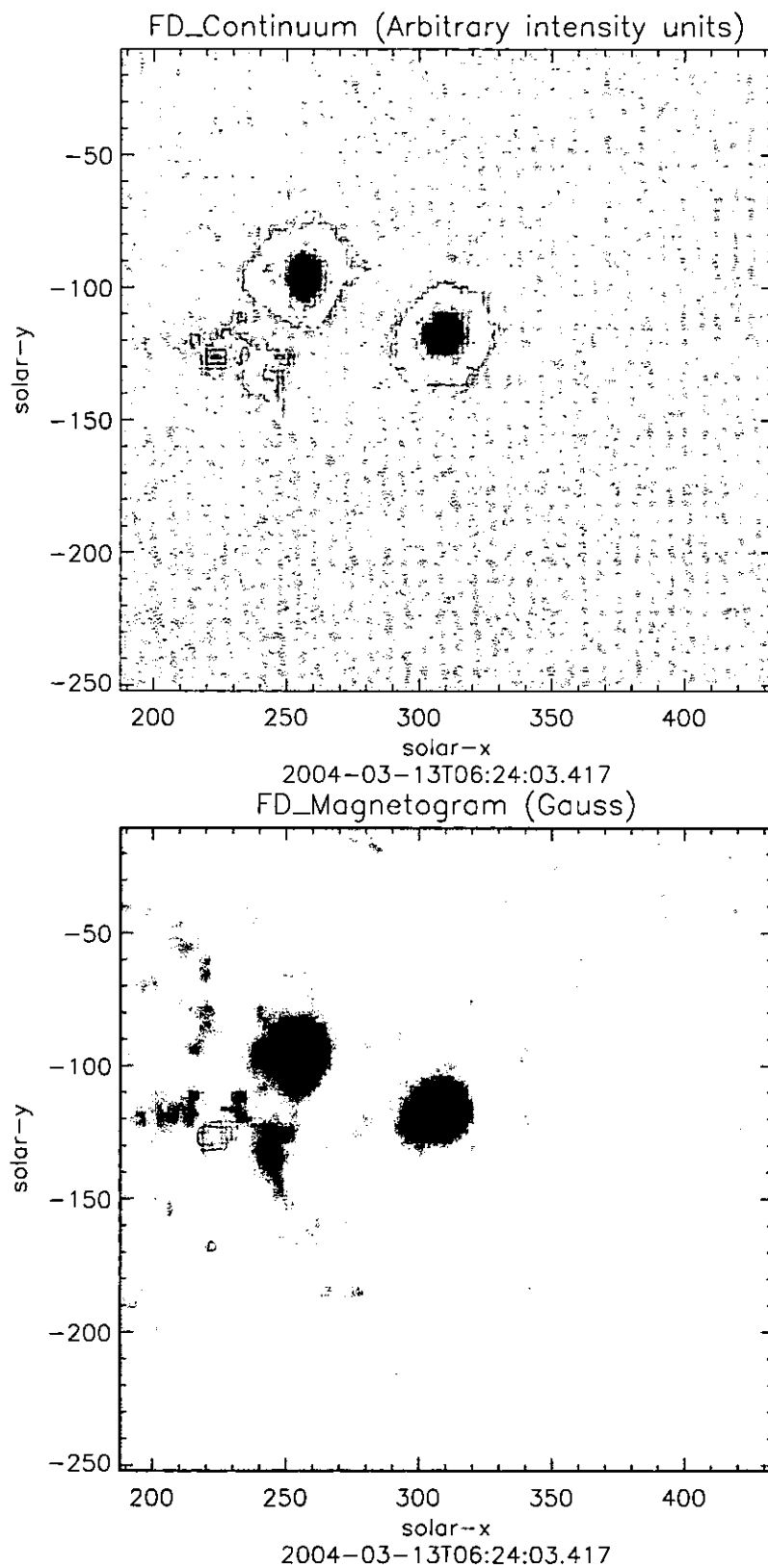


Figure B.3: MDI WL and magnetogram of AR 10570 with f.o.v. of EJECT_V3 s29740.

APPENDIX B. CDS WIDE SLIT & TRACE ACTIVE REGION DYNAMICS

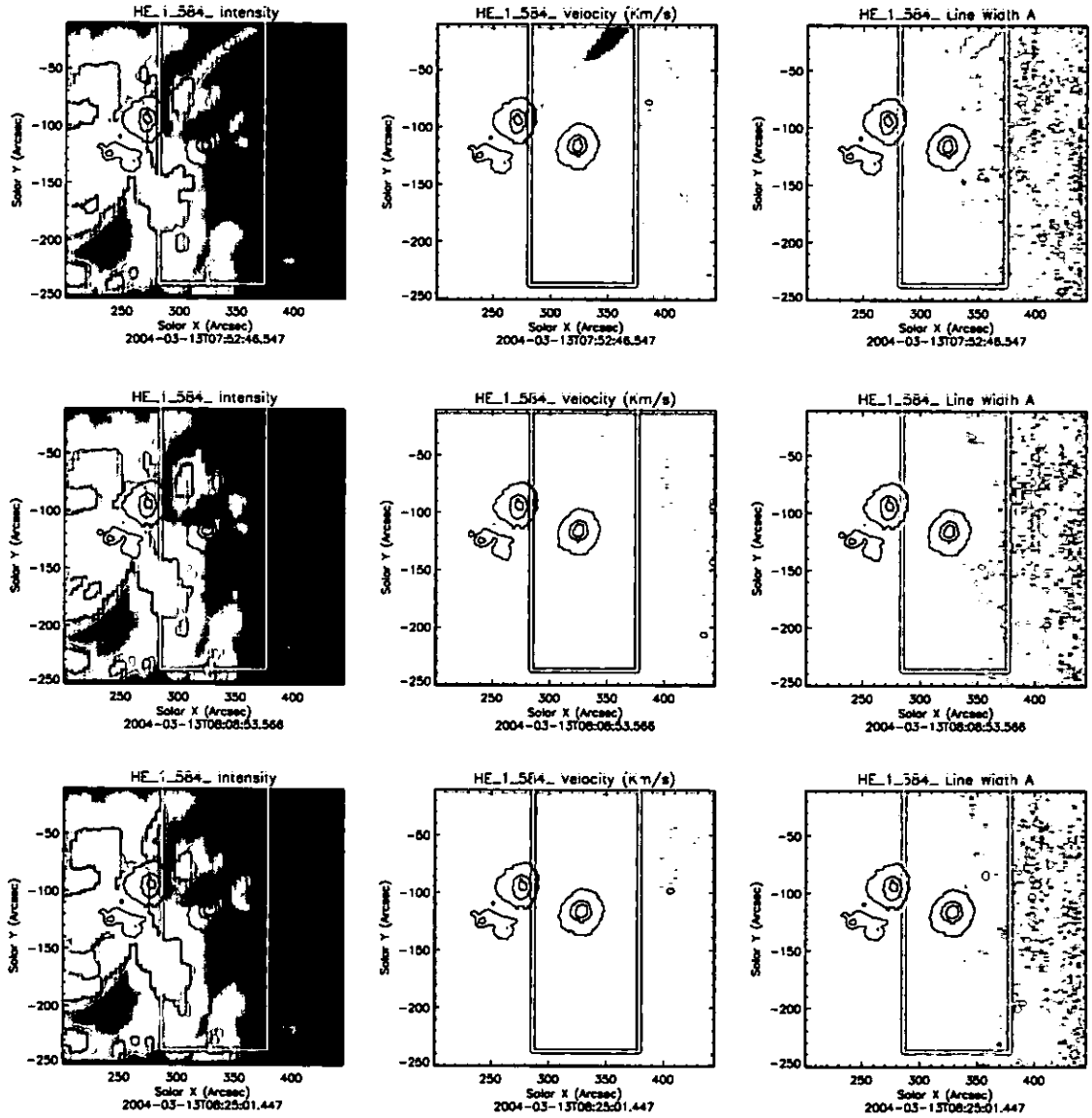


Figure B.4: EJECT_V3 s29740r00-02 in He I overplotted with the wide slit f.o.v. and MDI intensity white light contours.

APPENDIX B. CDS WIDE SLIT & TRACE ACTIVE REGION DYNAMICS

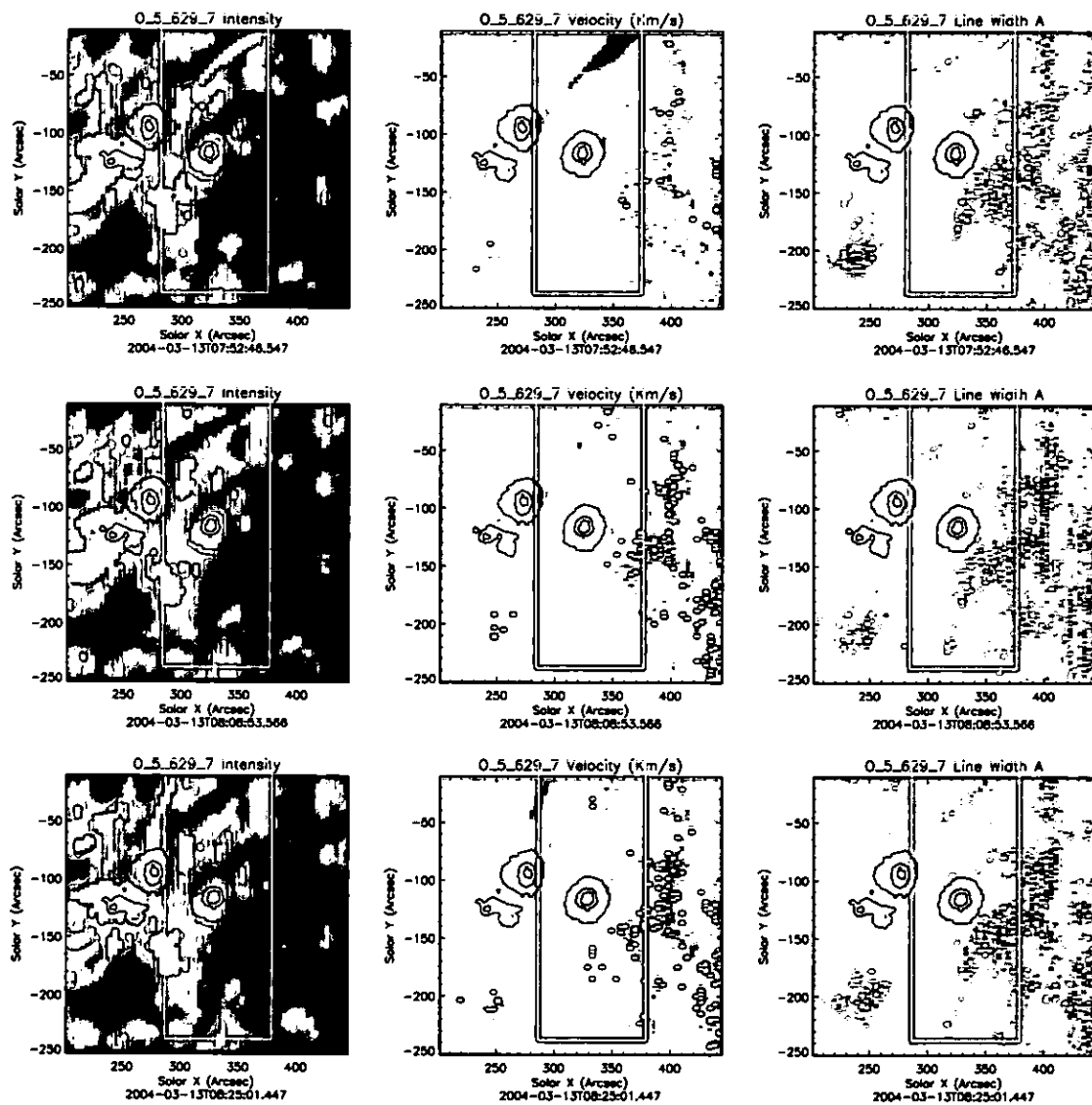


Figure B.5: EJECT_V3 s29740r00-02 in O V overplotted with the wide slit f.o.v. and MDI intensity white light contours.

APPENDIX B. CDS WIDE SLIT & TRACE ACTIVE REGION DYNAMICS

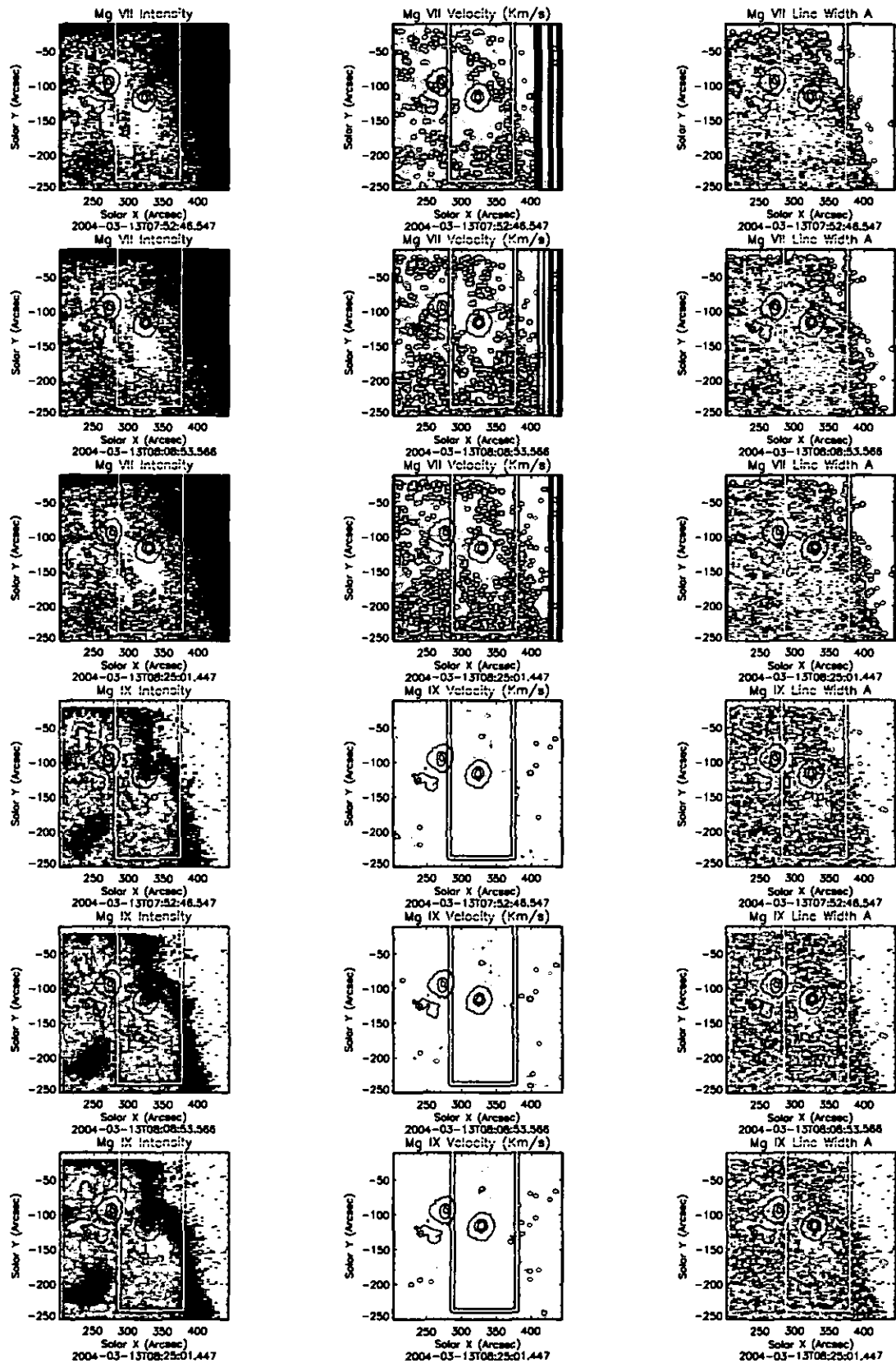


Figure B.6: EJECT.V3 s29740r00-02 in Mg VII/IX overlotted with the wide slit f.o.v. and MDI intensity white light contours.

APPENDIX B. CDS WIDE SLIT & TRACE ACTIVE REGION DYNAMICS

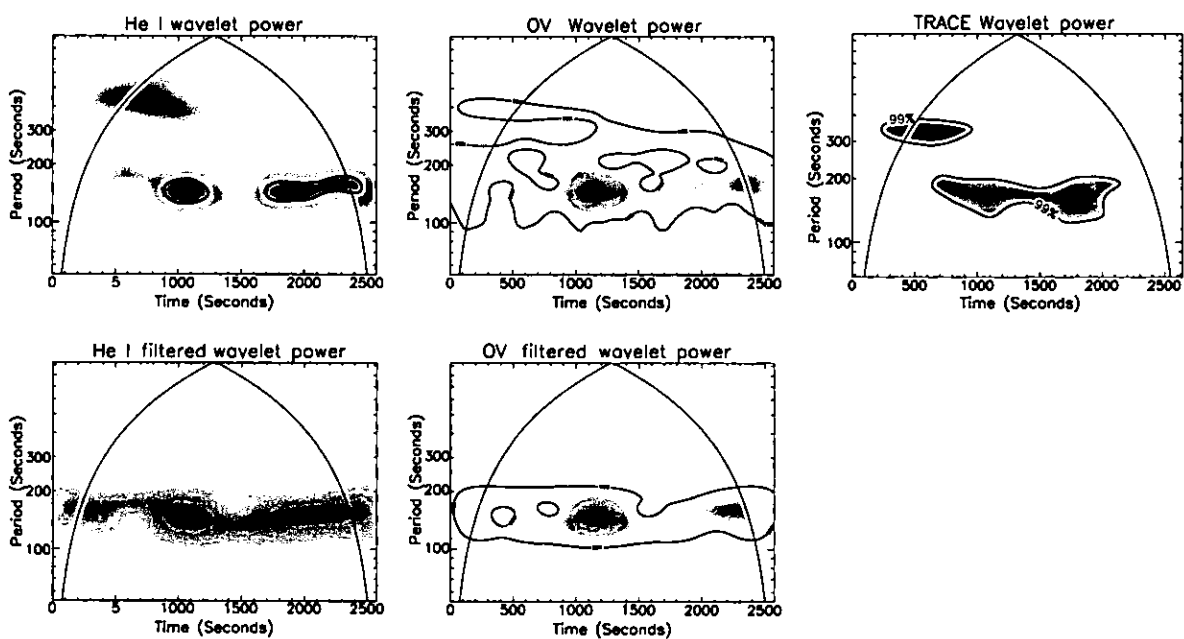


Figure B.11: Wavelet power spectra for the He I, O V and TRACE time series. The bottom two plots show the wavelet power spectra for the filtered He I and O V time series. Contours indicate 99% confidence levels. Note TRACE time series begins 480 s before CDS He I & O V.

Appendix C

Contents of the CD-ROM

The CD-ROM contains the electronic components of the thesis relevant to the work described in Chapters 5 and 7, in addition to html and pdf versions of the thesis. The CD uses a web interface; to access the contents open the file *index.htm* which contains the home menu of the CD. Use the navigation bar at the top of the page to select the relevant chapters.

C.1 Active region structure and dynamics (Chapter 5)

Movies of intensity, running-difference intensity and Doppler velocity can be viewed using the drop-down menus for each respective spectral line. The movies show the active region viewed at the Western solar limb. The dynamic nature of the region at He I and O V temperatures can be seen, along with the Doppler velocity trends within the O V loop and macrospicule. The Doppler velocity movies in the coronal lines also demonstrate the difficulties in determining absolute velocities in these lines.

C.2 CDS wide slit & TRACE active region dynamics (Chapter 7)

The CDS wide slit data obtained during the Loop Variability Campaign can be viewed as intensity, intensity running-difference and intensity average-difference movies, along with co-temporal TRACE and MDI observations, with the wide slit field of view overplotted.

APPENDIX C. CONTENTS OF THE CD-ROM

Of particular interest are the CDS wide slit movies which show images of sunspot active regions at chromospheric and transition region temperatures. These regions are highly dynamic at these temperatures, whilst appearing quiescent when viewed with TRACE. The residual burn-in profiles of the narrow slit, after calibration, are visible within the centre of the observations. Solar rotation has been removed from the wide slit movies; the position of the burn-in profiles then appears to move to the left, representing their fixed position on the detector. As mentioned in Chapter 7, part of the O V image is missing as this line is dispersed onto the edge of the NIS-2 detector.

The wide slit movies for the 12th and 13th show the dynamic plasma flow channels, also observed within the EJECT_V3 rasters. The sunspot plume above the umbra is clearly visible in O V. The propagating waves observed within the TRACE 171 Å loops are visible by eye on the 13th within the wide slit FOV, and are particularly clear in the 0800 UT data.

C.3 Html and pdf versions of the thesis

The CD-ROM contains html and pdf versions of this thesis which may be accessed by selecting the relevant options from the navigation bar.

Bibliography

- Ahmad, Q. R., Allen, R. C., Andersen, T. C., et al. 2002, *Physical Review Letters*, 89, 011301
- Aschwanden, M. J. 2004, *Physics of the solar corona* (Praxis Publishing Ltd., Chichester UK, and Springer, New York, 2004)
- Aschwanden, M. J., Fletcher, L., Schrijver, C. J., & Alexander, D. 1999, *ApJ*, 520, 880
- Baliunas, S. L., Donahue, R. A., Soon, W., & Henry, G. W. 1998, in *Astronomical Society of the Pacific Conference Series*, 153–+
- Banerjee, D., O’Shea, E., Doyle, J. G., & Goossens, M. 2001a, *A&A*, 380, L39
- . 2001b, *A&A*, 371, 1137
- Beckers, J. M. & Schultz, R. B. 1972, *Sol. Phys.*, 27, 61
- Beckers, J. M. & Tallant, P. E. 1969, *Sol. Phys.*, 7, 351
- Beer, J. 2000, *Space Sci. Rev.*, 94, 53
- Bentley, R. D. 1999, *CDS Software Note*, #54
- Berghmans, D. & Clette, F. 1999, *Sol. Phys.*, 186, 207
- Bewsher, D. 2002, Ph.D Thesis, University of St. Andrews, Scotland
- Bewsher, D., Parnell, C. E., Pike, C. D., & Harrison, R. A. 2003, *Sol. Phys.*, 215, 217
- Bohlin, J. D., Vogel, S. N., Purcell, J. D., et al. 1975, *ApJ Lett.*, 197, L133

BIBLIOGRAPHY

- Bray, R. J., Cram, L. E., & Durrant, C. J. 1991, *Plasma loops in the solar corona* (Cambridge Astrophysics Series, Cambridge: Cambridge University Press, 1991)
- Bray, R. J. & Loughhead, R. E. 1974, *The solar chromosphere* (The International Astrophysics Series, London: Chapman and Hall, 1974)
- Breeveld, E. 2000a, *CDS Software Note*, #56
- . 2000b, *CDS Software Note*, #55
- Brekke, P. 1999, *Sol. Phys.*, 190, 379
- Brekke, P., Kjeldseth-Moe, O., & Harrison, R. A. 1997, *Sol. Phys.*, 175, 511
- Brynildsen, N., Maltby, P., Foley, C. R., Fredvik, T., & Kjeldseth-Moe, O. 2004, *Sol. Phys.*, 221, 237
- Brynildsen, N., Maltby, P., Fredvik, T., & Kjeldseth-Moe, O. 2002, *Sol. Phys.*, 207, 259
- Brynildsen, N., Maltby, P., Kjeldseth-Moe, O., & Wilhelm, K. 2003, *A&A*, 398, L15
- Buchholz, B., Ulmschneider, P., & Cuntz, M. 1998, *ApJ*, 494, 700
- Caligari, P., Moreno-Insertis, F., & Schussler, M. 1995, *ApJ*, 441, 886
- Carcedo, L., Brown, D. S., Hood, A. W., Neukirch, T., & Wiegmann, T. 2003, *Sol. Phys.*, 218, 29
- Carlsson, M. & Stein, R. F. 1997, *ApJ*, 481, 500
- Chapman, G. A. 1994, in *Proceedings from IAU Colloquium 143: The Sun as a Variable Star: Solar and Stellar Irradiance Variations*. Edited by J.M. Pap, C. Frolich, H.S. Hudson, and S. Solanki, (Cambridge: Cambridge Univ. Press), p.117, 117→
- Chiu, Y. T. & Hilton, H. H. 1977, *ApJ*, 212, 873
- Christensen-Dalsgaard, J. 2002, *Reviews of Modern Physics*, 74, 1073
- Christopoulou, E. B., Skodras, A., Georgakilas, A. A., & Koutchmy, S. 2003, *ApJ*, 591, 416

BIBLIOGRAPHY

- Cooper, F. C., Nakariakov, V. M., & Tsiklauri, D. 2003, *A&A*, 397, 765
- Cowsik, R., Singh, J., Saxena, A. K., Srinivasan, R., & Raveendran, A. V. 1999, *Sol. Phys.*, 188, 89
- Cranmer, S. R. 2002, *Space Sci. Rev.*, 101, 229
- De Moortel, I. 2000, Ph.D Thesis, University of St. Andrews, Scotland
- De Moortel, I., Hood, A. W., Ireland, J., & Walsh, R. W. 2002a, *Sol. Phys.*, 209, 89
- De Moortel, I., Ireland, J., Hood, A. W., & Walsh, R. W. 2002b, *A&A*, 387, L13
- De Moortel, I., Ireland, J., & Walsh, R. W. 2000, *A&A*, 355, L23
- De Moortel, I., Ireland, J., Walsh, R. W., & Hood, A. W. 2002c, *Sol. Phys.*, 209, 61
- Deforest, C. E. & Gurman, J. B. 1998, *ApJ Lett.*, 501, L217+
- Del Zanna, G. 1999, Ph.D Thesis, University of Central Lancashire, England
- . 2003, *A&A*, 406, L5
- Del Zanna, G. & Mason, H. E. 2003, *A&A*, 406, 1089
- Delaboudiniere, J.-P., Artzner, G. E., Brunaud, J., et al. 1995, *Sol. Phys.*, 162, 291
- Dere, K. P., Bartoe, J.-D. F., & Brueckner, G. E. 1989a, *Sol. Phys.*, 123, 41
- Dere, K. P., Bartoe, J.-D. F., Brueckner, G. E., Cook, J. W., & Socker, D. G. 1989b, *Sol. Phys.*, 119, 55
- Dere, K. P., Landi, E., Mason, H. E., Monsignori Fossi, B. C., & Young, P. R. 1997, *A&AS*, 125, 149
- DeRosa, M. L. & Toomre, J. 2004, *ApJ*, 616, 1242
- Di Giorgio, S., Reale, F., & Peres, G. 2003, *A&A*, 406, 323
- Domingo, V., Fleck, B., & Poland, A. I. 1995, *Sol. Phys.*, 162, 1

BIBLIOGRAPHY

- Doyle, J. G. & Madjarska, M. S. 2003, *A&A*, 407, L29
- Doyle, J. G., van den Oord, G. H. J., O'Shea, E., & Banerjee, D. 1998, *Sol. Phys.*, 181, 51
- Dunn, R. B. & Zirker, J. B. 1973, *Sol. Phys.*, 33, 281
- Farge, M. 1992, *Annual Review of Fluid Mechanics*, 24, 395
- Fludra, A. 2001, *A&A*, 368, 639
- Fredvik, T., Kjeldseth-Moe, O., Haugan, S. V. H., et al. 2002, *Advances in Space Research*, 30, 635
- Golub, L., Krieger, A. S., Silk, J. K., Timothy, A. F., & Vaiana, G. S. 1974, *ApJ Lett.*, 189, L93+
- Gurman, J. B., Leibacher, J. W., Shine, R. A., Woodgate, B. E., & Henze, W. 1982, *ApJ*, 253, 939
- Habbal, S. R. & Gonzalez, R. D. 1991, *ApJ Lett.*, 376, L25
- Hale, G. E. 1908, *ApJ*, 28, 315
- Handy, B. N., Acton, L. W., Kankelborg, C. C., et al. 1999, *Sol. Phys.*, 187, 229
- Hansteen, V. H., Betta, R., & Carlsson, M. 2000, *A&A*, 360, 742
- Harrison, R. A., Bryans, P., & Bingham, R. 2001, *A&A*, 379, 324
- Harrison, R. A., Sawyer, E. C., Carter, M. K., et al. 1995, *Sol. Phys.*, 162, 233
- Haugan, S. V. H. 1997, *CDS Software Note*, #47
- Huang, N. E., Shen, Z., Long, S. R., et al. 1998, *Proc. R. Soc. Lond. A*, 454, 903
- Innes, D. E., Inhester, B., Axford, W. I., & Wilhelm, K. 1997, *Nature*, 386, 811
- Ireland, J., Walsh, R. W., Harrison, R. A., & Priest, E. R. 1999, *A&A*, 347, 355
- Kjeldseth-Moe, O. & Brekke, P. 1998, *Sol. Phys.*, 182, 73

BIBLIOGRAPHY

- Spruit, H. C., Nordlund, A., & Title, A. M. 1990, *Ann. Rev. Astron. Astrophys.*, 28, 263
- Sterling, A. C. 2000, *Sol. Phys.*, 196, 79
- Suematsu, Y. 1998, in *ESA SP-421: Solar Jets and Coronal Plumes*, 19–+
- Tandberg-Hanssen, E. 1995, *The nature of solar prominences* (Dordrecht ; Boston : Kluwer, c1995.), 358–+
- Thomas, J. H. & Weiss, N. O., eds. 1992, *Sunspots: Theory and observations; Proceedings of the NATO Advanced Research Workshop on the Theory of Sunspots*, Cambridge, United Kingdom, Sept. 22-27, 1991
- Thompson, W. T. 1994, *CDS Software Note*, #13
- . 1998, *CDS Software Note*, #51
- . 1999, *CDS Software Note*, #53
- . 2000, *CDS Software Note*, #49
- . 2003, *Personal communication*
- Thompson, W. T., Haugan, S. V. H., & Young, P. 1998, *CDS Software Note*, #46
- Torrence, C. & Compo, G. 1998, *Bull. Amer. Meteor. Soc.*, 79, 61
- Walsh, R. W. & Ireland, J. 2003, *Astronomy and Astrophysics Review*, 12, 1
- Wang, T. J., Solanki, S. K., Innes, D. E., Curdt, W., & Marsch, E. 2003, *A&A*, 402, L17
- Williams, D. R., Mathioudakis, M., Gallagher, P. T., et al. 2002, *MNRAS*, 336, 747
- Wilson, O. C. 1978, *ApJ*, 226, 379
- Withbroe, G. L., Jaffe, D. T., Foukal, P. V., et al. 1976, *ApJ*, 203, 528
- Yamauchi, Y., Moore, R. L., Suess, S. T., Wang, H., & Sakurai, T. 2004, *ApJ*, 605, 511
- Young, P. R., Del Zanna, G., Landi, E., et al. 2003, *ApJS*, 144, 135
- Zhukov, V. I. 2005, *A&A*, 433, 1127

BIBLIOGRAPHY

Phew!